UNIVERSITY OF SOUTHAMPTON

FACULTY OF ENGINEERING, SCIENCE AND MATHEMATICS
School of Engineering Sciences

Abrasion-corrosion of Cast CoCrMo in Simulated Hip Joint Environments

by

Dan Sun

Thesis submitted for the degree of Doctor of Philosophy

May 2009

UNIVERSITY OF SOUTHAMPTON
ABSTRACT
FACULTY OF ENGINEERING, SCIENCE & MATHEMATICS
SCHOOL OF ENGINEERING SCIENCES

Doctor of Philosophy

By Dan Sun

Metal-on-metal (MoM) hip joint replacements have been increasingly used for younger and more active patients in recent years due to their improved wear performance compared to conventional metal-on-polymer bearings. MoM bearings operate at body temperature within a corrosive joint environment and therefore are inevitably being subjected to wear and corrosion as well as the combined action of tribo-corrosion. Issues such as metal sensitivity/metallosis associated with high levels of metal ion release triggered by the wear and corrosion products remain critical concerns. During the past few decades, significant research has been conducted into understanding the wear/lubrication mechanisms within the MoM hip joints in order to improve their performance and thereby prolonging their life. However, not much attention has been given to the combined effect of wear and corrosion of such devices in the hip joint environment, in addition, the role of third body particles and the effects of proteins have not been well understood.

In this work, a systemic approach is presented for the first time for the mapping of abrasion and tribo-corrosion performance of a cast CoCrMo (F75) in simulated hip joint environments. The effects of third body particles have been studied in the MoM context using 4 μm SiC, 1 μm and 300 nm Al_2O_3, as well as sub-micron $BaSO_4$. Modified tribo-testers (micro-abrasion, nanoindenter/scratching) incorporating a novel electrochemical cell have been used to monitor the abrasion-corrosion behaviour of the alloy *in situ*. The effects of solution chemistry, abrasives size / concentration and presence of proteins on the wear / corrosion level, wear-corrosion mechanisms, and the depassivation/repassivation kinetics of the CoCrMo have been explored. A variety of surface and sub-surface characterization techniques have been employed to identify the microstructual wear mechanism interactions. Results show that the change of protein concentration (0, 25% and 50% bovine serum) and pH (pH 7.4 and pH 4.0) of the test solutions can significantly influence the protein adsorption behaviour, which subsequently influence the wear rates (synergy), wear mechanisms as well as the wear-induced corrosion currents of the CoCrMo. For abrasion-corrosion tests, reducing abrasive size from 4 μm to 300 nm and/or abrasive volume concentration from 0.238 vol% to 0.006 vol% results in different abrasion-corrosion wear mechanisms (rolling or grooving abrasion) and the average wear-induced corrosion currents show a linear correlation with wear rates for 4 μm and 1 μm abrasives. For low volume concentration (< 0.03 vol%) slurries containing bovine serum, organo-metallic conglomerates have been found within the wear scars. These conglomerates help separate the surfaces, impose less damage to the surface passive film and polish the wear scars through a chemical mechanical polishing mechanism. In addition, tribo-corrosion tests at micro-/nano- scales reveal the effects of single abrasive particle on the surface/sub-surface microstructual change. This investigation has revealed the nanoscale wear mechanisms that generate nanoscale wear debris, the mechanical mixing of the surface nanostructure with adsorbed denatured protein and also the slip/dislocation systems that are present near and on abraded surfaces that are likely to disrupt the surface passive films. The findings give a better understanding of the evolution of the sub-surface nanocrystalline structures and tribo-layers formation seen for the retrieved implants. This near surface nanostructure layer and phase transformation might offer better wear resistance through these inherent self-protecting mechanisms (i.e. increased hardness); conversely, it may become the precursors to debris ejection and enhanced ion-release into the CoCrMo joints.

This work established an experimental technique that gives greater understanding of the tribo-corrosion behaviour of cast CoCrMo in simulated hip joint environments. In particular, the roles of third body abrasive particles and proteins have been addressed, which are relevant to clinical applications. The material multi-scale wear mechanisms as well as the evolution of the surface / sub-surface microstructures and tribo-layers have been elucidated, which provide new insights into the *in vivo* wear mechanisms of CoCrMo. The findings of this study may provide some important indications for improved MoM joint materials, design, manufacture and evaluation.

CONTENTS

LIST OF TABLES

LIST OF FIGURES

DECLARATION OF AUTHORSHIP

I, Dan Sun, declare that the thesis entitled

Abrasion-corrosion of Cast CoCrMo in Simulated Hip Joint Environments

and the work presented in the thesis are both my own, and have been generated by me as the result of my own original research. I confirm that:

- this work was done wholly or mainly while in candidature for a research degree at this University;
- where any part of this thesis has previously been submitted for a degree or any other qualification at this University or any other institution, this has been clearly stated;
- where I have consulted the published work of others, this is always clearly attributed;
- where I have quoted from the work of others, the source is always given. With the exception of such quotations, this thesis is entirely my own work;
- I have acknowledged all main sources of help;
- where the thesis is based on work done by myself jointly with others, I have made clear exactly what was done by others and what I have contributed myself;
- parts of this work have been published as:

    1. Sun, D., Wharton, J., Wood, R., Le, M., Rainforth, M. *Microabrasion-corrosion of cast CoCrMo alloy in simulated body fluids*. Presented at the 34th Leeds-Lyon Tribology Symposium, Lyon, France, 2007. **Tribology International**, 42 (2009), 99-110.
    2. Sun, D., Wharton, J., Wood, R. *The Effects of proteins and pH on tribo-corrosion performance of cast CoCrMo – a combined electrochemical and tribological study*. Presented at the 5th China International Symposium on Tribology, September 2008, Beijing. **Tribology – Materials, Surfaces & Interfaces,** 2 (2009), 150-160.
    3. Sun, D., Wharton, J., Wood, R. *Effect of protein adsorption on the wear-corrosion behaviour of cast CoCrMo alloy in simulated healthy and infected joint environments*. In the 16th International Colloquium Tribology, 15-17 Jan, 2008. Stuttgart /Ostfildern, Germany.
    4. Sun, D., Wharton, J., Wood, R. *Micro-abrasion mechanisms of cast CoCrMo in simulated body fluids.* Presented at the 1st International Conference on Abrasive Processes, September 2008, Cambridge. **Wear** (2009), doi: 10.1016/j.wear.2009.03.005.
    5. Sun, D., Wharton, J., Wood, R. *Abrasive size and concentration effects on the tribo-corrosion of cast CoCrMo alloy.* Presented at the 35th Leeds-Lyon Tribology Symposium, September 2008, Leeds. **Tribology International** (2009), doi:10.1016/j.triboint.2009.03.018.
    6. Sun, D., Wharton, J., Wood, R. *Microabrasion-corrosion of cast CoCrMo – effects of micron and sub-micron sized abrasives.* Accepted for oral presentation at the 17th International Conference on Wear of Materials, April 2009, Las Vegas. **Wear** (2009), doi:10.1016/j.wear.2009.01.011.

Signed: **Date:**……………05/05/2009……

ACKNOWLEDGEMENTS

I would like to thank my two supervisors, Professor Robert Wood and Dr Julian Wharton, for their kind guidance, inspiration and endless support during this work. I also thank them for motivating my interest in academics, and for giving me their trust, and the opportunity to pursue a career in academics. I thank Dr Martin Browne, Professor Mark Taylor, Dr Prasanna Srinivasan from University of Southampton for their suggestions and help during the relevant technical discussions. I would also like to extend my thanks to Professor Duncan Dowson, Dr Yu Yan and Professor Zhongmin Jin from University of Leeds for their suggestions, inspirations in the subject of orthopaedic tribology and encouragement given to me during the time we met.

I wish to thank the technicians within School of Engineering Sciences, Mr Steve Pilcher for his assistance in modifying / maintaining the micro-abrasion rig, Mr Robert Barnes, Mr Chris Williams and Mr Dave Beckett for assisting in machining samples. The help and advice of Drs Terry Harvey, Ling Wang, Jelili Bello and Shuncai Wang throughout the project is also gratefully acknowledged. I would like to express my appreciation to all my colleagues in the national Centre for Advanced Tribology at Southampton, in particular, Mandar, Lily, Jun Sun, Ramkumar, James, Mark, Fitri, Nick and Jenny for numerous stimulating discussions, support and encouragement. Others who provided help include Dr Graham Beamson (NCES, Daresbury) for his guidance during XPS analysis, Miss Le Ma, Dr Peng Zeng and Professor Mark Rainforth from University of Sheffield and Mr Kevin Lee, Dr Paul Warburton from London Centre for Nanotechnology for the preparation of FIB sections and interpreting the results.

I am grateful to all my friends at Southampton, Guoping Li, Zoe Yao, Yan Hou, Jing Lv, Kun Wei, Hairong Mu, Qian Li, Patrick Gong, Jia Wan, Xiaoguang Qiao, Hong Zhang, Liang Zhu and many others for being the surrogate family during the years I stayed here and for their continued moral support.

Finally, I am forever indebted to my parents, parents-in-law and my husband Yan Jin for their endless love, understanding, patience and encouragement. The magnitude of their contribution can not be expressed in a few words, so it is to them that this thesis is dedicated.

LIST OF ABBREVIATIONS

THR: total hip replacement
MoM: metal-on-metal
MoP: metal-on-polymer
CoC: ceramic-on-ceramic
UHMWPE: ultra-high-molecular-weight-polyethylene
HCP: hexagonal close packed
FCC: face centre close packed
SF: synovial fluid
HA: hyaluronic acid
3D: three-dimensional
BSA: bovine serum albumin
pI: isoelectric point
CV: cyclic voltammetry
EIS: electrochemical impedance spectroscopy
EHL: elastohydrodynamic lubrication
PMMA: poly(methyl methacrylate)
OCP: open circuit potential
ENM: electrochemical noise measurement
EPN: electrochemical potential noise
ECN: electrochemical current noise
SEM: scanning electron microscopy
FIB-SEM: focused ion beam- scanning electron microscopy
XPS: X-ray photoelectron spectroscopy
AFM: atomic force microscope
EBSD: electron beam scattered diffraction
PBS: phosphate buffered saline solution
BS: bovine serum
Ag/AgCl: silver/silver chloride
SC: sliding-corrosion
AC: abrasion-corrosion
EDX: energy dispersive X-ray analysis
ISE: ion-induced secondary electron
CPE: constant phase element
DC: direct current
SWR: specific wear rate
NC: nanocrystalline
S%: percentage synergy
SIT: strain induced phase transformation
FEA: finite element analysis
TEM: transmission electron microscopy
SKP: scanning Kelvin probe

LIST OF SYMBOLS

λ: fluid-film thickness to surface roughness ratio
h_{min}: minimum film thickness
R_q: root mean square surface roughness value
S_s: Sommerfield number
η: viscosity
$\overline{U}$: entraining velocity
W_N: load
R: radius
E’: equivalent elastic modulus
E: Young’s modulus
η_0: base viscosity
α': pressure-viscosity index
V: wear volume loss
K: wear coefficient
L: sliding distance
H: hardness
E_{corr}: corrosion potential
i_{corr}: corrosion current density
η_{op}: over potential
β: Tafel slope
i: current density
i_0: exchange current density
W_m: mass of the material
M_r: molar mass
Q: charge
z: number of electrons
A: area
t: time
F: Faraday’s constant
S: synergy
T: total material wear rate
W_0: material lost purely due to the mechanical process
C_0: material lost purely due to the corrosion process
C_w: wear-enhanced corrosion
W_c: corrosion-enhanced wear
V_{w-c}: volume loss by wear-enhanced corrosion
P: density
I: measured current
I_0: baseline current
I_{peak}: peak current
I_{∞}: baseline current at $t = \infty$
b: diameter of the wear scar
κ: specific wear rate
T_{sc}: total material loss due to 2-body sliding wear
T_{ac}: total material loss due to 3-body abrasion and corrosion
S_{ac}: synergy interaction under the abrasion-corrosion condition
Z: impedance
R_s: solution resistance
Q’: constant for defining impedance
ω: angular frequency
n: CPE exponent
R_p: polarization resistance
I_s: intensity from the film

I_s^0: intensity from the substrate
X_s: local concentration in mole fraction
d: film thickness
λ_s: attenuation length
σ_y: yield strength
k_y: strengthening coefficient
d_g: grain diameter
S_c: severity of contact
v: abrasive volume fraction
$H^{'}$: effective hardness
S*: critical contact severity
I_{ave}: average current noise level
I_a: electrochemical current measured during abrasion-corrosion
I_{corr}: corrosion current measured prior to abrasion when sample is under static immersion
τ: time constant
N_p: number of entrained particle
D_p: diameter of the abrasive particle
F: frictional force
μ: coefficient of friction

Chapter 1

Introduction

1.1 Background of hip joint replacements

Before the advent of artificial hip and knee replacements, patients with severe arthritis and/or injured joints often suffered from continuous pain and decreased functional capacity of their joints. Today, the prosthetic joint replacement has drastically improved the life-quality of millions of patients worldwide. For most patients, end-stage arthritis occurs in the lower extremities such as the hip and knee. Therefore, hip and knee joint replacements have taken a considerable share of the artificial joint market. For example, 50,000 total hip replacements (THRs) are performed each year in the United Kingdom [2]. The design and development of joint replacements are receiving constant attention in terms of improvement in wear and corrosion performance. This current investigation will focus on the cast CoCrMo alloy commonly used for metal-on-metal (MoM) hip replacements.

THR material configurations that are commonly seen include metal-on-polymer (MoP), metal-on-metal (MoM), and ceramic-on-ceramic (CoC), see Figure 1.1. The material selection for a hip replacement normally depends on the surgeon's preference, the patient's age group and their activity level.

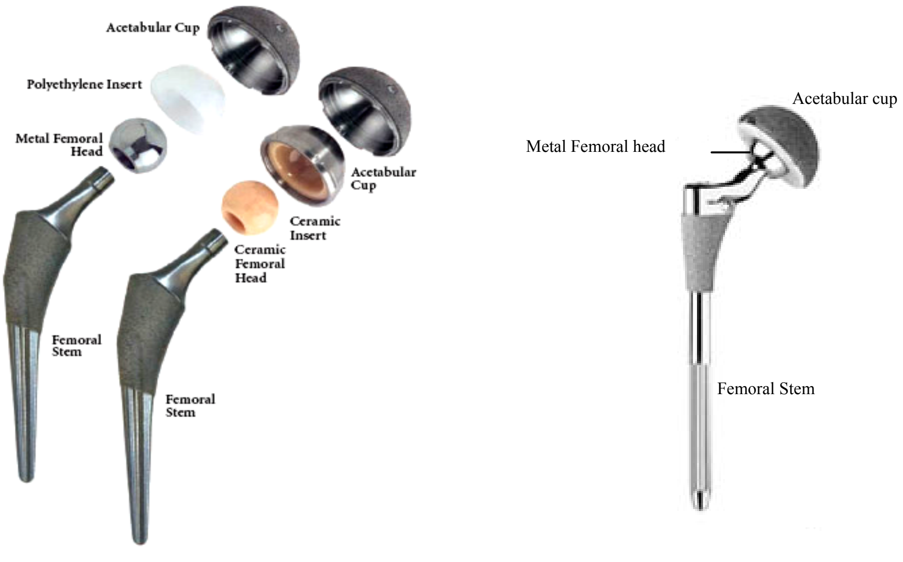

Figure 1.1: Typical examples of metal-on-polymer, ceramic-on-ceramic and metal-on-metal total hip replacement designs [3, 4].

In the last few decades, the MoP bearing design has been the most widely used in hip replacement surgery [5]. However, the side effect of osteolysis (bone resorption) induced by high level of polymeric particle release from the bearing surfaces is driving the development of more wear resistant hip implants [6]. In recent years, MoM bearings have received renewed interest for hip arthroplasties. In addition to the fact that MoM implants exhibit much lower volumetric wear compared with the MoP joints, they also permit the use of thinner acetabular cups and larger diameter femoral heads, with the advantage of reduced dislocations without incurring the risk of fracture associated with ceramic-on-ceramic implants [7].

Table 1.1 summarizes the existing and potential hip joint material combinations, their advantages / drawbacks.

Table 1.1: Existing and potential material combinations for hip replacements [5].

Materials	Advantage	Disadvantage
Metal-on-polymer	Low cost, high manufacture precision not required	Production of large number of wear particles with higher risk of osteolysis
Ceramic-on-polymer	Low cost, low toxicity	
Metal-on-metal	High wear resistance, can self-polish moderate surface scratches	Metal sensitivity, long-term and systemic reactions to metal debris and /or ions not known
Ceramic-on-ceramic	Higher wear resistance than MoM, high biocompatibility	Sometimes high wear, higher cost, technique-sensitive surgery, risk of fracture
Ceramic-on-metal	Highest wear resistance, lowest wear rate (100 times lower than the MoM [8]).	Latest development, undergoing clinical trials

The development of modern MoM THRs with large diameters (in the order of 38-66 mm) has enabled the introduction of a new generation of hip resurfacing based on the MoM system (Figure 1.2). Resurfacing is an attractive alternative to THRs as it replaces the femoral head and acetabular surfaces with a highly polished metal surface, hence minimum bone removal is achieved. It also allows better stress transfer to the proximal femur and offers inherent stability and an optimal range of movements [9]. With these significant advantages, MoM hip resurfacings have been increasingly advocated for younger and more active patients and currently it takes about 10% of the market share for hip implants. Early results with MoM hip resurfacing were promising and complications commonly seen in the THRs such as earlier implant stem loosening appears to be rare with such a configuration [9].

Figure 1.2: An example of cast CoCrMo 52 mm MoM hip resurfacing system

Table 1.2 shows the comparison between total hip replacements and hip resurfacing devices.

Table 1.2: Comparisons between total hip replacements and hip resurfacings [10].

	Total Hip Replacement	**Hip Resurfacing**
Loading	Higher level of stress shielding	More natural
Activity	Patients are advised to refrain from strenuous activities	Patients have been observed to be able to carry out previous pre-op activities
Proprioception	High	Low
Economics	Cheaper procedure	More expensive to the health-care provider, higher cost of the prosthesis, longer operating time and higher skills required
Targeted patients	Suitable for older patients with lower bone quality. Revision more complicated.	Suitable for younger patients with stronger bone. Better bone. reservation, easier for revision procedure

1.2 Present challenges for MoM bearings

As the new generation of MoM hip resurfacing has only gained popularity in recently years, long-term performance data are not yet available. However, since these joints are targeted for younger and more active patients, an improved service life performance is needed for such devices. Potential complications associated with hip resurfacings are thought to be similar to those expected with MoM THRs, such as infection, pain, joint loosening, etc [11]. Metallosis, *i.e.*, release of metal wear product such as debris and ions, is also a major concern in relation to *in vivo* wear / corrosion of such devices, since concentrations of metal debris/ions are higher if the prosthesis is worn or loose. Concern has been raised about the biological effect of the elevated levels of metal ions and particles found in the blood, tissues and lympho-reticular system in patients with MoM bearings [9], but no definite conclusions have been reached to date with regard to the possible systemic and local effect of metal wear/corrosion products from MoM arthroplasties [11]. Nevertheless, orthopaedic engineers and surgeons have been constantly striving to improve wear and corrosion performance of MoM bearings.

1.3 Objectives of this study

Extensive studies on the effect of wear [12-23] and corrosion [24-27] of metallic hip implants have been carried out in the past, however, only in recently years has the interest in the combined effects of wear and corrosion emerged. Also quite surprisingly, for cast CoCrMo alloy - the major alloy used for hip resurfacings, little knowledge has been obtained so far in terms of its tribo-corrosion behaviour under hip joint environments. The reports on its detailed material degradation mechanisms *in vivo* and *in vitro* are sparse in the literature. This project aims to improve the understanding of tribocorrosion behaviour of the cast CoCrMo alloy, especially tribological processes involving third body abrasive particles. It will help to develop better insights into the material degradation processes that occur in tribo-corrosion systems and ultimately contribute to the evaluation and development of such materials for hip resurfacing applications. This work will provide a comprehensive characterization on the tribo-corrosion performance of cast CoCrMo in hip joint environments with the focus on the effects of third body particles. This thesis aims to answer the following questions:

- What are the tribological, electrochemical and tribo-corrosion characteristics of cast CoCrMo in different simulated body fluids and under various tribological conditions including two-body sliding, three-body abrasion, nanoindentation and nano-scratching? Knowledge of how different test conditions influence the wear rate, corrosion levels and repassivation kinetics is fundamentally important in order to fully understand the MoM performance.

- What is the influence of proteinaceous material and pH level of the hip joint fluids? In particular, the effect of protein adsorption on the tribo-corrosion performance of the cast CoCrMo alloy needs to be addressed.

- What is the influence of abrasive particle size, concentration and hardness on the abrasion-corrosion behaviour of the cast CoCrMo? The interrelationship of these parameters is currently not fully understood.

- What is the effect of a single abrasive particle and how can this be linked to the overall material degradation of cast CoCrMo caused by multiple abrasives? The understanding between wear mechanisms seen at microscopic and nanoscopic scales needs to be explored.

- How does the overall surface degradation of cast CoCrMo relate to sub-surface microstructual changes resulting from the abrasion-corrosion processes? Can laboratory results be more closely related to the actual wear mechanisms often seen clinically on retrieved MoM implants?

- Can mechanical and electrochemical models be constructed for the *in vitro* tribo-corrosion process for cast CoCrMo? These are essential for establishing a more comprehensive understanding of the MoM bio-tribo-corrosion performance and assisting the future development of MoM designs, materials and/or surface modifications.

1.4 Thesis structure

This thesis consists of four parts, containing 10 chapters. The first part is the literature review, introducing the relevant subject areas, background information of the present study and state of arts in the research field. It is divided into sections that are relevant to the subject areas under study, such as the overview of hip replacements, hip joint environment, tribology, corrosion and tribo-corrosion of MoM joints. Information regarding existing testing techniques have also been included aiding the explanation of current research interests and analysis methods. These sections are intended to provide background information and to gain an initial understanding on the subject areas covered in this study.

The second part of the thesis consists of a single chapter on methodology. This chapter explains the materials, e.g., cast CoCrMo alloy, various abrasives and test solutions, used in this research, utilising information obtained from the supplier and literature. Further characterization of the test specimen is also carried out here, with experiments such as microscopy and microhardness testing. The details of tribological and electrochemical testing techniques, the design and modification of the existing equipments, as well as the post-test analysis techniques have also been covered in this part.

Part three of the thesis is divided into five chapters (Chapters 4 to 8). Chapter 4 elucidates the static corrosion properties of the cast CoCrMo, which includes results from open circuit potential measurement and potentiodynamic polarization. Work here is used to facilitate the understanding the behaviour of the alloy, which was subjected to further experiments in the following chapters. Chapter 5 presents and discusses results obtained from two testing conditions, namely, sliding-corrosion and abrasion-corrosion of cast CoCrMo using either zero or high volume fraction of SiC abrasives. In this chapter, the author adopted repeatable and reproducible test conditions which have been reported in the literature, the results obtained here can then be served as a bench mark data for future result comparisons. The specific wear rates, wear-induced electrochemical noise, synergy and wear scar profiles resulted from various test solutions have been discussed. Chapter 6 focused on the effects of pH associated with healthy and infected joints, its influence on protein adsorption and subsequently their effects on the tribo-corrosion performance of CoCrMo under similar test conditions as used in Chapter 5. Chapter 7 discusses the results obtained for various abrasion-corrosion tests employing abrasives with different size, concentration and hardness. Volume fraction of the abrasive test slurries has been gradually decreased towards clinical levels. The relationship between mechanical and electrochemical processes has been compared between different test conditions. Chapter 8 looks at the effect of a single abrasive particle during the abrasion-corrosion process. It aims to elucidate the microscopic and nanoscopic deformation mechanisms of the cast CoCrMo surface which is subjected to a repeated contact stress.

The third part, Chapter 9, combines the results from the previous five chapters and discusses specific wear rates / wear mechanisms, wear-induced corrosion current noise as well as repassivation kinetics as the abrasive size scales down from large to small, multiple to single abrasives. Tribological and electrochemical models were established for various abrasion-corrosion tests explaining the roles of proteins and different abrasives used. The surface deformation and sub-surface microstructual changes have been compared for surfaces that have undergone multiple and single contact stress conditions, and have been linked to the observations for *in vivo* studies in the literature.

The conclusions from all the work are summarized in Chapter 10. The contribution of the current work to the existing knowledge is shown. The answers to the questions raised in Chapter 1 have been addressed and suggestions for future work are also provided in this chapter.

Chapter 2

Literature Review

This chapter presents an extensive literature review of the main research topics for the present investigation. This is a multidisciplinary research project covering a wide range of subjects including biomaterials (specifically bio-metallic materials), protein biology, tribology, corrosion (electrochemistry) and tribo-corrosion. The focus of this literature review has been on the tribo-corrosion performance of metal-on-metal hip replacements under *in vivo* and *in vitro* body environments.

2.1 Hip replacements

2.1.1 An overview

The human hip joint is a complex bearing system with low friction. It provides stability due to the ball-and-socket configuration while at the same time, allowing a moderate range of motion [28]. The joint may lose its function due to trauma, disease or by abnormal usage. Each year, thousands of people who suffer from joint failure undergo hip replacement surgery, where the malfunctioned hip joint is replaced with an artificial hip implant. The hip replacement is a very common solution for osteoarthritis, rheumatoid arthritis, avascular necrosis, and traumatic arthritis. The cause and effects of arthritis are not under the scope of this study and will not be discussed further.

As mentioned previously in Chapter 1, the materials commonly used for modern hip replacements are metal-on-polymer (MoP), metal-on-metal (MoM), ceramic-on-ceramic (CoC) and ceramic-on-polymer (CoP). Historically, MoP bearings have been the dominating configuration in the total hip replacement field [5] and this type of hip prostheses is still the subject of considerable development at present. A major drawback of MoP bearings is the potential for high level of polymer (normally ultra-high-molecular-weight-polyethylene, UHMWPE) particle production. The natural biological response to these particles, *i.e.* immune system of the host, can alter the local pH around the implant and subsequently influence the balance between bone formation and resorption, and hence resulting in accelerated osteolysis (bone loss) [29].

In recent years, metal-on-metal (MoM) hip replacements based on CoCrMo alloys have increasingly become the preferred choice due to their superior wear resistance, longer service duration and reduced inflammatory osteolysis resulting from such devices. MoM hip resurfacing is one of the preferred options for younger and/or more active patients, as it replaces only the femoral head and acetabular surface and is less invasive. The detailed information regarding MoM hip replacements will be discussed in the following sections.

2.1.2 Bio-metallic materials for hip replacements

2.1.2.1 Stainless Steel

Stainless steels were amongst the first metals used in orthopaedics. Surgical stainless steel alloys are made with varying amounts of iron, chromium, and nickel. Stainless steels are resistant to uniform corrosion as a result of the presence of a thin adherent oxide film (passive film). They contain at least 11% chromium, which as a solid-solution alloying element in iron, aids the formation of a protective surface oxide film *in vitro* [30].

Types 316 and 316L (L designates low carbon) are the most commonly used stainless steels. The amount of alloying elements is kept low enough for 316L to be internally homogeneous, however this improves the corrosion resistance at the cost of reduced strength. While many implants are still manufactured from steel alloys, its use is now mostly limited to plates and screws and as such are not put under large loads for long periods of time. Fatigue failure and the susceptibility to pitting and crevice corrosion of stainless steels are limitations in the manufacture of modern stainless steel joint replacement implants.

2.1.2.2 Titanium and its alloys

Titanium (Ti) and its alloys exhibit high strength, low density, high corrosion resistance (dependent on the surface oxide layer) and modulus match with bone that is closer than any other implant alloys, these properties make it a good option for many load bearing applications [31]. However, titanium implants that were used as bearing surfaces became associated with tissue blackening and metallosis (caused by the presence of wear debris) resulting in a high level of aseptic loosening. Higher levels of this kind of failure were recorded for titanium alloys than for cobalt-chromium or stainless steel alloys [32]. In addition, the mechanical strength of Ti and its alloys are also reported to be lower than CoCrMo.

2.1.2.3 Cobalt based alloys

Cobalt (Co) based alloys, or more particularly CoCrMo, were firstly used in MoM implants over 40 years ago [33]. CoCrMo are more suitable for joint prostheses than stainless steels and due to their high strength (modulus of elasticity of CoCrMo alloys is about 210-230 GPa), excellent fatigue resistance and good corrosion resistance [34]. CoCrMo alloys contain chromium which forms a surface oxide that imparts a high corrosion resistance; it also forms carbides that increase the material strength. Co based alloys can be manufactured by either wrought or cast techniques. Wrought Co based alloy is made by forging the material at elevated temperatures under high pressure. The microstructure of such alloy consists of a face centred cubic (FCC) matrix with fine hexagonal close packed (HCP) platelets. Wrought CoNiCrMo is not recommended for the bearing surfaces of joint prosthesis because of its poor frictional properties with itself or other materials, but its superior fatigue and ultimate tensile strength make it suitable for applications which require a long service life without stable or dynamic failure [35].

Cast CoCrMo on the other hand, has been more widely adopted for hip bearing applications. Typically these alloys are divided into two categories: high carbon (>0.2 wt.%) and low carbon (<0.05 wt.%). Several studies have shown that the high carbon alloy has better wear resistance than the low carbon type [21, 36]. In particular, in the hip resurfacing industry the implant devices are mainly made of high carbon cast CoCrMo through a lost wax investment casting technique with the material composition conforming to ASTM F-75, see Table 2.1.

Table 2.1: Composition (wt.%) of CoCrMo alloy (ASTM F-75).

Specimen	**Co**	**Cr**	**Mo**	**Si**	**Mn**	**Ni**	**Fe**	**C**
ASTM-F75	Bal.	26.5– 30.0	4.5 – 7.0	≤ 1.0	≤ 1.0	≤ 2.5	≤ 1.0	≤ 0.35

At room temperature (*i.e.* 25 ºC), cast CoCrMo processes a microstructure in which a network of blocky carbides stand proud of the cobalt rich matrix at the microscale level (Figure 2.1). It is believed that these hard asperities can protect the softer matrix and reduce wear in the event of lubrication film starvation [37]. As shown in Figures 2.1, the cast CoCrMo microstructure shows blocky-shape $M_{23}C_6$ primary carbides (10-30 μm in size), where M is Cr, Mo and Co [23].

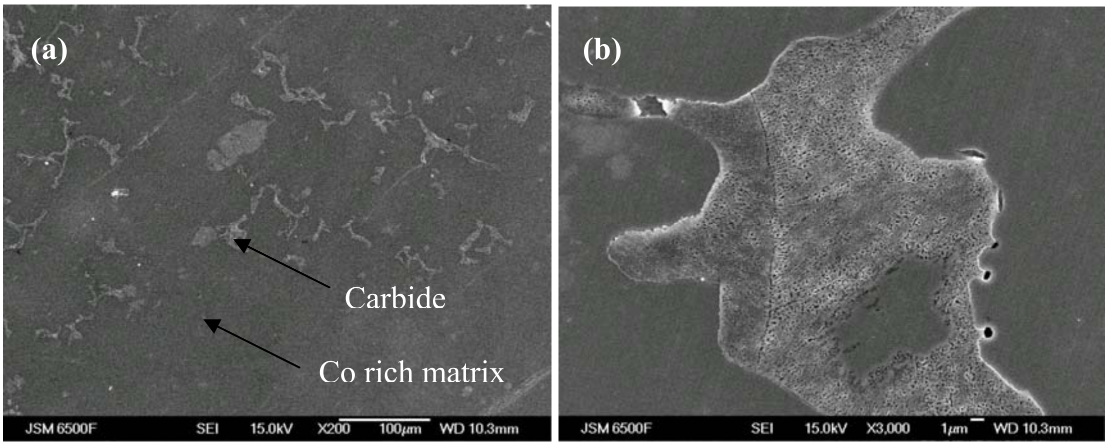

Figure 2.1: SEM image showing microstructure of cast CoCrMo: (a) network of carbides and (b) a higher magnification image of carbide.

CoCrMo alloys exhibit two allotropic forms, the HCP phase which is thermodynamically stable at room or human body temperature and the FCC phase, which becomes stable at elevated temperatures. However, the HCP phase is difficult to generate under normal cooling conditions and in most CoCrMo alloys the FCC structure is retained at room temperature. Accordingly, the FCC to HCP phase transformation is inhibited due to the limited chemical driving forces available at the transformation temperature [38]. The HCP phase resulting from martensitic reaction is known as ε-martensite. The metastable FCC phase can transform to HCP by plastic transformation (strain induced phase transformation, SIT) [39]. The martensitic phase resulting from the wear process has been identified at the subsurface of CoCrMo for pin-on-disc wear test specimens as well as the retrieved hip joint [40].

2.1.3 Metal-on-metal hip replacements

2.1.3.1 Metal-on-metal total hip replacements

Metal-on-metal (MoM) articulations have been seen as one potential solution to the problems associated with polymeric particle induced osteolysis. The observation that a small number of patients with first-generation MoM THR (the McKee-Farrar prosthesis in 1960s [33]) exhibited good clinical and radiographical results after 20 years *in vivo* have led to the development of second generation MoM hip prostheses, and in 1988 the Metasul prosthesis (CoCr on CoCr) was introduced into clinical practice [41]. The MoM total joints usually have ball components with ball diameter 28-32 mm. The remarkable tribological performance of the current MoM total replacement joints is attributable to improved materials, excellent manufacturing procedures and careful design of the head radius and the clearance.

2.1.3.2 Hip resurfacing

Resurfacing the damaged surfaces of the hip joint is not a new idea, and the history of the development of resurfacing is reported elsewhere [42]. It was not until the introduction of large diameter (38-66 mm) CoCrMo MoM devices that resurfacing became a viable alternative to THR. Cast CoCrMo alloy is commonly used for this type of prosthesis. The second generation of hip resurfacing was introduced by Heinz Wagner in Germany in 1991 [43]. A resurfacing device replaces the femoral head and acetabular surface and has a major advantage over THR in that most of the femoral head is retained. Minimum bone removal is achieved and this has great benefit for patients with a more anatomically sympathetic solution. However due to the nature (e.g., bone quality) of the femoral bone, hip resurfacing is not suitable for all patients, but is currently used in ~10% of patients receiving hip prostheses [44]. The theoretical advantages and disadvantages of hip resurfacing compared to conventional THR has been summarized by Roberts *et al* [9], as shown in Table 2.2.

Table 2.2: Advantages and disadvantages of hip resurfacings [9].

Advantages	Disadvantages
- Initial preservation of proximal femoral bone stock - More normal loading of femur eliminating proximal femoral stress shielding -Easier and more durable revision of femoral component if required - Reduced risk of leg lengthening/shortening - Reduced risk of dislocation - Improved range of movement - Improved function/activity level - Low wear bearing reducing risk of peri-prosthetic osteolysis - Better revision ability	- No long-term outcome data - No published controlled studies - Technically more demanding - New modes of failure-femoral head collapse

2.1.4 Design factors considered for MoM bearings

2.1.4.1 Femoral head radius and clearance

Good lubrication of the MoM bearing is essential for prolonging the implant life. The femoral head diameter is the most important geometric parameter in determining the lubrication of the artificial joints [44]. It has been reported that the predicted lubrication film thickness increases steadily as the femoral head diameter of the implant increases, due to the development of lubrication regimes from boundary to mixed [45]. Such an advantage has been utilized in large-diameter MoM hip resurfacing prostheses [8], however, it should be noted that the lubrication improvement in such a device can only be realized with appropriate clearances. Too large a clearance could shift the lubrication regime from mixed back to boundary [8]. The smallest diametrical clearance limit of 20 µm and optimal clearance of 100-150 µm have been recommended by Wimmer *et al*. [46].

2.1.4.2 Load

The normal cycle of human gait consists of two phases – the stance phase (begins with heel-strike and ends with toe-off,) and swing phase (begins with toe-off and ends with heel-strike) [47]. It was reported that the variation of hip-joint force during a walking cycle is characteristically two-peaked in form and the maximal loadings at the joints normally occur immediately before or after the transition from single to double support or *vice versa*, see Figure 2.2 [48].

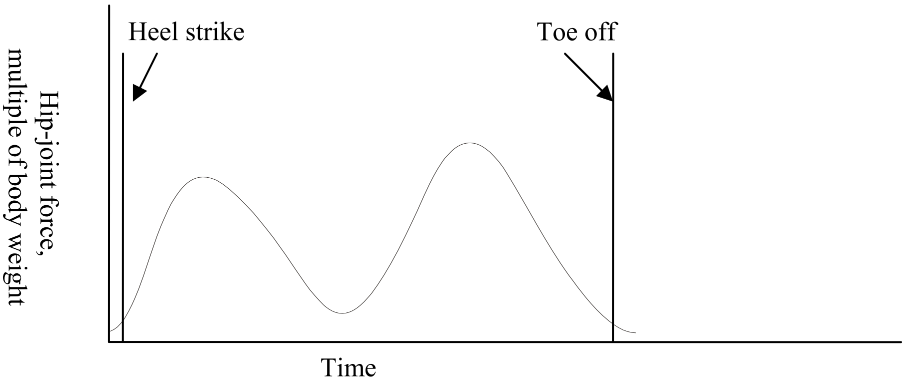

Figure 2.2: Hip joint force during the normal walking cycle [48].

The human hip joints may be subject to loads externally applied in addition to gravitational, muscle tension and inertial force actions [49]. Because of the muscle tension, compression on the hip is approximately the same as body weight during the swing phase of walking. Peak joint forces can range from 300-400 % body weight at normal walking speed, to 550 % body weight during fast walking and jogging and as high as 870 % body weight during stumbling [50]. This type of severe loading may be significant and may contribute to loosening of the hip implant. Bergmann *et al.* [51] carried out a comprehensive study on the forces and moments acting at the hip prosthesis and believed that higher activity levels could result in significant increases in the load experienced by the hip.

2.1.4.3 Other concerns associated with MoM bearings

Despite the improvement in the design and performance of the hip replacements, prevention of premature failure of hip implants is a continuing problem for physicians and orthopaedic engineers. Indeed, the lifespan of hip implants (normally 10-15 years [52]) is significantly lower than the 30-year goal set by the orthopaedic community. Over the past 10-30 years, researchers have experimented with various bearing surfaces in an attempt to evaluate the wear performance of artificial hip joints and therefore prolong their lives. The self-mating MoM articulation shows relatively low volumetric wear (lower than MoP and CoP) and friction coefficients comparable to other orthopaedic bearing materials [53]. However, low volumetric wear values do not necessarily correspond with a low number of wear particles. With an average size far below 1 μm, it has been estimated that up to 10^{14} particles could be released from a MoM articulation each year and subsequently these will migrate into the surrounding tissue [54]. Although *in vitro* cell culture studies have shown that various nanometer sized metal particles are potentially damaging to living cells at relatively low concentrations, these submicron sized metal particles have very limited capacity to activate macrophages to produce osteolytic cytokines at the volumes likely to cause bone resorption *in vivo* [8]. However, metal particles are not biologically inert and concerns exist regarding their potential genotoxicity. Elevated metal-ion levels associated with the corrosion process have been observed in patients with MoM joints [55]. However the boundaries between normal and toxic levels of the metal-ion concentrations are not as yet fully established and are still being investigated. Therefore, concern with metal debris and metal-ions and their potential toxicity still remains. The available data are insufficient to address the above concerns, and long-term studies are necessary to determine if the benefits of MoM bearings outweigh the associated risks.

2.2 The hip joint environment and proteins

2.2.1 Synovial fluid

Human joints are divided into two basic structural groups: diarthroses and synarthroses. Diarthroses are also called synovial joints, in which synovial fluid is present, and synarthroses, in which there is no fluid. The hip joint belongs to the category of synovial joints. Synovial fluid (SF) can be found in a healthy natural synovial joint which serves two major functions - to provide nutrition for the joint (the cartilage relies on molecular exchange with the SF for its metabolic and nutritional needs) and to lubricate the joint. Like other human body fluids, SF contains Chlorine ions (Cl^-). The exact constituents of SF are not fully known and it can vary from patient to patient or even from synovial joint to synovial joint. However, the main components of SF are known to be hyaluronic acid (HA) and proteins.

The protein content of SF is about 20 mg cm^{-3} and the major proteins are albumin, gamma-globulin, transferrin and seromucin [28]. Different conclusions have been reached on the effect of various components of SF on friction and wear of hip prosthesis, but the general agreement is that albumin and HA are the most important components, where albumin enhances boundary lubrication through adsorption on the joint material surface and HA is responsible for high viscosity which helps to increase the hydrodynamic component of the lubrication and decrease friction coefficient.

Figure 2.3 shows the three-dimensional (3D) chemical structure of a human albumin molecule. The molecule mainly consists of amino acids joined by peptide bonds. The basic structure of an amino acid consists of four parts: an amino group (-NH_2), a carboxyl group (-COOH), a central carbon (C) and a side chain. Bovine serum albumin (BSA) has similar molecular mass (66,430 g mol^{-1}) to the human albumin (67,000 g mol^{-1}). Each BSA molecule contains 582 amino acids and the major and minor axes of the BSA molecule are 14 and 4 nm, respectively [56]. The proteins in their natural states are normally folded. They only become unfolded or denatured (loss of their spatial structure) when undergoing 'denaturisation'.

Figure 2.3: Structure of human serum albumin [57].

For a patient who has undergone hip replacement surgery, the cartilage and the synovial joints have been largely damaged or removed and synovial fluids are limited within the joints. The joint fluid during the early post-operative period is mainly a mixture of blood and body fluids. The pH of the fluid surrounding a recently implanted prosthesis has been measured to be approximately pH 5.5 [58], with this value approaching the equilibrium physiological value of pH 7.4 within approximately ten days. However, it was suggested that the pH of the implant site can be as low as approximately pH 4.0 [59] (tissue acidosis) in cases of loosening or infection. It has been reported that acidosis (decreased local pH) is linked directly to the pain felt by the patient *in vivo* and contributes to sustained pain [60].

2.2.2 Adsorption of proteins

In a short time (<1 s) after implantation, proteins can be observed on biomaterial surfaces. In seconds to minutes, a monolayer of proteinaceous material adsorbs on most surfaces. The protein adsorption event occurs well before cells arrive at the surface [61]. The protein adsorption/reaction with the solid surface, particularly a metal surface, has attracted much attention in the literature [62-70]. It is widely accepted that the protein adsorption process involves protein transport (diffusion) from the bulk solution to the surface, adsorption onto the surface, conformational changes or orientation to a more stable position on the surface, and protein desorption to the bulk solution, as schematically shown in Figure 2.4 [71]. Proteins also tend to unfold or denature on the surface of some materials in order to minimize the free energy of the system. The driving forces for protein adsorption include both enthalpic and entropic contributions, the details of which are summarized in Table 2.3 [72]:

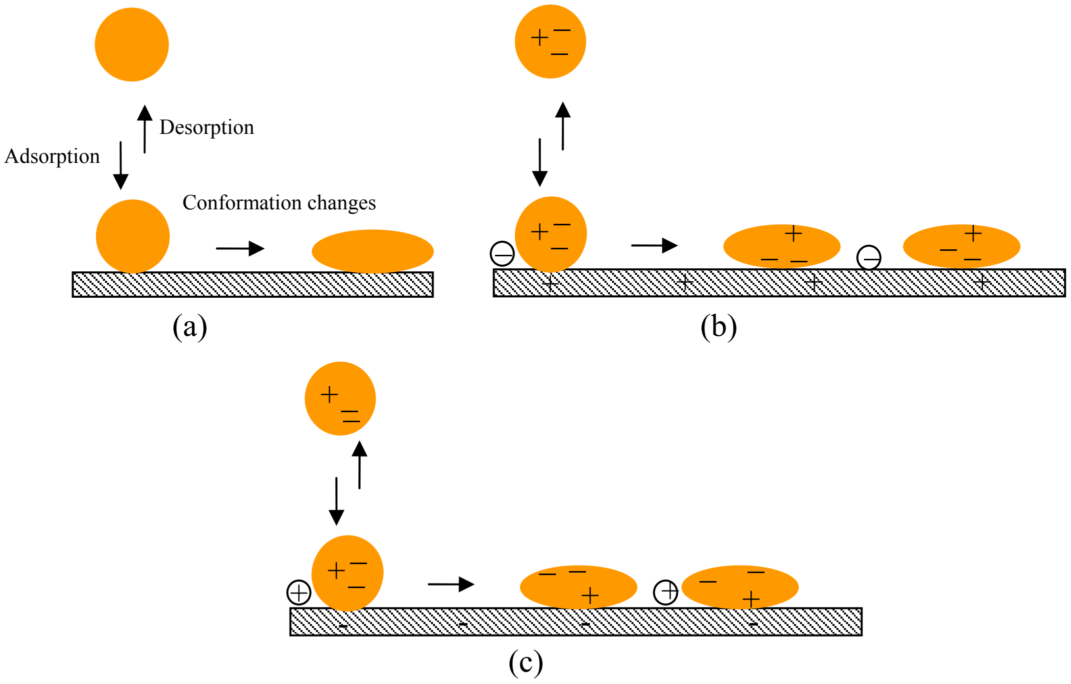

Figure 2.4: Protein adsorption from bulk solution to a surface [71]. (a) Protein adsorption onto neutral surface, (b) protein adsorption onto positively charged surface and (c) protein adsorption onto negatively charged surface.

Table 2.3: Energy contribution for protein adsorption [72].

Enthalpic contribution	**Entropic contribution**
• Van der Waals interactions • Hydrophobic interactions • Electrostatic interactions between oppositely charged surfaces and proteins (domains).	• Release of counter-ions and/or salvation water. • Reduction of the amount of ordered structure (e.g., α-helix or β-sheet) due to adsorption-induced conformational changes

The overall protein charge shows a strong dependence on the pH level of the surrounding environment [73-75]. This is important for the protein adsorption process, which is influenced by electrostatic attraction between a charged surface and an oppositely charged protein molecule as well as the electrostatic repulsion between the likely charged protein molecules. The charge of the protein is also important for their affinity to joint structures and also possibly for their entrainment onto the bearing surfaces. It has been reported that positively charged proteins can be entrained into the joint more rapidly than negatively charged proteins, and they also remain within the joint for a longer duration [76].

When a protein is present in a solution which is more acidic than the isoelectric point (pI), the protein will present a net positive charge, otherwise, it will be negatively charged [73]. The pI for the major proteins that are typically present within serum-based solutions are: albumin pI~4.5 [73], gamma globulin pI~8 [73], transferrin pI~5.7 [74], and fibrinogen pI~5.0 [75]. It has been well-documented that the pH level can directly influence the adsorption behaviour of proteins onto various substrate surfaces [77-79]. The pH dependency of the protein adsorption has been reported with the maximum adsorption typically found close to the isoelectric point (pI) [80]. As the protein net change decreases, the protein-protein interaction becomes more favourable and the protein-solvent interaction becomes less favourable. It has also been reported that an increasing concentration results in an increasing degree of multilayer formation. Multilayers can be expected to be more loosely adsorbed than the layer in direct contact with the surface [80]. Indeed, protein interactions with a passive film on a metallic surface are of considerable interest since they influence film breakdown, metal-ion release and film repassivation processes [81]. In addition, the relationship between pH and protein adsorption and how this affects the overall wear-corrosion performance of the CoCrMo alloy is generally still not well understood and will be addressed in Chapter 6 of this thesis.

Several techniques have been employed to investigate protein adsorption in order to understand the underlying mechanisms. The amount of proteins adsorbed onto and/or desorbed from a metal surface has been quantified through static immersion tests in conjunction with radio labelled proteins or quartz crystal microbalance measurements [70, 82]. Other techniques such as cyclic voltammetry (CV) and electrochemical impedance spectroscopy (EIS) have been used to study the relation between protein adsorption and electrical double layer capacitance [83-85]. It was found that the mechanisms and kinetics of protein adsorption onto metal surfaces depend on multiple factors such as type and concentration of proteins [70] , metals and their surface oxide [67, 86-88], applied potential [64, 71], metal surface roughness [89], temperature [28] and pH [90]. The effect of proteins on the wear and corrosion of metallic implants will be discussed later in this chapter.

2.3 Tribology of metal-on-metal hip joints

The word tribology was introduced in 1966 [91]. It originated from the Greek word '*tribo*' meaning 'rubbing' and it is the science of surfaces interacting under an applied load and in relative motion [92, 93]. The subject includes the study of friction, lubrication and wear. The definitions of these are listed below:

- Friction is the resistance encountered when one body moves over another with which it is in contact [93].

- Lubrication is the entrainment of fluids or release of solid lubricant into a contact, it occurs when opposing surfaces are completely separated by a lubrication film. For lubricated contacts, the applied load is carried by pressure generated within the film and frictional resistance to motion arises entirely from the shearing of the film [92, 93].

- Wear can be defined as the progressive damage, which occurs on the surface of a component or components as a result of their motion. Wear normally involves materials loss and is almost inevitable in the presence of friction [93].

2.3.1 Lubrication regimes of natural and artificial hip joints

The tribological performance of a hip joint depends on the fluid film (lubrication film) covering its surfaces [94]. A high ratio of fluid-film thickness to surface roughness (λ ratio) is desirable in order to reduce the friction and wear (Equation 2.1).

$$\lambda = \frac{h_{\min}}{[(R_{q1})^2 + (R_{q2})^2]^{1/2}} \qquad \ldots\ldots 2.1$$

Where $h_{\min}$ is the minimum film thickness (m), R_{q1} and R_{q2} are the root mean square (r.m.s) surface roughness values (m) of each surface.

A full appreciation of the tribological behaviour of the hip replacement can only arise through an understanding of their lubrication. There are three main lubrication modes [92], namely:

I. Boundary lubrication ($\lambda<1$): the surfaces are separated only by lubricant molecules or a tribo-film chemically attached to one or both surfaces. In the absence of the tribo-film, there will be pure metal-metal asperity contact.

II. Hydrodynamic lubrication ($\lambda>3$): also called full film lubrication. The sliding surfaces are separated by a fluid film that is thick in comparison to the roughness of the surfaces. In a hip joint context, the formation of such a film would depend on the loads on the joints, the surface sliding velocities, the lubricant fluid properties (e.g., constituents, pH, etc) and the implant geometry [95].

III. Mixed lubrication (elastohydrodynamic lubrication - EHL) ($1<\lambda<3$): intermediate lubrication regime between boundary and full film lubrication. It involves elastic deformation of the bearing surface and the piezo-viscous nature of the joint fluid.

Under EHL, the lubricant prevents the surface from interacting directly, but pressure waves conducted through it can produce elastic deformations in one surface opposite asperities in the other. This permits maintenance of a thicker lubrication film than would be otherwise expected. The result is excellent lubrication, with a slightly higher coefficient of friction than in pure hydrodynamic lubrication and with relatively low wear rates [96].

An idealised Stribeck curve has been constructed to demonstrate the representative values of the coefficient of friction in the various lubrication regimes, see Figure 2.5. The curve also shows the trends in coefficient of friction as the Sommerfield number (S_s) is increased [92].

$$S_s = \frac{\eta \overline{U} R}{W} \qquad \ldots\ldots 2.2$$

Where η is the lubricant viscosity (Pa. s), $\overline{U}$ is the entraining velocity (m s^{-1}), W is the load (N), R is the effective radius (m) of the femoral head.

Dowson and Jin [17] suggested that in order to achieve the minimum friction and wear, it is essential that the spherical bearing of the hip joint operates much nearer to the fluid film than to the boundary end of the mixed regime in a Stribeck curve.

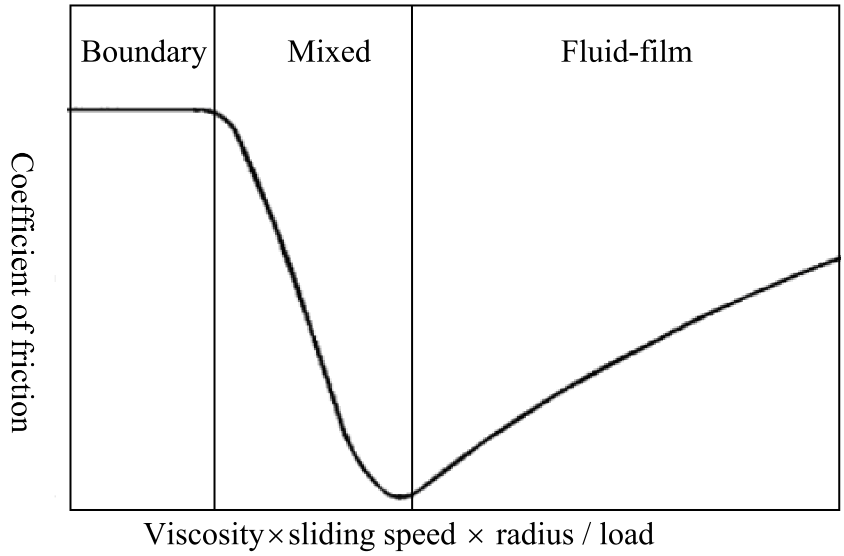

Figure 2.5: An idealized Stribeck curve shows modes of lubrication in hip joints [97].

Hamrock and Dowson [98], have developed the lubrication film thickness formula appropriate for the metal-on-metal hip implant (ball-in-socket), which can be expressed as follows:

$$h_{\min} = 2.8R\left(\frac{\eta\overline{U}}{E'R}\right)^{0.65}\left(\frac{W_N}{E'R^2}\right)^{-0.21} \qquad \ldots\ldots 2.3$$

Where $h_{\min}$ is the minimum film thickness (m) for the contact, E' is the equivalent elastic modulus $E' = \dfrac{E}{(1-\upsilon^2)}$, E = 210 GPa and υ = 0.3 for CoCrMo alloy, R is the equivalent radius, which a function of the head radius R_{head} and cup radius R_{cup}, see Equation 2.4 (m), $\overline{U}$ is the entraining velocity or half of the sliding velocity (m s^{-1}), W_N is the normal load (N), η (Pa. s) is the viscosity of a joint lubricant and is defined by Equation 2.5.

$$\frac{1}{R} = \frac{1}{R_{head}} - \frac{1}{R_{cup}} \qquad \ldots\ldots 2.4$$

The Barus equation gives the viscosity relationship with pressure, Equation 2.5.

$$\eta = \eta_0 \exp(\alpha' P) \qquad \ldots\ldots 2.5$$

Where η is the viscosity of a lubricant (Pa.s), η_0 the base viscosity (Pa.s) and α' the pressure-viscosity index for the particular lubricant (Pa^{-1}), and P is the hydrostatic pressure.

The minimum film thickness calculation for a ball on flat [92] point contact configuration, which is relevant to the experimental set up of the present study, has a different form and can be expressed by

$$h_{\min} = 1.79R\left(\alpha E'\right)^{0.49}\left(\frac{\overline{U}\eta_0}{E'R}\right)^{0.68}\left(\frac{W_N}{E'R^2}\right)^{-0.073} \qquad \ldots\ldots 2.6$$

The mechanisms of lubrication in natural joints are still a matter of some debate. In 1966, elasto-hydrodynamic lubrication (EHL) has been proposed by Tanner [99] to be the lubrication regime for natural joints, with the predicted lubrication film thickness of 0.1 μm. However, it seems unlikely that EHL alone would explain the lubrication mechanism; as human joints were too rough (~ 1 μm R_a value) [100]. Linn *et al*. [101, 102], with animal models, concluded that both hydrodynamic and boundary lubrication were acting concurrently. Only in 1986, Dowson and Jin [103, 104] found that the 'micro-EHL' effect produced local pressure on the asperities that squashed the high spots, giving a much smoother surface. This meant that although the fluid film thickness calculated (0.5 μm) were about the same as the undeformed roughness of the cartilage surfaces, when the 'smoothing' was taken into account, full fluid film lubrication was perfectly possible. This was the first time theoretical studies began to agree with the experimental observations of Roberts *et al*. [105].

Artificial hip joints replace the bearing surface of the natural joints and cause inevitable change in the local biological system (e.g., SF excretion). The lubrication models developed previously for natural joints may not apply to hip replacements and therefore the true lubrication regime for hip replacements has been the subject of much debate. It is suggested that the lubrication in replaced joints is primarily EHL, with the lubricant, produced by regenerating synovial tissues, resembling normal joint fluid [96]. In recent studies, Scholes and Unsworth [106] further predicted the lubrication modes of the artificial joints with different material combinations, and reported that mixed lubrication occurred for both MoP and MoM joints, whereas full film lubrication occurred for all ceramic joints, which was considered to be due to the much lower surface roughness of the ceramic components. Jin *et al*. [52, 107] based on numerical results, suggested that fluid film lubrication could be achieved for MoM bearing provided that the surface finish of the bearing surface and the radial clearance are chosen correctly and maintained. Other researchers also reported that boundary lubrication occurred in MoM bearings in simulator studies with proteins as the boundary lubricant [108].

2.3.2 Wear of hip replacements

2.3.2.1 Running-in and steady-state wear of hip replacements

The wear of hip replacement components is known to consist of two distinct phases: a relatively high-wear ‘running-in’ phase (also known as ‘bedding-in’) which often occurs within the first million cycles, followed by a ‘steady-state’ phase when the wear rate is relatively constant and much lower [7, 21], see Figure 2.6. A number of hypotheses have been proposed to explain these two distinct phases, including polishing of the metallic bearing surfaces and increasing conformity between the two articulating surfaces [16]. A third phase which is featured by a suddenly accelerated wear rate (failure), which occurs rarely and has not been commonly reported.

The above behaviour has been seen in numerous hip simulator studies and tribo-meter tests. Although steady-state occurs over the majority of the component life, it is the ‘running-in’ phase that is most likely to generate wear debris, initiate abrasive wear and cause ion release [109]. For example, MoM bearings are believed to attain very low wear rates of 1–5 µm y^{-1} after an intense running-in wear in the order of 35 µm y^{-1} [40]. It is believed that during the running-in period of cast CoCrMo MoM bearings, it is the hard carbides (which are standing proud of the Co-rich matrix) that come into contact, which effectively inhibits the matrix-to-matrix adhesive wear. The carbides may be broken off during this period giving rise to third body hard particles contributing to the subsequent abrasion process. Although the running-in period only takes up a very small portion of the MoM component life, the wear loss generated during this period can be significant. When the MoM system reaches a steady-state wear, it is more likely for nano-sized metal debris to be generated during joint movement.

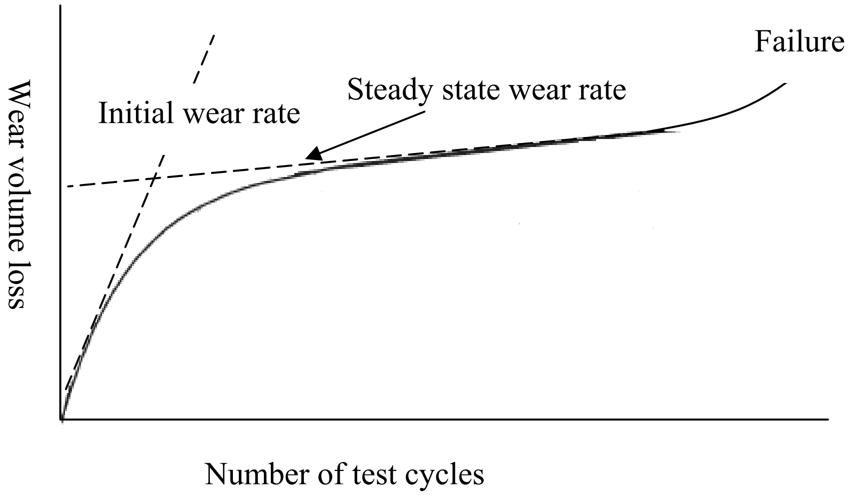

Figure 2.6: Volumetric wear as a function of wear test cycles showing biphasic behaviour of the hip replacement during wear, slope of the dashed lines corresponds to the wear rate [110].

Figure 2.7 shows examples of the wear damage seen on retrieved CoCrMo heads, where scratches with width of microns were evident. These scratches are likely to have been caused by third body particles generated *in vivo* [111-114].

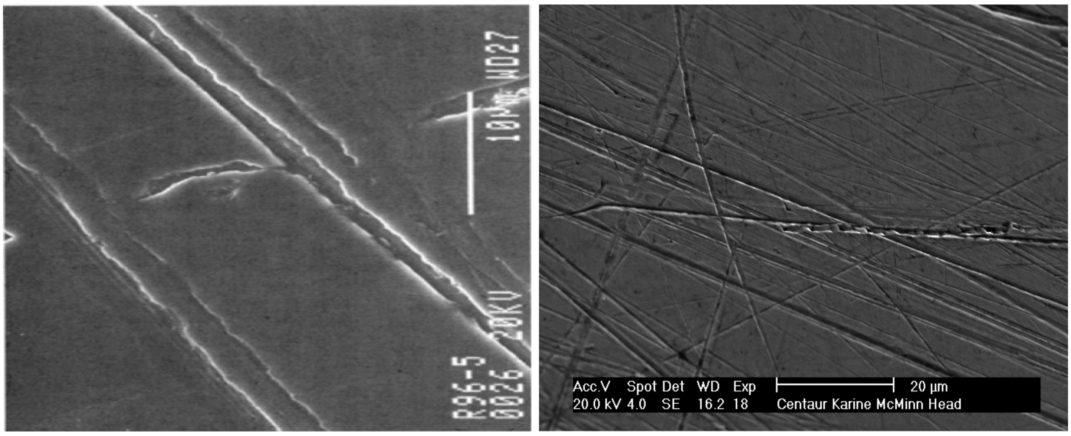

Figure 2.7: Wear damage seen on retrieved CoCrMo heads, [37, 115].

2.3.2.2 Wear mechanisms of MoM implants

Various phenomena can cause wear, such as adhesion, abrasion, delamination, corrosion. In the context of hip joint tribology, wear occurs through four major mechanisms: (a) adhesion, (b) abrasion, (c) corrosion and (d) fatigue [116]. The wear mechanisms associated with biomedical implants, particularly hip joints, are found to be a mixture of the above mechanisms and are a function of the following variables: type of materials used, contact stresses, lubricant and clearance, surface hardness and roughness, type of articulation due to motion, number of cycles, solution particle count / distribution, and oxidation [6].

(a) Adhesive wear

Adhesive wear occurs when two solid surface slides over one another under pressure. Surface asperities of the softer surface are plastically deformed, leading to material transfer and high friction, and eventually softer material is adhered to the harder surface [93].

(b) Abrasive wear

In abrasive wear, material is removed or displaced from a surface by hard particles or by hard protuberance on a counterface, forced against and sliding along the surface. Two-body grooving and three-body rolling wear modes are involved in abrasive wear [92]. The possible mechanisms of abrasive wear can be one of the following:

- Micro-cutting
- Fracture
- Ploughing

(c) Corrosive wear

Corrosive wear occurs as a result of an electrochemical reaction on a wear surface. The most common form of corrosive wear is through oxidation (oxidative wear) and is normally coupled with other mechanical wear.

Clinically, wear involving oxidation has been believed to be one of the reasons that accounts for the wear of metallic hip implants. Metals react with the oxygen rich biological environment and form a thin protective film that prevents corrosion. This film forms when exposed to *in vivo* conditions. However, the film can be stripped off when undergoing surface contact. Once the film is removed, the implant metal may degrade releasing metal-ions and particles. The formation of particulate creates three body wear that dramatically increases wear rates due to the substantial increase in roughness. This detrimental cycle applied on the film, metal-ion release and reformation of new film is referred to as oxidative wear [117].

(d) Fatigue wear

Material surfaces undergo fatigue wear due to the repeated contact stress. Wimmer *et al.* [46] suggested that for MoM surfaces under repeated contact stress, surface fatigue prevails initially. Cr– and Mo– carbides are fractured and torn off the surfaces bringing about additional surface fatigue. Bucher *et al.* [40, 118] found that the retrieved MoM sub-surface microstructure changed into a nanocrystalline structure. They also identified cracks, propagating through the nanocrystalline layer, suggesting that surface fatigue within a nanocrystalline surface layer could contribute to particle generation in metal-on-metal joints.

2.3.2.3 Wear of hip replacements by third body particles

Several studies have addressed the causes of the surface damage by third body particles [112-114]. Howie *et al.* [112] when investigating the long-term wear of the retrieved MoM components identified four types of wear on the implant bearing surfaces, namely, (i) polishing, (ii) fine abrasion, (iii) multidirectional dull abrasion (due to the non-linear relative movement of the bearing surfaces) and (iv) unidirectional dull abrasion. Types (ii) to (iv) are three body abrasive wear in nature, covered 18%, 5% and 2% of the femoral heads surface area within the contact zone. In addition to hard carbides from the CoCrMo alloy and other CoCr based debris, the third body particles that are present in the articulating joint and damaged surfaces also consist of bone fragments, precipitated calcium phosphate, and Poly(methyl methacrylate) (PMMA) from the bone cements [112].

Lippincott *et al.* [113] identified three body abrasive wear on the retrieved MoM surfaces, with the abradant being made up from detached hard carbides. This work suggested that the multi-directional motion of the CoCrMo components *in vivo* along with the abrasive slurry of small carbides may be the mechanism to produce the ‘lapped and highly polished’ wear zone surfaces on the retrieval implants. Reinisch *et al.* [114] studied wrought MoM bearing surfaces for a series of revised total hip joints and identified multidirectional scratches and surface embedded particles in the articulating zone of retrieved femoral heads. The damage was reported to be caused by Al_2O_3 third body particles, which were related to the manufacturing process that involves grit blasting with corundum (Al_2O_3) to achieve the desired implant surface roughness. This indicated that many of the similar MoM systems studied earlier would have been subjected to the same kind of three body wear by Al_2O_3 particles, even though this has been rarely discussed in the literature.

Indentation type of surface damage due to the presence of third-body particles can take place during the wear of hip joints, Figure 2.8. The indents originate from hard particles, which indent the metal matrix during rolling, or represent those areas, in which carbides had been fragmented [46].

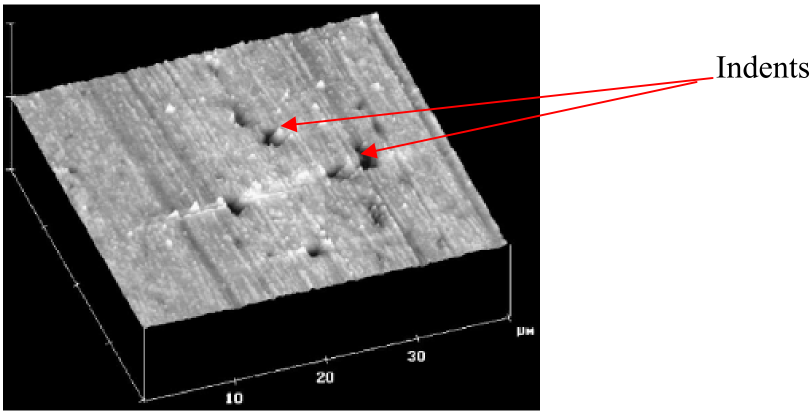

Figure 2.8: An AFM image of the ball from a MoM hip joint revealing the topography of grooves and indents. Indents which may be caused by the third-body particles are visible [46].

2.3.2.4 Wear rate and debris formation

Despite the complexity in wear mechanisms, a common starting point for investigating wear loss is the Archard wear equation which has been shown to apply to abrasion and adhesive wear. The Archard law asserts that wear volume loss V (mm^3) is directly proportional to the load W (N) on the contact, sliding distance L and is inversely proportional to the surface hardness H (Pa) of the wearing material [93].

$$V = K\frac{WL}{H} \qquad \ldots\ldots 2.7$$

Where K is know as the dimensionless wear coefficient. In engineering applications the quantity $\frac{K}{H}$ is defined as k (mm^3 N^{-1}m^{-1}), a dimensionless wear coefficient or specific wear rate and represents the volume of material removed by wear per unit distance slid per unit normal load on the contact.

MoM bearings have a much lower wear rate (20 to 100 times lower [119]) and produce significantly smaller volumetric concentration wear particles comparing to the MoP bearings [120]. However, the number of particles produced each year for MoM bearings has been estimated to be 6.7×10^{12} to 2.5×10^{14} which is 13 to 500 times the number of polyethylene particles produced per year by typical MoP bearings [54]. The UHMWPE debris isolated from retrieved tissues vary in size and morphology, ranging from 250 μm large platelet like debris to sub-micrometer globule-shaped spheroids 0.1-0.5 μm in diameter [121]. MoM generated particles are mainly nanometers in linear dimension [119, 122] and it is believed that the majority of metal wear particles are transported away from the periprosthetic tissue [44]. The initiation of bone resorption has been shown to be dependent on debris size and concentration with debris in the 0.1-1.0 μm size range and a volumetric concentration of 10-100 μm^3 per macrophage cell being the most biologically reactive [123]. Therefore it was concluded that the polymer debris are more likely to cause osteolysis than metallic debris [124]. However, metal wear particles are not bio-inert, the particles remained in the periprosthetic area have been associated with tissue necrosis [44] and concerns exist regarding the risk of delayed type hypersensitivity [119], potential genotoxicity [125] and carcinogenicity [126].

Table 2.4 summarizes the volumetric wear rate, dominant wear debris diameters and biological response generated by different hip replacements. It can be seen that the material combination plays an important role in the wear process and wear debris formation in the hip replacements.

Table 2.4: Typical volumetric and linear wear rates, particle sizes and biological responses in different bearings for hip implants.

Bearing materials	**Vol. wear rate (mm^3 / million cycles) [120]**	**Linear wear rate (µm / million cycles) [120]**	**Dominant particle diameters / µm [127]**	**Biological responses [127]**
MoP	30-100	100-300	Polymer, 0.01-1.0	Macrophages / osteclasts / osteolysis
MoM	0.1-1.0	2-20	0.01-0.1	Low osteolysis, cytotoxicity
CoC	0.05-1.0	2-20	0.01-0.02 0.1-10	Bio-inert, low cytotoxicity, Macrophages / osteoclasts / osteolysis

Factors that can contribute to the wear of implant materials have been listed below:

- Type of hip replacement (materials combination) [120]
- Wear testing methods (rig used)
- Lubricants viscosity [106, 128] and chemistry [36, 129],
- Materials composition (high or low carbon) [130, 131], surface conditions (hardness and roughness) [6], manufacturing process (as-cast, heat treated, or wrought) and the resultant microstructures (carbide precipitation or solid solution) [23, 36, 122, 132] (for MoM components)
- Macro and micro-geometry of the hip replacements (e.g., large diametral clearances exhibited higher amounts of wear compared to those specimens with smaller diametral clearances) [23].

2.3.3 Wear testing of hip replacement materials

A wide range of laboratory equipments, test methods and measuring systems have been employed to measure wear and to study wear mechanisms of hip replacements. The most commonly used techniques are:

- Pin-on-disc tribo-meter

- Reciprocating pin-on-plate tribo-meter
- Hip joint simulator

The pin-on-disc method is particularly useful in the evaluation of the nature of wear and friction of material pairs under well controlled, steady-state conditions of load, sliding speed and environment [131]. The pin-on-plate method sacrifices the steady sliding speed between specimens, but partially simulates the reciprocating action broadly associated with the hip joint [133]. For more comprehensive test results, a hip joint simulator test is required for comparative evaluation of hip joints with different designs and/or material combinations. Hip simulators can generate three-dimensional loading and motion patterns experienced by natural hip joints, and may provide a lubricating condition similar to the human joint condition [8]. However such tests are generally expensive and time consuming.

Recently, the micro-abrasion (ball cratering) test rig has been employed to study the wear [45] and wear-corrosion [134, 135] of CoCrMo for hip joints applications. Abrasive slurry is introduced, thus accelerated wear in extreme test conditions can be achieved under repeatable test conditions. This technique has provided another alternative for early device screening techniques.

2.4 Corrosion in bio-environments

Corrosion is the gradual degradation of materials by electrochemical attack, and is a concern particularly when a metallic implant is placed in a hostile corrosive human body environment [49]. For healthy human hip joints, the synovial fluid found in the joints is at ~ 37 ºC and with a normal physiological pH 7.4, Cl^- level ~ 0.9%. The protein concentration in the synovial fluid varies between 14-35 mg/ml depending on the diseased state [136], and the local pH can be as low as 4.0 under an severely infected condition [59].

2.4.1 The liquid/metal interface

When a metal is immersed into an electrolyte, charge will be re-distributed at the metal-electrolyte interface prior to any corrosion reaction. Such charge distribution depends on a few factors including the electronic properties of the metal, the adsorption of molecules from the electrolyte and the chemisorption of anions [137]. As is shown in Figure 2.9, the region of charge separation near the interface is defined as the electric double layer, or double layer. The electron transfer and separation behaviour of the metal-electrolyte interface resembles a capacitance being connected in parallel to a resistance [137].

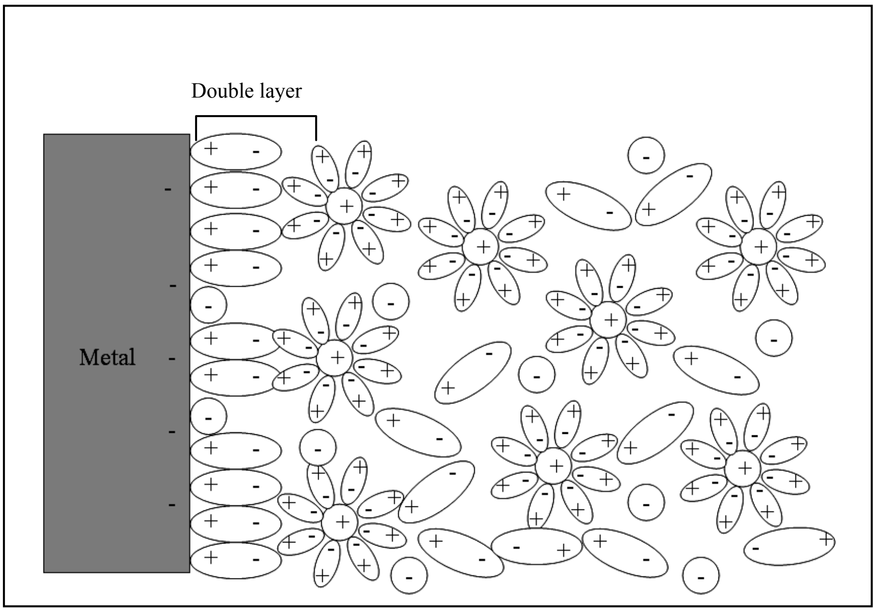

Figure 2.9: Electric double layer at metal-electrolyte interface in the presence of chemisorbed anions. The metal surface is in excess of negative charge in this case [138].

2.4.2 Corrosion of metallic implants

Corrosion is an essential aspect in the evaluation of biocompatibility of any kind of human implant material, as it plays a crucial role in the release of metal cations into the body environment (surrounding tissues) and in the degradation of the implants (decrease the structural integrity) [139]. It is therefore important to understand the electrochemical processes that influence the corrosion reaction. Generally, corrosion takes place by means of cathodic and anodic reactions. Cathodic reactions consist of the reduction of the oxidising agent, and anodic reactions consist of oxidation of metal (M) [140].

Cathodic reactions:

$O_2 + 2H_2O + 4e^- \rightarrow 4OH^-$ (oxygen reduction reaction)

$2H^+ + 2e^- \rightarrow H_2\uparrow$ (hydrogen evolution reaction)

Anodic reactions:

$M \rightarrow M^{z+} + ze^{-}$ Or

$2M + 2zH^{+} \rightarrow 2M^{z+} + zH_2\uparrow$ (acidic environment)

$2M + O_2 + 2H_2O \rightarrow 2M(OH)_2$

$M + H_2O \rightarrow 2e^{-} + MO + 2H^{+}$ (neutral or alkaline environments)

For CoCrMo alloys, the possible anodic reactions may be [141]:

$Co \rightarrow Co^{2+} + 2e^{-}$

$Cr \rightarrow Cr^{2+} + 2e^{-}$ (acidic environment)

$2Co + O_2 \rightarrow 2CoO$

$4Cr + 3O_2 \rightarrow 2Cr_2O_3$ (neutral or alkaline environments)

Figure 2.10 schematically illustrates the metal reaction in a liquid environment involving both anodic and cathodic reactions. The mass transfer (transport of reactants/products) to and away from the metal/electrolyte interface, as well as the charge transfer at the metal/electrolyte interface has been shown here.

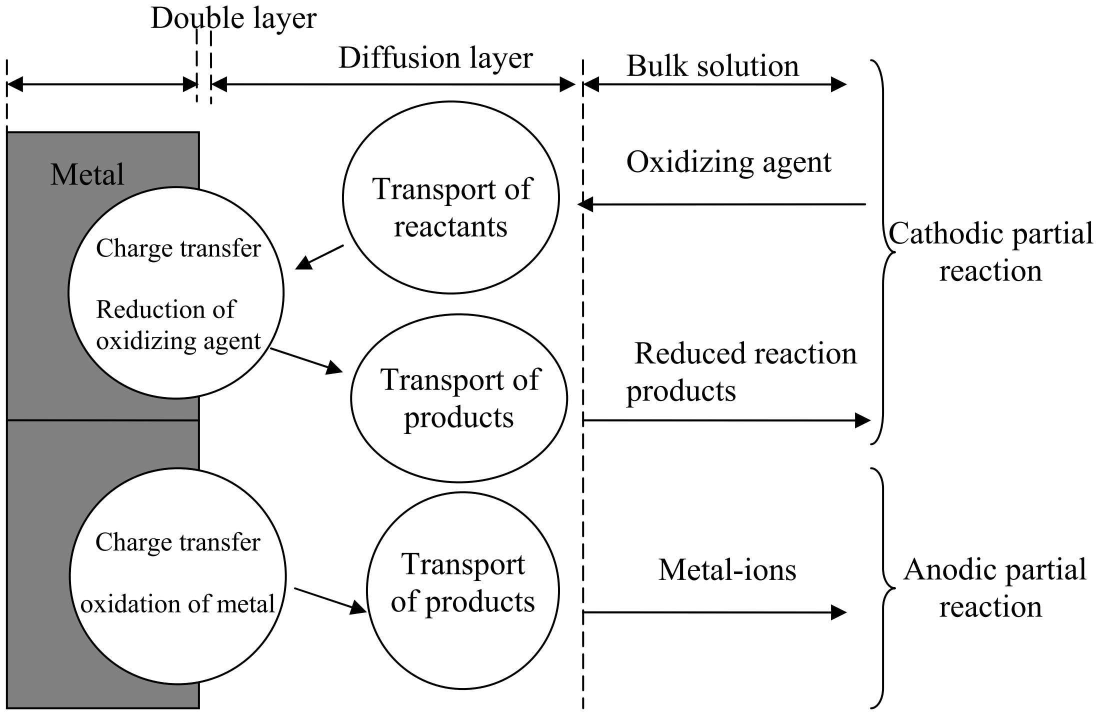

Figure 2.10: Reaction steps during the corrosion of a metal in liquid environments [137].

2.4.3 Corrosion and metal-ion release

Although corrosion resistant alloys such as stainless steels, CoCrMo alloys and Ti alloys have been employed for modern orthopaedics, corrosion is still an inevitable phenomenon when the implant is subjected to the human body environment. Corrosion of Co based alloys is regulated to a large degree by the presence of chromium oxide film. The surface oxide is highly insoluble at physiologic pH, but the acidosis associated with local infection is probably sufficient to produce pH below 6.0 that will produce significant loss of the passive layer and may interfere with normal repassivation [96].

Corrosion can limit the strength and the life of the material, leading to accelerated mechanical failure of the implant [139]. Some corrosion products have been implicated in causing local pain and swelling near implant region [142]. The release of solid corrosion products (predominantly consisting of metal oxides and hydroxides) may trigger local biological reactions in the human body, causing accelerated bone resorption and eventually bone loss [143]. The same corrosion product could also cause necrosis, fibrosis and inflammation [139].

The adverse effects of the metal elements used in MoM hip replacements remains a serious concern, as an increasing population of patients are intended to be younger, more active people who may have a postoperative life expectancy of longer than 30 years. It is well-documented that patients receiving MoM implants have increased / elevated metal-ion concentrations in blood and urine analyses [144, 145]. Metal-ions can bind with proteins and once bound these metal-ions are transported and either stored or excreted. Cobalt is transported from tissues to the blood and eliminated in urine within 48 h. Chromium and nickel has been reported to build-up in surrounding tissues, bone marrow and red blood cells. Excessive amounts of cobalt are considered to be carcinogenic because it inhibits the repair of damaged DNA and have also been associated to the patients' symptoms of pain, instability, and spontaneous dislocation. Necrosis of bone, muscle, and the joint capsule have been associated with Co ions [145].

Cr has two preferential valences Cr^{3+} and Cr^{6+}. There is substantial literature on Cr^{6+}, which is more biologically active (due to its high oxidizing ability), and can penetrate cell membranes. It is believed that it can be made carcinogenic by being reduced to Cr^{3+} in red cells and that it can cause contact dermatitis [146]. Figure 2.11 shows an example of the adverse effects that could be brought about by high levels of chromium ion concentrations.

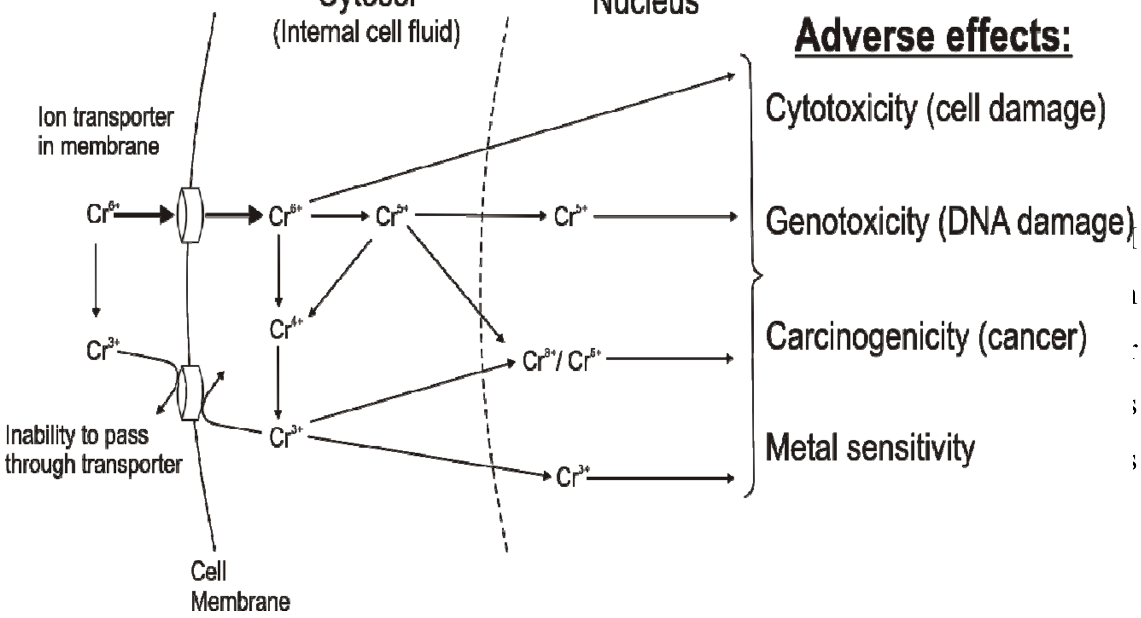

Figure 2.11: Possible adverse effects caused by chromium ions [147].

Table 2.5: Ion levels in patients with MoM resurfacing or with MoM THRs [148].

	Median Co ion level (nmol L^{-1})	**Median Cr ion level (nmol L^{-1})**
Hip resurfacing	38	53
THR	28	22
Upper limit for patients without implants	5	5

Montero-Ocampo *et al*. [149] reported that lower carbon content in the CoCrMo could contribute to greater chemical and microstructual homogeneity and thus a better corrosion resistance. This may result in a lower release rate of corrosion products from the implant but at a price of lower mechanical strength of the surface. The corrosion behaviour of CoCrMo (wrought) has also been investigated by Munoz and Mischler [150]. The corrosion potential and current were found to be influenced by both the presence of phosphate ions and proteins (albumin). The adsorption of phosphates reduces the corrosion rate of the alloy. While for albumin, on one hand it limits adsorption of phosphate ions thus accelerating corrosion, but on the other hand, it can modify the passive film properties and by acting as a cathodic inhibitor, can reduce the corrosion rate. The corrosion behaviour of CoCrMo has also been found to be dependent on the time of exposure to biological solutions [151]. Decreased corrosion rates were reported with increasing exposure time, which has been related to the enhanced protectiveness of the passive film formed with time.

2.4.4 Protein binding and its effect on metal dissolution

It has been well-documented that Co, Cr, Fe and Ni bind with albumin at carboxylate and tyrosine positions or bind with the –SH group of a single cysteine residue. Past studies have demonstrated that the primary high affinity binding site for the transition metals such as Cu(II), Ni(II) and Co(II) in humans is located at the N-terminus of albumin [152-154]. Protein will bind to metal-ions forming metal-protein-complexes or metalloproteins. An example of a metal-protein-complex is given in Figures 2.12.

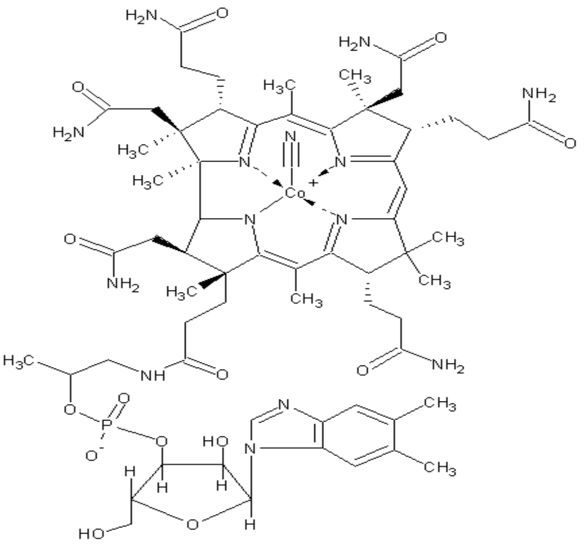

Figure 2.12: Structure of vitamin B12 showing the binding site with cobalt [155].

Research has shown that proteins have different affinities for different metals, probably as a result of various ligands in their molecular structure that have different bonding energies and therefore different affinities for specific cations [156]. Williams and Clark [157] have studied the effect of albumin on the corrosion rate of pure metal powders. They found that the corrosion of aluminium (Al) and titanium (Ti) was unaffected by the protein. The corrosion rates of Cr and Ni showed a slight increase, while Co and Cu dissolved to a much greater extent in the presence of protein. Williams *et al.* [158], found that under fretting proteins decreased the corrosion rate of the stainless steel plates, but did not have an appreciable effect on titanium alloys. The above studies imply that the corrosion rate of a metallic material is dependent on the composition of the specimen as well as the testing conditions. In a recent study on the effect of synovial fluid on corrosion properties of CoCrMo alloys [159], proteins were found to be adsorbed on the surface. It is hypothesized that a protein (normally negatively charged) film reduces the rate of corrosion by acting as a negatively charged barrier preventing corrosive anions (*e.g.* Cl^-) approaching the CoCrMo interface, the same proteins encourage a ligand-induced dissolution mechanism for increasing the ion release. Contu *el al.* [160], on the other hand, attributed the increased corrosion resistance of CoCrMo in bovine serum to the inhibition effect of proteins on the hydrogen evolution reaction, generating a diffusion barrier which causes the anodic dissolution to be under diffusion control. Goldberg *et al.* [161], carried out a series of scratch tests on CoCrMo (ASTM F75) specimens in protein containing solutions and found a decrease in peak currents in the presence of protein (decrease in corrosion rate). This was attributed to the barrier effects of the adsorbed protein preventing water from reaching the specimen surface, or lubrication resulting in less material removed from the surface during scratching.

2.4.5 Corrosion testing techniques

2.4.5.1 Potentiodynamic polarization

When a specimen is placed into the electrolyte, both reduction and oxidation reactions occur on its surface, which can be monitored by the measurement of cathodic and anodic currents. Anodic currents are present wherever corrosion is occurring. If the rate of oxidation is equal to the rate of reduction, the net current measured on the surface will be equal to zero. The equilibrium potential at which this occurs is called the open circuit potential (OCP) or corrosion potential (E_{corr}). This potential is measured relative to reference potential. The corrosion current density, i_{corr} (A cm^{-2}), is determined at the E_{corr}. It represents the actual corrosion rate in this state where the metal surface, although described as being in equilibrium, has many tiny anodic and cathodic regions therefore corrosion occurs at a specific rate given by the current density.

The departure of the potential of an electrode from the OCP (or reversible) value when an external current flows is called polarization. Polarization characteristics can be measured experimentally by conducting potentiodynamic polarization tests. Figure 2.13 shows a schematic potentiodynamic polarization curve of a passive alloy.

As can be seen in Figure 2.13, the scan starts from point 1 and progresses in the positive direction until termination at point 2. There are a number of notable features on the curve. The E_{corr} is located at point A. At this potential the sum of the anodic and cathodic reaction rates on the electrode surface is zero. As a result, the measured current will be close to zero. This is due to the fact that the potentiostat only measures the current which it must apply to achieve the desired level of polarization. As the potential increases, the curve moves into region B, which is the active region. In this region, metal oxidation is the dominant reaction. Point C is known as the passivation potential, E_{p}, and as the applied potential increases above this value the current density is seen to decrease with increasing potential (region D) until a low, passive current density is achieved (Passive region - region E). Once the potential reaches a sufficiently positive value (Point F, sometimes termed the breakdown potential E_{bd}) the applied current rapidly increases (region G). This increase may be due to a number of phenomena, depending on the alloy/environment combination. For some alloys, typically those with a very protective oxide, such as cobalt, the sudden increase in current is due to oxygen evolution.

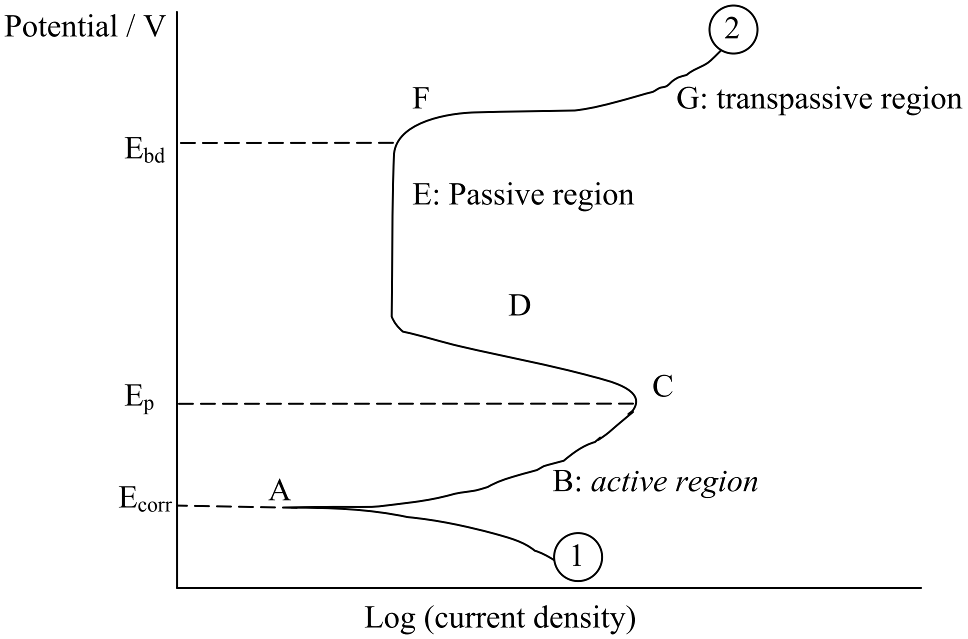

Figure 2.13: Schematic of a potentiodynamic polarization curve for a passive alloy.

From the anodic polarization curve it is possible to determine the ability of the material to passivate in a specific electrolyte, the potentials over which a passive layer exists and the rate of corrosion in this passive region. The closer the primary passive potential is to the OCP, the more likely the tendency to passivate, and the lower the passive current density the quicker the material will passivate. The potentiodynamic polarization scans also yield information about the corrosion rate. For reactions which are essentially activation controlled (*i.e.*, charge transfer controlled reactions), the current density can be expressed as a function of the overpotential, η_{op} (V), where $\eta_{op} = E_{\text{applied}} - E_{\text{corr}}$ as follows:

$$\eta_{op} = \beta \log \frac{i}{i_0} \qquad \text{……2.8}$$

This expression is known as the Tafel equation [162], where β is the Tafel slope, i the applied current density (A cm^{-2}), and i_0 the exchange current density (the reaction rate at the reversible potential for that particular reaction, in A cm^{-2}). Thus, the Tafel slope for the anodic and cathodic reactions occurring at open circuit may be obtained from the linear regions of the polarization curve, as illustrated in Figure 2.14. Once these slopes have been established, it is possible to extrapolate back from both the anodic and cathodic regions to the point where the anodic and cathodic reaction rates (i.e., currents) are equivalent. The current density at that point is i_{corr} and the potential at which it falls is the E_{corr}.

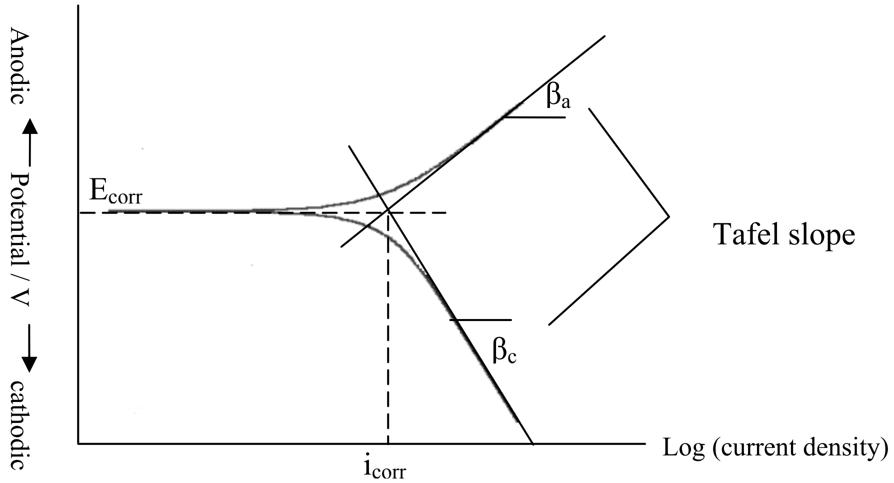

Figure 2.14: Typical Tafel plot showing corrosion potential and corrosion current density.

The corrosion current density may be combined with Faraday's law, and the material mass loss due to the current flow under OCP can be obtained:

$$W_m = \frac{M_r Q}{zF}$$

$$Q = i_{corr} At \qquad \text{……2.9}$$

Where W_m is the mass of material removed (g), M_{r} the molar mass of the specimen (g $\mathrm{mol^{-1}}$), Q the total charge (C) passed, z the number of electrons transferred in the reaction, and F is Faraday's constant (96500 s A $\mathrm{mol^{-1}}$), A is the area the current flow through and t is time.

2.4.5.2 Electrochemical noise measurements

Electrochemical noise is defined as the naturally occurring fluctuations in the corrosion potential and/or galvanic current of corroding electrodes [163]. Electrochemical noise measurement (ENM) can be used for the detection and evaluation of localized and general corrosion behaviour of the material. It is particularly sensitive to a localized corrosion process whereas the more traditional techniques (such as polarization tests) produce little information [164].

Electrochemical noise monitoring can be further subdivided into electrochemical potential noise (EPN) measurements and electrochemical current noise (ECN) measurements. The combined monitoring of potential and current is particularly useful. Fluctuations in the corrosion potential can indicate a change in the thermodynamic state of corrosion processes, while a change in the current noise is an indicator of the corrosion kinetics. Potential and/or current noise measurements have been employed in many tribo-corrosion tests to estimate corrosion rates and material depassivation/repassivation behaviour [165, 166].

2.4.5.3 Electrochemical impedance spectroscopy

Electrochemical impedance spectroscopy (EIS) is a non-destructive technique for examining many chemical and physical processes of the solid/solution interface. For example, by applying a small AC voltage across the metal/electrolyte interface, EIS is able to examine the interfacial properties of a metal in simulated body environments [167]. By knowing the response of the metal solution interface to the applied potential, how the interface is changed by adsorbed species onto the surface and/or metal dissolution can be studied. The metal / solution interface can be modelled using an ‘equivalent’ circuit consisting of simple components like resistors or capacitors which can help extraction of parameters of interest.

2.5 Tribo-corrosion of metallic implant materials

2.5.1 Synergistic effect

The synergistic effect or synergy refers to the phenomenon that occurs when wear and corrosion act together to create a total effect that is greater / or less than the sum of the individual effect of wear and corrosion.

Wear and corrosion processes involve many mechanical and electrochemical mechanisms, the combined action of which often results in significant increase (synergism, additive effects) and sometimes a decrease (negative synergy, antagonism) in material degradation [134, 168-170]. Strong synergistic processes (positive and negative) have been found for MoM components in artificial hip joint environments [134] depending on the type of materials pairings used. Synergy was also found to be affected by the presence of protein in the artificial hip joint environments [133, 171]. In the ball-on-disk tests conducted by Yan *et al.* for wrought CoCrMo in simulated body fluids [133], it was found that the corrosion effect on wear was the largest component of damage accounting for synergy in the tribocorrosion system.

The appropriate approach for evaluating synergy during wear-corrosion process has been a subject of much debate. The various methods proposed for measuring wear-corrosion synergism (or synergy, S) can be found in [172]. The ASTM standard G119-93 [173] has given a general guideline for determining synergy during abrasion-corrosion tests.

The synergy, S, (mm^3 N^{-1} m^{-1}) in abrasion-corrosion process is defined by the following Equation,

$$S = T - W_0 - C_0 \qquad \text{......2.10}$$

Where T (mm^3 N^{-1} m^{-1}) is the total material wear rate from a specimen exposed to the specified conditions, W_0 (mm^3 N^{-1} m^{-1}) is the pure mechanical wear rate, which is the material loss from a specimen when the electrochemical corrosion rate has been minimized by cathodic protection during the wear test, C_0 (mm^3 N^{-1} m^{-1}) is the material lost purely due to the corrosion process and is calculated based on the corrosion current density (i_{corr}) obtained during a potentiodynamic polarization scan.

Because i_{corr} is normally very small, the C_0 value calculated is often negligible (a few orders of magnitudes lower that W_0), and S is often estimated as

$$S = T - W_0 \qquad \text{......2.11}$$

The S can be divided into two components, W_c is the corrosion-enhanced wear and C_w is the wear-enhanced corrosion [134]:

$$S = C_w + W_c \qquad \text{......2.12}$$

The volume loss ($V_{\text{w-c}}$) caused by wear-enhanced corrosion could be determined from the electrochemical current noise data using Faraday's Laws [174, 175]:

$$V_{w-c} = \frac{QM_r}{z\rho F} \qquad \text{……2.13}$$

$$Q = \int_{t_0}^{t_i} (I - I_0)dt \qquad \text{……2.14}$$

Where Q is the total charge released during the wear assisted corrosion process (C), , which equals to the area under the current-time curve, M_r is the molar mass of the substance, F is the Faraday constant (96485 C mol^{-1}), ρ is the density of the material, t_0 and t_{i} are the starting and finishing time of the test (s), respectively, I is the measured current and I_0 the base line current noise in (A).

Hence C_{w} can be calculated as $V_{\text{w-c}}$ per unit load per unit sliding distance:

$$C_w = \frac{V_{w-c}}{W_N L} \qquad \text{……2.15}$$

Where W_N (N) is the applied load and L (m) is the sliding distance. In addition, the corrosion rate (in mm^{3}N^{-1}m^{-1}) without the mechanical element (C_0) is defined as:

$$C_0 = \frac{(i_{corr} At)M_r}{zF\rho W_N L} \qquad \text{……2.16}$$

Where A is the area (m^2) of the specimen exposed to the electrolyte during the potentiodynamic polarization scan.

2.5.2 Tribo-corrosion testing techniques

As stated earlier, most alloys used in bio-applications rely on a surface oxide film (the passive film) to provide protection against corrosion. The immersion of such materials in an electrolyte allows *in situ* characterization of the surface state through electrochemical techniques like OCP measurements, polarization measurements and impedance measurements [176].

In the presence of stress and strain, fretting, or wear, the possibility of mechanically assisted corrosion significantly increases, and the rate of corrosion can also increase [26, 177]. Such disturbance to the system will give rise to electrochemical noise. Various researchers have developed different wear testing methods coupled with *in situ* electrochemical techniques to investigate the nature of the oxide film damage of metallic specimens and studying the subsequent depassivation/repassivation events. These wear testing methods include scratching tests [161, 174, 178, 179], sliding tests [171, 175, 176, 180, 181], fretting [182, 183], abrasion [184], microabrasion [134, 167, 185-188], erosion [169, 189] and micro/nano-indentation [190-193]. The commonly used *in situ* electrochemical techniques have been summarized in [194] which include: (i) the application of a constant potential by means of a potentiostat and monitoring the variation of current with time, (ii) monitoring the current and potential changes that result from galvanic effect between the wear scar and the non-damaged (passive) surface or a counter electrode under open circuit conditions, (iii) application of a linear potential scan and recording of the current while rubbing and (iv) application of a small amplitude AC signal at open circuit potential or at constant imposed potential and measurement of electrochemical impedance as a function of frequency.

2.5.3 Tribo-corrosion of CoCrMo alloys

Only a few studies have focused on the tribo-corrosion performance of cast CoCrMo alloy in a biological environment. As this alloy is the major material used for MoM hip resurfacings, more effort is needed to establish a comprehensive understanding of the tribo-corrosion behaviour of cast CoCrMo in simulant body environments.

Goldberg *et al.* [161], carried out a series of scratch tests on CoCrMo (ASTM F75) specimens and measured the current transients resulting from depassivation and repassivation of the exposed reactive alloy. The exponential function (Equation 2.17) shows the correlation between peak currents and time constants for repassivation [161]:

$$I(t) = I_{peak} \exp\left(\frac{-(t-t_0)}{\tau}\right) + I_{\infty} \qquad \ldots\ldots 2.17$$

where I_{peak} is the peak current ($I_{peak} = I_{max} - I_{\infty}$), τ is the time constant for repassivation, t_0 is the time to produce the scratch, and I_{∞} is the baseline current at $t = \infty$.

Contu *et al*. [141, 160], studied the effects of pH and proteins on the tribo-corrosion behaviour of cast CoCrMo under fretting-corrosion test conditions. It was found that the repassivation rate slowed down with increasing pH because the co-precipitation of unstable Co oxide species hindered the formation of the Cr oxide passive film under alkaline condition. It has also been reported that the presence of protein reduced the corrosion current at both neutral and acidic conditions due to a barrier effect hindering both charge and mass transfer. However, pure bovine serum has been used in this study and the relatively low conductivity of the test solution has not been considered in this study.

Yan et al. [195-197], have studied the bio-tribo-corrosion behaviour of wrought CoCrMo under sliding wear using wet-cell pin-on-plate tribo-meter. Wear rates and the associated metal ion release has been investigated for high and low carbon wrought CoCrMo in various testing solutions simulating body fluids. A metal-protein complex was found on the surfaces which grew and developed with the metal oxides (Cr_2O_3/CoO etc) as sliding progressed. They later employed a friction simulator coupled with an integrated electrochemical cell to study the link between swing phase load, lubricant, and ion release under a dynamic loading [198].

2.6 Summary

A review of the literature covering biomaterials, orthopaedics (hip replacements), protein biology, tribology, corrosion and tribo-corrosion has been carried out in this chapter. The hip replacement history has been carefully discussed and the development of modern design of MoM bearings and MoM hip resurfacings has been reviewed. The wear, corrosion as well as the tribo-corrosion behaviour of CoCrMo has been emphasized based on both clinical and laboratory results. The reports on the cast CoCrMo, especially in the context of hip joint tribology, is generally lacking. This calls for detailed investigations on the tribo-corrosion performance of such a material in biological environments. A better understanding needs to be established for the material micro-/nano-scale wear processes induced by micron/sub-micron sized abrasives. Further investigation of the role of proteins and other environmental factors on the tribo-corrosion performance of cast CoCrMo alloy is required and would be a significant contribution to this topic.

Chapter 3

Methodology

This chapter describes the experimental methodology, including material preparation and characterization, rig design and modification, in addition to the test conditions for static electrochemical analysis and dynamic tribo-corrosion tests with *in situ* electrochemical noise measurements. It also reviews additional techniques used for the present investigation such as nano/micro-indenation and scratching, as well as the post-test analysis methods involving various microscopic techniques such as scanning electron microscopy (SEM), Focused ion beam scanning electron microscopy (FIB-SEM), X-ray photoelectron spectroscopy (XPS) and atomic force microscope (AFM).

3.1 Experimental plan

The focus of this study is to characterize the tribo-corrosion performance of cast CoCrMo alloy, more particularly abrasion-corrosion with the presence of third body particles in simulated hip joint environments. A microabrasion tester has been chosen as the major test rig for the following reasons:

- Robust abrasive wear test that is repeatable
- Need to study 3-body abrasive wear
- Easy incorporation of electrochemical cell
- Understanding depassivation/repassivation behaviour of the alloy
- Electrochemical noise measurements
- Small samples

To further investigate the secondary wear mechanisms that may be involved in abrasive wear, nano-indentation / nano-scratching tests have also been carried out. The detailed set up and modification of the microabrasion rig is described in Section 3.3. The structure of the experimental work is shown in Figure 3.1. The experiments of this study can be divided into three phases. Phase I involves the basic electrochemical characterization of the alloy including open circuit potential and potentiodynamic polarization, the results of which are to be compared with the subsequent electrochemical data obtained during dynamic test conditions (e.g., microabrasion). Phase II of the experiments includes the investigation of protein adsorption using surface characterization techniques such as AFM and XPS as well as electrochemical techniques such as EIS to determine the adsorbed protein morphology and surface layer thickness. This investigation may facilitate the understanding of effects of the surface films on the alloy during the tribo-corrosion processes. Phase III of the experiments focuses on the micro-abrasion-corrosion testing of cast CoCrMo in various test conditions involving multiple abrasives. The effects of test solution constituents and pH, abrasives size / hardness / concentration are studied. The experiments then moves onto investigating the effects of a single abrasive by employing wet-cell micro/nanoindentation and nano-scratching. The worn surface characteristics are studied using post-test analysis including SEM, FIB and AFM. It should be noted that the emphasis of this study is not to simulate the actual clinical wear, but to establish a test for mechanistically evaluating the wear and tribo-corrosion characteristics of cast CoCrMo that may be related to clinical wear-corrosion performance.

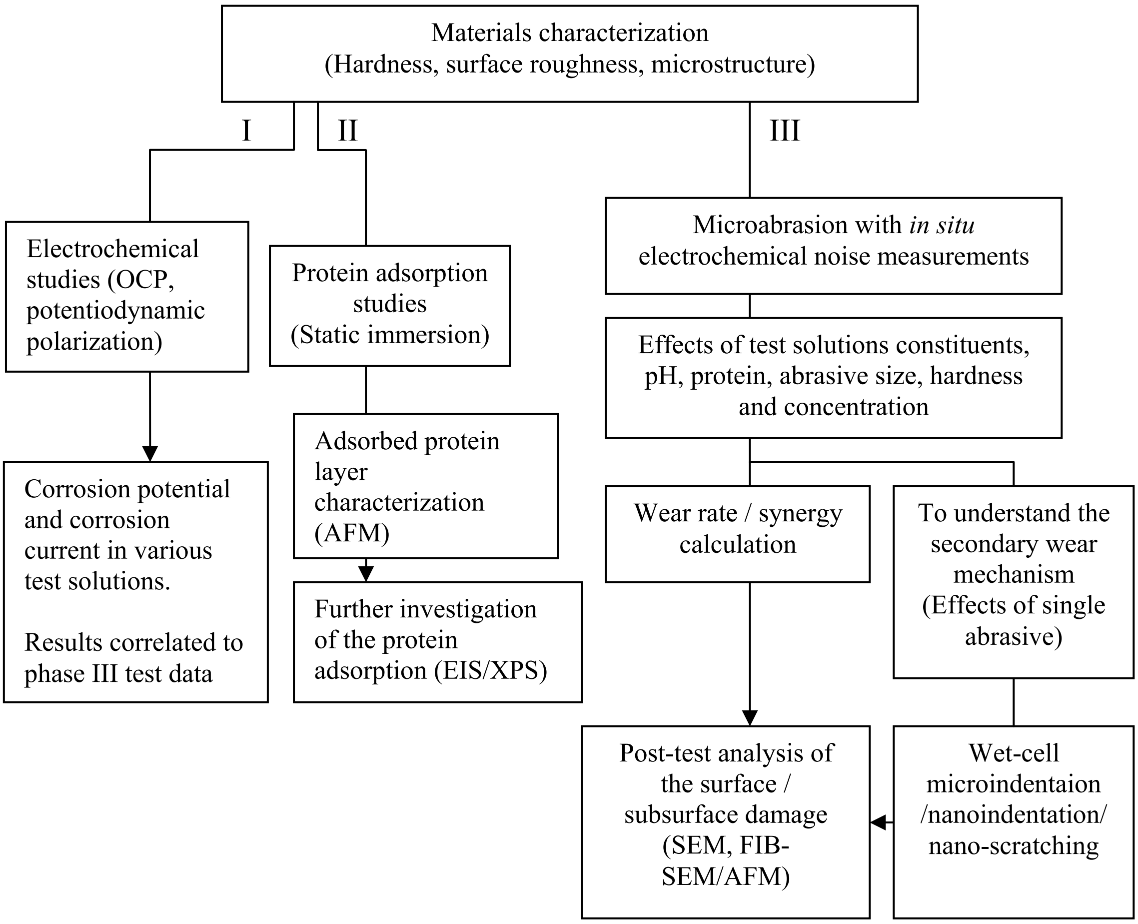

Figure 3.1: The map of experimental work undertaken for the present study.

3.2 Materials

3.2.1 Cast CoCrMo

The chemical composition of the cast CoCrMo (ASTM F-75) has been introduced in Chapter 2. Rectangular specimens (20 mm × 10 mm × 3 mm) were used for wear tests and circular specimens (15 mm in diameter and 3 mm thick) were used for polarization tests. Figure 3.2 (a) shows the optical image of the polished specimen after etching in a solution containing 15 cm^3 HCl, 10 cm^3 acetic acid and 10 cm^3 HNO_3 for 5 min. A network of block carbides (dark colour) is clearly visible in the cobalt rich matrix. The AFM image in Figure 3.2 (b) shows a typical carbide block standing proud of the surface and having a different microstructure from the matrix (Figure 3.2 (c)). The carbides are about 200 nm higher than its surrounding Co-rich matrix and are typically 25 μm in size. SEM imaging concurrent with crystal orientation determination using electron beam scattered diffraction (EBSD) (Figure 3.3) determines that FCC is the dominating crystallographic structure of a polished/etched specimen surface and the grain size ranges from 100 to 600 μm. The details of the phase identification method by EBSD can be found in Section 3.6.3.

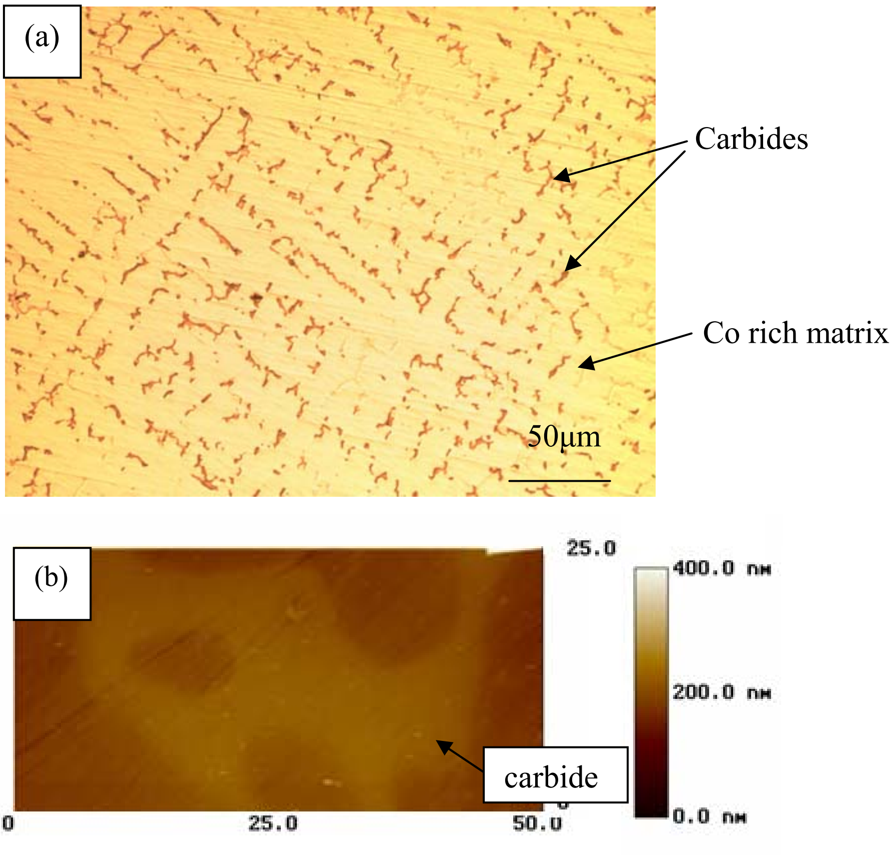

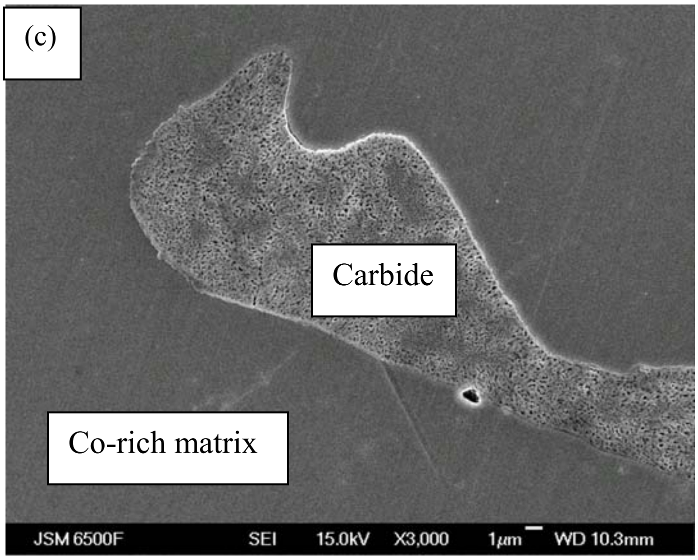

Figure 3.2: (a) Cast CoCrMo after etching (b) An AFM image of protruding carbide, and (c) A primary carbide ($M_{23}C_6$ where M = Co, Co and Mo) in the Co-rich matrix.

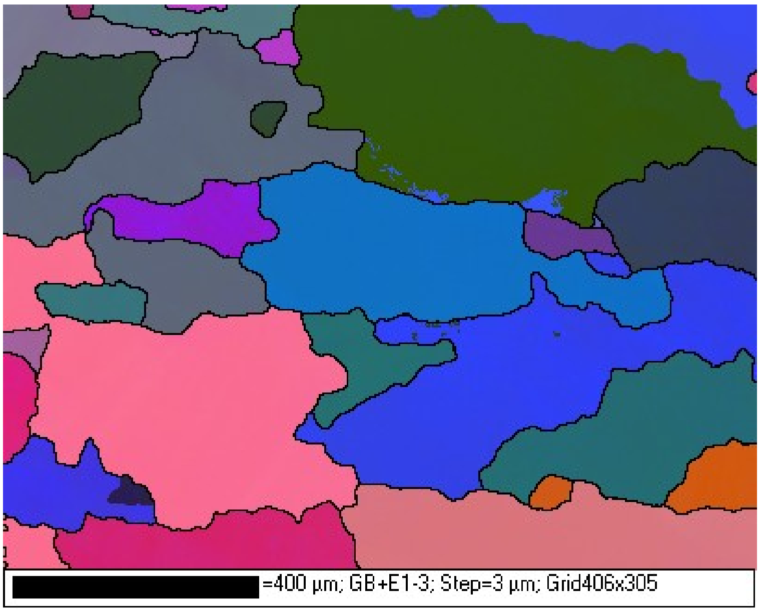

Figure 3.3: EBSD mapping showing the grain size distribution of cast CoCrMo.

3.2.2 Test solutions

In order to study the effects of protein, protein concentration and phosphates on the effect of wear and corrosion of cast CoCrMo, four types of test solutions were used in this study:

(a) 0.9 wt.% NaCl
(b) Phosphate buffered saline solution (PBS)
(c) 25% and **(d)** 50% bovine serum (BS) (Harlan® SERA-LAB)

The 0.9 wt.% NaCl is a simple simulated body fluid which was chosen for its similar chloride (Cl^-) level to that in human body fluids. Test results from this simple chloride solution will serve as a benchmark for comparison against data from the other more complex test solutions. The 25% BS solution is the recommended protein concentration and has been adopted widely in both simulator tests and other tribo-meter tests for hip replacement study [97, 134, 199]. Likewise, the 50% BS was used to evaluate the effect of increased protein concentration. Whereas PBS was used to investigate the effect of phosphate ions on the wear and corrosion behaviour of the cast CoCrMo alloy. The composition of the test solutions are listed in Tables 3.1 and 3.2. The solution conductivity for the test solutions are also reported in Table 3.3. Although the Cl^- level varies for different test solutions (0.63% to 0.9%), all the test solutions used in the present study were highly conductive, and the difference between each other is negligible.

For 0.9 wt.% NaCl, 25% and 50% bovine serum test solutions, two pH levels were used for each test solution, namely pH 7.4 (representing the healthy joint condition) and pH 4.0 (representing the infected joint condition). This is to investigate the effect of pH on the protein adsorption behaviour and their subsequent influence on the tribo-corrosion performance of the CoCrMo alloy. By buffering the pH from 7.4 to 4.0, only about 10^{-4} M Cl^- (equivalent to the amount of added H^+) has been added into the solution. The effect of the increased Cl^- is therefore negligible compared to the initial Cl^- level (0.15 M) in the 0.9 wt.% NaCl.

Table 3.1: Serum composition from Harlan ® SERA-LAB.

Composition	**Quality profile**
Sodium	140 mmol L^{-1}
Potassium	8.0 mmol L^{-1}
Glucose	6.7 mmol L^{-1}
Urea	6.4 mmol L^{-1}
Total protein	61.83 g L^{-1}
Albumin	32 g L^{-1}
Calcium	1.97 mmol L^{-1}
Phosphate	3.02 mmol L^{-1}
Total bilirubin	7 µmol L^{-1}
Aspartate Aminotransferase	32 U L^{-1}
Alanine aminotransferase	12 U L^{-1}
Lactate dehydrogenase	809 U L^{-1}
Amylase	33 U L^{-1}
Triglyceride	0.88 mmol L^{-1}
Cholesterol	1.8 mmol L^{-1}
Magnesium	1.22 mmol L^{-1}
Iron	19 µmol L^{-1}
Immunoglobulins	8.2 g L^{-1}

Where U L^{-1} is units per litre

Table 3.2: Composition of inorganic salt solutions.

Solutions	**Constituents in 1 L of distilled water**
0.9 wt.% NaCl	9 g NaCl dissolved in 1 L distilled water, pH adjusted to 7.4 using 0.1 M NaOH and 0.1 M HCl
Phosphate buffered solution	8 g NaCl, 0.2 g KCl, 1.44 g Na_2HPO_4 and 0.24 g KH_2PO_4, pH 7.4

Table 3.3: Conductivity of distilled water and all test solutions at room temperature.

Solutions	**Distilled water**	**0.9% NaCl**	**PBS**	**25% BS**	**50% BS**
Conductivity / mS cm^{-2}	0.0046	15.80	16.74	15.36	14.58

3.2.3 Abrasives

Four types of abrasives with different sizes, size distribution and hardness have been used for this study. 4μm SiC has been chosen as it was reported to give good test repeatability and reproducibility for microabrasion tests when used at high volume fraction (0.20 vol%) [200]. In the present study, a volume fraction (0.238vol%) is used (which is in line with the past literature [134]), the results serve as the starting test condition for obtaining a bench mark result for comparing with the subsequent results obtained from other test conditions. Micron and sub-micron (~ 300 nm) Al_2O_3 are chosen as these abrasives have hardness values close to the hardness range proposed for the different carbides present in the CoCrMo and their size are smaller and may better represent wear mechanisms seen in clinical application. Sub-micron sized $BaSO_4$ (one of the components in bone cement) is employed to study the effects of soft abrasives. All the abrasive properties and suppliers are specified in Table 3.4.

Table 3.4: Specification of the abrasives used in this study.

Abrasives	**Size and distribution**	**Hardness**	**Supplier**
SiC	4.3 ± 1.4 μm [201]	21-26 GPa [92]	Washington Mills Electro Materials Ltd, UK
Al_2O_3	1.62 ± 0.72 μm and 300 nm	18-20 GPa [92]	Logitech, UK
$BaSO_4$	Sub-micron	1.0-1.5 GPa [202]	American Elements, US

Micrographs of the abrasive particles used are shown in Figure 3.4. All abrasive particles are angular in feature despite the difference in their size and size distribution.

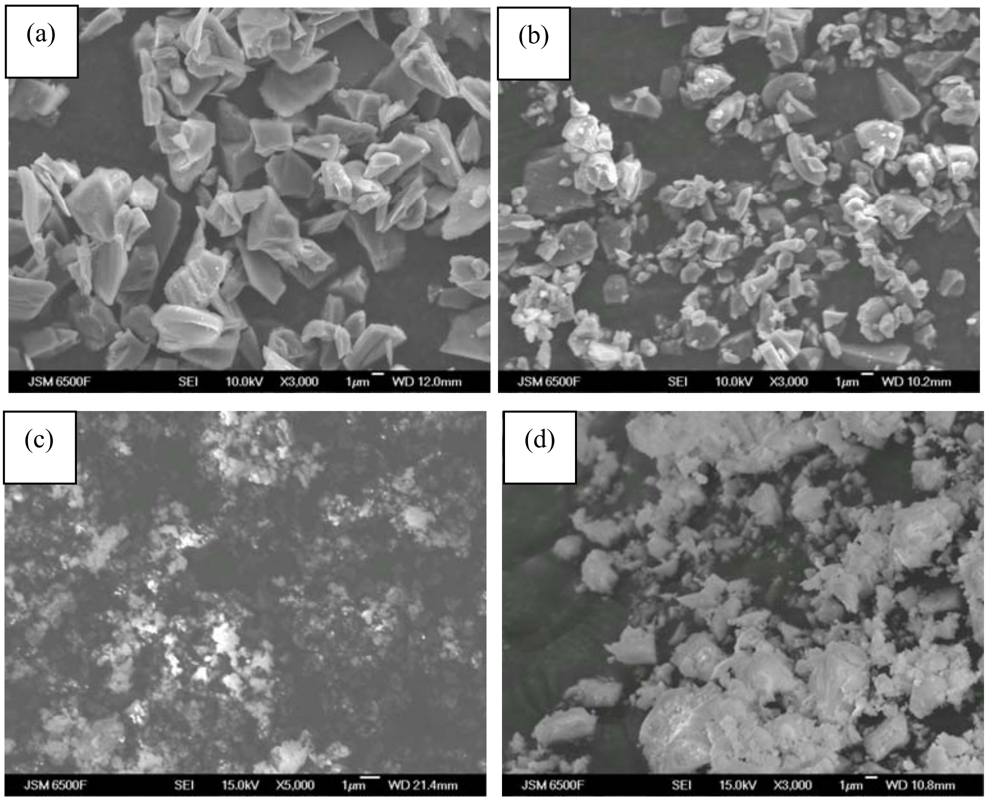

Figure 3.4: (a) 4.3 μm SiC, (b) 1 μm Al_2O_3, (c) 300 nm Al_2O_3, and (d) sub-micron sized $BaSO_4$ used for microabrasion test.

3.2.4 Specimen preparation

All the CoCrMo specimens were wet ground using 120 grit down to 4000 grit SiC paper. The specimens were then polished using 6 μm and 1 μm diamond pastes (BUEHLER, USA) on the respective polishing clothes (Struers Ltd, UK) for one minute, respectively. The specimens were ultrasonically washed in acetone followed by distilled water and dried in air before each test. The final surface roughness of the specimen was about 0.01 μm, measured by a surface profilometer (Taylor Hobson Talysurf 120L) which is consistent with a CoCrMo femoral component surface condition [148]. The Zirconia (ZrO_2) ball (25.4 mm diameter, Atlas Ball and Bearing Company Ltd, UK) used for microabrasion tests was conditioned by running multiple abrasion tests against a CoCrMo specimen with 1.0 g cm^{-3} SiC for 38 m in distilled water. The purpose of ball conditioning was to roughen the surface and improve particle entrainment and also the test repeatability. The average roughness of the worn ZrO_2 surface was about 0.11 μm. The zirconia ball was chosen for its excellent wear resistance as well as its chemical inertness and insulating properties.

The average hardness values of the cast CoCrMo specimen and the ZrO_2 ball have been measured using Vickers hardness indenter (Vickers Limited, Crayford Kent) with 10 kg (98 N) weight. 30 indentations were performed on each specimen and results (average Vickers hardness) are shown in Table 3.5.

Table 3.5: Vickers hardness of cast CoCrMo specimen and ZrO_2 ball.

Material	Load / kg	Average hardness (GPa)
CoCrMo (F-75)	10	4.0
ZrO_2 ball	10	13.0

3.3 Test Equipments

3.3.1 Microabrasion rig

Microabrasion is considered to be a three-body abrasion process where the abrasive particles are able to roll between the two surfaces [203]. In a microabrasion test, wear is caused by small (<10 μm) particles at low applied loads (<1 N). The wear processes produced by microabrasion tests could represent extreme conditions seen by the artificial hip and knee joints, such as abrasive particles (carbide fraction, metallic debris, bone cement, phosphate crystals or fractured bone debris) abrading / indenting the bearing surface which can cause surface damage of the joints resulting in further wear debris and/or adverse effects such as dissolution of metal ions [204].

Figure 3.5 shows the original structure of the microabrasion tester (Phoenix Tribology TE/66 Micro-Scale Abrasion Tester). It is designed based on an experimental technique developed by I. M. Hutchings and K. L. Rutherford of Cambridge University and is manufactured by Phoenix Tribology. The rig adopted in the national Centre for Advanced Tribology at Southampton has been further modified to enable *in situ* electrochemical measurements and the detailed modification can be found in Section 3.4.5.

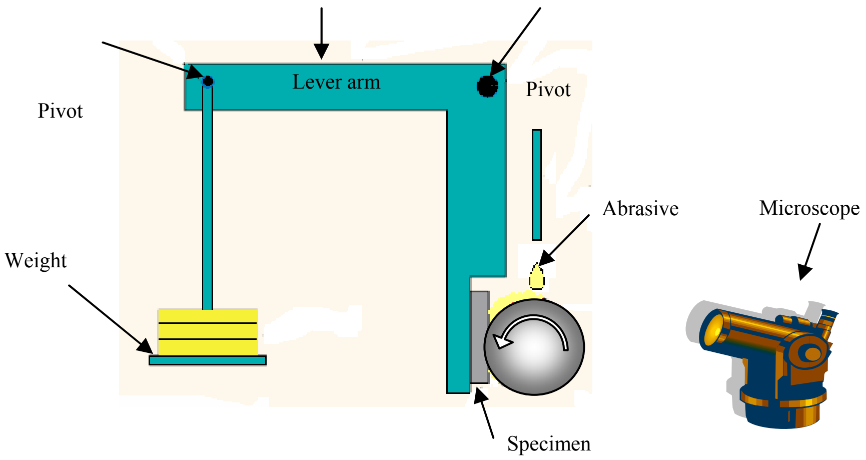

Figure 3.5: Structure of a micro-scale abrasion tester.

For each microabrasion test, the test specimen is mounted on a counterbalanced beam (arm) that hangs vertically from a pivot. The ball rotates against a specimen in the presence of an abrasive slurry producing a wear scar. The size of the wear scar can be measured *in situ* using a calibrated eye piece and the following equations are used to calculate wear volume and wear rate [134].

$$V = \frac{\pi b^4}{64R} \text{ (for } b \ll R\text{)} \qquad \text{……3.1}$$

Where V is the wear volume (m^3), b is the diameter of wear scar (m), and R is the radius of the ball (m). Assuming the specimen is homogeneous (*i.e.* the wear rate is constant such that the wear volume is proportional to the load and sliding distance), the specific wear rate κ ($m^3\ N^{-1}\ m^{-1}$) can be calculated by the Archard equation (Equation 2.7).

3.3.2 Nanoindentation and nanoscratching

The nano-indentation tester (NanoTest Platform System) used in national Centre for Advanced Tribology at Southampton is manufactured by MicroMaterials Ltd, UK. The instrument is positioned on an anti-vibration base and is enclosed in a temperature controlled cabinet which provides a thermally stable environment. The temperature is controlled at 25 ºC (with expected stability ± 0.1 ºC) inside the cabinet, and about 24 ºC outside.

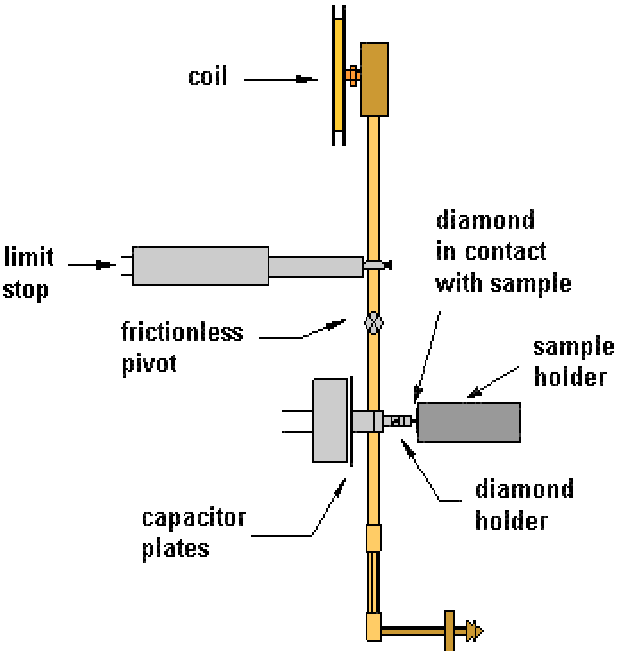

Figure 3.6: Design of the Nanotest pendulum [205] (original design [206]).

As shown in Figure 3.6, a counter weight and a coil are mounted at the top of the pendulum. The coil can move freely through a central annulus surrounded by a cylindrical permanent magnet. The indenter holder, to which an indenter is fastened, is located at the bottom of the pendulum. The pendulum is pivoted using a frictionless pivot located between the indenter holder and the limit stop. The motion of the indenter towards the specimen and into the specimen surface occurs when the coil is attracted towards a permanent magnet in response to the presence of a DC current in the coil. The voltage of this current is used to measure the applied force on the indenter. The limit stop, located above the pivot, is used to define the vertical position of the pendulum, and its position can be manually adjusted with a micrometer. The pendulum is vertical when it is touching the limit stop at which point the coil cannot move any further towards the magnet, hence the indenter cannot move any further towards the specimen. The counter weight is for fine adjustment of the pendulum so as to ensure that it is vertical against the limit stop [205].

The displacement (defined by the user input) of the indenter is measured by means of a two-parallel plate capacitor situated at the back of the indenter. One plate is attached to the indenter holder and moves with it while the second plate is fixed. When the indenter is pressing into the test specimen, the spacing between the parallel plates changes, hence the capacitance changes. By measuring this change using a capacitance bridge, the indenter movement can be measured. Data from the capacitance bridge are transferred as signals to the main electronic control unit, which contains a ramp generator that supplies the coil current. The data received from the capacitance bridge is then amplified, rectified, digitised and transferred via the IEEE bus to a computer [205].

The most frequently used indenter geometry in nanoindentation is the Berkovich indenter. The Berkovich indenter is a three-sided pyramid with the same depth-to-area relationship as the four-sided Vickers three sided pyramid which is commonly used in microhardness work. The Berkovich geometry is preferred to the Vickers because a three-sided pyramid can be ground to a point, thus maintaining its self-similar geometry to very small scales, ensuring a more precise control over the indentation process. The Berkovich indenter used for our nanoindentation test is of tip radius 50 - 100 nm.

Nanoindentation tests have been carried out at different indentation depths (ranging from 100 nm to 1000 nm) and various loading rates, to study their effects on the specimen hardness and reduced modulus. A nano-scratching test can also be carried out using the same equipment with a conical diamond tip (10 μm tip radius) attached. The test conditions for indentation and scratching tests are listed in Table 3.6. Single scratch and multiple scratches ($\times 5$ or $\times 20$ at the same location) tests were performed in air, 0.9 wt.% NaCl or 25% BS test solutions.

Table 3.6: Test conditions for nano-scratch and nano-indentation tests.

	Nano-indentation	**Nano-scratch**
Tip	Berkovich diamond tip Tip radius: 50-100 nm	Spherical diamond tip Tip angle: 60°, tip radius: 10 μm
Load	200 mN	200 mN
Test condition	Loading / unloading rate: 3 mN s^{-1} Indentation depth: 100 - 1000 nm In air, 0.9 wt.% NaCl or 25% BS Temperature: 25 °C or 37 °C	Scratching speed: 10 μm s^{-1} Scratching length: 500 μm In air, 0.9 wt.% NaCl or 25% BS Temperature: 25 °C or 37 °C

3.4 Electrochemical studies

3.4.1 Open circuit potential measurements

Corrosion potential *vs*. time tests were carried out in all test solutions shown in Section 3.2.2 in order to understand how swiftly the potential of the CoCrMo specimen achieves steady-state with time. A Gamry Instruments (PC4-750) potentiostat was used for these tests. The open circuit potential (OCP) was measured between a silver/silver chloride (Ag/AgCl) reference electrode and a working electrode (specimen). Measurements were taken at a sampling frequency of 0.2 Hz at 37 ºC in a Faraday cage for a total duration of 24 hours. The working electrode (specimen) was placed into an electrochemically inert holder, with an exposed surface area of 0.899 cm^2. 37 ºC was adopted because the adsorption of protein onto a solid surface is reported to be temperature dependent [28] and it should be similar to *in vivo* conditions found within the human body.

3.4.2 Potentiodynamic polarization

In order to study the corrosion properties (corrosion potential and corrosion current) of the material, potentiodynamic polarization measurements were carried out in a three-electrode electrochemical cell with a sweep rate of 1.0 mV s^{-1} using the instrument as described in Figure 3.7. Three electrodes were clamped into position within a glass vessel containing the test solution. In order to measure the cell potential of the working electrode (CoCrMo specimen), a silver/silver chloride (Ag/AgCl) reference electrode was placed as close to the surface of the working electrode as possible. The counter electrode (graphite) acted as a means to carry the current generated in the circuit and its potential was not of concern for this investigation. The container was sealed and held at a constant temperature of 37 ºC in a thermal bath. The polarization tests were performed after 30 minutes immersion to allow limited steady-state conditions to develop.

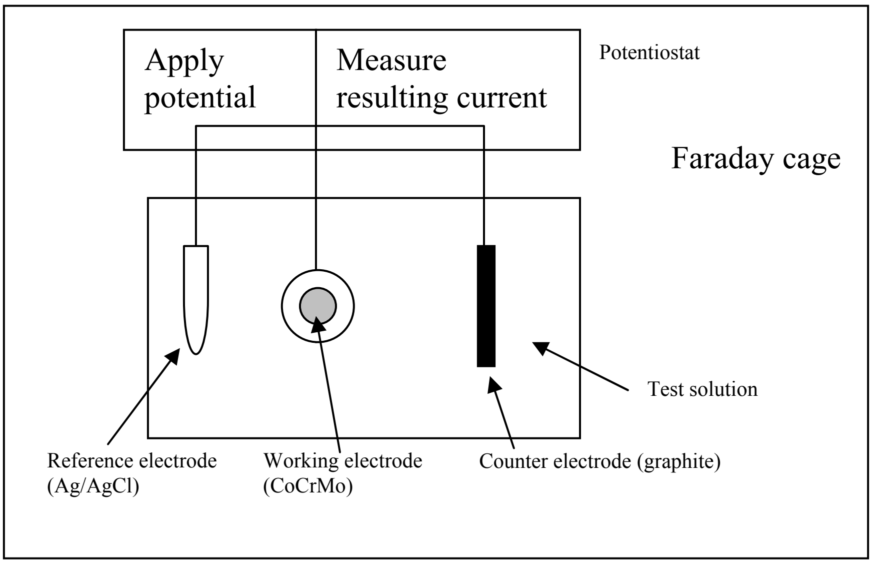

Figure 3.7: Set up for the potentiodynamic polarization test.

3.4.3 Electrochemical noise measurement

Electrochemical noise measurements, more specifically, current noise and potential noise were measured *in situ* and in real time during the microabrasion tests under different test conditions (varying test solutions and abrasive concentration). All specimens were immersed in the corresponding test solutions for 30 min prior to abrasion. A Gamry Instruments (PC4-750) potentiostat with ESA400 software was used. The electrochemical current noise was measured under the potentiostatic mode (with applied potential equal to OCP) during the wear tests to reveal the following information [164]:

1. To what extent does the specimen depassivate during the abrasion-corrosion process;
2. If there is any repassivation event occurring during the wear-corrosion process;
3. How does the specimen repassivate (repassivation rate) upon stopping of the abrasion.

The electrochemical potential noise measured during abrasion (at OCP) is not the actual corrosion potential of the wear scar but may include contributions from the ohmic potential drop between the point of measurement and the wear scar. Due to the high conductivity of the test solutions used, the ohmic potential drop is in the order of micro-volts and hence is negligible. The measured potential noise could indicate the corrosion potential change for the worn area with respect to the intact passive surface. The rate of the potential recovery could also indicate the repassivation rate of the material after the abrasion test [166].

3.4.4 Electrochemical impedance spectroscopy

Electrochemical impedance spectroscopy (EIS) was conducted in order to understand the effect of pH on the interfacial behaviour corresponding to protein adsorption onto the CoCrMo surface. A Gamry Instruments (PC4-750) potentiostat running EIS 300 software was used for this study. The three electrode cell consisted of a silver/silver chloride (Ag/AgCl) reference electrode, the working electrode (CoCrMo specimen) and a graphite counter electrode as shown in Figure 3.8. Circular specimens with an exposed area of 0.899 cm^2 were immersed into the test solutions for 30 min before testing to allow a limited steady-state condition to develop. This is consistent with the immersion condition for potentiodynamic polarization as well as the subsequent micro-abrasion, indentation and scratching tests. The sampling frequency was 0.1 Hz to 100 kHz, at 10 data cycles per decade with alternative circuit potential signal amplitude of ± 10 mV *vs*. OCP. The impedance spectra were analysed with the Gamry Echem Analysis software.

3.4.5 Microabrasion and *in situ* electrochemical noise measurements

A modified Phoenix Tribology microabrasion tester incorporating a liquid tank and three-electrode electrochemical cell was employed, as is shown in Figure 3.8. The tank has been designed so that the ball can rotate within the liquid with lip-seals effectively sealing the gap between the rotating shafts. A draining pipe was positioned at the rear of the tank, 5 mm above the level of the rotating ball contact point, in order to ensure that the contact point was always at a constant level below the solution surface and the solution level did not change during the test even with introduction of external fluid/slurry. The upper portion of the ball facilitates the slurry entrainment into the contact via a continuous slurry feed. A warm water jacket was used in order to test solution temperature at $37 \pm 2\ ^{\circ}C$. All test specimens were immersed for 30 min prior to abrasion tests.

The CoCrMo working electrode was attached to the modified microabrasion arm using silicon rubber sealant to avoid crevice corrosion. The Ag/AgCl reference electrode was modified so that it could be fitted into the arm. The counter electrode was platinized titanium (William Gregor Limited, UK) of dimension 20 mm × 15 mm × 1 mm and was attached to lower part of the arm.

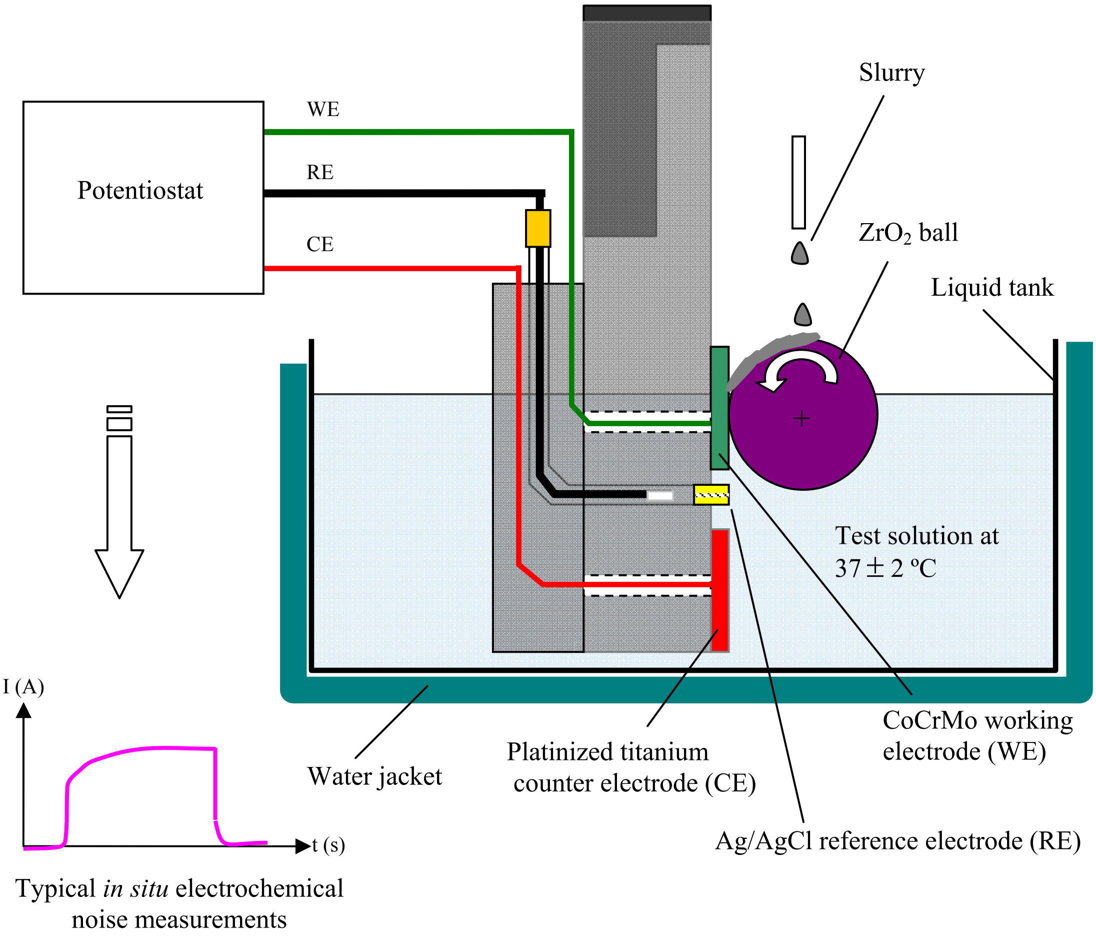

Figure 3.8: Schematic of the modified microabrasion rig with liquid tank and three-electrode electrochemical cell.

The abrasive slurries were made with the corresponding test solution for the abrasion-corrosion test and were pre-heated to 37 °C. No abrasives were used for sliding-corrosion (SC) and for abrasion-corrosion (AC) tests different abrasives slurries were made at volume fractions 0.006, 0.03, 0.072, 0.12 and 0.238, respectively, which is similar to test conditions adopted by [207]. A load of 0.25 N was applied for both SC and AC conditions which gives an initial contact pressure of ~100 MPa within the tribo-contact. This initial contact pressure level is of the same order of magnitude to that of the clinical condition; however the contact pressure will change as soon as the abrasives are introduced into the contact. At least two specimens were tested for each test condition. Due to the nature of this study, the test conditions differ at different stages of the research and hence are difficult to be summarized as a whole. More specified test programmes/test conditions can be found at the beginning of the following chapters for clarity.

In order to measure the pure mechanical element in the AC process, pure abrasion tests were done under cathodic protection conditions where specimens were potentiostatically held at -0.400 V *vs.* OCP. This potential was chosen as it was sufficiently negative to minimise anodic corrosion processes and not too low to cause hydrogen evolution. Table 3.7 summaries the test conditions for obtaining specific wear rates.

Table 3.7: Summary of Specific Wear Rates (SWR) and the corresponding test conditions.

SWR $\mathbf{mm^3\ N^{-1}\ m^{-1}}$	**Definition**	**Test conditions**
C_0	Material loss due to pure corrosion (static) under open circuit potential. C_0 is normally negligible compared to total material loss.	Calculated from the corrosion current density (i_{corr}) of the whole sample surface under potentiodynamic polarization using Faraday's law [174, 175]
T_{SC}	Total material loss due to 2-body sliding and corrosion	Sliding-corrosion
T_{AC}	Total material loss due to 3-body abrasion and corrosion	Abrasion-corrosion
W_0	Material loss due to pure mechanical wear AC condition	Pure abrasion under cathodic protection
S_{AC}	Synergy (wear-corrosion) interaction under AC condition	$S_{AC} = T_{AC} - C_0 - W_0 = C_w + W_c$ [134] $S_{AC}\% = \frac{C_w + W_c}{T} \times 100\%$
C_w	Material loss due to wear-enhanced corrosion under AC condition	Calculated using the electrochemical current noise data obtained under AC condition using Faraday's law [174, 175]
W_c	Material loss due to corrosion enhanced wear under AC condition	$W_c = S_{AC} - C_w$ [134]

After the microabrasion tests, the wear scar sizes were measured using a calibrated eye piece and the specific wear rates as well as synergy were evaluated following the procedure discussed in Sections 3.3.1 and 2.5.1, respectively.

Table 3.8 shows the viscosity values of various test solutions. The minimum film thickness and λ ratio calculated based on the Equations 2.1 and 2.5, as well as the possible lubrication regime as a result of different test solutions are also reported. Mixed lubrication has been found to be the possible lubrication regime at the beginning of all tests in the current study with film thickness of about 200 nm. For SC tests, as tests progress, the wear scar grows and the roughness of the worn specimen surface increases and therefore the regime could move from mixed to boundary lubrication. For AC tests on the other hand, the load will be transmitted through the particles ones the abrasives get entrained into the tribo-contact as the size of abrasives used is larger than the boundary film thickness.

Table 3.8: Initial lubrication film thickness and lubrication regime in various test fluids at 37 ºC.

	Distilled water	**0.9% NaCl**	**PBS**	**25% BS**	**50% BS**
Viscosity (cP) at 37 ºC	0.69	0.70	0.66	0.92	1.05
h_{min} (µm)	0.138	0.138	0.133	0.182	0.164
Initial λ ratio	1.51	1.51	1.45	1.98	1.79
Initial lubrication regime	Mixed	Mixed	Mixed	Mixed	Mixed

The viscosity values for some of the SiC and Al_2O_3 test slurries were measured at 37 ºC using a DV-II+ PRO Digital Viscometer (Brookfield, UK) at 20 RPM (i.e., constant shear rate 24.5 s^{-1}) and their values are shown in Table 3.9.

Table 3.9: Viscosity values (in mPa.s) for SiC and Al_2O_3 based slurries measured at 37 ºC and a shear rate 24.5 s^{-1}.

Abrasive vol%	**0**	**0.006**	**0.03**	**0.072**	**0.12**	**0.238**
SiC-0.9% NaCl	0.7	0.8	1.3	2.93	3.85	19.6
SiC-25% BS	0.9	1.05	1.56	4.5	6.7	20.5
Al_2O_3-25% BS	0.9	0.98	1.03	1.3	2.2	4.87

3.5 Wet-cell indentation and scratching tests

In order to obtain a more insightful understanding of the wear mechanisms involved during the abrasion-corrosion processes at micro- and nano-scales, indentation and scratching technique have been used under various test conditions at micro- and / or nano-scales. A wet-cell has been incorporated in the indentation/scratching instruments in order to simulate the immersed condition as in the body environment. In order to eliminate the artefacts of the polishing marks resulted from the metallographic preparation, the specimens were electro-polished using a solution of 7% perchloric acid and 93% acetic acid (volume) at temperature of 10 ºC and applied voltage 30 V for 60 seconds.

3.5.1 Wet-cell micro-indentation

A Vickers micro-hardness indenter is employed, which has been fitted with a wet-cell and a three-electrode electrochemical cell, see Figure 3.9. All specimens were immersed in the test solution for 30 min prior to indentation tests. During the tests, the single micro-indent test drives the indenter downward at a load of 9.8 N and drives upward after the intermission of 5 sec. Single or multiple indentation (the procedure was repeated 5 times with an intermission of 10 *s* at the same location) have been performed to investigate the material mechanical/electrochemical behaviour under single and multiple loading/unloading cycles.

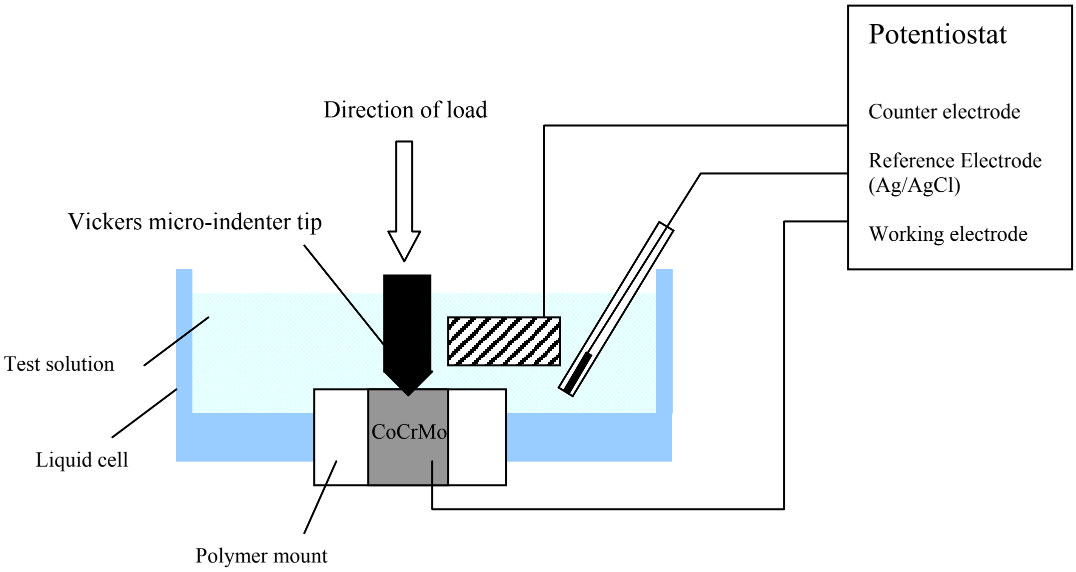

Figure 3.9: Set up for wet-cell micro-indentation.

3.5.2 Wet-cell nano-indentation and nano-scratching

The nanoindentation (NanoTest platform, MicroMaterials Ltd, UK) can be conducted in a liquid cell with a liquid cell extension arm and a Berkovich tip attached (see Figure 3.10). The same configuration can be used for nano-scratching test, but only a conical indenter can be used (tip radius of 10 μm and an included angle of 60°). All specimens were immersed in the test solution for 30 min prior to nano-indentation/scratching tests.

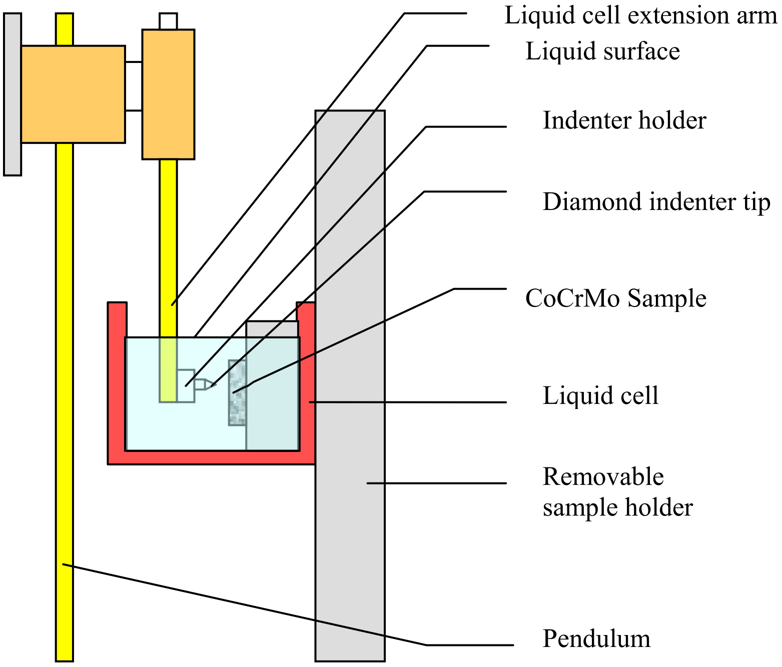

Figure 3.10: Set up for wet-cell nanoindentation and nano-scratching.

For the wet-cell nano-sratching test, the load was ramped up abruptly to 200 mN. A 500 μm long scratch was made at a scratching speed of 100 μm s^{-1} (maximum speed allowed by the instrument). Repeated scratches (5 or 20 passes) were made at the same location in order to investigate the effect of multiple scratch cycles on the local plastic deformation and electrochemical response of the material under study.

Electrochemical current noise measurement was performed with a three-electrode electrochemical cell being incorporated into the scratching test wet-cell. A 1000 μm single scratch was made in 0.9 wt.% NaCl and /or 25% BS. Data was collected using the Gamry potentiostat and the ESA 400 software.

3.6 Surface Characterization

3.6.1 Optical Microscopy

Optical investigations of the surfaces were achieved using an optical microscope (Olympus BH-2, Japan) coupled with a digital camera (Prosilica EC1350). This allowed a quick investigation of the specimen surface profile and the selected specimens were subjected to scanning electron microscopy for further investigation at higher magnifications.

3.6.2 Field Emission Gun Scanning Electron Microscopy (FEG-SEM)

Field Emission Gun Scanning Electron Microscopy (JEOL JSM-6500F) was used to analyse the specimens at much higher magnifications and resolution. An accelerating voltage of 15 kV and a working distance 10 mm were employed for the best image resolution. Energy Dispersive X-ray Analysis (EDX) can be done *in situ* to obtain elemental information on the point/area of interest during the SEM study.

3.6.3 Electron Backscattered Diffraction (EBSD)

EBSD is a very useful tool to perform crystal structure analysis and to aid phase identification. In EBSD a stationary electron beam impinges a tilted crystalline sample and the diffracted electrons form a pattern (Kikuchi pattern) on a special type of detector (fluorescent screen). This pattern is characteristic of the crystal structure, sophisticated algorithms have been developed to automatically capture and index the EBSD patterns [208]. The diffraction pattern can be used to measure the crystal orientation, measure grain boundary misorientations, discriminate between different materials, and provide information about local crystalline perfection. Phase identification can be accomplished by a direct match of the diffraction bands in an experimental EBSD pattern with simulated patterns generated using known structure types and lattice parameters (which have been put in to the EBSD system software). When the beam is scanned in a grid across a polycrystalline sample and the crystal orientation is measured at each point, the resulting map will reveal the constituent grain morphology, orientations, and boundaries. Further details of this technique can be found in [208].

3.6.4 Focused Ion Beam Scanning Electron microscopy (FIB-SEM)

Focused Ion Beam (FIB) allows material to be cut away (milling) from a defined area with square microns dimensions and hence the subsurface microstructure of the material can be revealed in detail (such as grain orientation, grain boundaries etc). Milling is achieved by accelerating concentrated gallium (Ga) ions to a specific site, which etches off any exposed material, leaving a very clean hole.

The subsurface microstructures of the as polished and worn CoCrMo surfaces were exposed by FIB milling using a JEOL 6500F FEGSEM with Orsay Physics Ion Column FIB at the University of Sheffield, Department of Engineering Materials. A layer of platinum (Pt) was deposited on the region of interest to prevent Ga^+ implantation and sputter erosion of the top portion of the surface. Specimens were tilted 55° from horizontal to make the ion beam perpendicular to the surface, giving a 35° angle between the imaging electron beam and the worn surfaces. A 700 pA Ga^+ ion beam was used for coarse milling and a 50 pA Ga^+ ion beam was used to polish the subsurface cross-sections. An accelerating voltage of 30 kV was used. SEM images of the subsurface microstructures were recorded with a 55° angle between the electron beam and the subsurface cross-section planes. Ion-induced secondary electron (ISE) images of the subsurface microstructures were recorded by tilting with a 35° angle between the ion beam and the sub-surface cross-sectional planes. EDX analysis was carried out at the sites of interest after milling and polishing.

3.6.5 Adsorption of protein on the cast CoCrMo

In order to study the adsorption of protein on the cast CoCrMo surface over a fixed period of time, a series of static immersion tests were carried out. The polished specimens were further cleaned by methanol to remove the possible surface charging before being transferred to a closed container with 25% BS at 37 ºC. Specimens were removed from the BS solution after a 30 min immersion and rinsed with copious amounts of distilled water to remove any loosely adhered proteins and dried in air. The specimens were then scanned using an atomic force microscope (AFM) (Veeco Dimension 3000, University of Sheffield, Department of Engineering Materials). The tapping mode was used for scanning the adsorbed protein layer on the specimen surface before and after the abrasion tests (specimens were rinsed with copious amount of distilled water and dried in air). The tip used was made of phosphorus (n-type) doped Si with a force constant 33.6 to 65.4 N m^{-1}. The scan frequency was 0.5 Hz.

To characterize the specimen surface film thickness and chemical composition, X-ray photoelectron spectroscopy (XPS) was carried out using a Scienta ESCA300 spectrometer (monochromatic Al Kα radiation at 14 keV and 200 mA) at the National Centre for Electron Spectroscopy and Surface Analysis (NCESS), Daresbury Laboratory, UK. The specimens were prepared under the same condition as for the EIS study. The specimens after immersion were rinsed with distilled water and air dried. Specimens were then kept in a vacuumed desiccator before XPS analysis. A pass energy of 300 eV was employed for the survey spectra and 150 eV for the high-resolution spectra scans of selected regions. The slit width of the electron analyzer was set at 1.9 mm for the former and 0.5 mm for the latter. Take-off-angles relative to specimen surfaces of 90° was employed. The carbon C1s line at 285.0 eV was used to reference the spectra. Curve fitting after background subtraction was conducted assuming a complex mixed Gaussian–Lorentzian peak shape.

Chapter 4

Electrochemical characterization of CoCrMo under static conditions

The aim of this chapter is to analyse the effect of different biological solutions on the electrochemical performance of the cast CoCrMo alloy. A series of OCP and potentiodynamic polarization tests were carried out in order to fully characterize the CoCrMo electrochemical performance under static (no fluid flow) conditions. The experiments aim to answer the following questions:

(1) Is the corrosion behaviour dependent on immersion time and solution chemistry?
(2) How does the protein and phosphate affect the corrosion behaviour of the CoCrMo alloy under static conditions?

The results from this chapter will serve as the baseline current / potential data, which are to be compared with the electrochemical noise results obtained during the dynamic tribocorrosion tests in the following chapters.

4.1 Effects of test solution constituents and immersion time

4.1.1 Open circuit potential

It can be seen from Figure 4.1 that the OCP of the CoCrMo increases rapidly for all solutions in the first 1800 s after immersion. After 15000 s, steady-state conditions are reached for all solutions (around -0.05 V). The time dependence of the OCP can be attributed to a number of mechanisms including mass transport of inorganic species (e.g., chloride, phosphate) or organic species (e.g,. proteins) to the specimen surface followed by the formation of an adsorption layer [150, 209]. These processes could change the surface chemistry of the CoCrMo and hence affect the alloy surface potential with time.

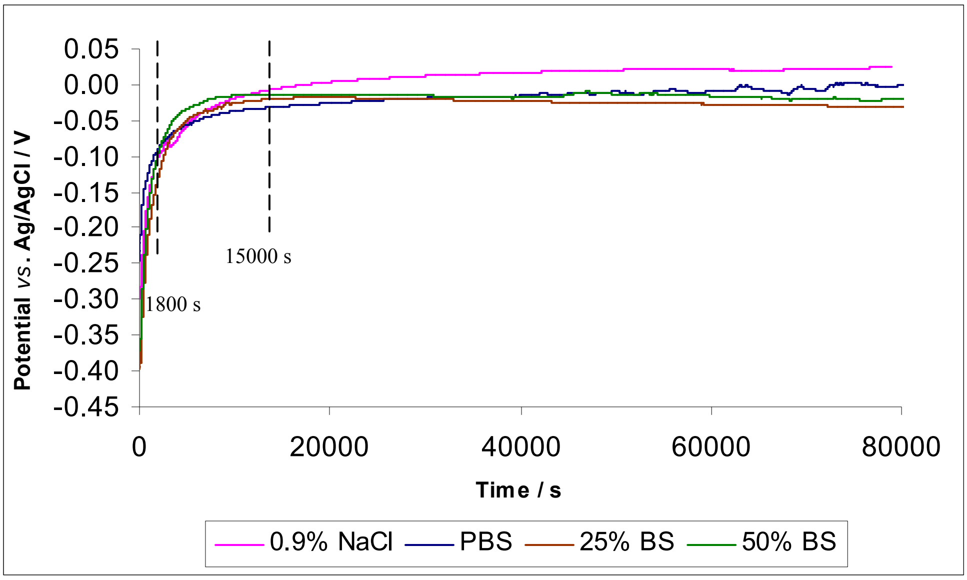

Figure 4.1: Open circuit potential of cast CoCrMo in the various test solutions at 37 ºC.

When a metallic specimen is immersed into an aqueous solution, water molecules will bind at the metallic/passive film interface, followed by inorganic ions such as Cl^-, Na^+, etc. If proteinaceous material is present, this will also interact with the surface and adsorb/desorb according to the relative concentration, size and charge of the biomolecules in the bulk solution. Proteins may adsorb intact or may unfold to minimize the free energy of the system. Consequently, the OCP of the material gradually stabilizes while the charged ions/molecules achieve their most stable states.

As the OCP of the CoCrMo specimens in all solutions achieve a 75-80% stabilization of the final value at 1800 s (consistent with [151]), a 30 min specimen immersion for the subsequent electrochemical and tribo-corrosion tests (to be discussed in Chapter 5) has been adopted for this current investigation to allow a limited steady-state condition to be developed.

4.1.2 Potentiodynamic polarization

Potentiodynamic polarization curves of cast CoCrMo in the various test solutions are presented in Figure 4.2, and a number of important observations have been made:

1. For NaCl, an active-passive region can be clearly identified in the potential range of 0.0 to +0.6 V. The broad shoulder at +0.7 V has been attributed to the

transpassive oxidation of Cr^{3+} to Cr^{6+}, which preceeds the large current rise due to the onset of H_2O oxidation (O_2 evolution) [210].

2. Phosphate buffered solution increased the corrosion resistance by shifting the E_{corr} in the more noble direction and gave a slightly lower i_{corr} compared with 0.9 wt.% NaCl. These results are in good agreement with [150] which have been attributed to the phosphate ion adsorption acting as a barrier on the surface for both anodic and cathodic reactions. However, a much lower E_{corr} was reported by Monuz *et al.* [150], although in that particular study the specimens were cathodically cleaned, oxide free CoCrMo surfaces. In addition, the small shoulder seen in the PBS polarization curve at +0.85 V can be attributed to the transpassive oxidation of Cr^{3+} to Cr^{6+}. The reactions involve oxidation of the Cr_2O_3 oxide and the $CrPO_4$ under layer beneath the Cr_2O_3 into CrO_4^{2-} which dissolves in the solution as is shown by Equations 4.1 and 4.2 [211].

$$Cr_2O_3 + 10OH^- = 2CrO_4^{2-} + 5H_2O + 6e^- \qquad \text{……4.1}$$

$$CrPO_4 + 8OH^- = CrO_4^{2-} + 9e^- + PO_4^{3+} + 4H_2O \qquad \text{……4.2}$$

3. The presence of proteinaceous material in the test solutions shifted the E_{corr} values in the negative direction, which is in good agreement with the published research literature [133, 209]. It is reported that protein hinders the oxygen evolution reaction and the charge transfer responsible for the passive film dissolution (or growth) [209]. Figure 4.2 clearly shows that the inorganic solutions resulted in similar cathodic kinetics (*i.e.* similar cathodic curves). However, the cathodic reaction rates for proteinaceous (BS) solutions were significantly different (10% > 25% > 50% > 100% BS). Consequently, an enhanced corrosion current density was found for the BS solutions, which decreased with increasing protein concentration (see Figure 4.3). When the protein concentration is low (*e.g.* 10 and 25% BS), the resulting adsorption film is relatively thin. Metal-protein complexes may form by protein binding to metal-ions, these complex species as well as free metal ions are transported away from the solution / passive film interface, thereby enhancing further dissolution of the alloy [212]. Similar findings have been reported elsewhere using 0.5 % bovine serum albumin (BSA) added to NaCl or PBS solutions [150]. However, for higher protein concentrations (*e.g.* 100% BS), both

the anodic and cathodic current density are lower (see Figure 4.3). In this instance, the CoCrMo surface can be considered to be more thoroughly covered by an adsorbed protein film which strongly inhibits the pathway for metal-protein complex transportation and thus hindering the overall charge transfer processes. The electrochemical results for the 100% BS solution are consistent with the findings reported by Contu *et al.* [160, 213]. However, it is worth noting that during this measurement the sample surface has gone through a potentiodynamic polarization process, the change of surface polarity may influence the protein adsorption behaviour and therefore may give rise to a different film thickness (hence different charge transfer inhibiting ability) as compared to a non-polarized sample surface [214].

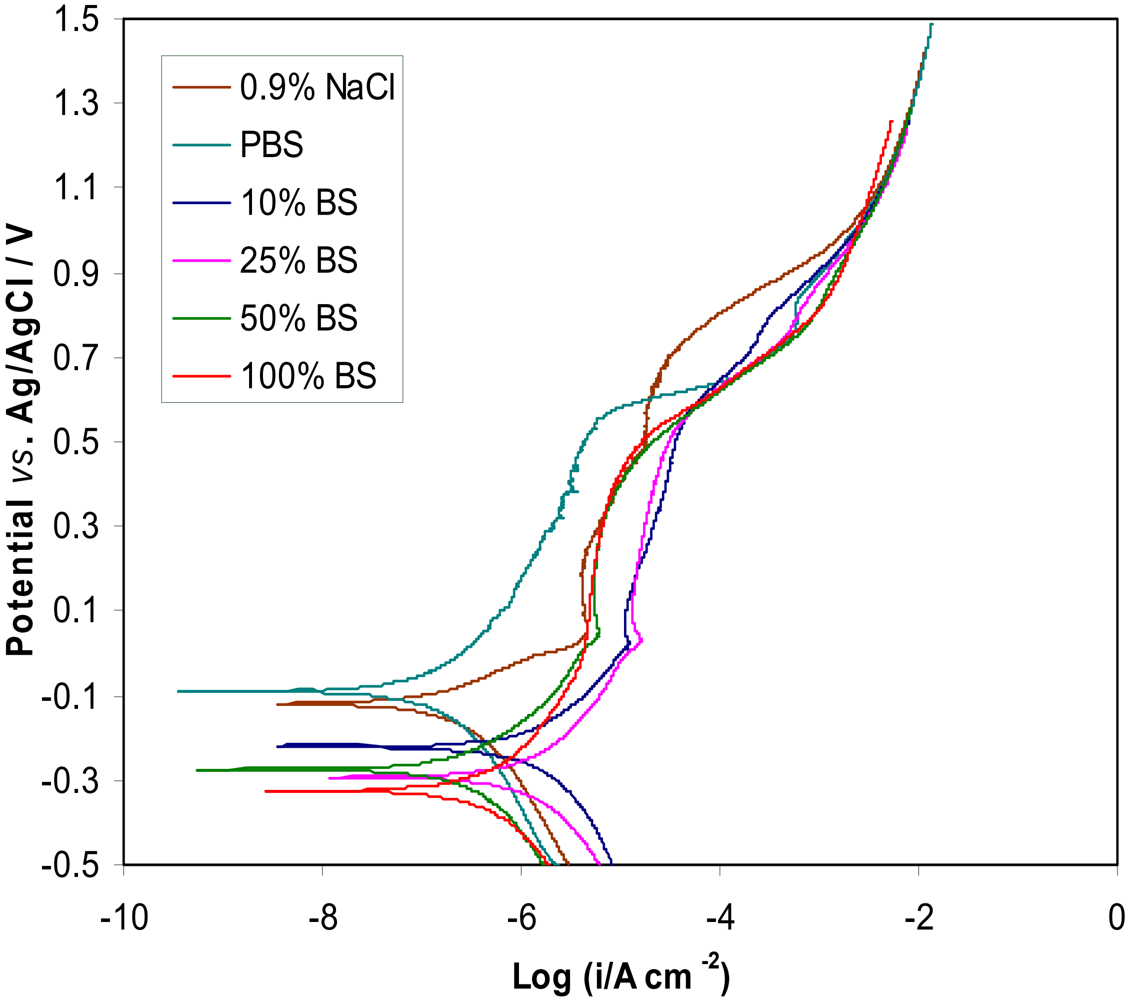

Figure 4.2: Potentiodynamic polarization curves of cast CoCrMo in various test solutions at 37 ºC (after 30 min immersion).

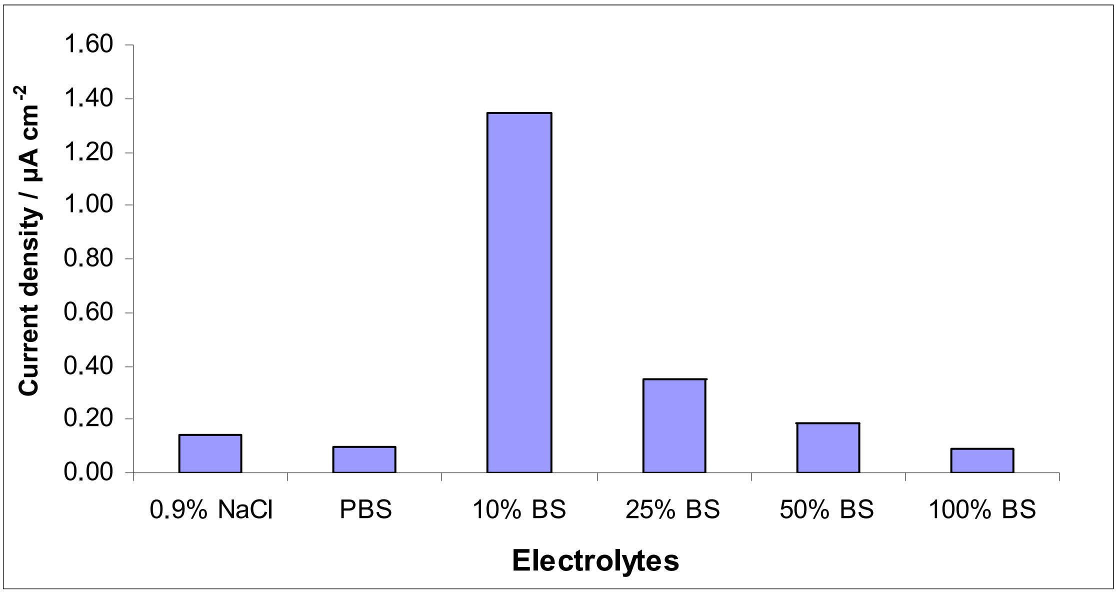

Figure 4.3: Corrosion current density of cast CoCrMo in the various test solutions determined from Figure 4.2.

Figure 4.4 shows the potentiodynamic polarization curves of CoCrMo after a 24 h immersion. Compared with Figure 4.1, all curves tend to collapse giving very similar values for both E_{corr} and i_{corr}. This suggests that for extended immersion times, the oxide / hydroxide film (0.9 wt.% NaCl solution), and the additional phosphate film (PBS solution) or protein adsorption film (BS solutions), although different in overall structure and composition, act as a physical barrier which hinders the further metal dissolution and improves CoCrMo corrosion performance.

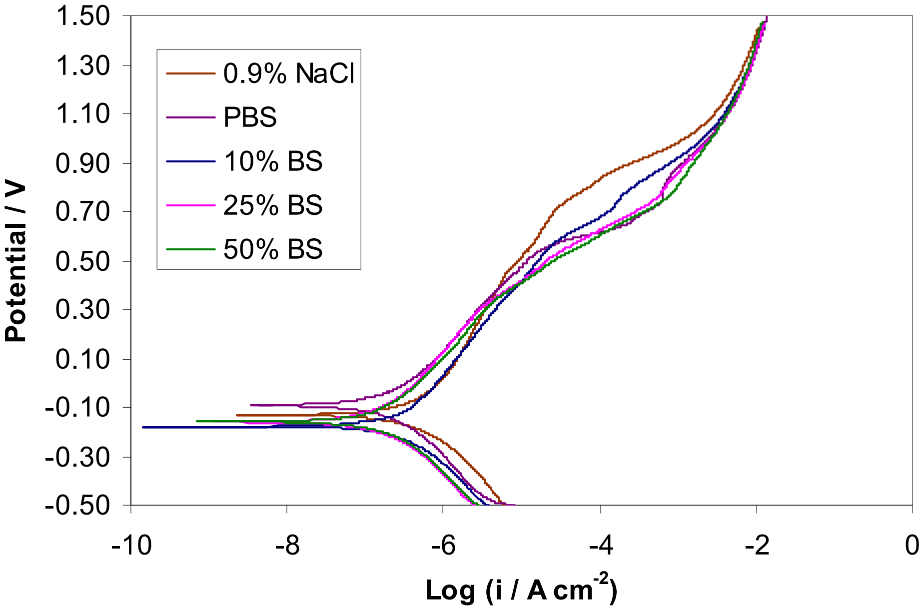

Figure 4.4: Potentiodynamic polarization curves of cast CoCrMo in various test solutions at 37 ºC (after 24 hours immersion).

Figure 4.5(a) and (b) compares the E_{corr} and i_{corr} values after different immersion times (30 min and 24 h). The trends clearly show that E_{corr} shifts in the noble (positive) direction and corrosion current density decreases with time for BS solutions. This is consistent with the literature [210] and indicates a general enhancement of the passive behaviour as the passive film matures with time.

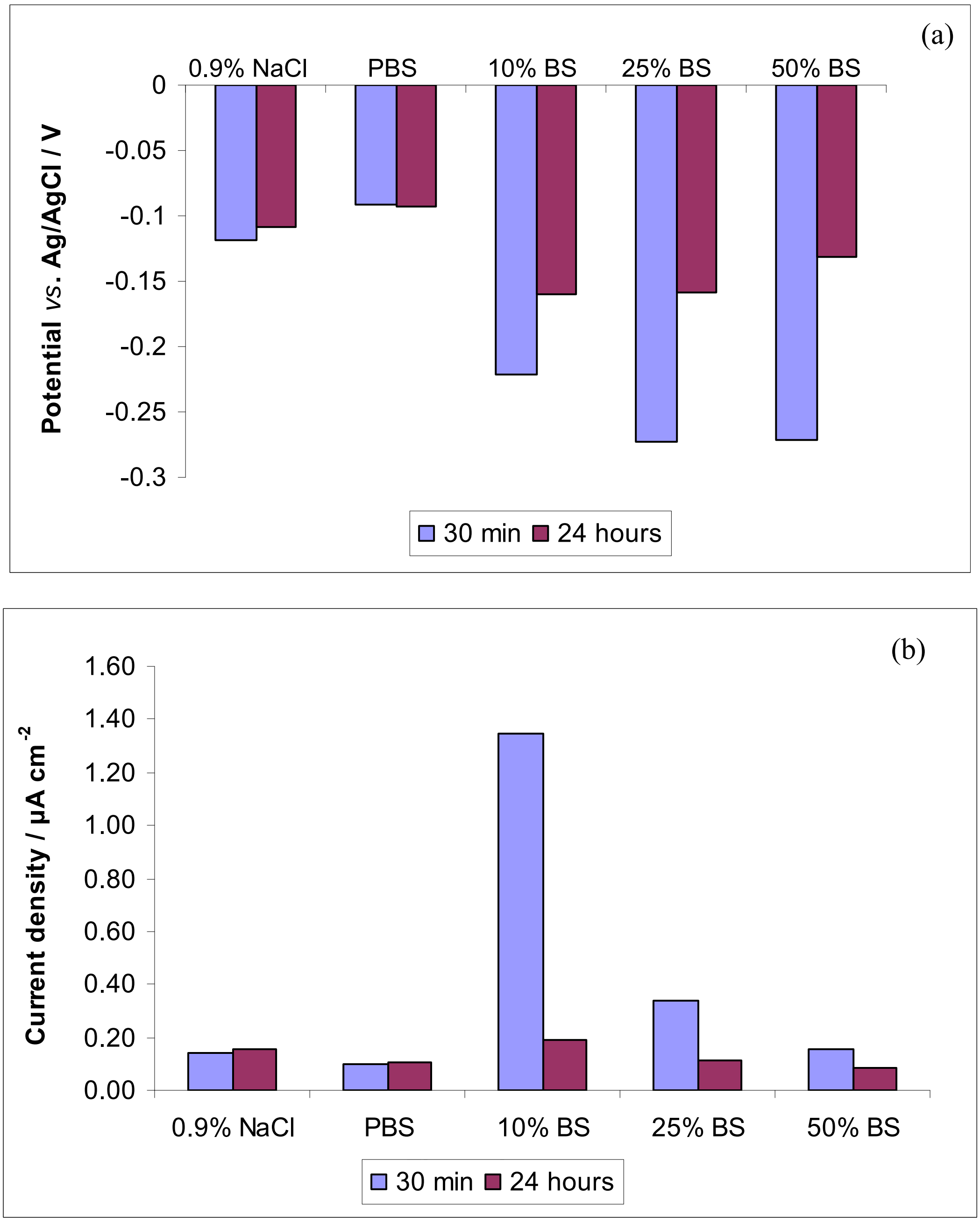

Figure 4.5: Comparison of **(a)** corrosion potential and **(b)** corrosion currents obtained at 30 min immersion and 24 hours immersion.

As previously discussed in Section 2.4, the hip joint fluid pH may change drastically under an infected condition, the local pH can be as low as 4.0 under severe infection [59] as compared to the normal physiological pH of 7.4. Therefore, it is important to understand how the pH of body fluid influences the corrosion behaviour of the CoCrMo implants. Figure 4.6 compares the corrosion currents obtained from potentiodynamic polarization within different pH test solutions. For 0.9 wt.% NaCl, reducing pH from 7.4 to 4.0 results in the corrosion current increasing by an order of magnitude. However, for the protein containing solutions, the acidic pH resulted in a decreased corrosion current, which may be attributed to the adsorbed protein film, inhibiting the charge transfer and the mass transport processes.

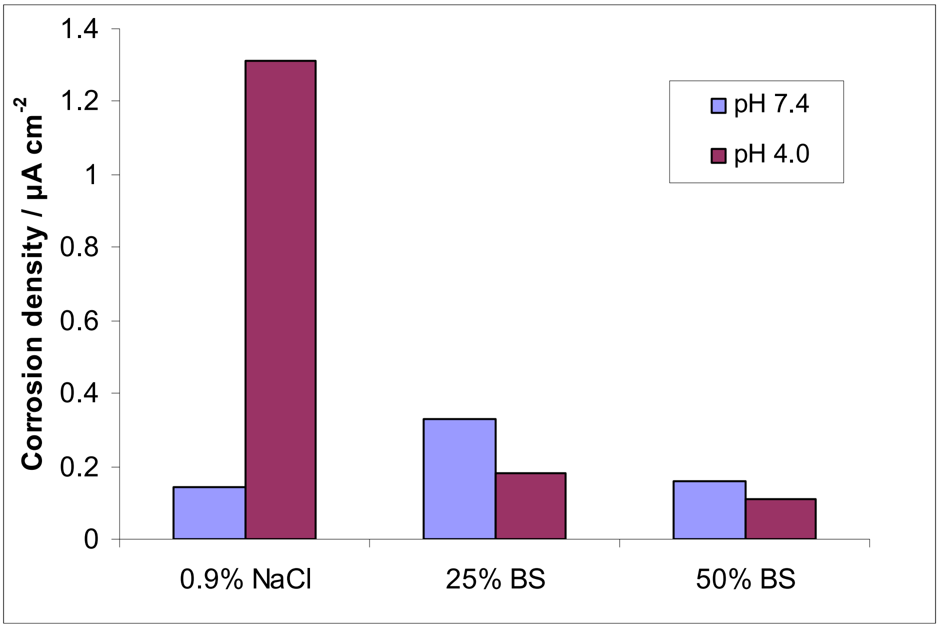

Figure 4.6: Corrosion currents obtained at 30 min immersion for various test solutions at pH 7.4 and pH 4.0.

4.2 Electrochemical Impedance Spectroscopy

The potentiodynamic polarization testing adopted in Section 4.1 may not be an accurate method to determine the surface film formation and / or protein adsorption mechanisms and kinetics, since these depend significantly on the applied potential [62]. In addition, during polarization, the surface charge on the specimen will be different from that at OCP, which will influence the formation of the adsorption layer of organic molecules [214]. Consequently for this part of the study, a less intrusive technique Electrochemical Impedance Spectroscopy (EIS) has been used to investigate the CoCrMo / test solution interface and the processes that occur on the metallic surfaces at OCP after a 30 min immersion. The test parameters have been specified in Section 3.4.4.

The spectra shown in Figure 4.7 (a) can be seen to exhibit two distinct regions. In the high-frequency region (100 to 100 kHz), the modulus of the impedance, |Z|, is independent of the frequency with a phase angle tending towards zero degrees, see Figure 4.7(b). This is consistent with resistive behaviour and corresponds to the solution resistance, R_s [83]. In the lower to medium-frequency region (0.1 to 100 Hz), a linear relationship is apparent between |Z| and frequency with a slope close to –1 and a phase angle of about –80°. This response corresponds to a capacitive behaviour for the CoCrMo/solution interface. In the low-frequency region, the expected resistive behaviour related to the polarisation resistance, R_p (which characterises the charge-transfer across the interface), is not in evidence; *i.e.* the region where |Z| is independent of the frequency. Overall, the spectra signify that an interfacial capacitive behaviour dominates with only one time constant distinguishable (minima in the phase angle).

Since the interfacial behaviour of an electrochemical reaction is analogous to an electrical circuit consisting for example of a specific combination of resistors (*R*) and capacitors (*C*), the electrochemical systems (spectra) under study can be described in terms of their equivalent circuit. In this instance the equivalent circuit consisted of only one *RC* time constant, see the insert to Figure 4.7(a). The usual procedures for the selection of best-fit were followed: (*i*) a minimum number of circuit elements are employed, (*ii*) the χ^2 error was suitably low ($\chi^2 \leq 10^{-4}$), and the errors associated with each element were up to 5% [215].

Due to surface heterogeneities present at the oxide/solution interface, including physical phenomena such as grain boundaries, impurities and surface roughness [216], the measured interfacial capacitive response was not ideal, as indicated by the deviation of the slope from –1, as well as the phase angle deviating from –90°. Consequently, a constant phase element (CPE) was introduced to fit the spectra. Its impedance may be defined by: $Z(\mathrm{CPE}) = [Q'(j\omega)^n]^{-1}$ in Ω cm^2 where Q' is a constant in Ω^{-1} s^n cm^2, ω is the angular frequency, and n is the CPE exponent (n is adjustable and lies between 0.5 and 1, with 1 being an ideal capacitor).

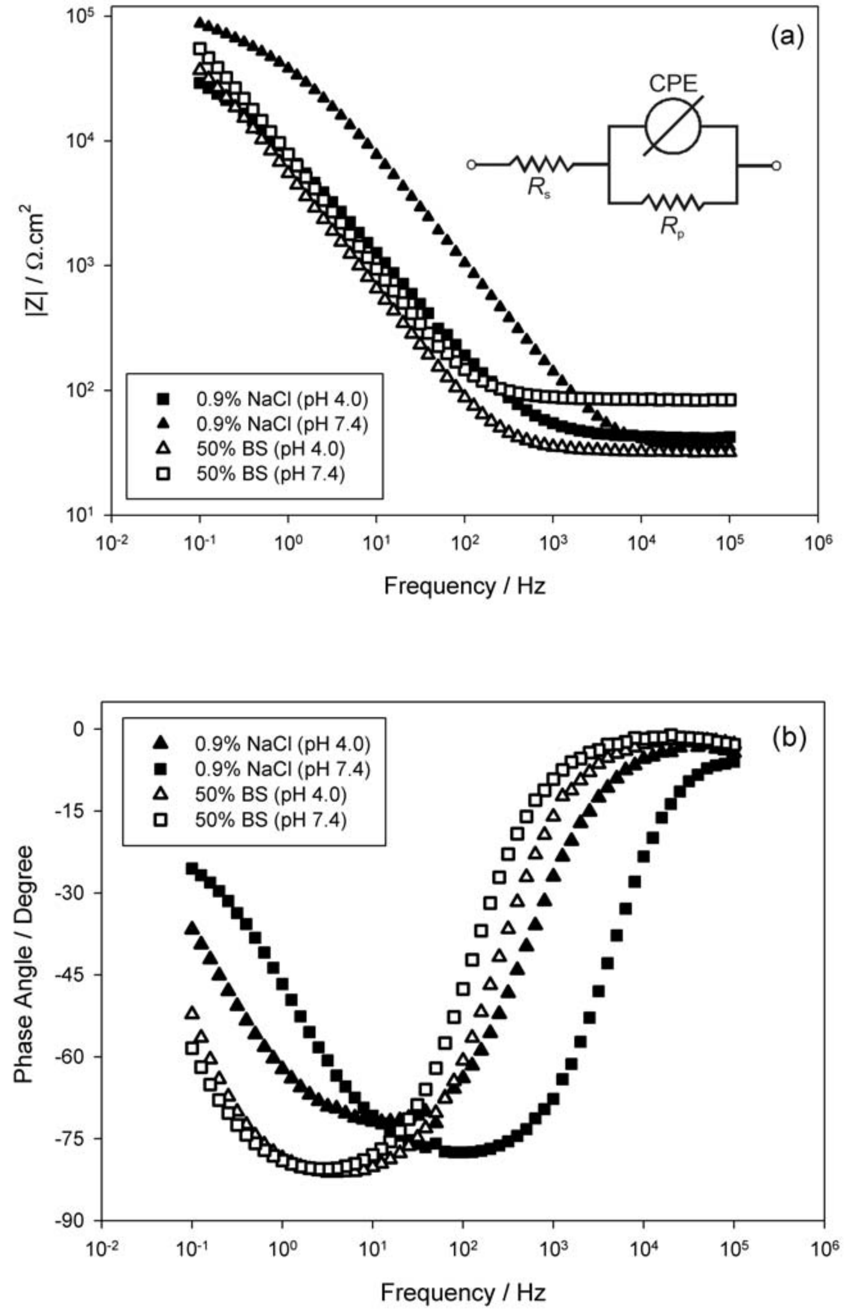

Figure 4.7: Electrochemical Impedance diagrams (Bode diagram, phase angle) for cast CoCrMo in the 0.9 wt.% NaCl and 50% BS test solutions. (a) Modulus of impedance vs. frequency and (b) phase angle vs. frequency.

The impedance data were fitted using the equivalent circuit as shown in the insert to Figure 4.7(a) and the resultant parameters are given in Table 4.1. For the 0.9 wt.% NaCl solutions, the interfacial capacitance can be attributed to a double-layer capacitance or to the capacitance of the surface oxide film, plus potentially the adsorption/desorption of hydrogen [217]. For the BS containing solutions, the interfacial capacitance can be attributed to a double-layer capacitance and/or surface oxide film, plus the adsorption/desorption of the proteinaceous materials. For 50% BS solutions, the capacitive frequency region can clearly be seen to extend deeper into the low-frequency region, with a increase in the capacitance values (Table 4.1), which could be associated to the adsorption of the biological species [150]. The similar behaviour (shift of curve minima towards low-frequency region) for 0.9 wt.% NaCl spectra at pH 4.0 could be related to greater adsorption of hydrogen [217]. For all spectra, the fitting procedure resulted in a value of the n generally around 0.9, which justified the use of the CPE. However, with the absence in the spectra of a low–frequency resistive response, i.e. almost a pure capacitive behaviour, this limits the accuracy in determining the R_p values.

Although the CoCrMo / solution interfaces were still in the process of attaining a steady-state condition after 30 min immersion, the EIS measurements were made in order to make direct correlations with the wear-corrosion testing in the following chapters. However, Contu *et al.* reported that the CoCrMo alloy in bovine serum only reached a true steady-state after 40 h [209]. In general, EIS data is often reported to show that the interfacial capacitance decreases and the R_p increases with immersion time as a consequence of passive film thickening [218].

Table 4.1: Fitted EIS parameters of CoCrMo in NaCl and BS solutions after 30 minutes immersion.

	0.9 wt.% NaCl		**25% BS**		**50% BS**	
	pH 4.0	pH 7.4	pH 4.0	pH 7.4	pH 4.0	pH 7.4
R_p / kΩ.cm^2	40.7	81.4	99.9	89.5	69.9	125.6
CPE, $Y_0 \times 10^{-6}$ / Ω^{-1} cm^{-2} s^n	26.4	3.8	32.7	18.7	33.1	23.4
n	0.830	0.832	0.910	0.907	0.924	0.877
Potential / V	-0.104	-0.166	-0.092	-0.137	-0.067	-0.166

In Table 4.1, the capacitance values for the BS solutions are higher than that for the 0.9 wt.% NaCl, corresponding to the initial partial coverage of the CoCrMo surface by adsorbed proteinaceous material. The lower capacitance values for pH 7.4 conditions signify that the adsorbed protein layer is more homogeneous / compact and thinner [209]. As pH 4.0 is close to the isoelectric points of the proteins within the serum [167], there is a greater tendency for protein adsorption and denaturation (less repulsions between adsorbed proteins) [219] and this therefore resulted in higher capacitance values. Nevertheless, the capacitance is not just dependent of the extent of the adsorbed protein, it is also a complex function of other parameters related to the CoCrMo / solution interface, which may also be dependent on the structural, physical and chemical properties of the proteins (thickness and structure of protein layer and the CoCrMo / protein / solution interface, etc.) [217].

A more noble potential and greater corrosion current were observed for the pH 4.0 0.9 wt.% NaCl solution, as shown in Table 4.1 and Figure 4.6. A similar trend has been reported in the literature [160, 209]. This might be explained by the Evan's diagram describing the open circuit potentials as shown in Figure 4.8.

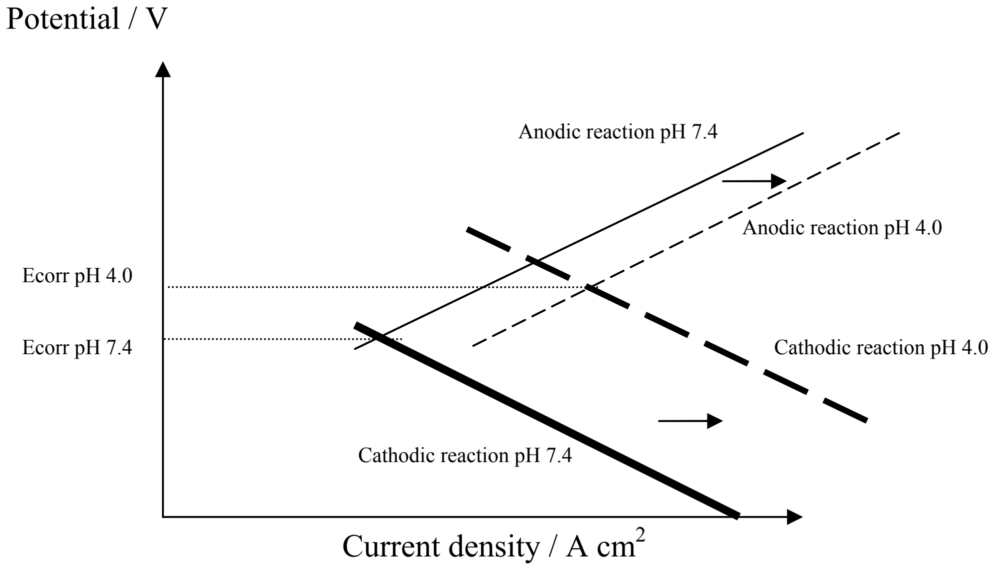

Figure 4.8: Evan's diagram showing influence of pH on corrosion potential and corrosion current density in 0.9 wt.% NaCl test solution.

For 0.9 wt.% NaCl, as pH 4 solution has increased H^+ concentration, the cathodic reaction (hydrogen evolution) accelerates, shifting the cathodic curve towards the right (bold solid line to bold dashed line). The anodic reaction curve corresponding to metal dissolution may also shift towards higher current density direction (thin solid line to thin dashed line), but due to the barrier effect of the surface oxide film, the shift is not to the same extent as the cathodic curve. The combination of the anodic and cathodic partial reactions results in an overall more noble corrosion potential and a higher corrosion current as indicated in the graph.

The presence of proteins may make the situation much more complicated due to a few competing processes taking place simultaneously. For pH 7.4 BS solutions, the protein will impede the cathodic reaction shifting the cathodic curve to the left. As the Co ions may form metal-organic complexes with the proteins, the anodic process may be accelerated (shifting the anodic curve to the right). However, the adsorbed protein at the same time could inhibit the charge transfer process (less oxygen transfer), which shifts the anodic curve to the left. When pH is adjusted to pH 4.0, the shifting of the anodic and cathodic curves may resemble that of pH 4.0 0.9 wt.% NaCl. The final OCP, the corrosion current and hence R_p of pH 4.0 BS solution will depend on the competition between the multiple processes.

The competing processes that are simultaneously occurring on the metal/solution interface are summarized as follows: (i) Cobalt is unstable in BS and dissolves to form metal-protein complexes [209] and therefore accelerate the metal dissolution; (ii) the adsorbed proteinaceous layer could reduce the transport of oxygen and/or dissolution products to and away from the CoCrMo surface, thus hindering the charge-transfer at the interface (passive diffusion or dissolution processes) [141, 160]; (iii) the different combinations of protein concentration and pH could influence the structure of the adsorbed layer (molecular structure, conformation etc), which subsequently affect the structure / compactness (packing density) of the adsorbed film. All these factors could affect the anodic/cathodic reaction kinetics of the system and influence the final values of the corrosion potential, R_p as well as corrosion currents.

4.3 X-ray Photoelectron Spectroscopy

While EIS only provides qualitative characterization of the protein adsorption behaviour, X-ray Photoelectron Spectroscopy (XPS) is capable of producing more detailed compositional information and quantification for the thickness of the adsorption film. The details of the XPS analysis condition has been stated in Section 3.6.4. Figure 4.9 (a) shows the XPS survey scan for a virgin CoCrMo surface as well as the surfaces immersed in 25% BS at pH 7.4 and pH 4.0, respectively. The curve for virgin CoCrMo surface was used as the benchmark providing reference chemical information. The peaks Co2p (~778.2 eV), Cr2p (~574.0 eV) and Mo2p (~227.7 eV) are evident from the virgin surface together with C1s (~283.1 eV) and O1s (~533.0 eV) representing the advantageous carbon and oxygen in the surface oxide layer, respectively. For the specimen immersed in pH 7.4 25% BS for 30 min, the peak intensity for all the metallic elements decreased significantly, with the Mo2p peak only just undetectable.

Additionally, a small N1s peak emerged at ~ 401 eV, which is the typical binding energy for amide functional groups [220]. For the specimen immersed in pH 4.0 25% BS, all the metal peaks were no longer visible, whereas a stronger N1s peak was shown at 401.2 eV, which represents protonated amine groups [221]. Figure 4.9 (b-c) also shows the curve fitting for the N element obtained under the two pH BS immersion conditions. The N-H peaks at 394.5 eV [222] (Figure 4.9 (b)) and 399.5 eV [223] Figure 4.9 (c)) were found, but N-O, N-N bonds at 402.5 eV [224] were only found for the pH 4.0 25% BS specimen surface. The peaks for C1s and O1s do not show any significant difference in intensity, which can be attributed to similar C and O contents being present in the protein layer. The XPS analysis suggests that the pH level of the surrounding medium could significantly influence the surface layer adsorption as well as the type of N- bonding formed within the adsorbed protein film.

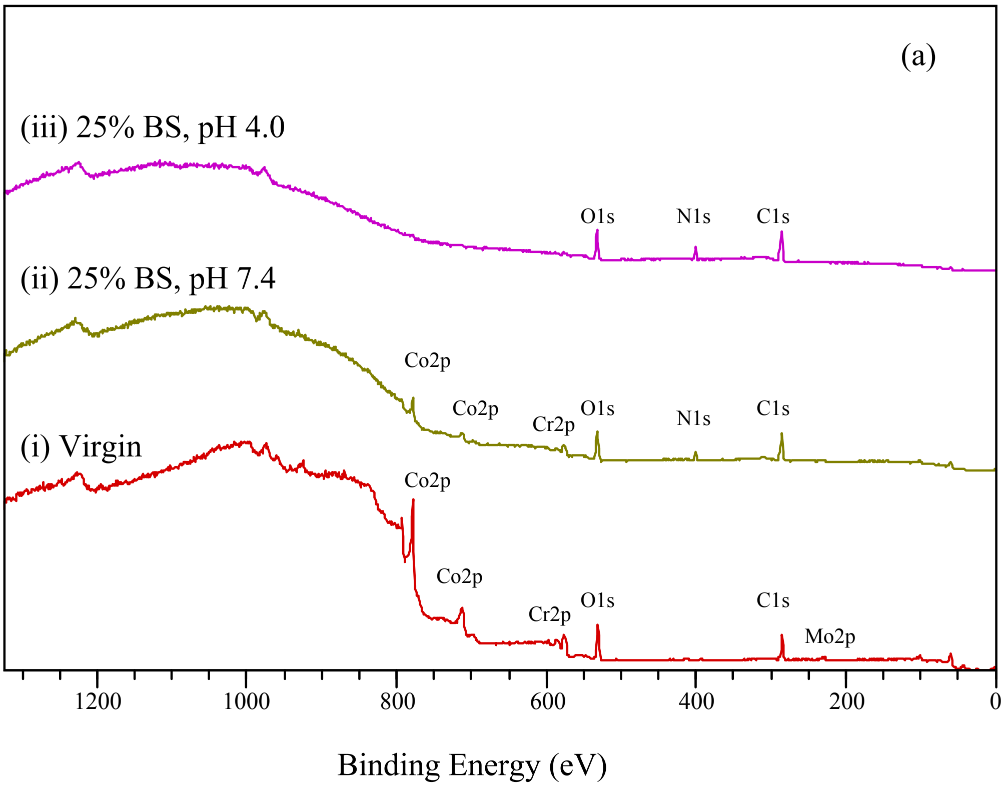

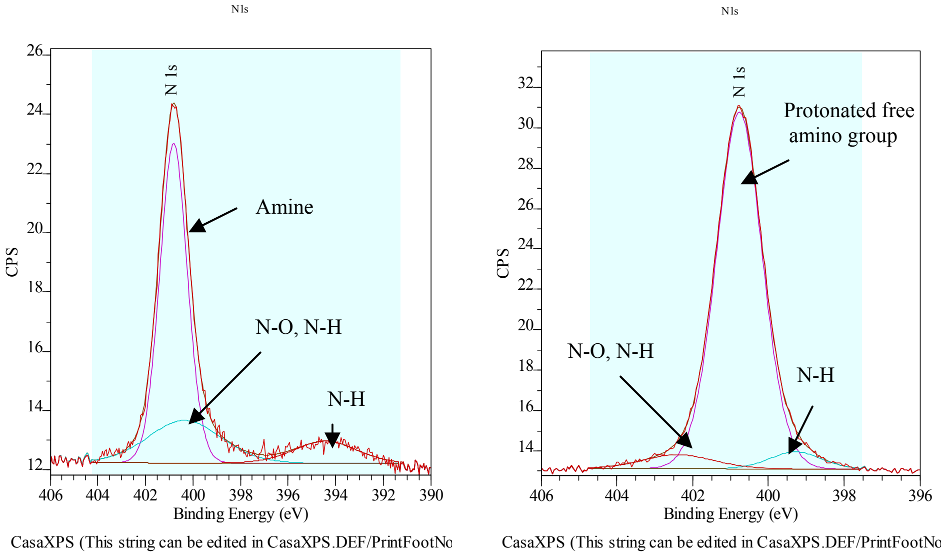

Figure 4.9: (a) XPS survey scan of CoCrMo surfaces obtained for different test solutions, (b) region scan of the N1s peak for pH 7.4 25% BS immersed specimen, and (c) region scan of the N1s peak for pH 4.0 25% BS immersed specimen.

By using the XPS peak intensity information, it is possible to determine the thickness of the surface film (oxide or the adsorbed protein film).Ton-That *et al.* suggested a method for measuring the thickness of surface films by XPS [225], using the following expression.

$$I_s = I_s^0 X_s \exp\left(-\frac{d}{\lambda_s \cos\theta}\right) \qquad \ldots\ldots 4.3$$

Where I_s is the intensity from the film, I_s^0 is the intensity from the substrate, X_s is the local concentration in mole fraction (=1), d is the film thickness, λ_s the attenuation length, θ the takeoff angle from the surface normal (0º in this study).

The method was also adopted by Sainio [226], where the effective attenuation length was replaced with an average practical effective attenuation length [227] for the film thickness calculation. The surface film (oxide, adsorbed protein) thickness values of the specimen calculated using Equation 4.3 are listed in Table 4.2.

Table 4.2: Surface film thickness obtained by XPS investigation (25% BS)

Virgin specimen oxide film	pH 7.4 adsorbed protein	pH 4.0 adsorbed protein
0.88 nm	1.93 nm	4.94 nm

The oxide film thickness 0.88 nm is close to what has previously been reported in the literature (0.8-1 nm) [150]. The protein film for pH 7.4 BS solution is 1.93 nm, which is appreciably smaller than the reported bovine serum protein molecules (*e.g.*, 4-8 nm for bovine serum albumin). This could be due to the ultra-high vacuum employed during the XPS analysis which has caused the dehydration of the protein molecules and subsequently reduction of their original volume. The pH 4.0 BS solution resulted in significantly greater protein film thickness; this can be associated with the enhanced protein adsorption due to the acidic environment as discussed earlier in the EIS studies. It is likely that multiple layers of proteins have adsorbed onto the CoCrMo surface under the acidic condition, while the protein layers formed under neutral pH condition could range from mono to possibly a few layers. The gradual disappearance of the metal peaks for specimens immersed in BS is expected as XPS provides information from the top surface (~3 nm). Thus, when the adsorbed protein film grows > 3 nm, it may block the metal substrate, as seen in the BS pH 4.0 specimen. The thicker protein film detected by the XPS for the pH 4.0 BS condition is consistent with the EIS results as discussed in Section 4.3.

4.4 Summary

DC electrochemical methods, namely OCP, potentiodynamic polarization tests, as well as electrochemical impedance spectroscopy have been conducted under static conditions (no fluid flow) to evaluate the cast CoCrMo corrosion performance in different biological fluids. It is found that the corrosion potential and corrosion current of the cast CoCrMo are influenced by the immersion time, test solution chemistry, pH as well as protein concentration. For 0.9 wt.% NaCl, reducing pH from 7.4 to 4.0 resulted in a corrosion current increasing by an order of magnitude. Whereas for the protein containing solutions, the acidic pH resulted in a decreased corrosion current, which may be attributed to the adsorbed protein film, inhibiting the charge transfer and mass transport processes. The increased protein concentration and decreased pH also result in a greater protein adsorption film thickness on the CoCrMo according to the EIS and XPS analysis. The following two chapters will present the effects of test solution composition and pH on the abrasion-corrosion behaviour of the cast CoCrMo under a dynamic test condition.

Chapter 5

Effects of hip joint simulant fluids on the abrasion-corrosion performance of cast CoCrMo

This chapter investigates the effect of different simulant body fluids (0.9 wt.% NaCl, phosphate buffered saline and bovine serum containing solution) on the microabrasion-corrosion performance of the cast CoCrMo. Material loss (specific wear rates) produced under various test conditions will be reported, the material depassivation/repassivation under the microabrasion-corrosion process will also be discussed in detail. Post test analysis involving AFM, SEM, FIB-SEM and EDX studies will reveal the specimen surface/sub-surface micro-structural change before and after wear tests under different test conditions.

5.1 *In situ* electrochemical noise measurements during microabrasion

The aim of this investigation was to obtain a better understanding of how the cast CoCrMo alloy behaves electrochemically (electrochemical current and electrochemical potential) and tribologically under different abrasion conditions, *i.e.* sliding-corrosion (*SC*) and abrasion-corrosion (*AC*) in the various test solutions. Also, this study aims to investigate the role of proteins, and phosphates on the extent of depassivation during the abrasion. The surface/sub-surface material damage has been investigated and models have been proposed to explain the complicated sub-surface structure resulting from various abrasion-corrosion processes. The test conditions for SC and AC tests are summarized in Table 5.1

Table 5.1: Summary of the test conditions for microabrasion-corrosion tests.

Test conditions	Sliding-corrosion	Abrasion-corrosion
Applied load (N)	0.25	0.25
Ball sliding velocity (m s^{-1})	0.05	0.05
SiC concentration (g cm^{-3})	Zero	1
Temperature (°C)	37 ± 2	37 ± 2
Electrochemical noise sampling frequency (Hz)	2	2

5.1.1 Electrochemical current noise measurement

Figure 5.1 shows the electrochemical current noise obtained using the four test solutions under sliding-corrosion and abrasion-corrosion conditions (1.0 g cm^{-3} SiC), respectively.

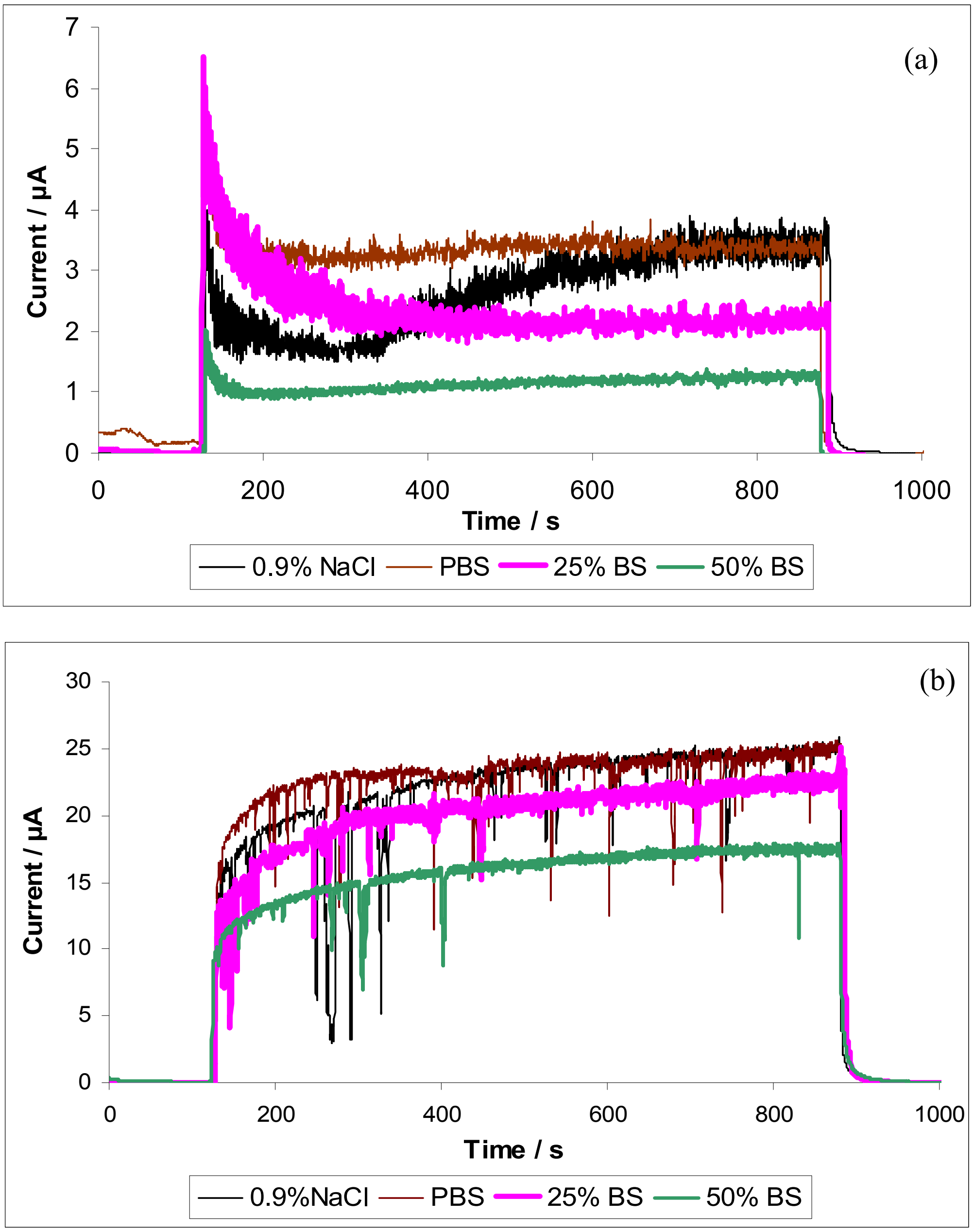

Figure 5.1: Electrochemical current noise under (a) sliding-corrosion and (b) abrasion-corrosion conditions (1.0 g cm^{-3} SiC) in various test solutions at 37 ºC.

As is shown in Figure 5.1 (a), electrochemical noise measurements start at zero seconds and ball rotation starts at 120 s. All current trends plotted under the SC condition show a sharp peak at the onset of the abrasion, which corresponds to sudden depassivation of the passive film leading to the exposure of the underlying CoCrMo surface. The currents then partially recover (decrease) as the CoCrMo repairs itself through a repassivation process. At the end of each test, the current level decreases abruptly to pre-abrasion levels. It is noted the current levels resulting from the inorganic solutions are generally higher than those of the serum solutions, especially towards the end of the test. The current level of 0.9 wt.% NaCl shows a particular trend, where after the sharp peak formed at the onset of the test (~ 4 μA), it decreases to a much lower level (~1.5 μA), before increasing again to a similar level as the PBS towards the end of the test ~3.5 μA), whereas for PBS and serum solutions, currents were relatively uniform after the initial sharp peak. Unfortunately, the reason for the particular trend seen for NaCl is unclear.

It is worth mentioning that the surface damage induced in the SC test conditions are due to the asperity contacts between the rotating ball and the CoCrMo surface. During the wear process, the wear scar is more anodic than the outside undamaged area. It is likely that within the scar area partial repassivation may occur due to the intermittent nature of the contact caused by the ball asperities. Hence micro-galvanic cells could be established in passive/active cells within the contact area and may partly contribute to the overall current flow. However, this micro-galvanic influence is not measurable and will not been discussed further in this present study.

Figure 5.1 (b) shows the electrochemical current noise generated under abrasion-corrosion conditions. Again, at the onset of abrasion, the currents in all solutions increase abruptly; however, due to the presence of SiC abrasives, repassivation within the scar is disrupted, and the currents continue increasing throughout the test. Short current transients can be observed during these tests which may correspond to partial repassivation events. As with the SC conditions, the currents return to the original values once abrasion ceases.

Overall, the average current levels in inorganic solutions are found to be 1.3 to 3 times higher than those in serum solutions according to Figure 5.1 (a) and (b). It is necessary to discuss the influence of proteinaceous material from both a mechanical and chemical aspect. As mentioned previously, the lower protein concentration could cause increased corrosion due to its ability to bind with metal ions. Alternatively, the same protein can become completely denatured in the tribological contact during the wear test, which could result in the formation of lubrication layer which reduces the friction of the tribological contact [161, 228]. This lubrication film could change the contact mechanism resulting in less passive film and underlying metal being removed and consequently less corrosion. The overall effect of proteinaceous material, whether it promotes or hinders the anodic corrosion during the wear process can only be truly understood by comparing the corrosion current density (i_{corr}) rather than the current levels alone.

The current density levels for static corrosion (from polarization curves, Figure 4.2), SC and AC conditions are reported in Table 5.2. Due to the limitation in the rig setup, the wear scar size cannot be measured *in- situ* during the actual tests. The current density can only be obtained upon completion of the test with the assessment of the final wear scar size. Current density values for SC and AC conditions are calculated by dividing the final current level immediately before the test ends by the wear scar area measured after the tests.

Table 5.2: Corrosion current density calculated based on current level (Figure 5.1) and the wear scar area.

Average current density /µA cm^{-2}	**0.9 wt.% NaCl**	**PBS**	**25% BS**	**50% BS**
[*] Static current density	0.11	0.03	0.33	0.16
[†] SC final current density	654 (0.0057)	1134 (0.0029)	808 (0.0028)	624 (0.0023)
[†] AC final current density	1391 (0.0181)	1385 (0.0182)	1181 (0.0197)	870 (0.0204)

[*]Exposed specimen area for static current density measurement: 0.899, scar areas in brackets in cm^2.

[†] Wear scar area is estimated using $A \approx \frac{\pi d^2}{4}$ ($d \ll D$), where d is the diameter of the wear scar and D the diameter of the ball.

In Table 5.2, it can be seen that the current density for SC is four orders of magnitude higher than under the static condition, whereas the current density in AC condition is typically five orders of magnitude higher than static corrosion. Therefore, the ball asperities and micro-abrasion have significantly enhanced the measured corrosion rate.

Comparing the relative corrosion performances for the SC condition, 0.9 wt.% NaCl resulted in lower corrosion current density in contrast to 25% BS, probably due to substantial BS protein binding with metal ions and thereby enhancing the CoCrMo corrosion. By acting as an anodic catalyser the effect of enhanced corrosion could predominate over the lubrication effect (reduce corrosion) brought about by the adsorbed protein. When 50% BS was used, the i_{corr} decreased, which can possibly be attributed to a more complete adsorbed protein layer coverage which impeded the metal/protein complex transporting away and hence reduced the charge transfer process. In addition, stronger lubrication may occur due to the higher solution viscosity. The PBS current density was almost twice that for 0.9 wt.% NaCl solution, this might be due to presence of phosphate resulting in different repassivation behaviour which subsequently affects the corrosion currents [150].

For the *AC* conditions, the 50% BS slurry produced the lowest i_{corr} followed by 25% BS, while 0.9 wt.% NaCl and PBS solutions gave similar performances. Although the wear scar size generated using the BS solutions were found to be larger, it is believed that the majority of the material removal that occurs in these protein containing slurries is primarily due to a mechanical process (which will be discussed later in Section 5.2). The presence of protein reduces the corrosion-induced current during abrasion, which is not consistent with the potentiodynamic polarization results (where protein accelerates corrosion under static conditions). This contradiction could be explained by the tribo-enhanced denaturisation of protein forming a physical barrier that inhibits the charge transfer process during the microabrasion.

5.1.2 Electrochemical potential noise measurement

Figure 5.2 (a) and (b) shows the electrochemical potential noise measurements for the *SC* and *AC* conditions, respectively. Three regions can be clearly seen. Region I, before the onset of the abrasion test, the different OCPs of the CoCrMo is clearly apparent for the various test solutions. Once abrasion starts (*i.e.* ball rotation or slurry feed / ball rotation), the potential instantaneously decreases corresponding to surface oxide film damage (depassivation). Within Region II the potential noise measurements for all four solutions maintain a relatively constant level. In Region III, the potential is seen to recover, this exponential recovery corresponds to a repassivation of the passive film and the slow charging of the double-layer capacitance.

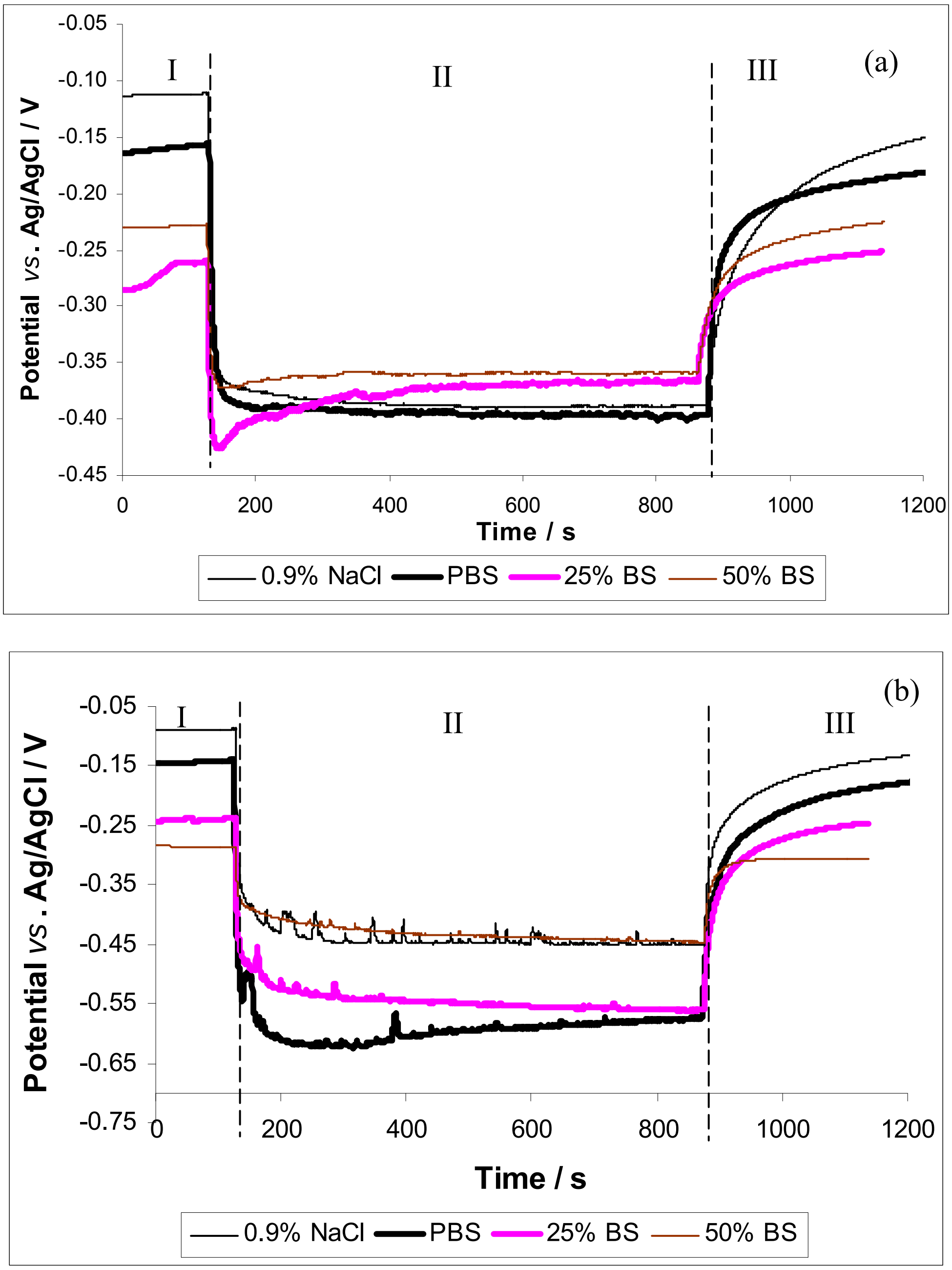

Figure 5.2: Electrochemical potential noise for (a) sliding -corrosion (no SiC) and (b) abrasion-corrosion (1.0 g cm^{-3} SiC) test conditions at 37 ºC.

The extent of potential shift during the wear test (*i.e.* the change in OCP or ΔOCP) has been highlighted in Figure 5.3 (a) and (b). Generally, the ΔOCP for the *SC* condition are lower than for the *AC* condition and also the BS solutions are lower than either PBS or NaCl solutions. These findings are in good agreement with Contu *et al.* [160]. In a protein-rich environment, such as for the BS solutions, the adsorbed biological molecules can lubricate the contact surfaces and therefore reduce the degree of damage induced by the wear processes. Conversely, for the *AC* conditions, the presence of the SiC abrasives within the contact overshadows any lubrication effects, and results in appreciably higher current levels. The tribo-enhanced denatured protein could impede the charge transfer and resulting in a smaller delta potential drop. The wear scar profiles shown in the next section will further illustrate the role of protein in the tribo-contact.

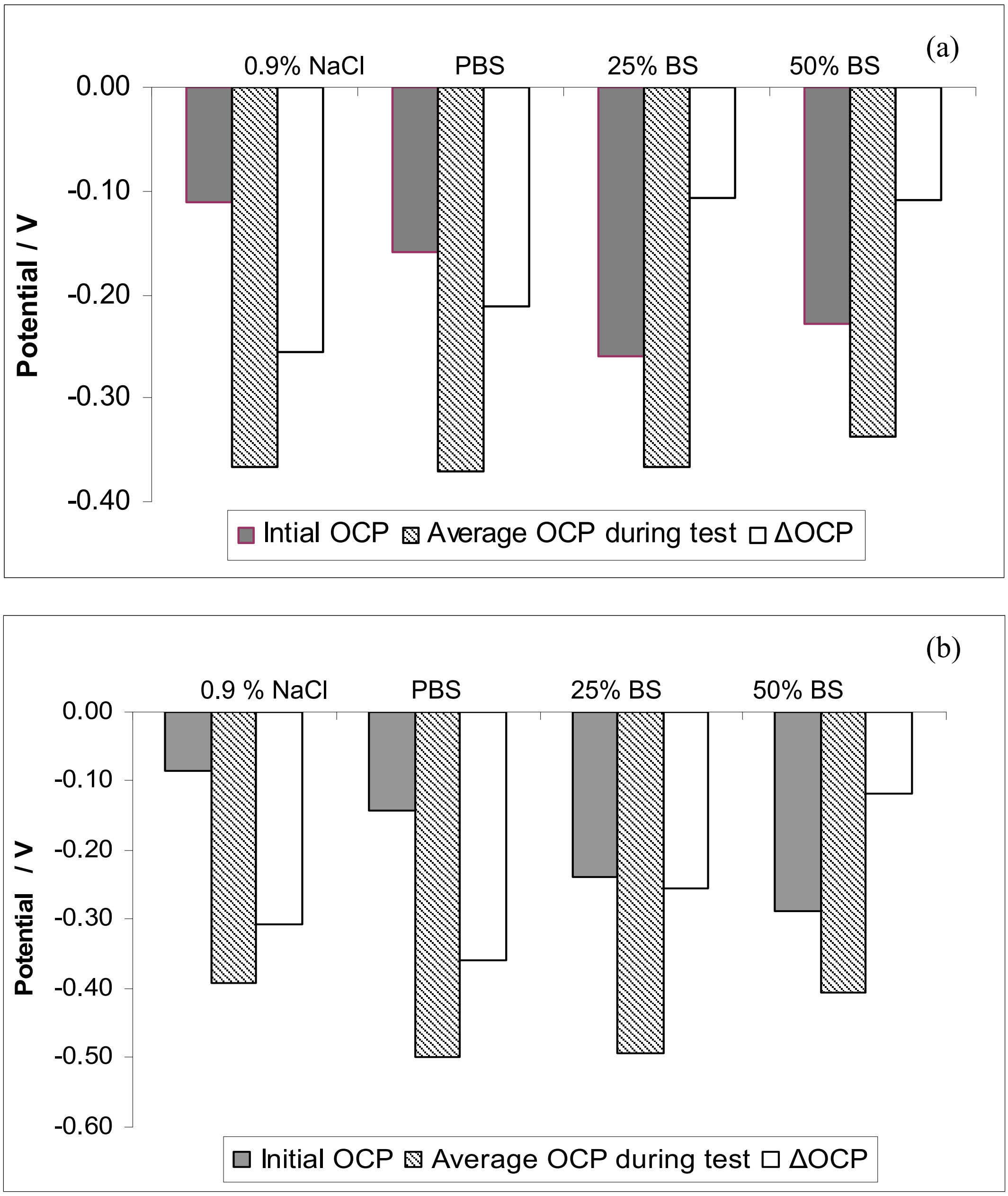

Figure 5.3: Delta OCP under different (a) sliding-corrosion and (b) abrasion-corrosion conditions in the four test solutions at 37 ºC.

Comparing Figures 5.2 and 5.3, the electrochemical current noise, after abrasion ceases, typically approaches the initial value (before abrasion) within approximately 2 seconds, while the potential recovery is rather slower (a few tens of seconds) for all test solutions. This indicates that although repassivation of oxide film effectively shuts down the anodic current, the surface had not entirely reached its stable state. This finding is consistent with Leinenbach *et al*. [229], where it was reported that when abrasion was stopped the current decreases as passivity (oxide reformation) of CoCrMo is restored and further metal-ion dissolution is hindered. In the present study, the wear process resulted in wear scar surface with different morphology and composition (mechanically mixed layer) compared to a virgin polished surface. After the oxide on the worn surface reforms, the OCP of the CoCrMo slowly approaches a similar value to that before abrasion, which is controlled by the slow recharging of the electric double-layer capacitance [230] at the metal / solution interface. This recharging is achieved by the oxygen reduction, a slow faradic process which is dominated by a diffusion controlled mass (oxygen) transport process [230, 231]. Therefore, it is reasonable to expect that the OCP recovery takes a longer time than that for the current (refer to Figure 5.4). The detailed analysis for repassivation kinetics under different test conditions can be found in Chapter 9.

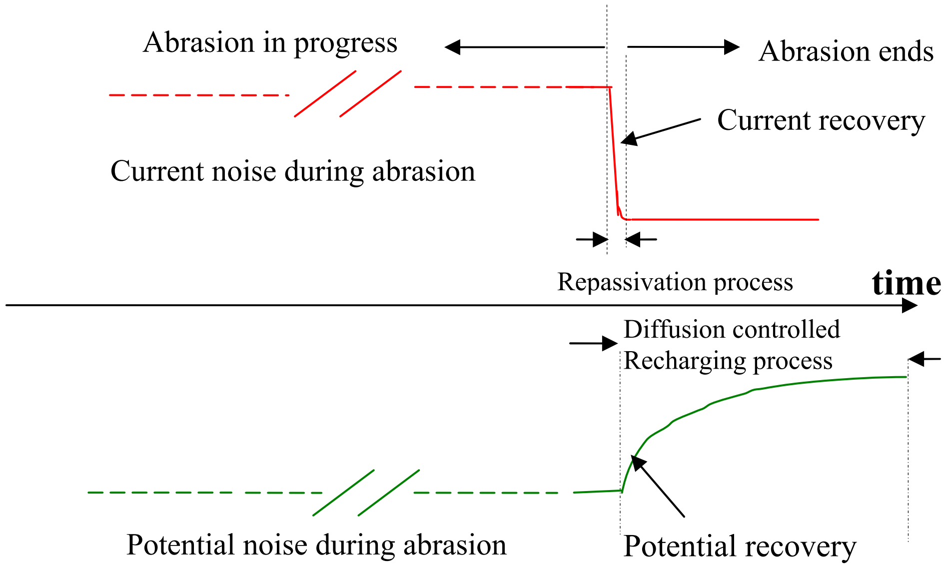

Figure 5.4: Schematic of the current and potential recovery after abrasion tests.

5.1.3 Summary

In this section, *in situ* electrochemical current noise and potential noise measurements obtained in different test solutions and under different abrasion conditions (SC and AC) have been compared and analysed. Results have shown that the presence of proteinaceous material decreased the measured current levels under both *SC* and *AC* conditions; the corresponding potential drop was also lower for BS solutions. This observed phenomenon is contrary to what was previously seen for the potentiodynamic polarization study, where the presence of protein produced enhanced corrosion rates. An explanation for this differing behaviour may be due to tribo-enhanced denaturisation of the proteinaceous material, which potentially obstructs charge transfer during microabrasion.

5.2 Specific wear rate of cast CoCrMo in different simulated body fluids

In this section, the specific wear rates (SWRs) obtained in the four test solutions and different abrasion conditions will be presented. The aim is to study the wear performance of the CoCrMo and to determine any synergistic effects. Using Faraday's law, the individual components of the synergy term can be obtained, for example the wear-enhanced corrosion (C_w) and corrosion-enhanced wear (W_c), which enable greater understanding of how CoCrMo corrosion affects wear under the different test conditions. The symbols used in this section can be found in Table 3.7.

5.2.1 Sliding-corrosion condition

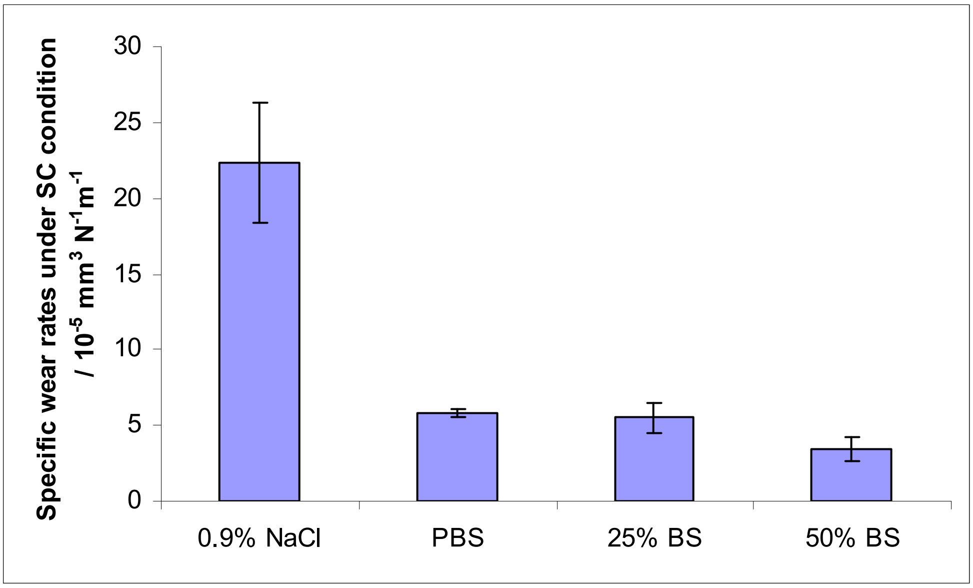

Figure 5.5: Specific wear rate obtained under the sliding-corrosion condition at 37 ºC for the four test solutions.

Figure 5.5 shows the total specific wear rate (T_{SC}) obtained under SC condition. NaCl has the highest specific wear rate of 22×10^{-5} mm^{-3} m^{-1} N^{-1}, but in the presence of either PBS or BS, the wear rate decreases to about 5×10^{-5} mm^{-3} m^{-1} N^{-1}. It has been seen in

Table 5.2 that the corrosion current densities of all the four solutions are at similar levels. For PBS or BS solutions, the adsorbed phosphate or proteins, have the potential to form a boundary lubrication layer or tribofilm which effectively reduced the specimen surface damage. Thereby, it is predominantly mechanical element (lack of boundary lubrication) that results in the much higher wear rate for 0.9 wt % NaCl.

5.2.2 Abrasion-corrosion condition

In order to measure the pure mechanical element in the AC process, 'pure abrasion' tests were conducted under cathodic protection conditions where specimens were potentiostatically held at -0.400 V *vs.* OCP. This potential was chosen as it was sufficiently negative to minimise anodic corrosion processes and not too low to cause hydrogen evolution. A viscosity enhancer, Dextran (a chemically inert polysaccharide) was added to the electrolyte in an effort to decouple the effect of viscosity for the organic solutions (25% and 50% BS). Two types of Dextran solutions (Dextran-A and Dextran-B) were made accordingly to give similar viscosities as that found for the 25% BS (0.92 mPa.s) and 50% BS (1.05 mPa.s) at 37 ºC, respectively (refer to Table 3.8).

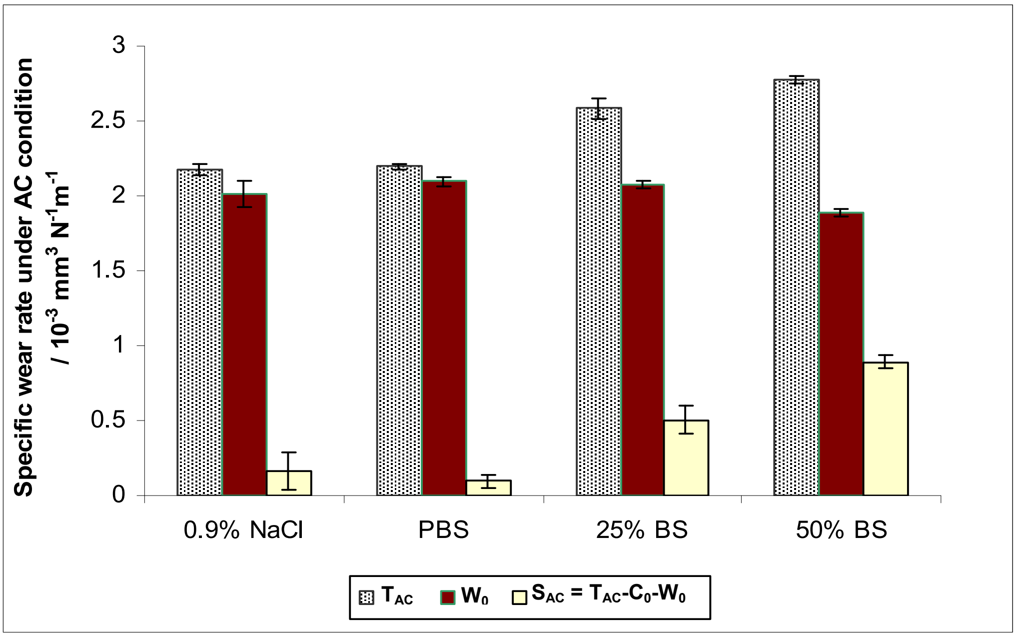

Figure 5.6: Total specific wear rates obtained under the abrasion-corrosion condition at 37 ºC .W_0 is obtained under cathodic protected condition, C_0 is obtained from i_{corr} in the potentiodynamic polarization curve.

Figure 5.6 shows the specific wear rates obtained under the AC condition. The pure corrosion element C_0 is a few orders of magnitude lower than T_{AC} and is therefore negligible. It has been found that the presence of proteinaceous material increased the total specific wear rate T_{AC} and significantly enhanced the percent synergy $(\frac{S_{AC}}{T_{AC}} \times 100\%)$ from 7% and 4% (for NaCl and PBS) to between 20% and 30% (for 25% and 50% BS, respectively). However, a higher total wear rate in the test solutions does not necessarily correspond to a higher corrosion rate according to the electrochemical current noise data (refer to Figure 5.1 (b)). This counter-intuitive trend in wear rate and current level can be related to the influence of the synergistic effects (S_{AC}) that may occur in the different test solutions (to be explained in the following text). The pure abrasion (W_0) appears to decrease at higher viscosity (1.05 mPa.s), however the reason for this still remains unclear.

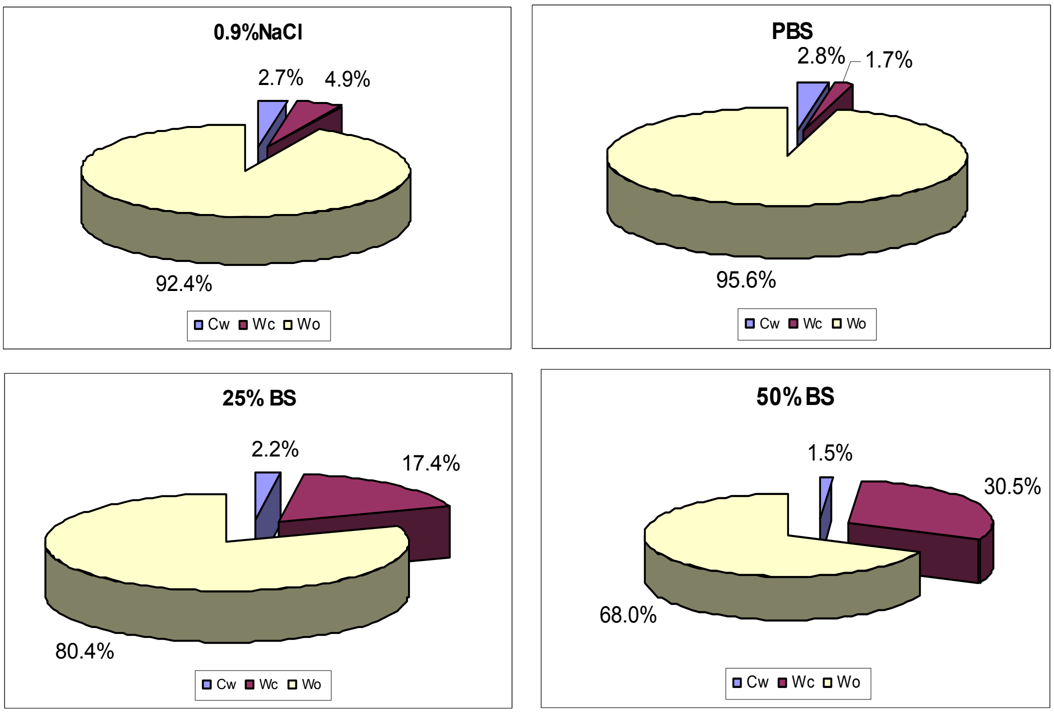

Figure 5.7: Percentage of volume loss for CoCrMo in four test solutions.

As can be seen from Figure 5.7, pure mechanical damage is a major cause of the material loss for all cases, however, the synergy between mechano-electrochemical processes clearly contributes to the wear-corrosion degradation. In all four solutions, the effect of wear on corrosion ranges from 1.5% (for 50% BS) to 2.8% (for PBS). This indicates that the mechanical damage did not significantly affect the electrochemical process due to the good corrosion resistance of the CoCrMo alloy. The presence of phosphate seems to reduce the W_c, which may be due to metal forming phosphate / hydroxyphosphate compounds on the surface [232] which reduced the friction and hence generated less wear. However, for the proteinaceous slurries, the W_c dominates the synergy (S_{AC}). This could be due to the influence of protein adsorption on the surface mechanical properties [233], in addition, the denatured protein may form an adhesive layer on the specimen surface which could help to enhance the particle entrainment and increased particle rolling efficiency during the microabrasion process. In this circumstance, it is more appropriate to use the term protein-enhanced wear rather than W_c as the protein appears to have enhanced the material loss both chemically and mechanically.

5.2.3 Electrochemical and mechanical interactions

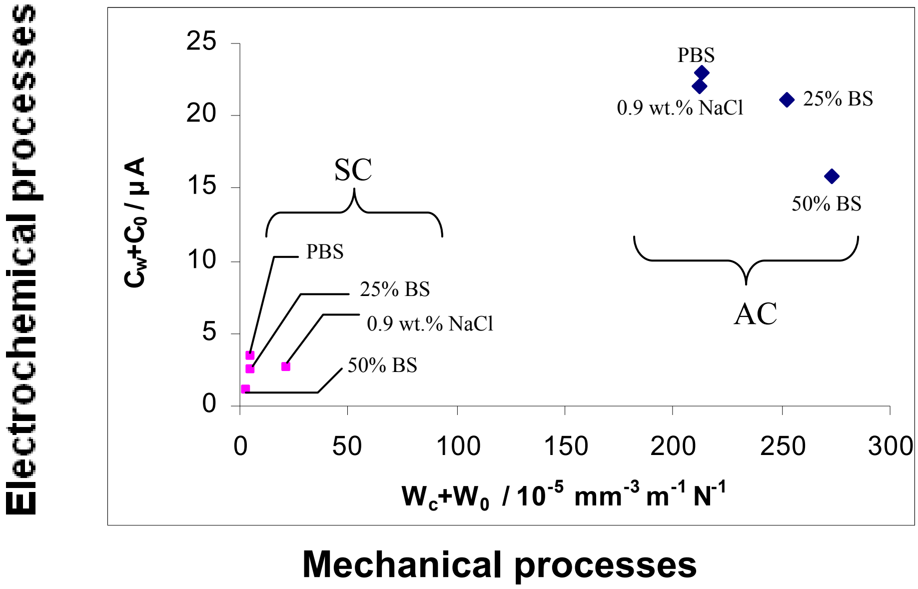

Figure 5.8: Relationship between total corrosion current and pure mechanical wear loss.

The correlation between the electrochemical processes $C_w + C_0$ (wear induced corrosion plus static corrosion) and the mechanical processes (pure abrasion plus corrosion induced wear) for both SC and AC conditions have been plotted in Figure 5.8. The corrosion currents for both the SC and the *AC* conditions decrease with increasing BS concentration. Possible explanations for this behaviour could include:

1. The extent of protein denaturisation is enhanced by the tribo-contact. The frictional heating between the bearing surfaces may bring the local contact point temperature to over 60 ºC (above which the protein denatures [234]). The protein may also undergo pressure-induced denaturation (>400 MPa for BSA [235]) due to the mechanical (shear) stress. The denatured protein layer may enhance the

impedance of the charge transfer process [36] at the anodic sites (freshly worn surface).

2. Proteins could adsorb onto the negatively charged surface, that is, the cathode (undamaged specimen surface) and/or the counter electrode, inhibiting the mass transport/ diffusion of the reduction reactants (oxygen). The reduction process is thereby limited which in turn hinders the anodic process.

5.2.4 Summary

Specific wear rates have been presented for CoCrMo in all test fluids under *SC* and *AC* conditions. The overall influence of corrosion on wear under these test conditions is relatively minor for all cases due to the good corrosion resistance of cast CoCrMo alloy. The effect of wear enhanced corrosion is calculated based on the electrochemical noise results and was shown to decrease with increasing mechanical wear rate in *AC* condition. This could be due to the tribo-enhanced denaturisation of protein that forms a physical barrier that hinders electron transfer. Alternatively, the corrosion enhanced wear was shown to increase in BS solutions, attributed to the enhanced particle entrainment due to the adsorbed protein layer formed on the surface or the deterioration of the surface mechanical properties due to the protein adsorption.

5.3 Post test analysis and wear mechanisms evaluation

This section will present the post-test analysis of the wear scars using SEM, FIB-SEM and EDX. The wear scar profile, surface and subsurface damage, as well as the elemental information of the area of interest will be discussed. The wear mechanisms will be correlated to the results obtained in the previous sections.

5.3.1 Scanning electron microscopy analysis

5.3.1.1 Sliding-corrosion wear scars

A SEM investigation of the wear scars produced under the various test conditions is presented in Figure 5.9. For comparison, Figure 5.9 (a) shows a polished cast CoCrMo specimen with a characteristic network of evenly distributed blocky carbides (~ 25 μm in size).

Figures 5.9(b)-(e) show the wear scars produced under the *SC* condition vary significantly in their profiles. For the 0.9 wt.% NaCl generated wear scar, Figure 5.9(b) clearly shows two-body grooving abrasion is the dominant wear mechanism [203]. The grooves are likely to be due to the asperity contact between the ball and the CoCrMo surface during the sliding process. The carbides in the CoCrMo in this case are not clearly evident. However, in Figure 5.9(c), the PBS appears to significantly reduce the overall two-body abrasion damage. This might be due to an adsorbed phosphate layer formed on the zirconia ball [236] and the CoCrMo surface [159] during the immersion process. This adsorbed phosphate layer may also influence the bearing surface lubrication and reduce the wear, but the effect is not as significant as compared with the proteinaceous BS solutions. Indeed, the protruding carbides (white arrows) appear unaffected, thus potentially contributing to the reduced wear. The carbides are more wear resistant under lubricated conditions and it can reduce the potential for adhesive wear of the Co rich matrix through 'matrix to matrix' contact of the two opposing metallic bearing surfaces [237].

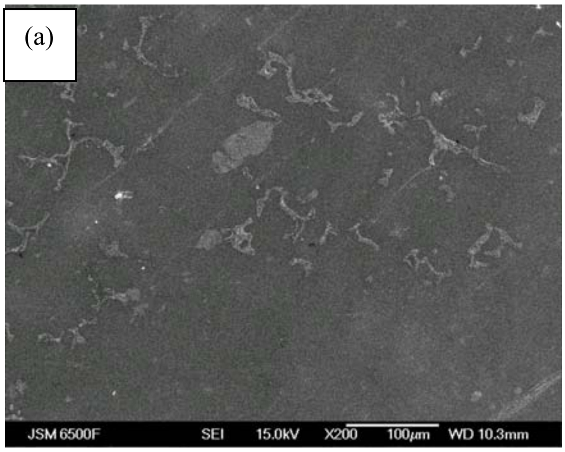

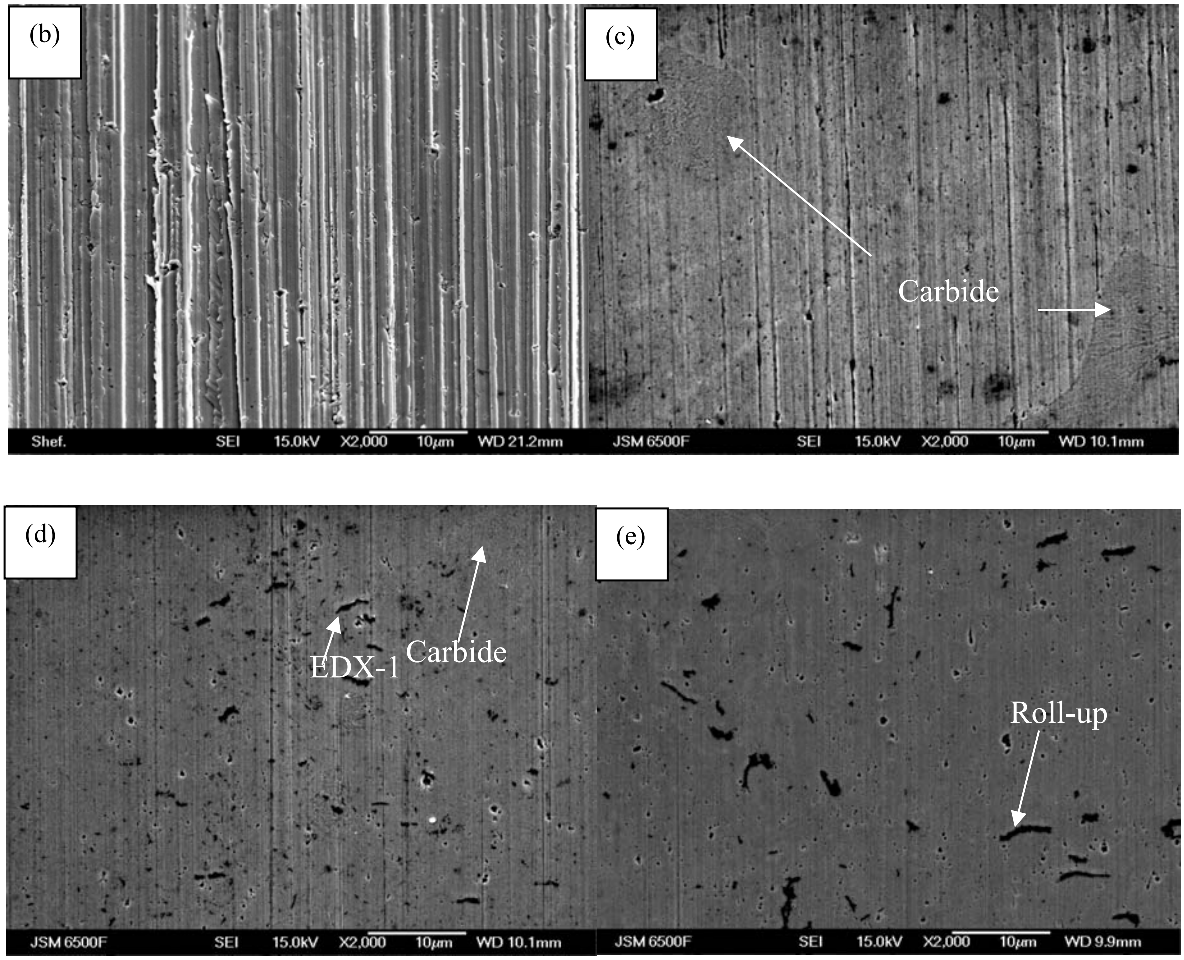

Figure 5.9: FEG-SEM images showing the wear scars produced in different test fluids under sliding-corrosion conditions. (a) Polished CoCrMo surface. Images were taken at centre of the wear scars: (b) 0.9 wt.% NaCl, (c) PBS, (d) 25% BS, and (e) 50% BS (ball rotating direction: top to bottom).

For the 25% and 50% BS solutions, the wear scars appear to be more polished, with only minor 2-body grooving at the scar centre for 25% BS, see Figure 5.9(d), and an almost groove-free surface for 50% BS, see Figure 5.9(e). It has been well documented that proteins will adsorb onto a metal surface immediately after immersion in a proteinaceous solution [61, 238]. The adsorption process takes place within milliseconds, and will continue until the metal/solution interface reaches a steady-state equilibrium [61]. During the present study, the CoCrMo and the ball were immersed in the solutions for 30 min prior to microabrasion. Within this time period, a protein layer is expected to form on both surfaces. The adsorbed protein layer could effectively protect the surface by acting as a lubrication layer [161]. The adsorbed protein layer improves the boundary lubrication effect and reduces the wear damage of the surface. Another feature identified within the wear scars formed in BS solutions is the black particles (or roll-ups with vertical dimension ranging from a few ten to a few hundred nanometers according to AFM analysis) with similar directionality (aligned perpendicular to the sliding direction). Similar rolling protein aggregates have been found by Murakami et al. [239] in their studies of artificial synovial joints under sliding motion. These particles found in the present study contain nitrogen (N) and elements of the alloy, based on EDX analysis (refer to Table 5.3), and could be the protein / wear debris mixture entrained in the tribo-contacts during the sliding process. These protein/wear debris conglomerates could also influence the CoCrMo/ZrO_2 interface by separating the bearing contact, polishing the CoCrMo surface through a chemical-mechanical polishing mechanism.

Figure 5.10 (a)-(c) shows AFM images of the as-polished CoCrMo, CoCrMo immersed in 25% BS at 37 ºC for 30 min, and after SC test in 25% BS at 37 ºC. The CoCrMo specimen after being immersed in 25% BS was entirely covered by nodular features as seen in Figure 5.10 (b), these features have been attributed to adsorbed protein molecules, as the scale of these features are consistent with the reported dimension (~ 4 nm) of an albumin molecule within serum [56]. The wear scar produced in 25% BS under the SC condition shows full coverage of protein aggregates with less distinguishable globular features. This could be due to the denaturisation of the protein molecules under mechanical stress. Similar layers have been identified by Serro *et al.* [67] using a BSA solution. The fact that denatured proteins covered the entire worn area was reported to indicate that the serum protein had adsorbed as a multilayer on CoCrMo (a single layer protein would be easily removed and would not cover the worn surface as effectively). Also, this present study is consistent with the findings from Wimmer *et al.* [46, 240], where a proteinaceous solid layer was found to cover a large area on retrieved hip joints, which was considered to be due to the denatured protein formed during the articulation.

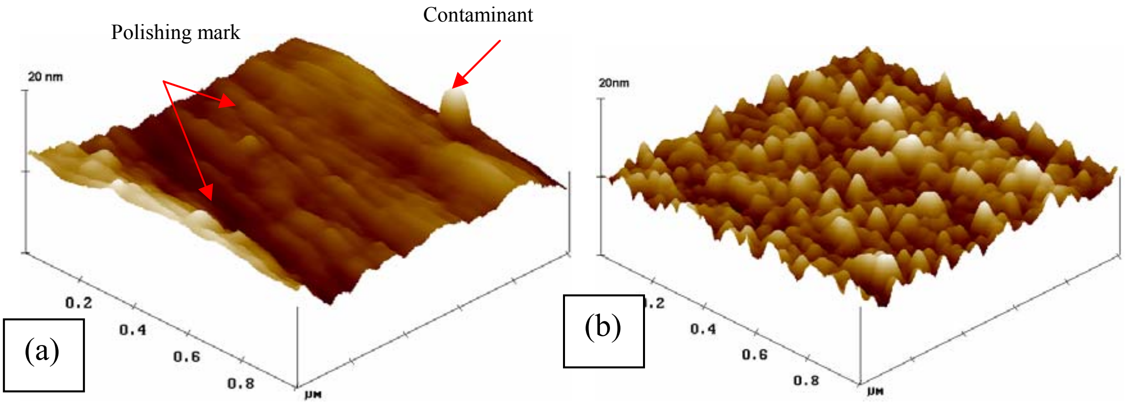

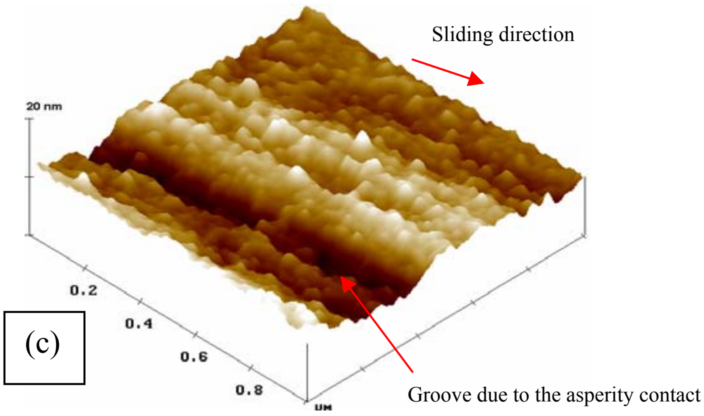

Figure 5.10: AFM study of the CoCrMo surface: (a) as polished, (b) after immersion in 25% BS for 30 min at 37 ºC and (c) after sliding-corrosion in 25% BS at 37 ºC.

5.3.1.2 Abrasion-corrosion wear scars

The wear scars generated under the AC condition, shown in Figures 5.11(a)-(d), show multiple indented surfaces without directionality, indicating that three body rolling abrasion was the dominant wear mechanism [203]. Higher magnification SEM images (see Figure 5.12) reveal that the wear scars produced in NaCl and PBS solutions have more platelet formation (angular / flaky surface features) compared to those produced in the BS solutions. Consequently, this suggests that the presence of protein may have affected particle / surface interaction and subsequently increased the particle rolling efficiency. The greater entrainment could also be due to the adsorbed protein onto the SiC abrasives [241]. Whereas, for inorganic solutions, the force acting on each particle is more likely to encourage SiC particles to skid through the contact while rolling. As such, overall the increase in the synergy for BS conditions may be attributed to the protein-enhanced wear in which the mechanical processes dominate over the electrochemical processes.

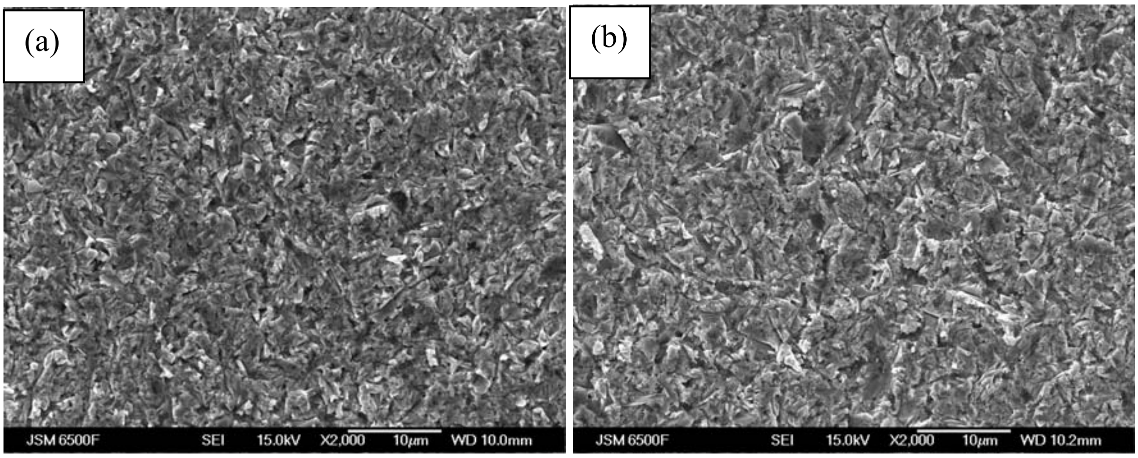

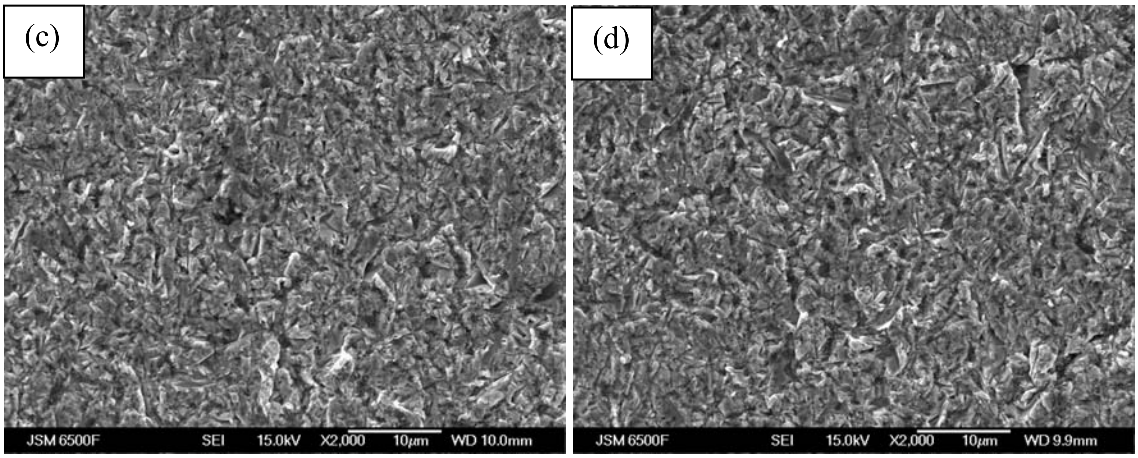

Figure 5.11: FEG-SEM images showing the wear scars produced in different test fluids under abrasion-corrosion conditions. (a) 0.9 wt.% NaCl, (b) PBS, (c) 25% BS, and (d) 50% BS (ball rotating direction: top to bottom).

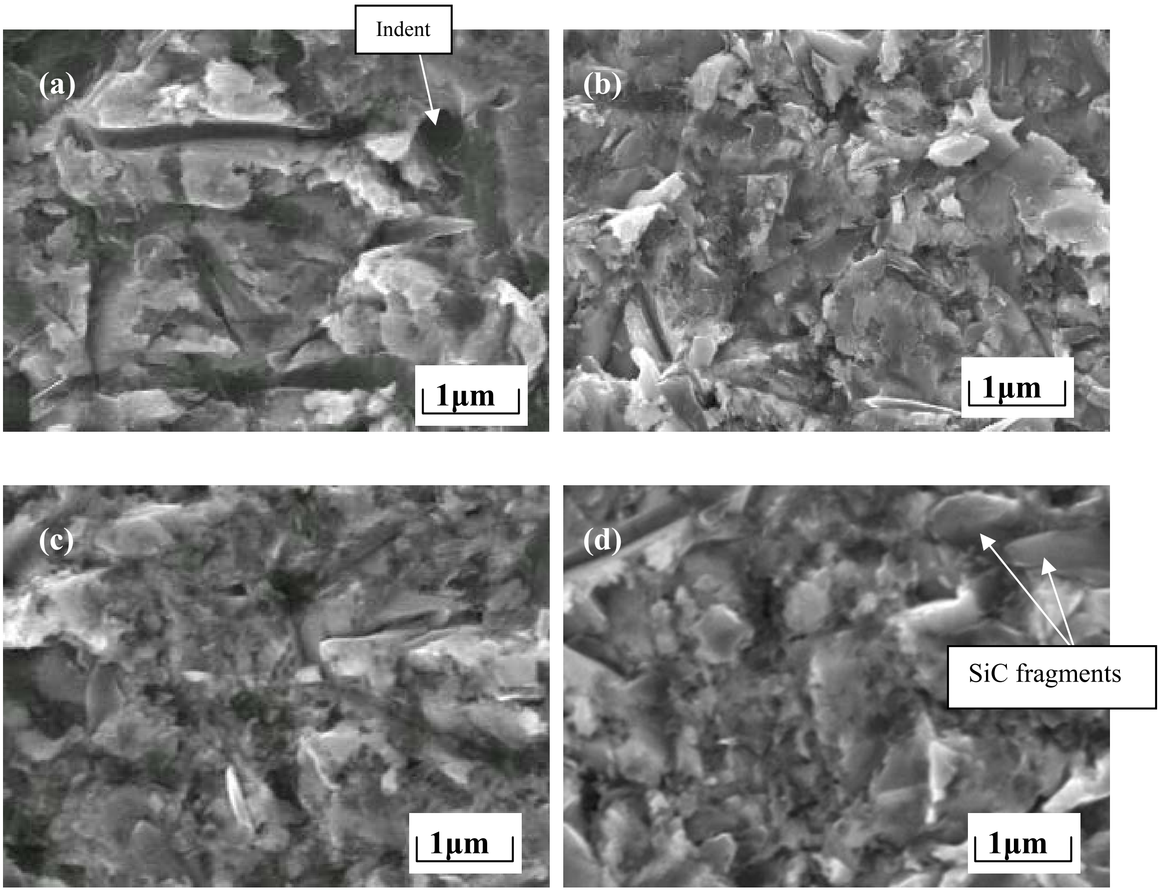

Figure 5.12: SEM study of the wear scar surface morphology produced under abrasion-corrosion conditions (a) 0.9 wt.% NaCl, (b) PBS, (c) 25% BS, (d) 50% BS. Images taken at centre of the wear scar, ball rotating direction: top to bottom.

5.3.2 FIB-SEM investigation

Focused ion beam combined with scanning electron microscopy (FIB-SEM) was used to analyse the worn specimens produced in 0.9 wt.% NaCl and 25% BS solutions. The cross-sections of the sub-surface structures have been compared with a virgin unworn specimen. Figure 5.13 shows the cross-section of a polished CoCrMo specimen. The top layer is the platinum deposit used to protect the specimen during the Ga ion milling process.

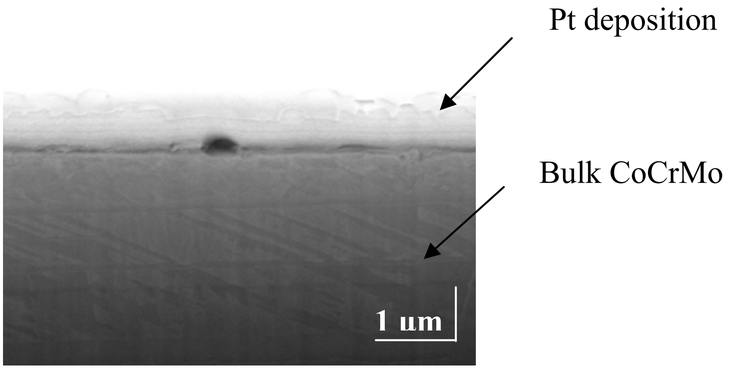

Figure 5.13: FIB-SEM image of a polished CoCrMo specimen.

5.3.2.1 Sliding-corrosion wear scars

The FIB results for wear scars produced under *SC* conditions in a 0.9 wt.% NaCl solution are presented in Figures 5.14 and 5.15, both parallel and perpendicular to the sliding direction, respectively. Cross-sectional images were taken parallel or perpendicular to the sliding directions, respectively. Two-body grooving abrasion is the major wear mechanism as evident from Figures 5.14(a) and 5.15(a). A thin nanocrystalline layer (NC) can be identified immediately below the wear scar surface, which has a variable thickness across the section (~ 0.5 - 1.0 µm in thickness). In particular, this layer is less distinguishable under areas of minor surface damage, as seen in Figure 5.14(b). However, this nanocrystalline layer is more prominent where there is severe deformation, *e.g.* under plastic deformation lips formed during the microploughing, see Figures 5.15(b). The NC layer is less prominent for the SC wear scar produced in the 25% BS solutions (less that 0.5 µm in thickness, Figure 5.16). This correlates with the SEM results, in Figure 5.9, where the presence of proteinaceous material has lubricated or protected the tribological contact and reduced the extent of the surface / subsurface damage. The EDX analysis (see Figures 15, 17 and 18) of the NC layer chemical composition is summarized in Table 5.3

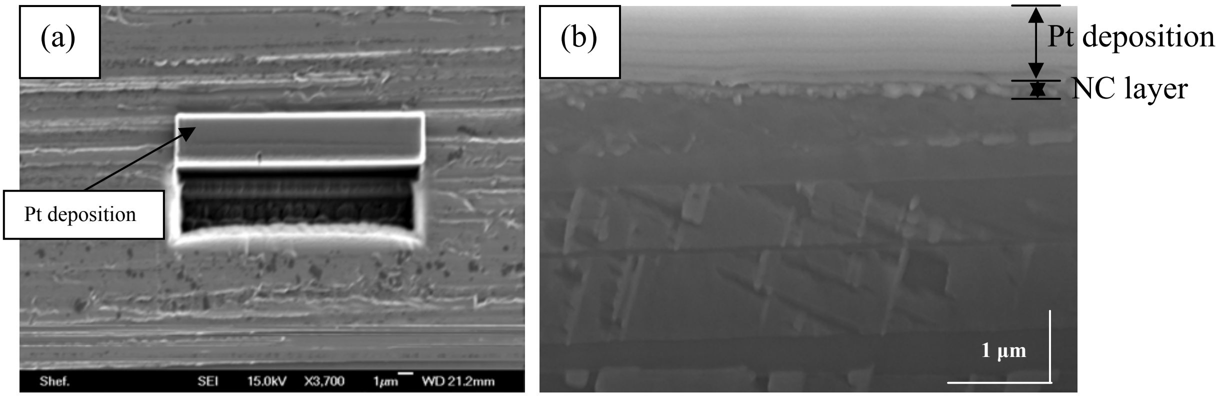

Figure 5.14: FIB-SEM image of wear scar (produced under sliding-corrosion conditions in a 0.9 wt.% NaCl solution) parallel to the two-body grooves (a) top view and (b) a higher magnification of the side view. Images taken at the centre of the wear scar, sliding direction: left to right.

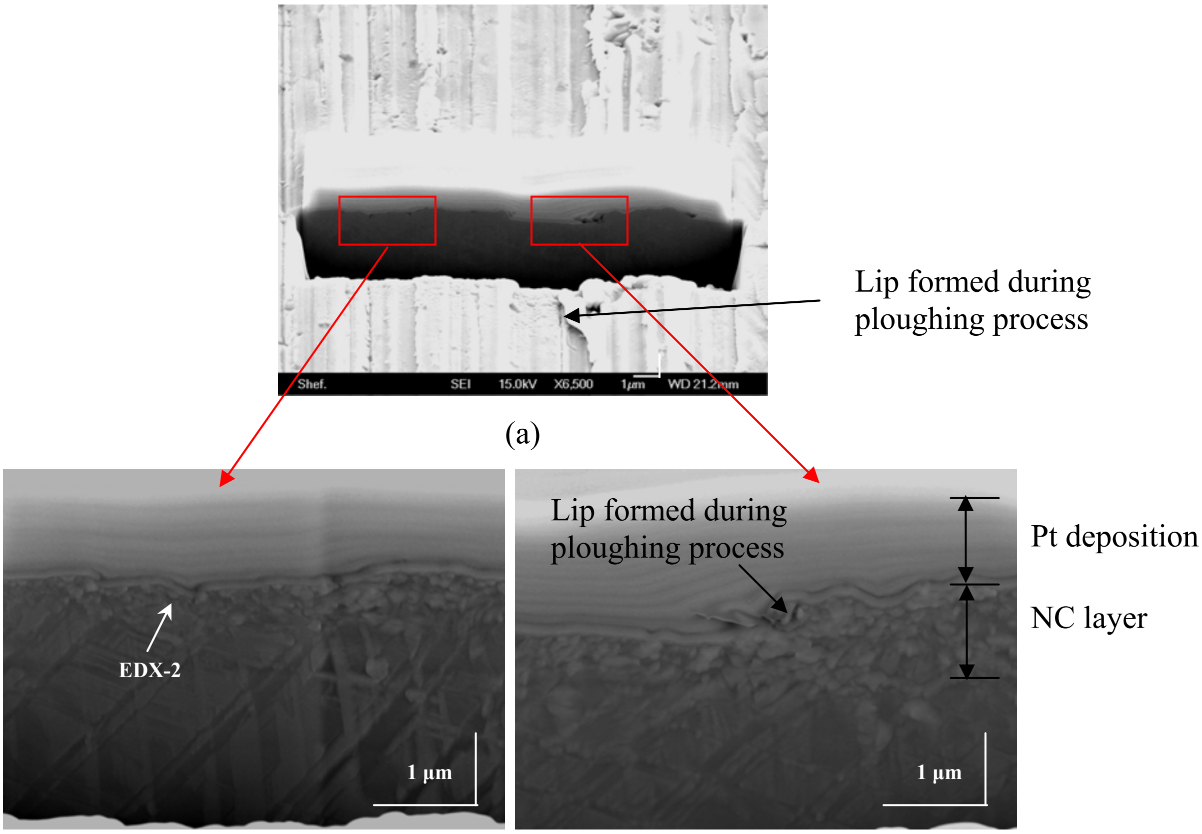

(a)

(b)

Figure 5.15: FIB-SEM image of wear scar (produced under sliding-corrosion conditions in a 0.9 wt.% NaCl solution) perpendicular to the two-body grooves (a) top view and (b) a high magnification of the side view (sliding direction: top to bottom).

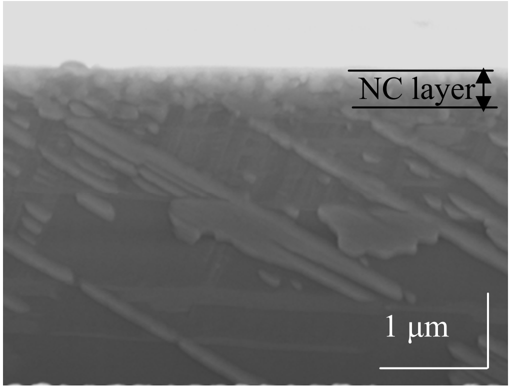

Figure 5.16: FIB-SEM image of wear scar (produced under sliding-corrosion conditions in 25% BS solution) perpendicular to the two-body groove (sliding direction: top to bottom).

5.3.2.2 Abrasion-corrosion wear scars

For the wear scar produced under *AC* in 0.9 wt.% NaCl, see Figure 5.11 (a), multiple indents without directionality are seen revealing that the three body rolling abrasion is the main wear mechanism. A more pronounced nanocrystalline layer, which is between 2-3 µm thick (compared to 0.5-1 µm for *SC* condition), with voids and embedded abrasive particle fragments, is visible in Figure 5.17.

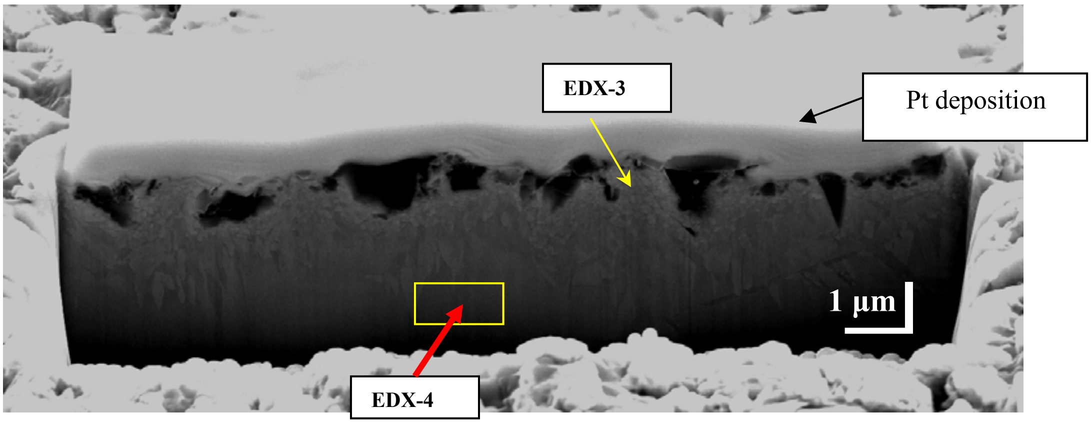

(a)

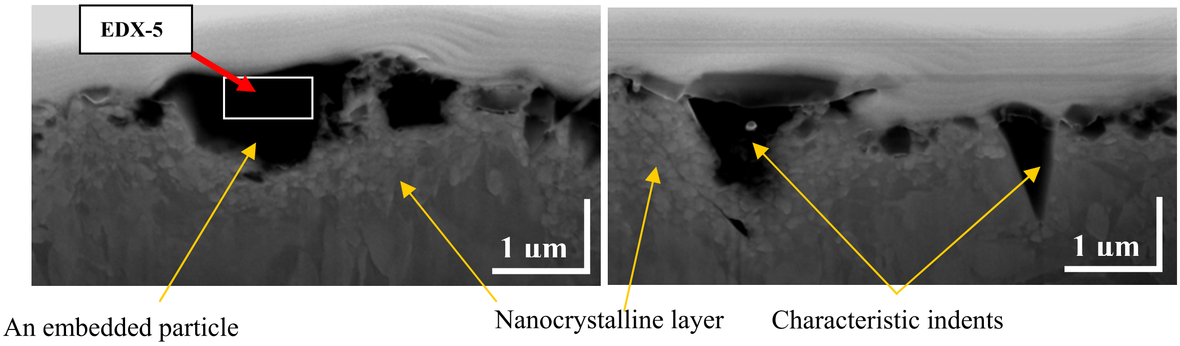

(b)

Figure 5.17: FIB-SEM image of the wear scar (abrasion-corrosion in 0.9 wt.% NaCl) (a) top view and (b) side view.

Figure 5.18 shows the subsurface layer formed under *AC* conditions in the 25% BS solution. In contrast to Figure 5.17, where the cross-sectional image shows several deep, sharp indents and embedded particles scattered throughout the cut area, the subsurface layer formed in the BS solution has in comparison numerous closely packed indents. This can be attributed to the presence of proteinaceous material which enhanced the particle entrainment and more severe indentation. The abrasive particles could also experience more rolling per unit sliding distance, which correlates with the less platelet formation as is seen in Figure 5.12(c) and (d). The better abrasion efficiency of abrasives in the BS solutions explains the greater total wear rate resulted from such condition, see Figure 5.7. The chemical composition of the NC layer can be found in Section 5.3.3. Although no detectable nitrogen (N) is evident according to the EDX analysis, the NC layer formed in BS solutions is likely to have ingress of protein / organo-metallics.

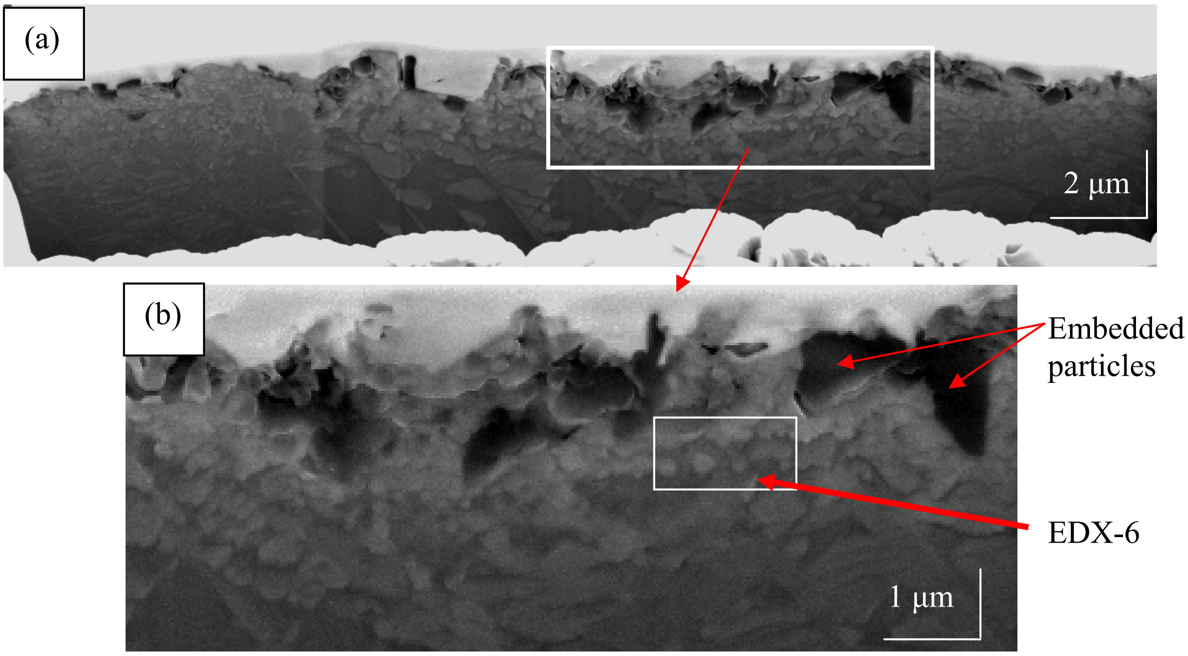

Figure 5.18: FIB-SEM image of the wear scar produced under abrasion-corrosion in 25% BS (a) top view and (b) a higher magnification of the highlighted area.

Despite the visible differences observed in the SEM study, a nanocrystalline layer has been found for wear scars formed in both the BS and non-BS solutions. Büscher and Fischer [40], have similarly identified a NC layer below the worn surface of the retrieved hip joints. They have attributed the NC layer to the recrystallization mechanism resulting from rotating clusters of atoms formed during the plastic deformation process at the surface. Based on the Hall-Petch relationship [242] (Equation 5.1), which described the effect of grain size on yield strength of a polycrystalline material, it was suggested theoretically, that the NC surface with increased yield strength should be beneficial, since this may reduce the effect of three body abrasion by increasing the resistance against surface fatigue by indentation [40]. This layer also helps to explain the origin of the nanometer sized metallic debris which is typically seen in the tribological system of the MoM artificial hip joints [118]. Such a mechanically mixed layer may also contain proteins and organometallic conglomerates. The general discussion of the NC layer formation involved in this present investigation will be summarized in Chapter 9.

$$\sigma_y = \sigma_0 + \frac{k_y}{\sqrt{d_g}} \qquad \ldots\ldots.5.1$$

where k_y is the strengthening coefficient (a constant unique to each material), σ_o is a materials constant for the starting stress for dislocation movement (or the resistance of the lattice to dislocation motion), d_g is the grain diameter, and σ_y is the yield stress.

Another possible process that may occur within the NC layer is the strain induced phase transformation (SIT) [243]. The severely deformed alloy surface has been subjected to high strain levels and could transform from the meta-stable FCC structure into a HCP phase [118, 243]. SIT has been described as a local phenomenon of nucleation and growth surrounding the stacking fault. In this case, the stress concentration near the defects could have exceeded the yield strength of the CoCrMo (~500 MPa [244]) and significantly increased the driving force for the structural change [38, 245]. Unfortunately, the nano- / micro-structural phases that are present in the NC layer could not be identified in the current study due to the limitation of the equipment.

5.3.3 Energy Dispersive X-ray analysis (EDX)

Table 5.3 shows the EDX results for Figures 5.15 (b), 5.17 (a-b) and 5.18 (b). Comparing to the bulk composition, the heavily deformed layer has a generally lower Mo content. This might be due to the scanned layer being mainly formed by abrading / indentation of the top layer of the material, the composition of which is rich in Cr and / or Co oxide and hydroxide [232]. The rolled-up conglomerates shown in Figure 5.9 (d) / EDX-1 are rich in C and contain trace amounts of N; this suggests there is a protein / debris mixture which has been rolled-up in between the contact (indicated by the particle orientation). The dark feature in Figure 5.17 (b) / EDX-5 is a fragment of a SiC particle that was embedded into the CoCrMo surface during the abrasion process.

Table 5.3: Elemental information obtained from the SEM / FIB-SEM images.

Element (wt.%)	**C**	**O**	**Si**	**Cr**	**Co**	**Mo**	**Ga**	**N**
Rolled particle (EDX-1)	17.52	--	0.94	23.73	48.63	6.09	--	3.10
Deformed layer (EDX-2)	--	--	--	27.81	67.10	1.78	3.3	--
Deformed layer (EDX-3)	3.95	3.10	2.33	23.08	66.02	--	--	--
Bulk (EDX-4)	5.14	--	2.28	24.59	61.18	3.13	--	--
Particle (EDX-5)	43.16	-	36.47	7.26	13.10	--	--	--
Deformed layer (EDX-6)	6.40	7.26	--	23.27	51.28	2.68	9.21	--

5.4 Summary

Table 5.4 summarizes the results from the various test solutions under both SC and AC conditions.

Table 5.4: Test results obtained under the various SC and AC test conditions.

Test	**Results**	**0.9 wt.% NaCl**	**PBS**	**25% BS**	**50% BS**
SC	SWR	——— Decrease ——→			
	Current noise	No trend			
	SEM	Severe 2-body grooving of carbide/matrix	2-body grooving of matrix	Minimum grooving of matrix	Polished wear scar
	NC layer	~ 1 µm	N/A	< 0.5 µm	N/A
	Boundary Lubrication	Minimum	Adsorbed phosphate	Adsorbed protein	More adsorbed protein
AC	SWR	——— Increase ——→			
	Current noise	——— Decrease ——→			
	SEM	Three body rolling			
	NC layer	~ 2 µm	N/A	~ 3 µm	N/A

Overall, relatively minor differences in the test solutions have been shown to significantly alter the predominant wear mechanisms and the extent of the microabrasion-corrosion performance for the SC and AC conditions. The presence of adsorbed PBS or proteinaceous material can fundamentally change the wear-induced corrosion potential/current variation, lubrication regime and/or wear mechanism compared with that obtained for the 0.9 wt.% NaCl solution. Under sliding-corrosion, the proteins that adsorbed onto the CoCrMo surface can form organo-metallic conglomerates during the tribo-corrosion process; such conglomerates enhance the separation of the surfaces and polishing the wear scar through chemical-mechanical polishing regime. A sub-surface nanocrystalline structure (a mechanically mixed layer which may contain proteins and organometallic conglomerates) has been identified for worn CoCrMo under both sliding-corrosion and abrasion-corrosion conditions. Such refined material structure may result in increased materials strength; conversely, it may also be the origin of the nanometer sized metallic debris which is typically seen in the tribological system of the MoM artificial hip joints. These findings have important considerations not only for the assessment of CoCrMo wear in simulant body fluids, but also crucially in determining the most suitable *in vitro* experimental approach for abrasion-corrosion studies and future directions for MoM design.

Literature is sparse for the tribological testing of CoCrMo alloys at micro-/nano-scales, especially in the context of artificial human joints, and a better mechanistic understanding is still yet to be developed to interpret the material performance from a material science perspective. From the present study, work hardening of the worn specimen surface is expected as a result of grain refinement, but the extent of the hardening under different wear conditions needs to be further identified. Also, the type/concentration of abrasives, pH and addition of proteins/lipids could bring about different effects on the wear results and hence the tribo-corrosion test results. As the current abrasion-corrosion tests involve simultaneous action of multiple abrasive particles, imposing repeated indentation/ploughing to the CoCrMo surface, it is of great interest to further explore the secondary wear mechanism induced by one single abrasive particle and subsequently bridge the understanding between single indentation/ploughing action and the three body abrasion mechanism of the alloy. This is the basis for additional work done using micro/nano-indentation and nano-scratching techniques, the detailed discussion of which can be found in Chapter 8.

Chapter 6

Effects pH and protein adsorption on the abrasion-corrosion performance of CoCrMo

The influence of pH at the implant site on the wear and corrosion behaviour of the CoCrMo has not attracted enough attention in the past. As mentioned previously in Section 2.2.1, the pH of the joint fluid under an infected condition can be as low as 4.0, much lower than the normal physiological pH 7.4. It has been well-documented that the pH level can directly influence the adsorption behaviour of proteins onto various surfaces [77-79]. Indeed, protein interactions with a passive film on a metallic surface are of considerable interest since they influence film breakdown, metal-ion release and film repassivation processes [81]. Previously in Section 4.2, it has been reported that a change of pH from 7.4 to 4.0 can significantly influence the corrosion potential/corrosion current of cast CoCrMo under a statically immersed condition. The pH variation can also influence the thickness of the protein adsorption layer on the CoCrMo surface in simulated body fluids. However, the effects of pH and protein adsorption on the overall wear-corrosion performance of the CoCrMo alloy are generally still not well understood.

This chapter further investigates the effects of pH levels (resembling that of healthy and infected hip joint environments) and protein adsorption, focusing on their individual and combined effects on the wear-corrosion behaviour (sliding wear-corrosion and abrasive wear-corrosion) of the cast CoCrMo alloy.

6.1 Influence of pH and protein adsorption on the wear scar profile

In order to investigate the influence of pH and adsorbed proteins on the wear mechanisms of the CoCrMo under microabrasion-corrosion, SEM images were obtained at the centre of wear scars from different test conditions. Figure 6.1 shows the wear scars produced for the 0.9 wt.% NaCl SC conditions. For pH 4.0, a more severely damaged (rougher) surface was generated compared to that produced in the pH 7.4 solution. It appears that the more acidic pH has a strong influence on the degradation of the CoCrMo surface. For the BS containing solutions (Figures 6.2 and 6.3), the wear scars appear to be polished, but also conglomerates are seen on the surface through SEM observation. These are conglomerates that contain traces of nitrogen and elements from the CoCrMo alloy as determined by EDX analysis and are generally aligned perpendicular to the ZrO_2 ball rotation. These conglomerates appear to be similar in morphology to those seen in Chapter 5. As suggested previously, the heat and high shear stresses generated within the tribological contact could result in denaturation of proteins which can rapidly lead to aggregation/precipitation [246, 247], it is therefore suggested that these conglomerates (‘roll-ups’ and patchy layers) could be thermally/mechanically denatured proteins (formed by the shear stresses present at the ball-protein film interface), which mix with wear debris and organo-metallic compounds that are formed during the wear-corrosion process. Murakami *et al.* [239] found similar rolling-up of proteins in the studies of artificial synovial joints under a sliding condition and a lowering of friction by the rolling motion of proteins. The precipitation of protein has also been studied as a function of temperature, concentration and time by Liao *et al.* in a hip simulator [248], however, the exact morphology of the precipitated proteins from their tests were not discussed.

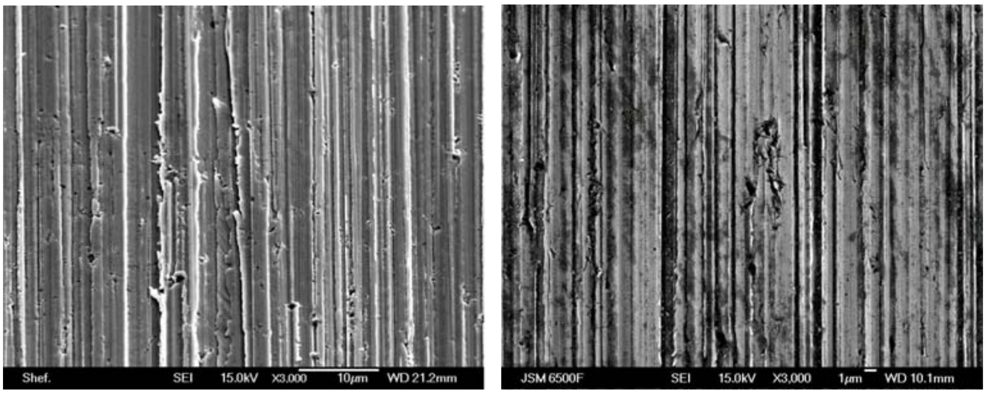

Figure 6.1: SEM images of wear scars generated in: (a) 0.9 wt.% NaCl (pH 7.4) and (b) 0.9 wt.% NaCl (pH 4.0).

The wear scar morphology generated by BS containing solutions seems to be affected by both the pH level and the protein concentration, see Figures 6.2 and 6.3. Decreased pH or increased protein concentration resulted in a more polished wear scar surface and increasing roll-up formation within the wear scar, this could be due the greater tendency for protein adsorption at pH 4.0, which has been evidenced from the EIS and XPS analysis. In addition, there is a greater tendency for protein denaturation under more acidic pHs (greater hydrogen ion concentration) [249] and higher protein concentrations [248], which could also explain the more extensive formation of protein conglomerates at pH 4.0 and at the higher BS concentration. These roll-up particles could also reduce the friction by their rolling action [239] and thus give rise to the more lightly polished wear scars and lower wear rates.

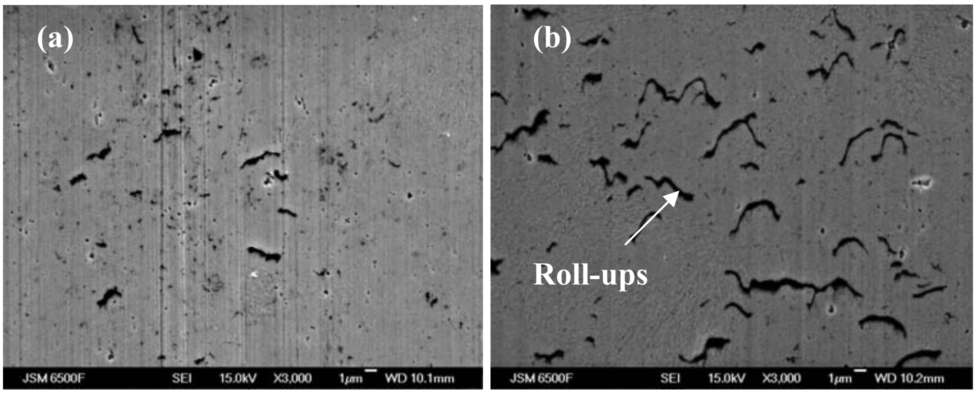

Figure 6.2: SEM images of wear scars generated in: (a) 25% BS (pH 7.4) and (b) 25% BS (pH 4.0).

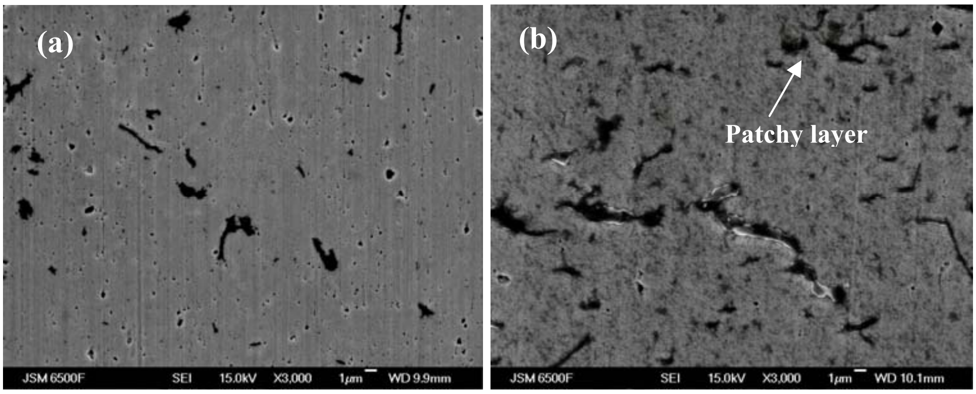

Figure 6.3: SEM images of the wear scars generated in: (a) 50% BS (pH 7.4) and (b) 50% BS (pH 4.0).

The wear scars generated under the AC conditions are characterised by multiple indents without any directionality for both the NaCl and BS solutions. Figures 6.4 (a) and (b) give two examples of the wear scars produced under the AC condition in 0.9 wt.% NaCl and 50% BS, respectively. The wear scar features clearly indicate that three-body rolling abrasion is the dominant wear mechanism in both cases. The influence of proteins on the wear rates and wear-induced corrosion currents under different conditions will be discussed in the following sections.

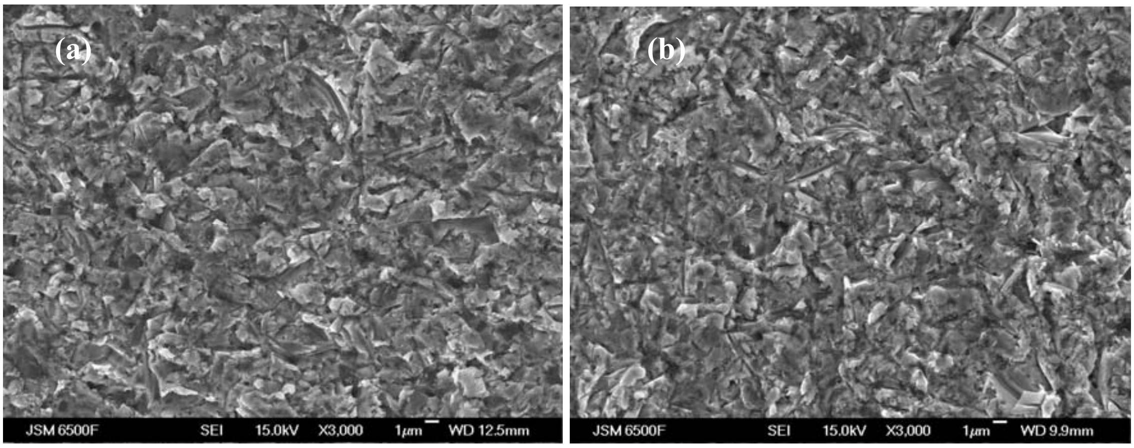

Figure 6.4: Typical wear scar morphology produced under abrasive wear-corrosion (a) 0.9 wt.% NaCl (pH 7.4) and (b) 50% BS (pH 4.0).

6.2 Electrochemical noise measurements

Figures 6.5 (a) and (b) show the electrochemical current noise measured during the SC tests at pH 7.4 and 4.0, respectively. All current noise curves show a sharp transient at the beginning of the tests corresponding to sudden rupture of the surface passive film. The curves tend to stabilize as the tests progress and recover to their pre-sliding level at the end of the tests when the ball stops sliding, corresponding to the repassivation (oxide film reformation) of the damaged surface.

For both pH levels, the 0.9 wt.% NaCl solution resulted in the highest current levels, which can be attributed to the wear being mainly produced by the asperity contact between the ball and the specimen, causing depassivation by mechanical removal of oxides. Whereas for the BS solutions, the adsorbed proteins may form a tribo-film within the tribo-contract, which lubricates the bearing surface under boundary lubrication and reduces wear and oxide removal. Thus, the area of depassivation is reduced, resulting in relatively low corrosion currents. In general, the acidic environment resulted in higher current levels. These results are consistent with other workers such as Merritt et al. [73], and are likely to be due to the increased corrosive nature of the pH 4.0 test solutions, leading to a increased charge transfer rate (faster metal dissolution and greater metal ion release) [215]. Although the adsorption of proteins was enhanced by lowering the pH, overall, the wear-induced corrosion current levels in the BS containing solutions were not affected by increased protein film thickness.

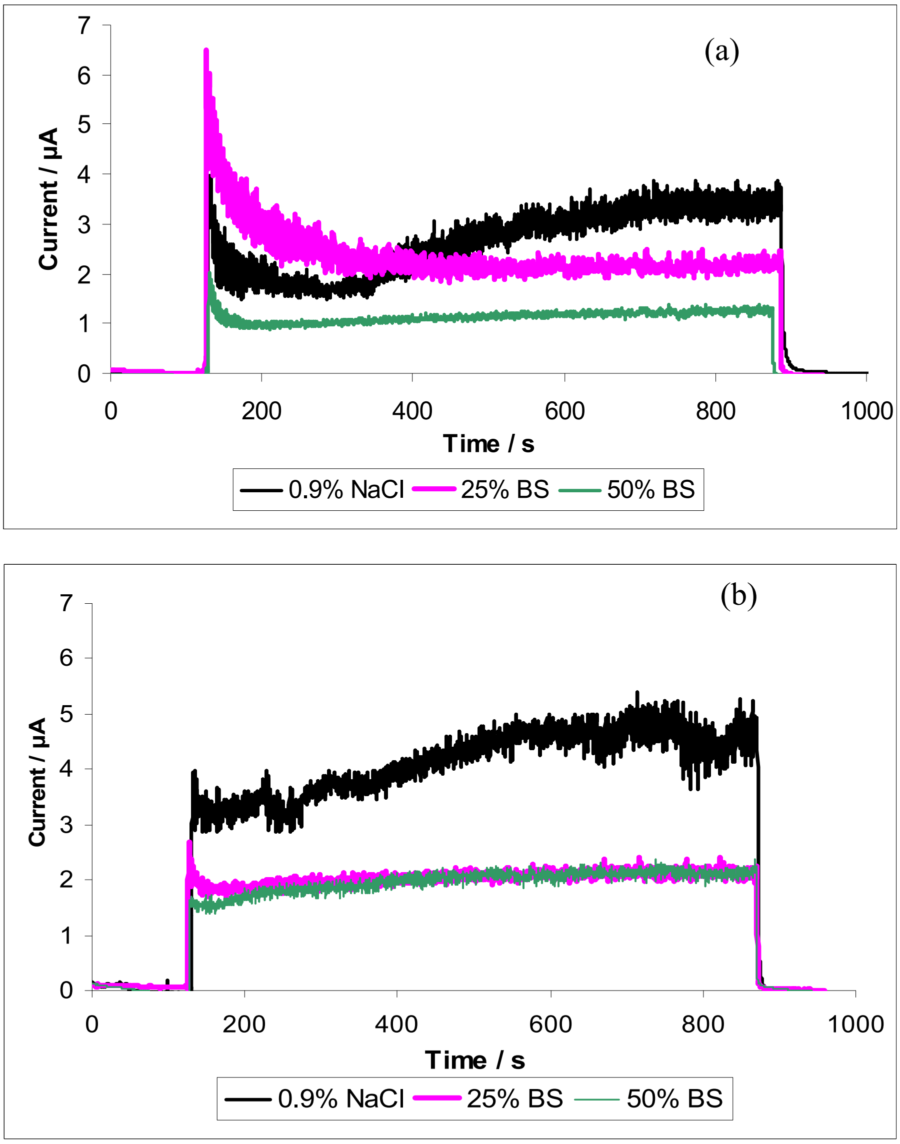

Figure 6.5: Cast CoCrMo electrochemical current noise under sliding-corrosion conditions at 37 ºC; (a) pH 7.4 and (b) pH 4.0 test conditions.

Figure 6.6 shows the electrochemical current noise generated under AC conditions. As with the SC condition, the currents in all solutions increase abruptly at the onset of the tests, however, due to the presence of the SiC abrasives, repassivation within the scar has been disrupted, resulting in the current levels gradually increasing during testing. Short current transients can be observed during these tests which may correspond to partial repassivation events. Again, the currents return to the original values once abrasion stops, showing effective repassivation and protein coverage.

It can be seen that under neutral pH conditions, the BS solutions give rise to relatively low current densities (similar to the SC conditions), which has been attributed to the possible physical barrier (charge inhibiting effects) induced by the adsorbed protein

[135]. However, under pH 4.0, all three test solutions give similar current noise levels (~28 µA towards the end of tests). The more acidic pH, in addition to the severe damage, clearly outweighed the protein charge inhibiting effects. The nascent and highly reactive surface is exposed to the acidic environment intermittently, which dominates the charge transfer process and is likely to result in elevated metal-ion release.

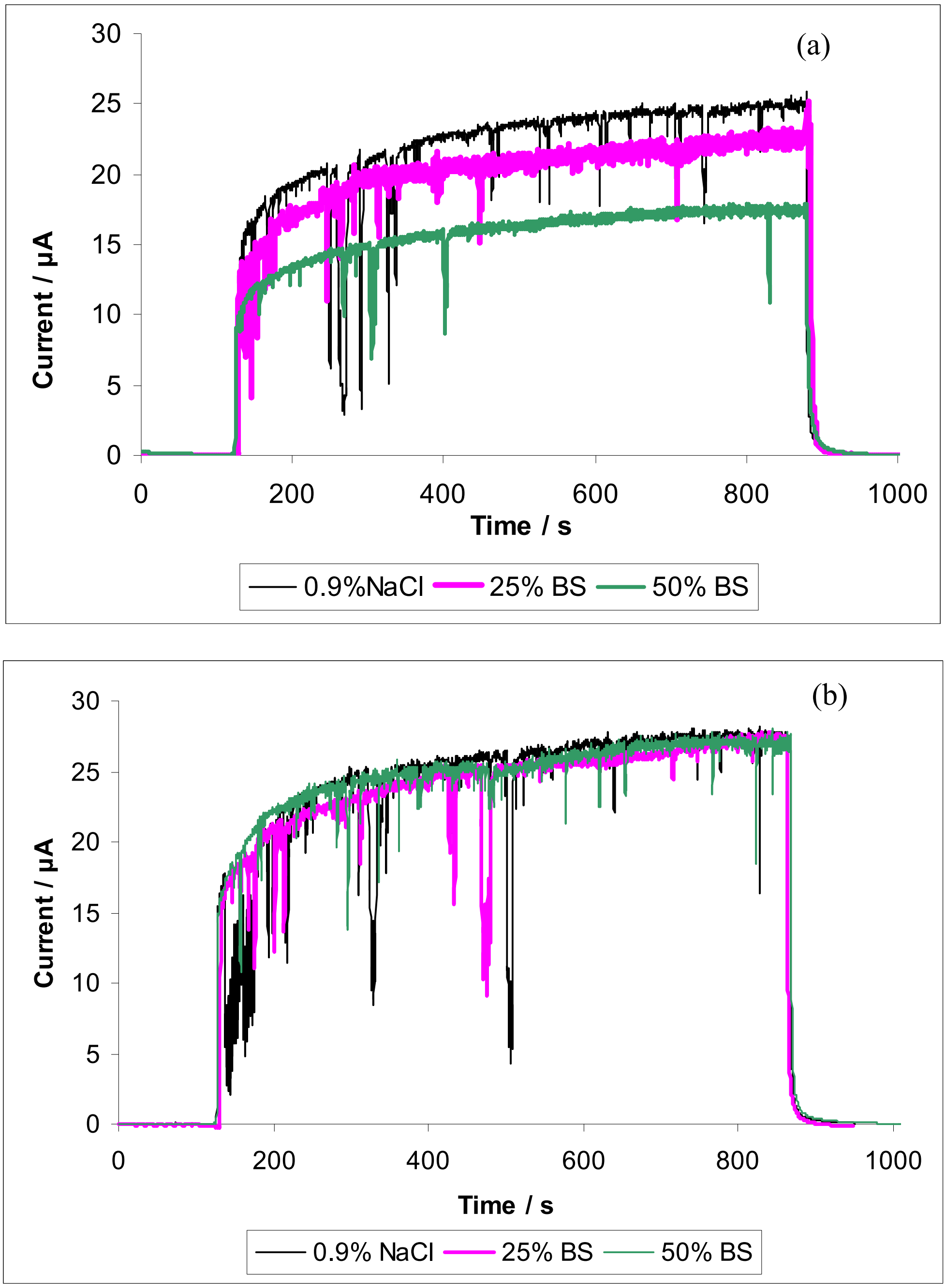

Figure 6.6: Cast CoCrMo electrochemical current noise under abrasion-corrosion conditions at 37 ºC; (a) pH 7.4 and (b) pH 4.0 test conditions.

6.3 Influence of pH on specific wear rates of cast CoCrMo

According to Figure 6.7(a), the SWRs from the SC tests for both pH levels are two orders of magnitude higher than that for clinical wear rates (2-20 µm y^{-1} [53], which is in the order of 10^{-6} $mm^3N^{-1}m^{-1}$) due to the accelerated testing process adopted in this study. The SWRs for 0.9 wt.% NaCl were appreciably higher under pH 4.0 than for pH 7.4 under SC conditions. The CoCrMo surface is more susceptible to corrosion attack in acidic environments [215], which resulted in corrosion-enhanced wear. For both BS containing solutions, significantly lower SWRs resulted compared to the 0.9 wt.% NaCl tests. In addition, the acidic pH resulted in a further decrease of the SWR. This can be attributed to the enhanced protein adsorption under pH 4.0 as shown in the EIS and XPS analysis, see Sections 4.2 and 4.3. The enhanced formation of protein conglomerates as seen in Figures 6.2 and 6.3 can also explain the reduced SWRs for BS solutions. The fact that the majority of the proteins are positively charged at pH 4.0 could also result in enhanced protein entrainment into the bearing contact [76], which could also contribute to the a better lubrication and reduce wear damage under such conditions. It can be seen that the use of 50% BS can result in more than a 75% reduction of SWRs for pH 7.4 tests and nearly 95% SWR reduction for pH 4.0 tests.

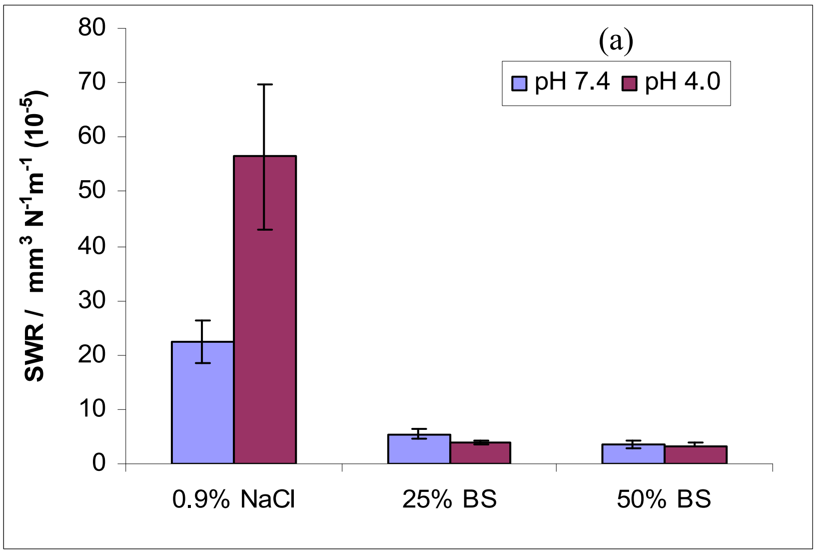

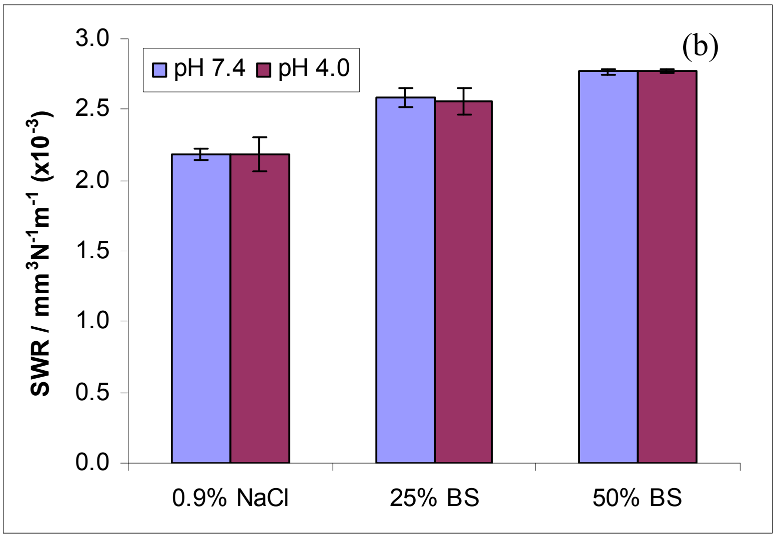

Figure 6.7: Effect of pH on the specific wear rate of cast CoCrMo under (a) sliding-corrosion and (b) abrasion-corrosion.

Conversely, for AC conditions, see Figure 6.7 (b), the SWRs are an order of magnitude higher as compared to the SC results. A slight increasing trend is seen for SWRs with increasing protein concentration. The effect of protein surface coverage on the enhanced wear rate has been attributed to the enhanced particle entrainment [135]. The greater entrainment could also be due to the adsorbed protein onto the SiC abrasives [241]. The pH in this study does not seem to have a significant influence on the SWRs, probably due to the surface damage under the AC condition being relatively severe.

The material degradation processes have been decoupled into mechanical processes (W_0 + W_c) and electrochemical processes (C_0 + C_w) as defined in Chapter 3. The correlation between electrochemical processes and mechanical processes for both SC and AC conditions can be seen in Figure 6.8. For the SC condition, Figure 6.8(a), it can be seen that at both pH conditions the corrosion currents decreased with decreasing mechanical wear associated with increasing BS concentration under sliding. Therefore, the presence of protein is beneficial to the MoM surface protection for both pH conditions. However, under the AC conditions, Figure 6.8(b), a different trend was revealed, where increasing protein concentration resulted in increased mechanical damage. At pH 7.4, the proteinaceous solutions resulted in higher SWRs but lower corrosion current. This may be due to protein enhanced particle entrainment that in turn increases the mechanical wear. On the other hand, the lower current is probably due to the inhibition of charge transfer by the presence of proteinaceous material. A pH 4.0 solution accelerates the corrosion when the surface oxide film is under repetitive damage and exposed to the corrosive environment, this process competes with the protein charge inhibiting effect, giving rise to a constantly high current level for both proteinaceous and non-proteinaceous test solutions. The pH 4.0 solutions resulted in generally higher SWRs and wear-induced current (14%, 20% and 67% increase in total metal ion release for 0.9 wt.% NaCl, 25% and 50% BS, respectively). This suggests that the co-existence of low pH and third body particles is the most unfavourable condition, where increased material deterioration both mechanically and electrochemically occurs.

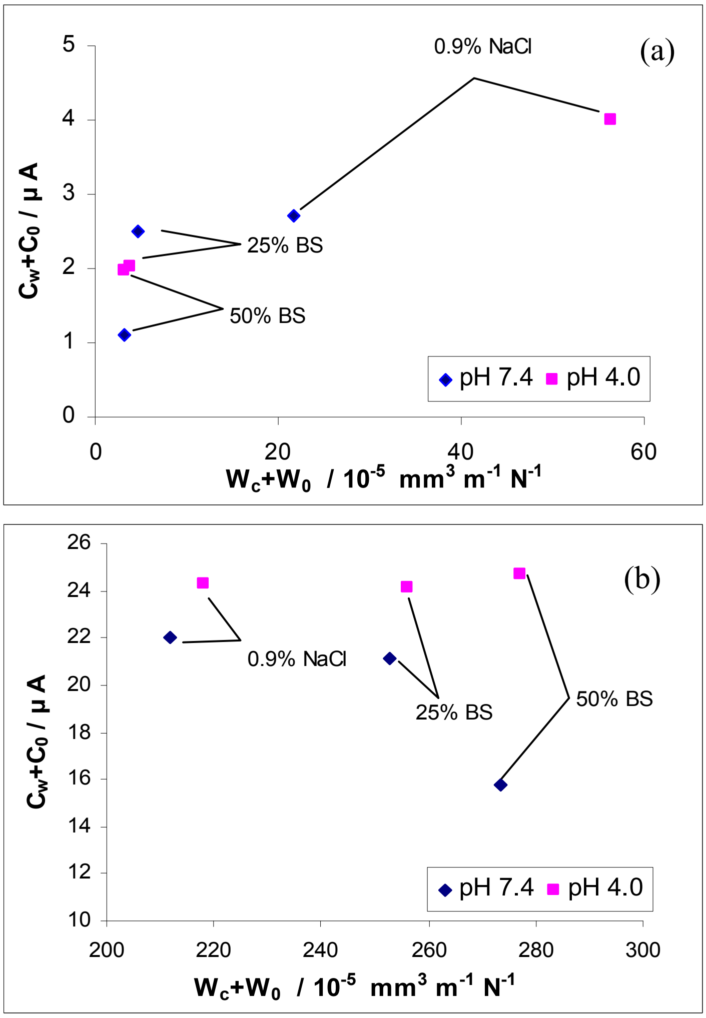

Figure 6.8: Correlations between mechanical processes and electrochemical process (a) sliding-corrosion and (b) abrasion-corrosion at applied OCP potential.

6.4 Summary

A detailed tribo-corrosion characterization combining electrochemical techniques, surface characterization and tribological tests in simulated hip joint environments has been carried out on a cast CoCrMo alloy. Both the electrochemical and surface characterizations show that the adsorption of protein onto the cast CoCrMo surface is influenced by the solution pH and the protein concentration. The extent of the protein adsorption subsequently affects the tribo-corrosion behaviour of the alloy. Combining the results obtained previously in Chapter 4, the effects of pH and protein concentration on the surface properties and tribological behaviour of cast CoCrMo have been combined and summarized in Table 6.1.

Table 6.1: Effects of pH and protein concentration on the test results obtained from this study.

	pH 7.4	pH 4.0
EIS (static immersion)	Without protein: Increased capacitance due to greater adsorption of hydrogen → Increasing BS %: Increased capacitance, reduced polarization resistance due to greater adsorption of proteins	
XPS (static immersion)	Without protein: oxide film 0.88 nm thick / N/A → Increasing BS%: Increased adsorption film thickness, greater protein adsorption	
SEM (worn surface)	Without protein: Greater mechanical degradation for SC condition → Increasing BS %: Less mechanical damage, more polished wear scar surface for SC condition	
SWR	Without protein: Increased wear rate for both SC and AC conditions → Increasing BS%: decreased SWRs for SC and increased SWRs for AC condition	
ECN	Without protein: increased wear-induce corrosion current noise for both SC and AC conditions → Increasing BS% (pH 4): wear-induced current noise remains constant for both SC and AC conditions	

This chapter also shows that the presence of proteinaceous material on the surface is essential for improving surface separation between the MoM bearing surfaces and thereby minimizing wear-corrosion rates. The presence of 50% bovine serum protein can effectively reduce the SWRs by 75% for the pH 7.4 sliding corrosion condition. Although acidic pH conditions representing infected joint environments may not significantly affect the wear rates of the MoM components, it has been shown to increase wear-induced corrosion current (by as much as 67%) and therefore accelerated metal-ion release. Generation and entrainment of third body particles (from the wear debris) aggravate both the wear rate and metal-ion release. The co-existence of third body particles and acidic pH are especially detrimental to the abrasion-corrosion performance of the CoCrMo alloy by significantly increasing both wear and corrosion. In the absence of abrasives, the presence of a serum layer on the MoM surfaces could serve to reduce wear and corrosion.

Chapter 7

Effect of abrasive size and concentration on the abrasion-corrosion performance of cast CoCrMo

Previous literature has shown third-body abrasive wear [237, 250] is one of the predominant wear mechanisms of MoM hip joints *in vivo*. Sub-micron sized hard particles such as fractured carbides, bone cements, bone and metal debris are recognized as the agents inducing third-body abrasion [112]. The overall clinical wear rate of MoM joint is reported to be 2-20 μm/year [53] which is in the order of 10^{-6} $mm^3N^{-1}m^{-1}$. It is believed that during the running-in period, it is the hard carbides on both articulating surfaces that come into contact, and hard carbide particles are very likely to be generated during the articulation. If we assume that the wear takes place uniformly on a 52 mm diameter cast CoCrMo (containing about 5 vol% carbides) MoM resurfacing joint, and the carbides remain in the surrounding hip joint fluids (assuming the fluid volume in the joint is about 10 ml [251]), the volume fraction of carbides will be about 0.0005-0.001 vol% for 1 million cycle of usage within the joint fluid. The relatively soft metal debris are also likely to be generated during the running-in phase due to the abrasion process, and they will also be ejected during each articulation during the subsequent use (steady-state wear). The debate on whether the wear-corrosion induced debris/metal ions are harmful to the human body remains a concern, since there is an increasing number of younger/more active patients who are receiving MoM joint replacements, the particle/ion burden is therefore for a potentially much longer duration. However, no reported incidents relating to debris/ion release have been recorded.

The current author has compared the third body abrasive wear performance of the cast CoCrMo in inorganic and organic test solutions in Chapters 5 and 6. The abrasion tests carried out in Chapter 5 employed high volume concentrations of 4 μm SiC (~1 g cm^{-3}) in the test slurries. Although this is a well-established testing condition that gives good repeatability and reproducibility for engineering materials and coatings [200], it is less representative of the *in vivo* conditions and tests on biomaterials. In this chapter, the size, volume fraction of the abrasives have been brought down to much lower levels, aiming to better represent the possible third-body abrasive wear mechanisms that occur *in vivo*. Micro-abrasion-corrosion with sub-micron sized (and relatively soft) abrasives has been attempted for the first time, this has allowed the abrasion-corrosion response of cast CoCrMo to different abrasives and concentrations to be investigated under conditions which might be related to the clinical applications.

7.1 Wear mechanism evaluation

Figure 7.1 shows SEM images of the wear scar morphologies generated in 4 μm SiC containing slurries. The wear scars produced under 0.238 vol% and 0.12 vol% 4 μm SiC in both 0.9 wt.% NaCl and 25% BS solutions appear similar and consist of multiple indented surfaces without directionality, indicating that three-body rolling abrasion was the dominant wear mechanism [203]. As the abrasive volume fraction decreases, the wear mechanism changes from rolling abrasion followed by mixed mode to finally grooving abrasion. The wear scars produced using 1 μm Al_2O_3 slurries (Figure 7.2) also show a multiple indented feature at 0.238 vol%, but the transition from rolling to grooving occurs at an abrasive volume of 0.12 vol%. It is worth mentioning that for the 1 μm Al_2O_3 slurries, the wear scar morphology appears to be different to that for 4 μm SiC slurries, i.e., shallower but more numerous indents / grooves were evident per unit area.

For both abrasive types, the wear damage appears to be higher in 25% BS at abrasive volume fractions greater than 0.03. This might be due to the increased friction due to protein coated surfaces enhancing slurry/particle entrainment. However, for abrasive volume fractions lower than 0.03, the wear is less severe for 25% BS. The protein may precipitate or aggregate under frictional heating and/or high shear, the denatured protein (e.g., dark conglomerates) shown in Figures 7.1 (d2) and 7.2 (e2) mix with metal debris and may further protect the surface by rolling within the contact and polishing the surface and/or further separate the surface to allow smaller particles to skid/slide through the contact without further damaging the specimen surface.

For all wear scars and abrasives used, the wear damage has occurred on both the Co rich matrix and the hard carbides. The hard carbides are abraded by the abrasive particles with higher (4 μm SiC) or similar hardness (1 μm Al_2O_3). This may be due to the angular abrasives being used, which results in localized high contact stress which exceeds the yield strength of the carbide. Such high contact pressure may not only cause the deformation/removal of the matrix material, but also deformation/fracture of the carbide.

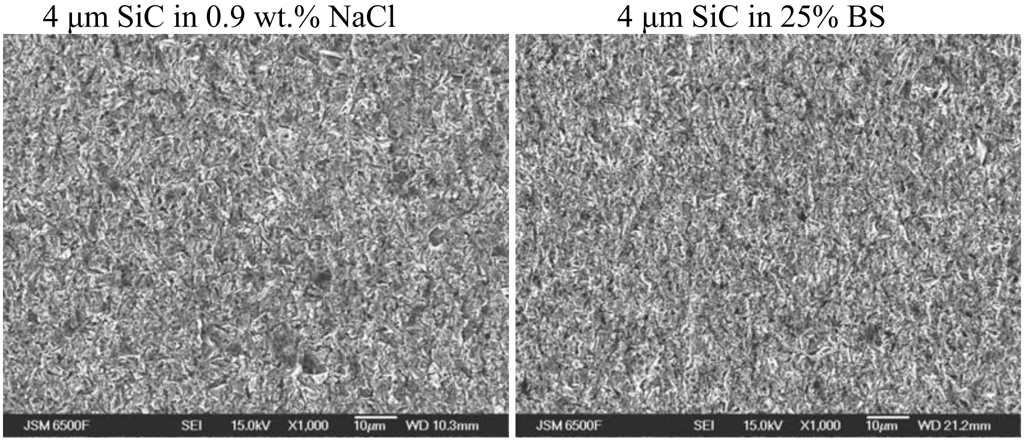
4 µm SiC in 0.9 wt.% NaCl
4 µm SiC in 25% BS

(a1) 0.12 vol% (Rolling) (a2) 0.12 vol% (Rolling)

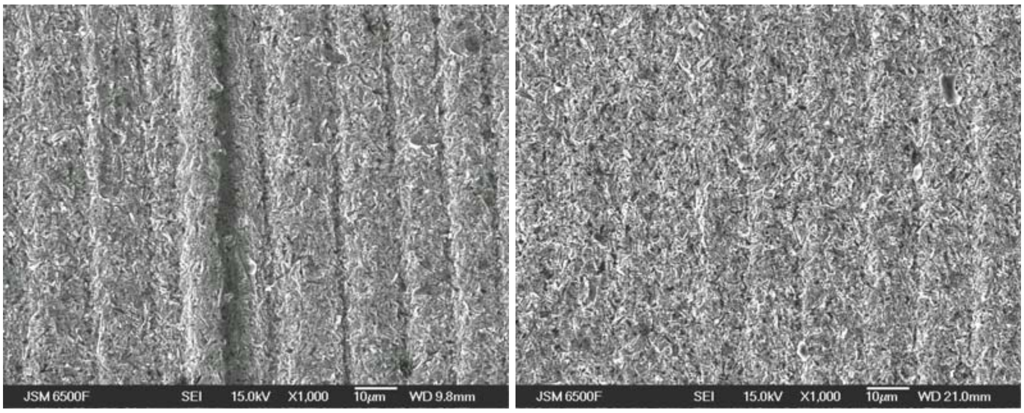

(b1) 0.072 vol% (Mix) (b2) 0.072 vol% (Mix)

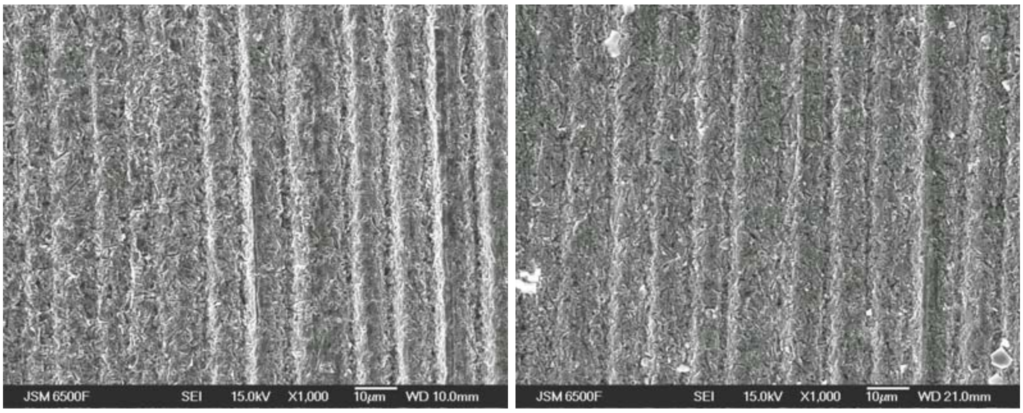

(c1) 0.03 vol% (Grooving) (c2) 0.03 vol% (Grooving)

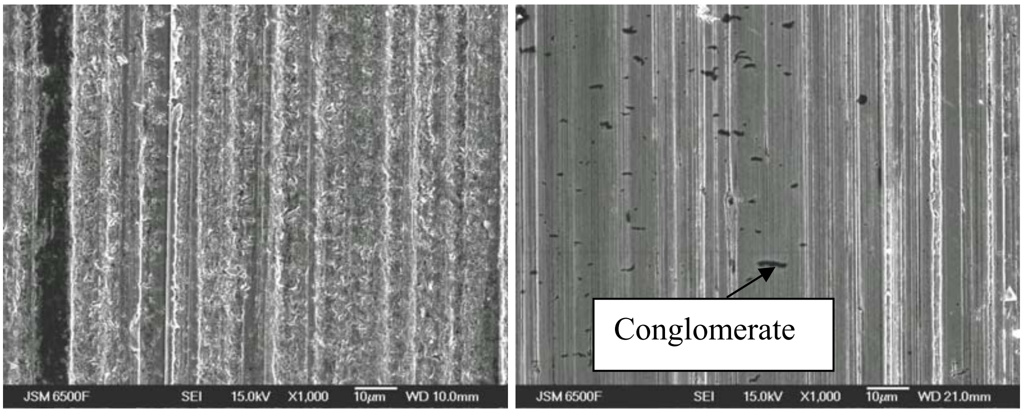

(d1) 0.006 vol% (Grooving)

(d2) 0.006 vol%
(Grooving + protein conglomerates)

Figure 7.1: SEM images of wear scars produced in different 4 µm SiC based slurries.

1 µm Al_2O_3 in 0.9 wt.% NaCl

1 µm Al_2O_3 in 25% BS

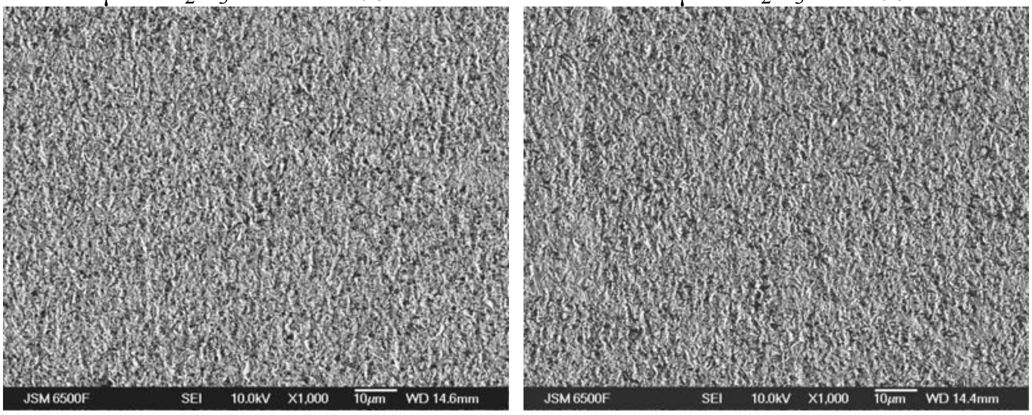

(a1) 0.238 vol% (Mix)

(a2) 0.238 vol% (Mix)

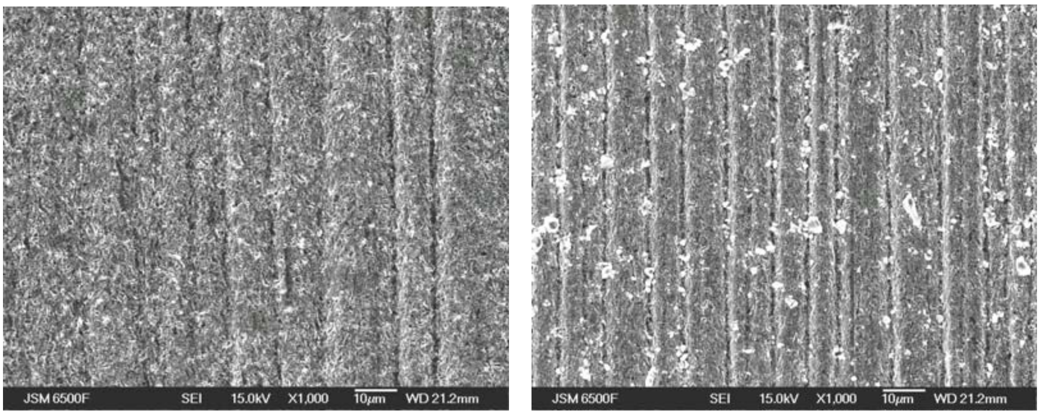

(b1) 0.12 vol% (Mix)

(b2) 0.12 vol% (Mix)

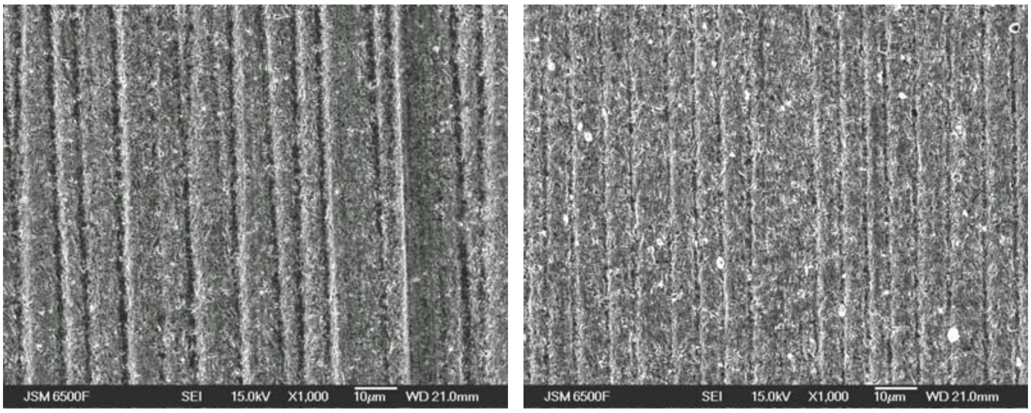

(c1) 0.072 vol% (Grooving) (c2) 0.072 vol% (Grooving)

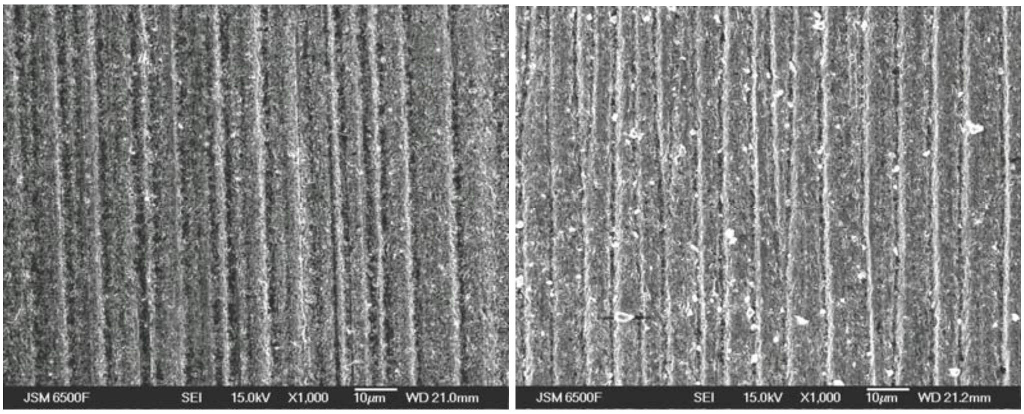

(d1) 0.03 vol% (Grooving) (d2) 0.03 vol% (Grooving)

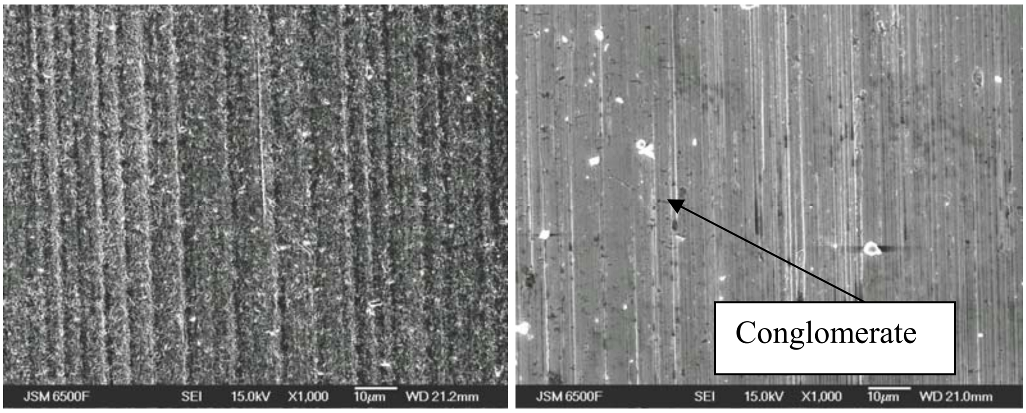

(e1) 0.006 vol% (Grooving) (e2) 0.006 vol%
(Grooving + protein conglomerates)

Figure 7.2: SEM images of wear scars produced in different 1 μm Al_2O_3 based slurries.

The wear scar images for the 300 nm Al_2O_3 tests are shown in Figure 7.3. Due to the quick settlement of this type of slurry, slurries with volume fraction higher than 0.072 vol% have not been tested. The predominant wear scar morphology for all test conditions was grooving abrasion. However, at 0.072 vol% for both test slurries, a pitted (indented) structure was found in between the grooves. Such features become less visible as the volume fraction of abrasives decreases. For BS containing solutions, protein conglomerates were found on the 0.006 vol% slurry test wear scar surface. EDX analysis showed that some of the conglomerates contain Al in addition to N, Co and Cr. Therefore small Al_2O_3 abrasives are likely to have become trapped within the conglomerates. The wear scar resulted from low slurry volume fraction (0.006 vol%) tests appear to be less damaged. This may be due to the polishing effect of the formation of protein conglomerates formed under this test condition.

300 nm Al_2O_3 in 0.9 wt.% NaCl | 300 nm Al_2O_3 in 25% BS

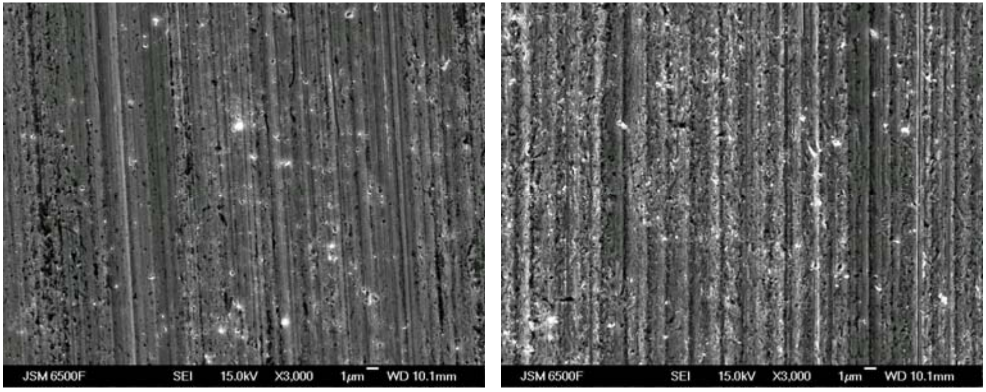

(a1) 0.072 vol% (Grooving) (a2) 0.072 vol% (Grooving)

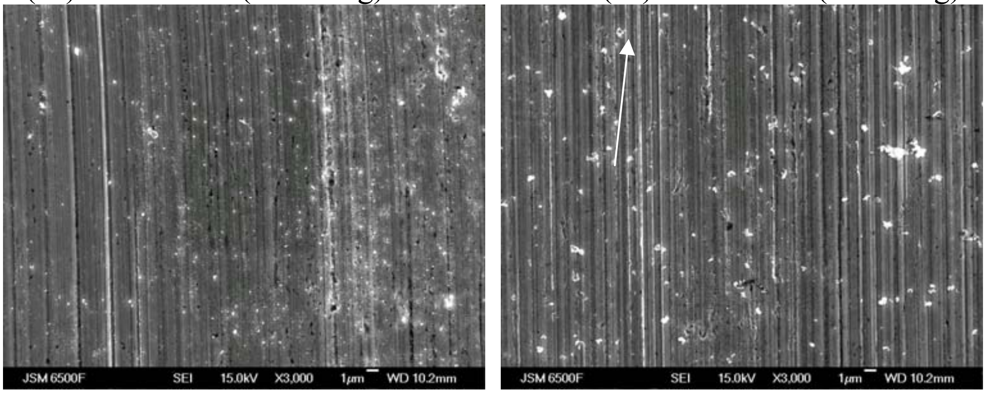

(b1) 0.03 vol% (Grooving) (b2) 0.03 vol% (Grooving)

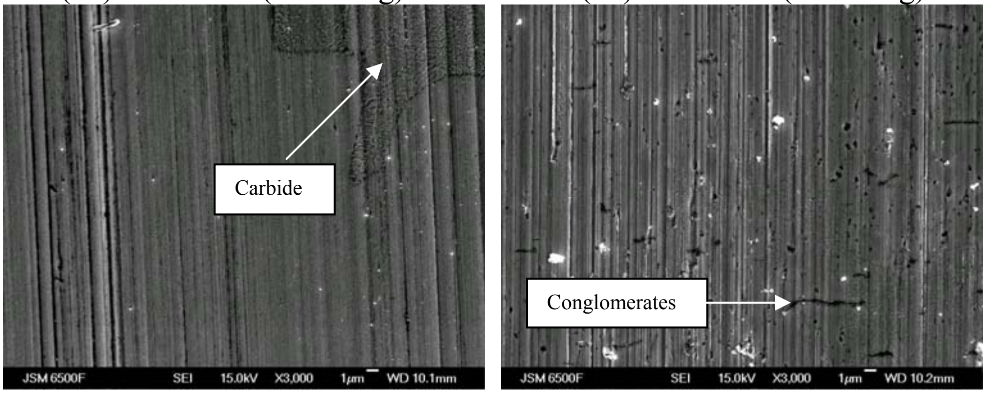

(c1) 0.006 vol% (Grooving) (c2) 0.006 vol% (Grooving + protein conglomerates)

Figure 7.3: SEM images of wear scars produced in 300 nm Al_2O_3 based slurries.

Figure 7.4 shows the micrographs for the sub-micron sized $BaSO_4$ 25%BS based slurries. In contrast to the wear scars produced by 300 nm Al_2O_3 slurries, the scar surfaces were less damaged and the carbides that are present in the CoCrMo largely remained intact. This is in contrast with the previous samples tested in the Al_2O_3 based abrasives, where abrasive damage was visible on both the Co rich metal binder and the hard carbides. Another feature is the truncated grooves shown in Figure 7.4. These grooves are likely to be caused by the relatively soft $BaSO_4$, which may be flattened / fragmented when entrained within the tribo-contact. Although the hardness of $BaSO_4$ is much lower than both the hard carbides and the Co matrix, it has been documented that even soft particles can lead to plastic deformation on a relatively hard surface [252, 253]. Additionally, as shown by Hamer *et al.* [252] and Sayles and Ioannides [254], the maximum pressure around a relatively soft particle trapped by conforming bearing surfaces could be significantly increased due to the hydrostatic stress experienced within the particle or the elastohydrodynamic action under lubricated conditions. These soft particles potentially may cause scratches on bearing couples such as metal-on-metal and ceramic-on-ceramic, and the more recently proposed surface-engineered bearing surfaces with coatings [255].

Proteinaceous conglomerates were seen in Figures 7.4 (c) and (d) for 0.03 and 0.006 vol% $BaSO_4$ slurries, the lower slurry concentration forming generally larger conglomerates. These conglomerates are believed to be formed in the same manner as shown in Figures 7.3 (c1) and (c2). However, the larger dimension for these conglomerates may be due to the lower abrasivity of the $BaSO_4$ resulting in less tearing/cutting of the roll-up particles. EDX analysis also revealed that a small fraction of conglomerates contain barium, implying some fragmented $BaSO_4$ has been involved in the formation of these organo-metallic roll-up particles. The detailed discussion on the interaction between proteinaceous material and the sub-micron sized particles can be found in Section 9.1.2.

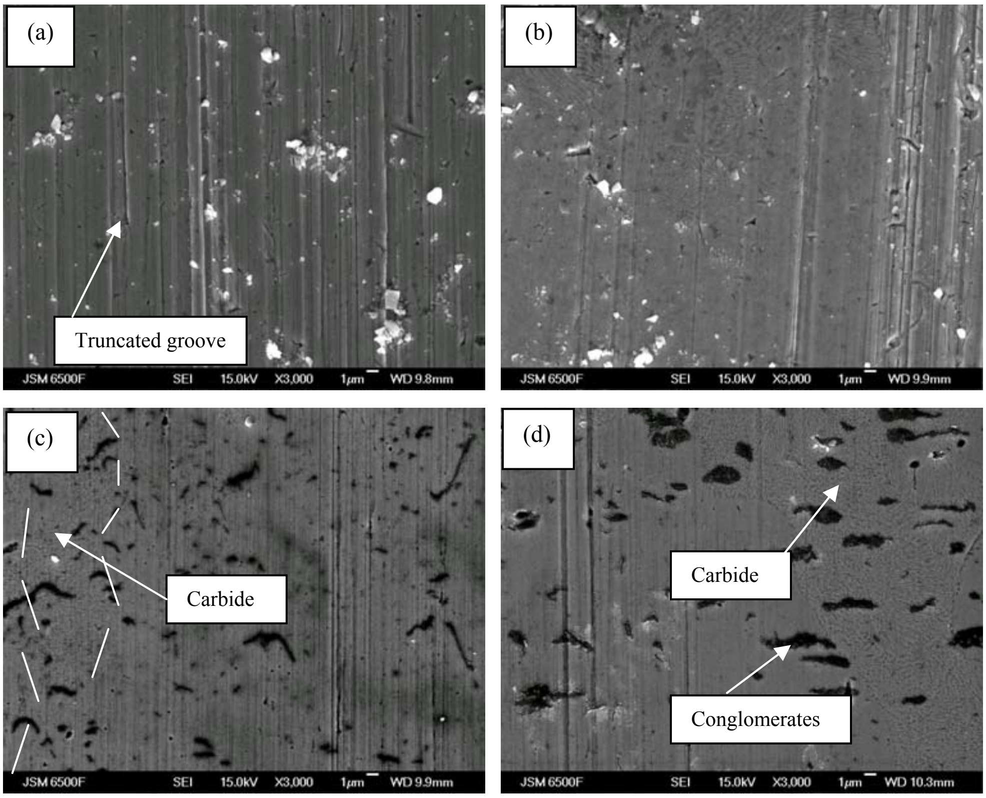

Figure 7.4: SEM images of wear scars produced in sub-micron sized $BaSO_4$ / 25% BS based slurries. (a) 0.12 vol%, (b) 0.072 vol%, (c) 0.03 vol% and (d) 0.006 vol%.

7.2 Effects of abrasive size and concentration on specific wear rates

The abrasion-corrosion specific wear rates (SWRs), for 4 μm SiC and 1 μm Al_2O_3 resulting from different abrasive test conditions are shown in Figure 7.5. These SWRs are two to three orders of magnitude higher than that of the clinical wear rate (order of 10^{-6} $mm^3N^{-1}m^{-1}$), due to the accelerated wear conditions adopted in the present study. Different wear mechanisms have been studied namely, rolling abrasion (R), mixed (M), grooving abrasion (G) and pure sliding (ZrO_2 ball on CoCrMo in the absence of abrasives) (S) identified by SEM analysis, as shown section 7.1. It can be seen that for both abrasive types, the SWRs decrease with decreasing abrasive volume fraction regardless of the test solution composition. The 1 μm Al_2O_3 abrasive slurry resulted in generally lower SWRs in comparison to the 4 μm SiC abrasive slurry. For both abrasives, the wear rates generated in BS containing solutions appear to be higher than in the NaCl solution at volume fraction greater than 0.03, but an opposite trend was found when volume fraction is below 0.03. Additionally, the SWR was found to be less sensitive to the abrasive volume fraction when the wear mechanism involves rolling abrasives (volume fraction ≥ 0.072) [256]. A shift in wear mechanisms away from rolling is seen for 1 µm Al_2O_3 tests at 0.12 vol% compared to 4 µm SiC at the same concentration. This may be explained by using the 'severity of contact' S_c introduced in [256].

$$S_c = \frac{W}{AvH'} \qquad \text{......7.1}$$

$$\frac{1}{H'} = \frac{1}{H_{ball}} + \frac{1}{H_{surface}} \qquad \text{......7.2}$$

Where W is applied load between the ball and the specimen, A is the contact area calculated by Hertzian's point contact theory, v is the volume fraction of abrasive in the slurry, and H' is the effective hardness given by Equation 7.2.

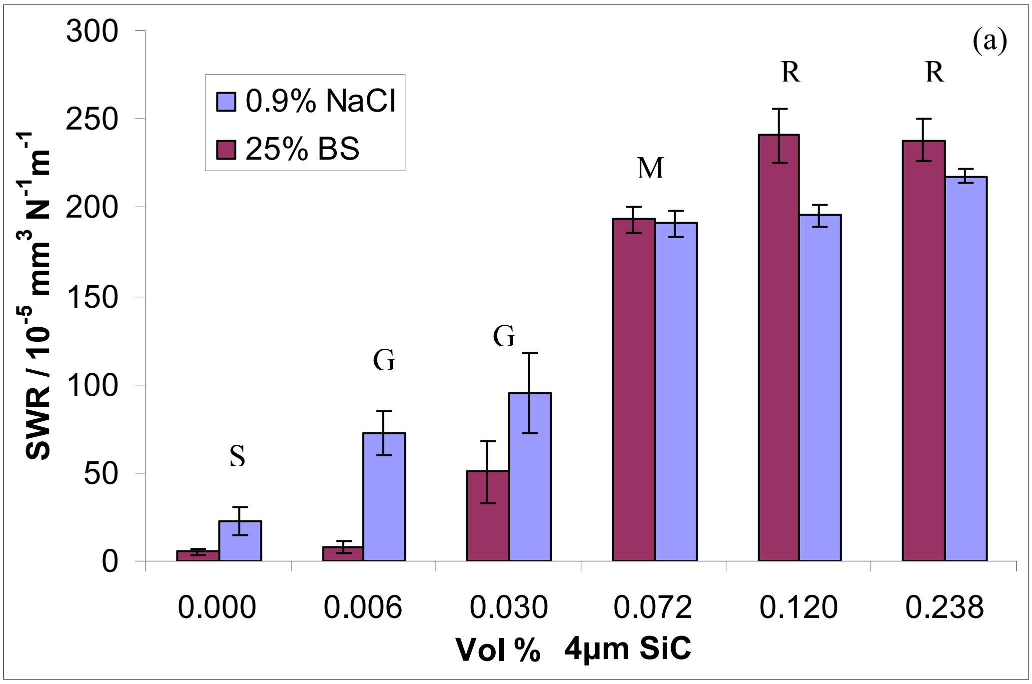

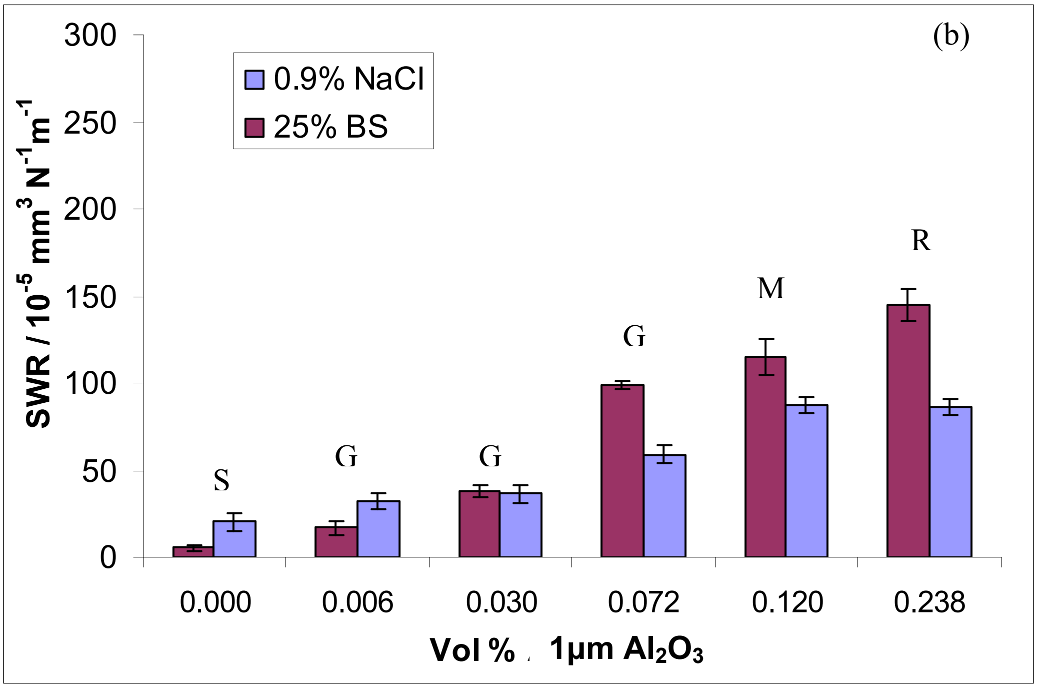

Figure 7.5: Abrasion-corrosion specific wear rates of cast CoCrMo under different test conditions, (a) 4 µm SiC, (b) 1 µm Al_2O_3. (Wear mechanisms: R = rolling abrasion, M = mixed regime, G = grooving abrasion, S = pure sliding).

Figure 7.6 shows the shift of severity of contact S_c as the volume fraction of the 4 µm SiC and 1 µm Al_2O_3 abrasive slurries change. It has been suggested in [256] that the wear mode will change from three body (rolling) abrasion to two-body (grooving) abrasion when S_c exceeds the threshold value S^*.

$$S^* = \alpha\left(\frac{H_s}{H_b}\right)^{\beta} \qquad \text{......7.3}$$

where α = -0.49 and β = 0.0076.

The S^* value is obtained empirically. When the S_c value falls in the narrow range of S^*, the mixed regime dominates. It can be seen from Figure 7.6 that the S_c of 4 µm SiC and 1 µm Al_2O_3 slurry both decrease as the volume fraction of abrasive slurry increases, with S_c values for 1 µm Al_2O_3 always being higher than that of 4 µm SiC (due to the smaller particle size of the Al_2O_3). Therefore 1 µm Al_2O_3 shows the first transition in wear mechanism from rolling to mixed (cross the solid line earlier) at 0.12vol%, while such a transition for SiC only occurs at 0.072 vol%.

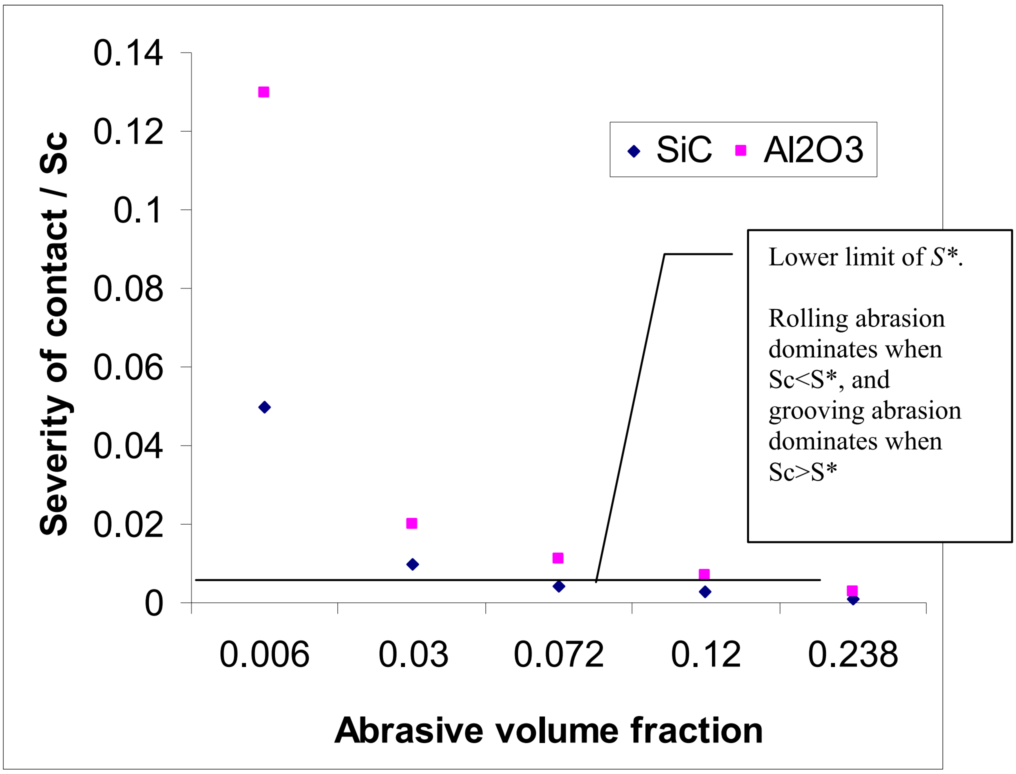

Figure 7.6: Severity of contact for 4 μm SiC and 1 μm Al_2O_3 slurries at various abrasive volume fractions.

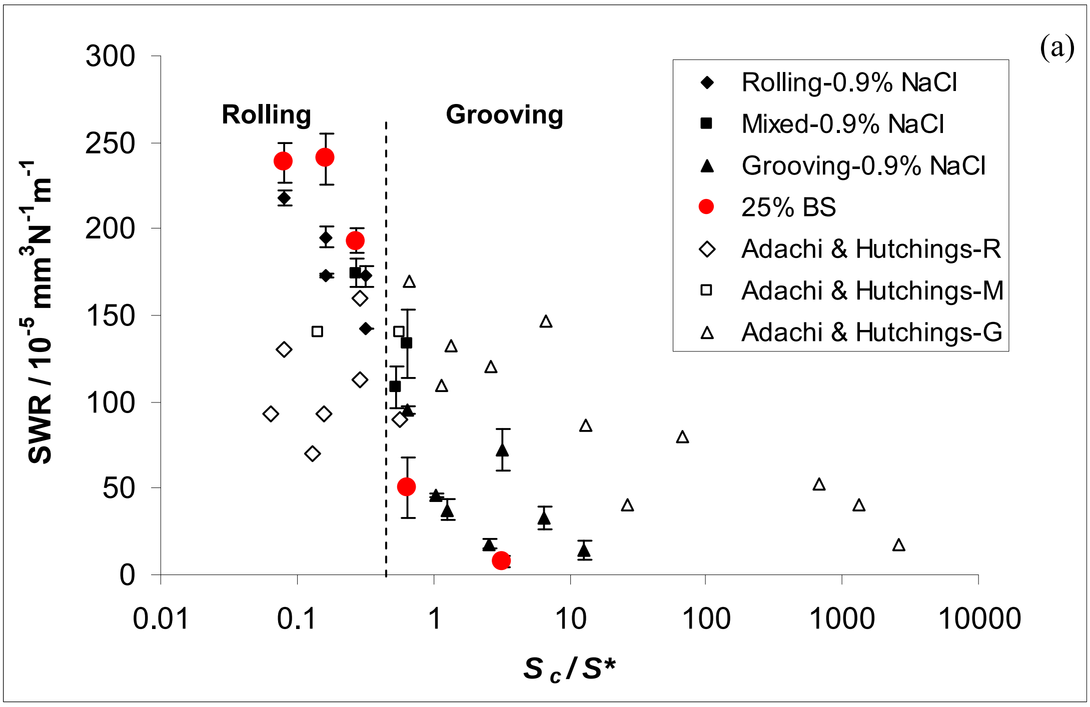

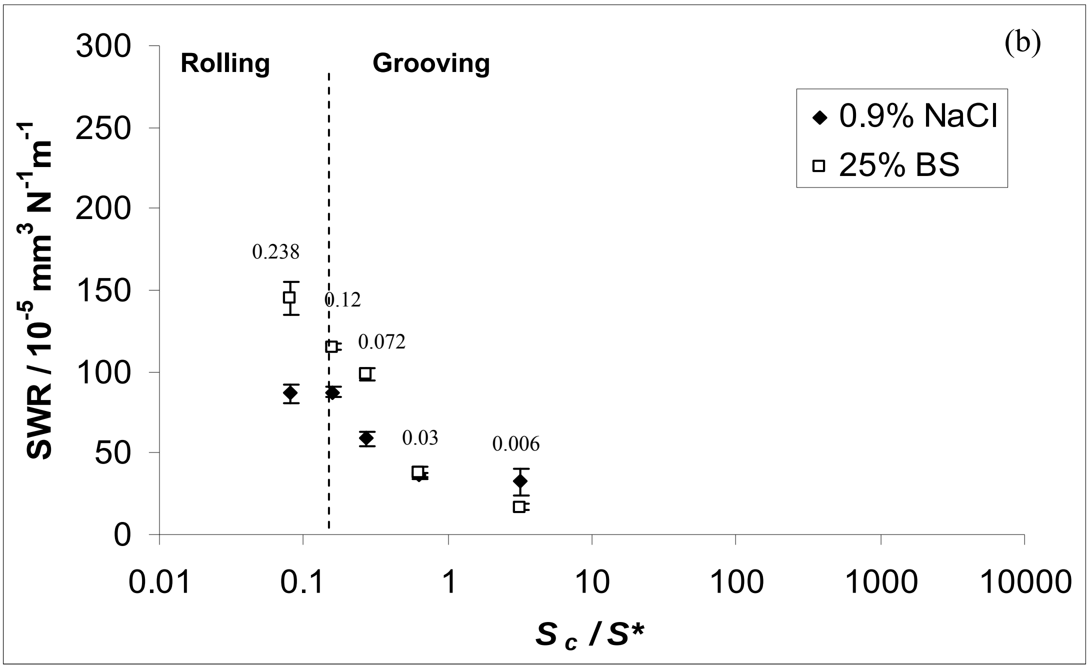

Figure 7.7: Specific wear rates observed in this work as a function of severity of contact Sc/S* for (a) 4 µm SiC based slurries and (b) 1 µm Al_2O_3 based slurries. Data from [256] has been replotted with the authors' permission.

Figure 7.7 (a) shows the SWRs of cast CoCrMo plotted against S_c/S^*, (S^* is the critical contact severity which is related empirically to the hardness ratio $H_{\text{sample}}/H_{\text{ball}}$ [256] and S^* is equal to 0.013 in this study) in 4 µm SiC and 1 µm Al_2O_3 slurries, respectively. The earlier results obtained by Adachi and Hutchings [256] for bearing surfaces of tool steels under similar test conditions to the present study have also been included for comparison purposes. It can be seen that for cast CoCrMo, the SWR shows a decreasing trend as S_c/S^* increases. However, such a declining trend was less distinct for the steel/steel contact. This might be attributed to the difference in the relative hardness of the ball and specimen employed in the different studies, which could influence the particle entrainment/particle motion. The wear regime and wear rate does show dependence on the S_c/S^* ratio in both the present and earlier studies. When $S_c/S^* <0.6$, rolling abrasion dominates, while for $S_c/S^* >0.6$, grooving abrasion dominates, which is similar to the finding by Adachi and Hutchings [256]. The SWR against S_c/S^* plot for 1 µm Al_2O_3 abrasive, Figure 7.7 (b), however, shows a transition at $S_c/S^* \sim 0.16$. This is mainly due to the nature of the abrasives used. As mentioned above, the transition of wear mechanism is dependent on the nature of the abrasive particle. Chapter 9 will discuss in details the factors that influence the wear mechanisms.

The SWRs for 300 nm Al_2O_3 are shown in Figure 7.8. The average SWR value is between 25 and 38 $\times 10^{-5}$ $mm^3N^{-1}m^{-1}$, and there is a slight decreasing trend with decreasing slurry volume fraction of slurries decreases. The SWR levels are generally lower compared to those generated by 4 µm SiC and 1 µm Al_2O_3 as shown in Figure 7.5, however, the scatter of this data set is much higher, implying a less reproducible test condition due to the easy agglomeration of the abrasives.

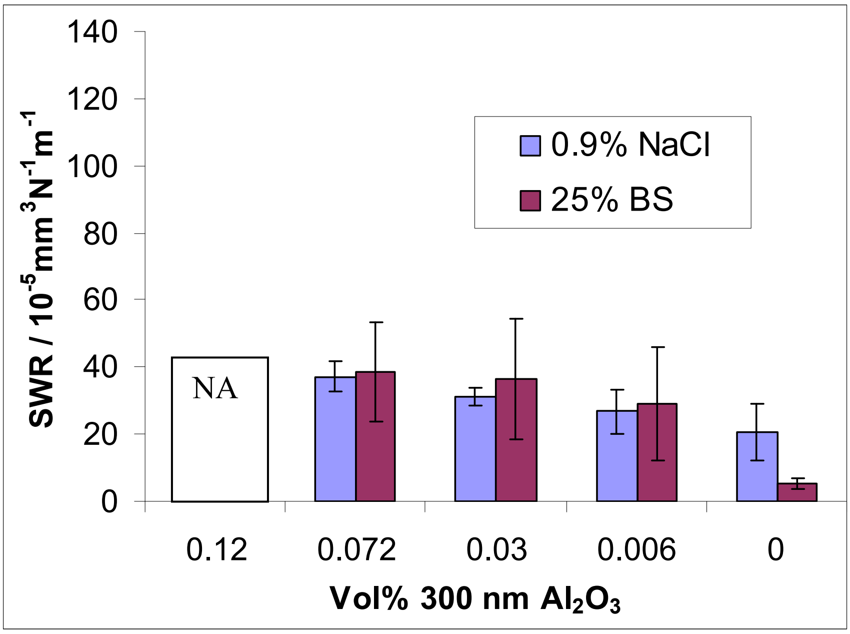

Figure 7.8: Specific wear rates for 300 nm Al_2O_3 slurry based microabrasion-corrosion tests.

7.3 Abrasion induced corrosion current

Figure 7.9 shows the typical electrochemical current noise obtained *in situ* during the micro-abrasion-corrosion tests for 4 µm SiC and 1 µm Al_2O_3. The average current noise level was calculated using Equation 7.4.

$$I_{ave} = \frac{Q}{t_{test}} = \frac{\int_0^t (I_a - I_{corr})\,\mathrm{d}(t)}{t_{test}} \qquad \ldots\ldots 7.4$$

Where Q is the total charge generated during the abrasion-corrosion process (C), t_{test} is the duration of the test (s), I_a is the electrochemical current measured during abrasion

(A), I_{corr} is the corrosion current measured prior to abrasion when the sample is under static immersion (A).

It can be seen that at the onset of the abrasion, the currents in both solutions increase abruptly, corresponding to the sudden depassivation of the surface oxide film. The currents are steady-state during the course of the test until the test stops, at which point the currents return to their original values due to the reformation of the oxide film (repassivation). The details of repassivation kinetics can be found in Section 9.3.

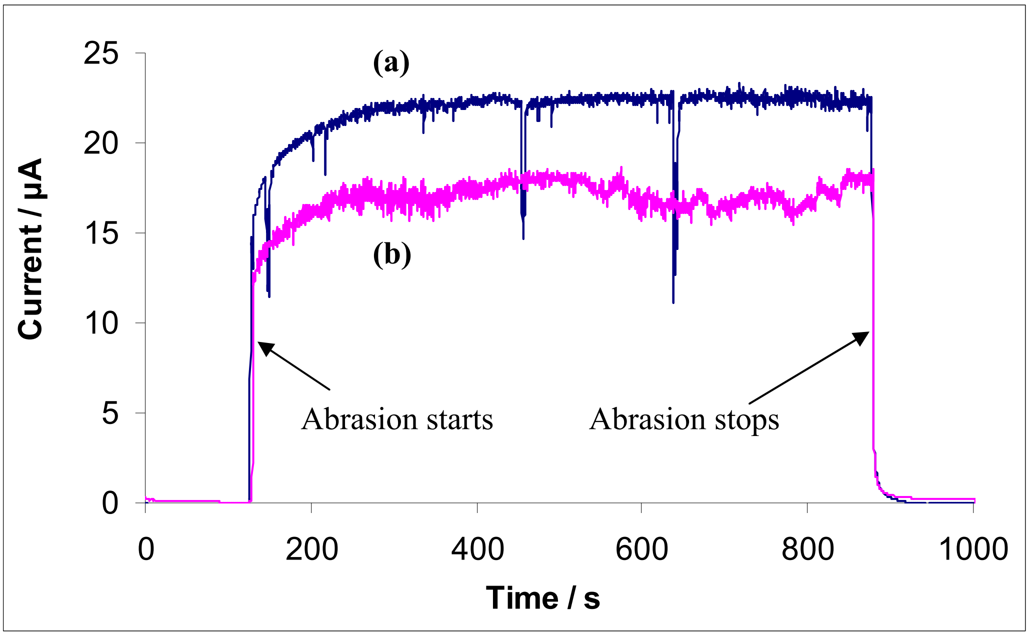

Figure 7.9: Representative electrochemical current noise measurements from abrasion-corrosion processes. (a) 0.12 vol% 4 µm SiC and (b) 0.12 vol% 1 µm Al_2O_3 in 0.9 wt.% NaCl.

Figure 7.10 shows the average current level obtained for the 4 µm SiC and 1 µm Al_2O_3. It can be seen that a lower volume fraction of abrasives resulted in lower electrochemical current level for all test conditions. For 4 µm SiC, 0.9 wt.% NaCl slurries resulted in generally higher current levels than that of 25% BS slurries. The 1 µm Al_2O_3/0.9wt.% NaCl slurry resulted in significantly lower current level than the 4 µm SiC/0.9 wt.% NaCl slurry at all abrasive volume fractions. However, the 1 µm Al_2O_3/25% BS slurry gave a comparable average current noise levels to that of 4 µm SiC/25% BS slurry at similar volume fractions. Also, when the wear mechanism involves rolling abrasives, the current level is less sensitive to the abrasive volume fraction, which is consistent with the trend for SWRs.

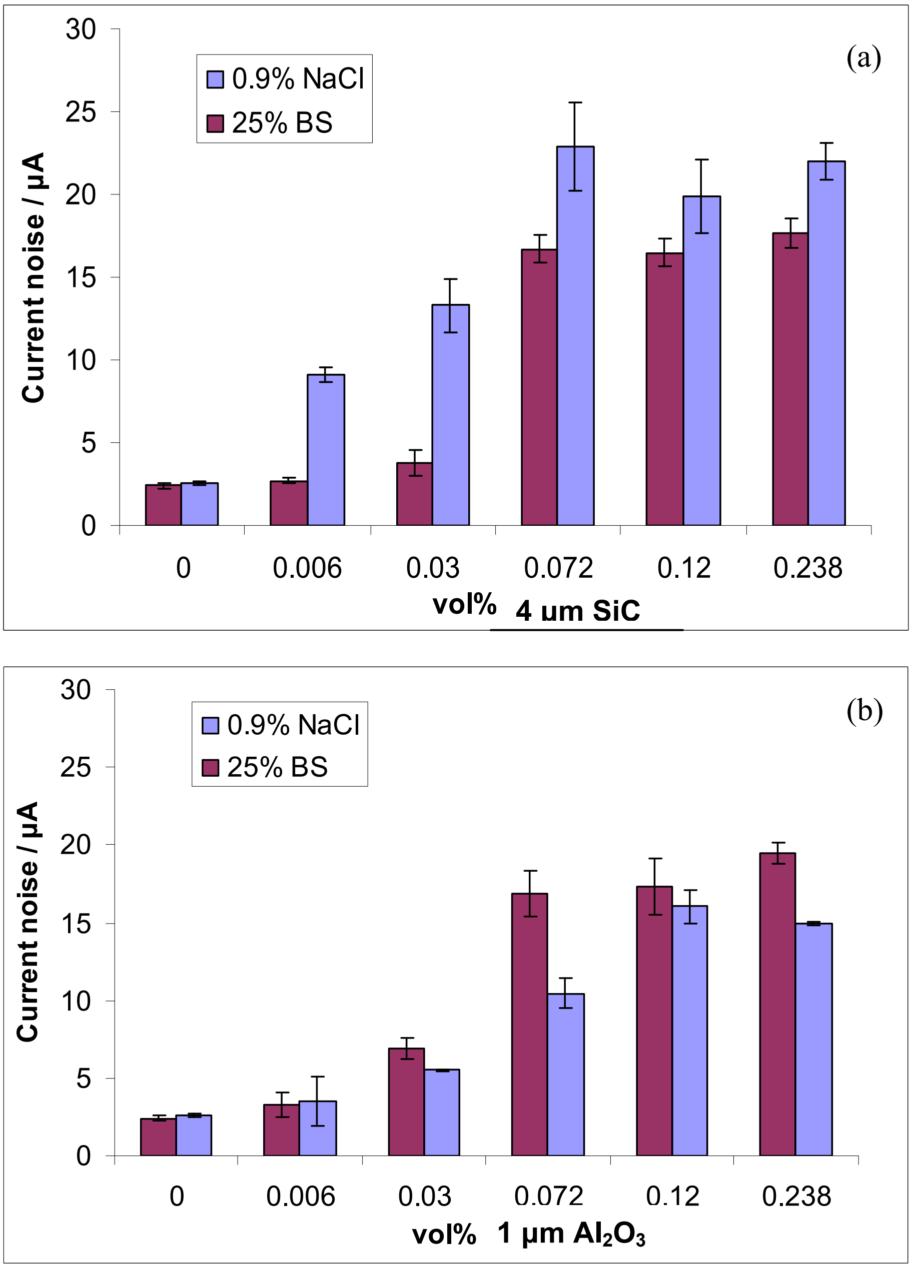

Figure 7.10: Average electrochemical current noise from abrasion-corrosion tests under different test conditions: (a) 4 µm SiC and (b) 1 µm Al_2O_3 abrasive slurries.

The average current noise data for 300 nm Al_2O_3 is shown in Figure 7.11 for different test conditions. A declining trend was found with decreasing volume fraction of concentration. In this case, the scatter of the average current noise appears to be less sensitive to their corresponding wear rate variation (Figure 7.8).

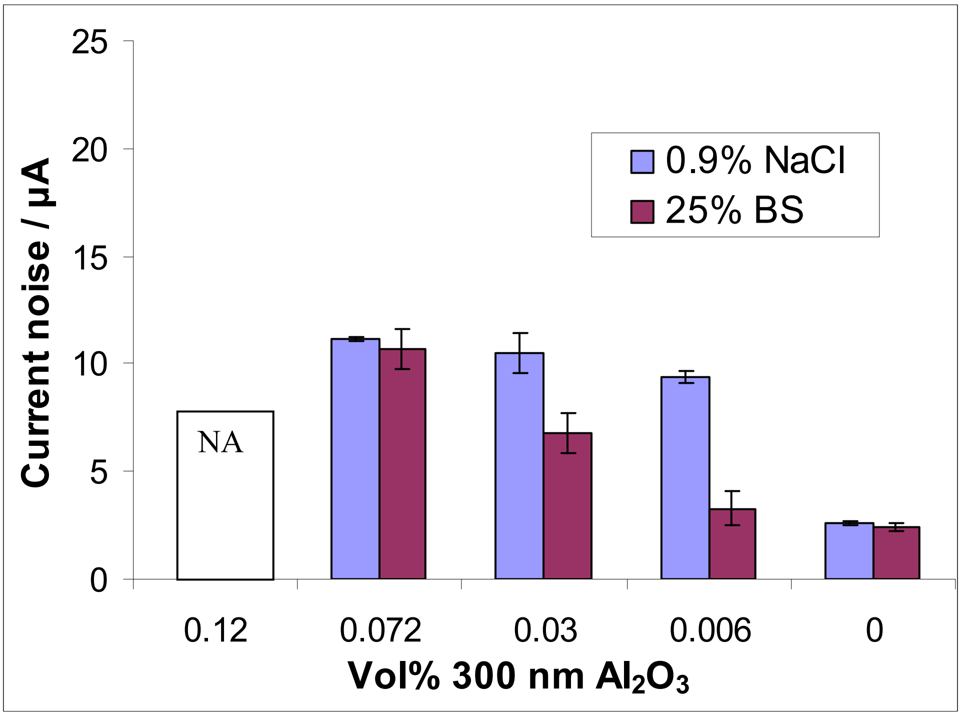

Figure 7.11: Average electrochemical current of 300 nm particle size abrasion-corrosion tests.

In the present study, the current noise immediately after the microabrasion-corrosion (0.238 vol% abrasives) can be closely described by a second order exponential decay function (Equation 7.5) for both 4 µm SiC and 1 µm Al_2O_3; no similar trend has been reported for other systems in the literature.

$$I(t) = I_0 + A_1 \exp\left(-\frac{t - t_0}{\tau_1}\right) + A_2 \exp\left(\frac{t - t_0}{\tau_2}\right) \qquad \text{……7.5}$$

Where $I(t)$ is the current level at time t, I_0 is the baseline current (corrosion current under static condition), A_1 and A_2 are current-related constants, which are possibly related to the different areas of corrosion activity within the wear scar, t_0 is the test duration, τ_1 and τ_2 are the time constants for repassivation, of which τ_1 is dominating in determining the repassivation time.

Figure 7.12 shows a representative curve fit for the repassivation processes seen for the cast CoCrMo abraded in 0.238 vol% 4 µm SiC / 25% BS slurry. The repassivation time is dominated by the first time constant τ_1. The repassivation time for all the 0.238 vol% test slurries appears to be similar (~1 s) for all test slurries and the presence of protein does not significantly influence the time constants (τ_1 and τ_2). This may be associated with the relatively high level of average current noise resulted from both test solutions. More comprehensive discussions regarding the repassivation kinetics of the abrasion-corrosion can be found in Chapter 9.

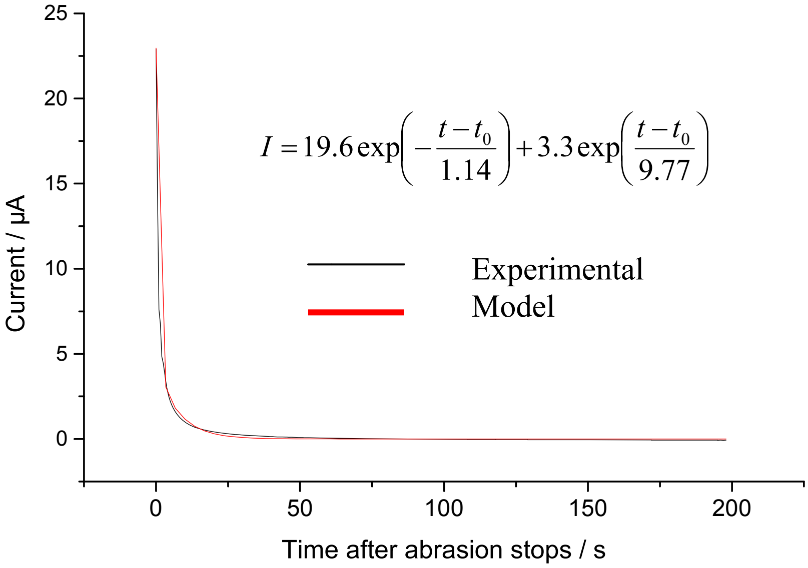

Figure 7.12: Repassivation processes for the cast CoCrMo abraded in 0.238 vol% 4 µm SiC slurry in 25% BS after abrasion stops.

7.4 The mechanical and electrochemical interaction

Figure 7.13 shows the interdependence of the mechanical processes (the SWRs) and electrochemical processes (the average electrochemical current level). It can be seen in Figure 7.13 (a) that 4 µm SiC/25% BS slurries result in generally lower current levels than 4 µm SiC/0.9 wt.% NaCl slurries, this is consistent with the studies conducted in Chapter 5. The data points can be grouped according to the wear regimes determined from the wear scar SEM images. When the tests involve rolling abrasion, both the average current noise and the SWR are greater, but the average current noise appears to be less sensitive to the SWR. However, when the tests are subject to grooving abrasion, the average current noise and the SWR were at lower levels and the average current noise is more dependent on SWR.

Figure 7.13 (b) shows the plot of electrochemical current level against the SWR for 1 µm Al_2O_3 slurries. Again the data points can be grouped into two regions according to the wear regimes induced in the tests. In this case, however, the data set of 1 µm

Al_2O_3/25% BS intersects that of the 1 μm Al_2O_3/0.9 wt.% NaCl when the wear mechanisms changes from grooving to rolling.

For both Figures 7.13 (a) and (b), a linear correlation is found for all test conditions with R-squared values greater than 0.93. The finding of this linear relationship is consistent with [257]. The slopes of the linear fit for 1 μm Al_2O_3 data (0.1318 and 0.2097, for 25%BS and 0.9 wt.% NaCl respectively) are approximately twice of those for 4 μm SiC (0.0678 and 0.088, respectively). This indicates that with the same amount of alloy being removed, the smaller sized abrasives could generate more electrochemical response (current) under the abrasion-corrosion. This could be attributed to the fact that the time for repassivation between particle impacts was reduced significantly by a reduction in particle size [258]. The above statement can also be supported by the SEM investigation, Figure 7.2, where the wear scars generated by 1 μm Al_2O_3 featured more numerous and finer indents/grooves. The results show that the sensitivity of the tribo-corrosion response is dependent on the nature of the abrasives, test solution, as well as the wear mechanisms.

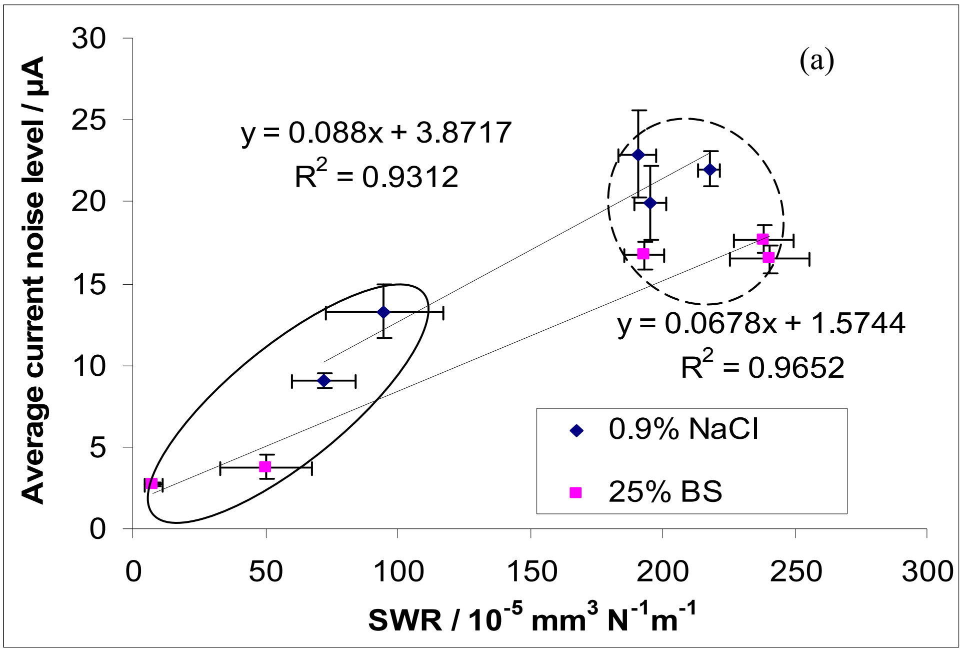

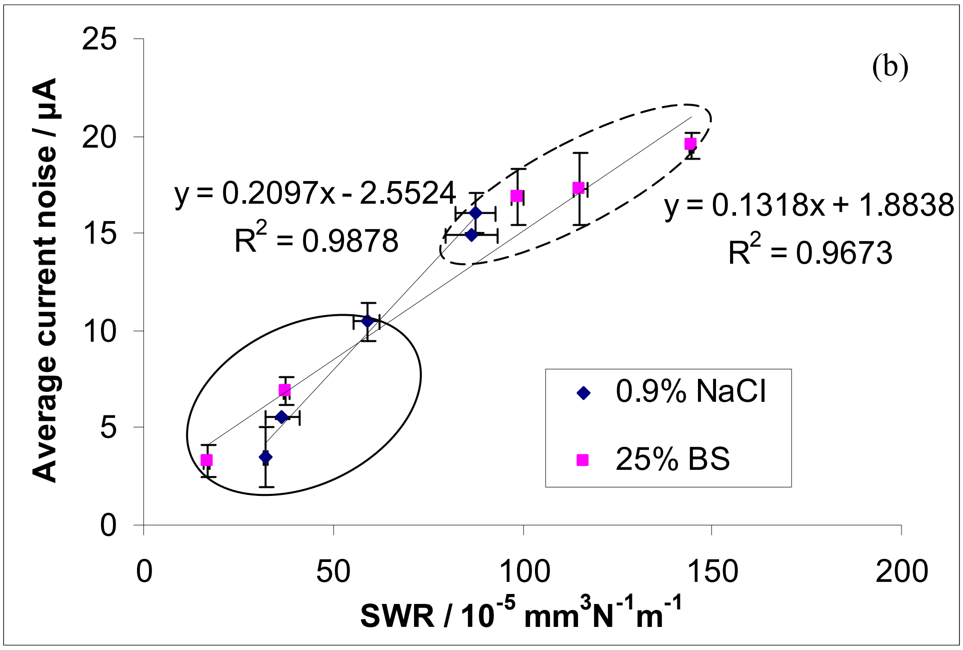

Figure 7.13: Correlation between the electrochemical processes and the mechanical processes. (a) 4 µm SiC slurries and (b) 1 µm Al_2O_3 slurries. Dotted circle represents tests involving rolling abrasion regime and the solid circle represents tests involving grooving abrasion regime.

Figure 7.14 shows the interdependence of the mechanical processes and electrochemical processes for the 300 nm Al_2O_3 based slurry test results. In contrast to Figure 7.13, the data do not show a distinct linear correlation. However, 25%BS based slurries resulted in generally lower corrosion-induced current for all corresponding SWRs.

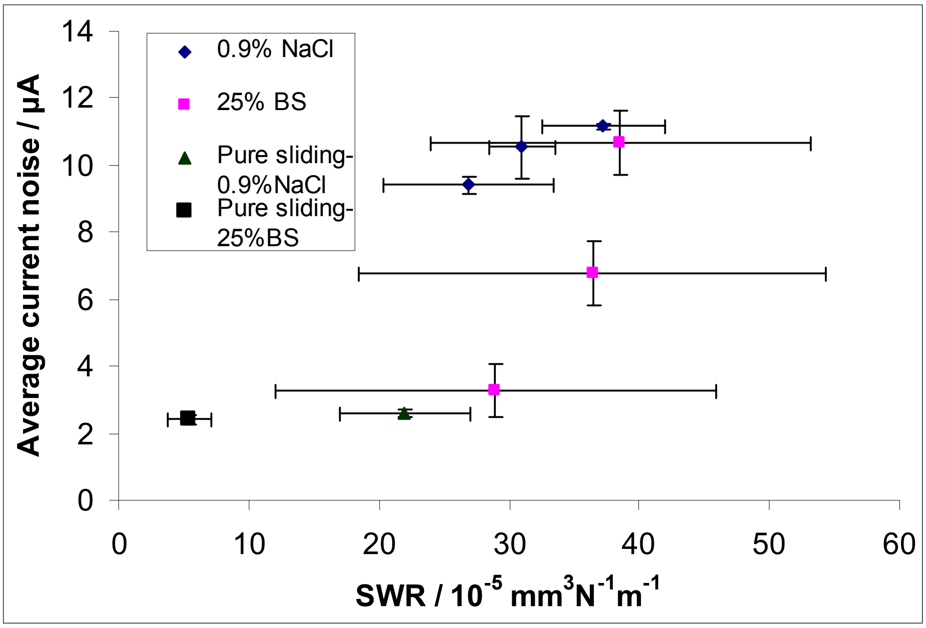

Figure 7.14: Correlation between the electrochemical processes and the mechanical processes for 300 nm Al_2O_3 abrasive slurries.

Figure 7.15 shows the average current noise plotted against SWRs for sub-micron sized $BaSO_4$ slurries with volume fractions 0.006 vol%, 0.03 vol% and 0.072 vol%. The SWRs and wear induced current were significantly lower than for 4 μm SiC and both Al_2O_3 slurries. The BS containing slurries again result in lower corrosion induced current under similar test conditions. The SWRs appear to be similar for the 25%BS and 0.9 wt.% NaCl test solutions for the same abrasive volume fraction used. The SWRs obtained for all test conditions are generally lower than the pure sliding SWR generated in 0.9 wt.% NaCl. As the volume fraction of abrasive decreases, the level of SWRs approaches that of the clinical wear rate (of the order of 10^{-6} $mm^3N^{-1}m^{-1}$). This may be associated with the much lower hardness of the $BaSO_4$ abrasives compared to the SiC or Al_2O_3; most of the particles pass through the contact without causing mechanical damage, or some of the soft $BaSO_4$ abrasives act as polishing agents removing the scratches generated by the previous abrasives. The large scatter shown in the data set again indicates the low reliability of the test conditions.

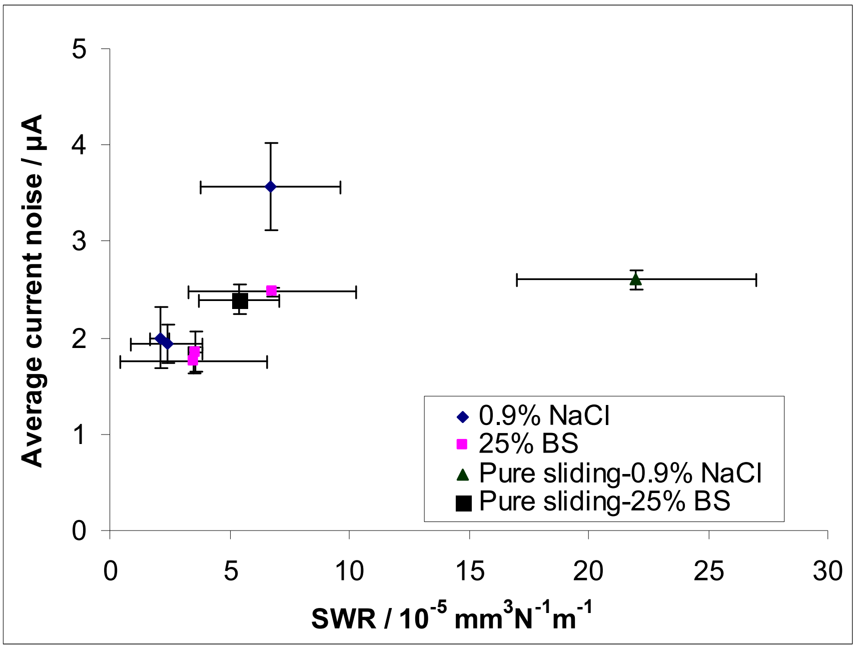

Figure 7.15: Correlation between the electrochemical processes and the mechanical processes for submicron sized $BaSO_4$ abrasive slurries.

7.5 Synergistic study

Mechanical and electrochemical processes take place concurrently in the tribo-corrosion tests, but the total material loss is not necessarily just the summation of mechanical wear and corrosion measured separately [134]. The synergistic term '*S*' is therefore introduced and defined as the difference between the total degradation (T) and the individual components for corrosion only (C_0) and wear only (W_0) [172], see equation 2.10.

The total wear-corrosion synergy S can be divided into its two components, W_c is the corrosion-enhanced wear and C_w is the wear-enhanced corrosion. These terms have been defined in Table 3.7.

The wear-enhanced corrosion (C_w) can be calculated from the wear induced current data by using Faraday's law (using I_{ave} from Equation 7.4) [166]. The corrosion-enhanced wear (W_c) can be calculated by using Equation 7.6.

$$W_c = [T - (W_0 + C_0)] - C_w \qquad \ldots\ldots 7.6$$

S% is defined as:

$$S\% = \frac{W_c + C_w}{T} \times 100\% \qquad \ldots\ldots 7.7$$

Table 7.1 shows the breakdown of SWRs obtained for 0.238 vol% 4 μm SiC and 1 μm Al_2O_3 abrasive slurries. It can be seen that the C_0 is negligible compared to the total wear loss T in most cases. The synergy is dominated by corrosion-enhanced wear (W_c), especially for the protein containing slurries. For abrasion-corrosion in the presence of proteins, the synergy is not purely an electrochemical-mechanical interaction, but is a more complicated mechanism affected by adsorbed proteins or denatured proteins (conglomerates within the contact). In such cases, although the W_c term is defined as purely mechanical, it also accounts for the unique properties of proteins, such as their viscosity, adsorption and precipitation.

Table 7.1: Specific wear rates under various test conditions at 0.238 vol% abrasives concentration.

(in 10^{-5} $mm^3N^{-1}m^{-1}$)	T	W_0	C_0	C_w	W_c	$S\%$
4 µm SiC-0.9% NaCl	217.7	201	0.033	5.8	10.9	7.7
4 µm SiC-25% BS	258	201	0.096	5.4	51.6	22.1
1 µm Al_2O_3-0.9% NaCl	86.3	76	0.033	4	6.3	11.9
1 µm Al_2O_3-25% BS	144.6	76	0.096	5.2	63.4	47.4

Figure 7.16 compares the calculated synergies *S*%, for the test conditions with 0.238 vol% abrasive slurry (4 µm SiC and 1 µm Al_2O_3). In all cases, the transition from mixed-mode to rolling abrasion region shows a significant improvement in repeatability. This is consistent with previous findings [259]. From Figure 7.16 (a), it can be seen that although errors of *S*% values have low confidence levels towards low abrasive volume fraction (due to the less stable test conditions), the 4 µm SiC gives a relatively constant *S*% between 0 to 20%. The *S*% level for 1 µm Al_2O_3 abrasives is similar to that of 4 µm SiC at volume fraction 0.006, 0.03 and 0.238. The negative synergy values for 1 µm Al_2O_3 slurry for 0.072 vo% and 0.12 vol% are due to bad particle entrainment in the contact leading to ridge formation under these conditions which alter the way in which material is being removed (ridge is in contact with the rotating ball, which supports the load and results in less abrasive damage). Figure 7.16 (b) shows the *S*% obtained from 25% BS based slurries. The synergy at an abrasive volume fraction 0.006 is negative, which is due to the presence of the protein effectively protecting the surface from the abrasive damage. The extremely negative synergy seen for 4 µm SiC abrasives (approx. -800%) can also be associated with a change in wear mechanism to polishing/small scale abrasion and reduction in the absolute number of entrained 4 µm SiC particles. In addition, the reduction in surface damage, e.g., Figures 7.1 (d2) and 7.2 (e2), implies that the effect of abrasion on corrosion (and the effect of corrosion on abrasion) is not significant in the presence of proteins at low volume fractions. This could be due to the formation of the protein/metal debris conglomerates effectively separating the tribo-contact and therefore reducing the abrasivity of the particles or transition in the wear process to protein/metal debris polishing wear. The negative synergistic effect has been reported for two-body abrasion of 316L steel under micro-abrasion-corrosion conditions (0.006 vol% 4 µm SiC, 180 m) [207]. This behaviour has been attributed to the longer test duration and corrosion having more of an influence. It also probably reflected

differences in repassivation kinetics and/or composition of the passive film reducing the overall level of two-body abrasion [207, 259].

As the abrasive volume fraction increases, *S*% for both 4 µm SiC and 1 µm Al_2O_3 abrasive slurries increases gradually, and converges when the wear regime moves into mix and three-body rolling, this is also consistent with the finding in [207].

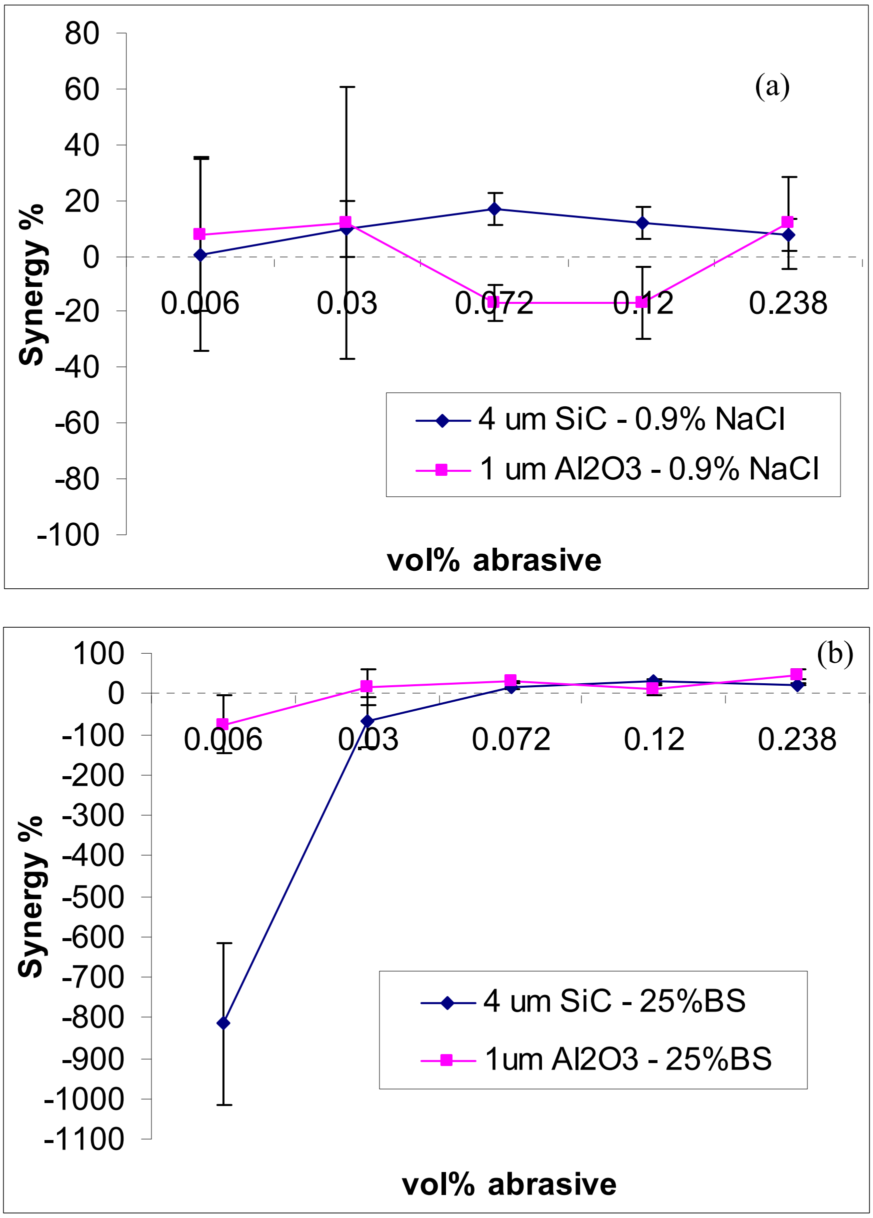

Figure 7.16: *S*% *vs*. abrasives concentration under various test conditions (a) 0.9 wt.% NaCl based slurry and (b) 25% bovine serum based slurry.

7.6 Summary

Results have been presented for the mechanical and electrochemical behaviour of a cast CoCrMo alloy in simulant body solutions using abrasive particles of various size and volume fractions. The abrasion-corrosion behaviour of the CoCrMo alloy was found to be dependent on the wear mechanism invoked from different test conditions, which is dependent on abrasive size, volume fractions, hardness as well as the presence of proteins. A linear correlation was found between the specific wear rates and the wear-induced corrosion current for 4 μm SiC and 1 μm Al_2O_3 abrasives at different volume fractions. For these two abrasives, reducing the size of the particles was found to be more effective in producing wear-induced corrosion current for the same amount of material removal, which implies a potentially higher metal ion release rate. No linear correlation was found when the abrasive size was further reduced (300 nm Al_2O_3 and sub-micron sized $BaSO_4$), but the wear-induced corrosion current generally increases as wear rate increases, although the test reproducibility decreases with smaller and softer particles being used due to the less controlled particle entrainment.

At low abrasive volume fractions (e.g., <0.03 vol%), the presence of protein generally resulted in less corrosion induced current, which may be associated with the organo-metallic conglomerates formed on the wear scar surfaces, which lubricates/separate the surfaces and reduce both wear and corrosion. The negative synergy found for 4 μm SiC and 1 μm Al_2O_3 abrasives at low slurry volume fractions confirms the beneficial effects of the protein/metal debris conglomerates in reducing wear damage. The wear results of soft $BaSO_4$ abrasives helps to underline the possible effects of sub-micron sized soft particles that are likely to be seen *in vivo.*

The findings of this chapter bring greater insights into the abrasion-corrosion behaviour and the mechanical-electrochemical interactions for the cast CoCrMo which could be associated with *in vivo* conditions where the entrained particles are smaller size and have low volume fractions. This work is useful in terms of mapping the performance of CoCrMo when wear particles/abrasives are induced in hip joints. The difference in the nature of the abrasive particles entrained in the hip joints could significantly affect the wear mechanism and the wear-induced corrosion (ion release) *in vivo*. Detailed models for soft particle entrainment/contact mechanics in MoM contacts are still yet to be established and may be an interesting area for future research.

Chapter 8

Micro- and nano-scale tribo-corrosion

The previous chapters detailed investigations into the microabrasion wear mechanisms of cast CoCrMo employing different abrasives in various simulant body fluids. While the wear damage seen on the CoCrMo surface under those test conditions was caused by the entrainment of multiple abrasives, the effect of a single abrasive particle is still not well understood. In this chapter, wet-cell micro-indentation, wet-cell nanoindentation and nano-scratch tests have been carried out, with the aim of simulating the wear damage induced by a single abrasive particle entrained in the CoCrMo joints. Surface / sub-surface characterization deploying SEM and FIB-SEM helps to reveal the micro / nano-scale surface / sub-surface micro-structural changes to the test specimen. Electrochemical current noise measurements were performed when appropriate and a mathematical model extracted for the repassivation process under the corresponding test condition. A greater understanding of the material multi-scale wear-corrosion mechanism as well as the evolution of the sub-surface nanocrystalline structures and tribo-layers is established.

8.1 Wet cell micro-indentation

8.1.1 *In situ* electrochemical noise caused by micro-indentation

The test set up for wet-cell micro-indentation has been described earlier in section 3.5.1. Single and multiple ($\times 5$) indents were performed in 0.9 wt.% NaCl and / or 25% BS in a fully immersed condition. Figure 8.1 (a) shows the load and current transient for a single indentation test made in 0.9 wt.% NaCl (applied load = 9.8 N). When the indenter comes into contact with the specimen surface and is driven downwards, a small anodic peak (less than 5 nA) emerges, which corresponds to the passive film rupturing. The current then recovers to the pre-indentation level when the indenter remained in its loading position. During unloading (indenter leaves the surface), an intense current peak (~ 20 nA) is generated. The surface oxide film may be ruptured/cracked during the indentation process; the reactive bare alloy surface may be exposed to the corrosive environment upon unloading of the indenter. The larger current peak which emerged during unloading is thought to be caused by the exposure of the bare metal over a larger area (which is previously covered by the indenter during loading) to the electrolyte solution. The anodic current flow during this process is partly due to the metal dissolution and partly contributed to the passive film formation. Figure 8.1 (b) shows the optical image of the micro-indent made. The detailed discussion on the microstructual change of the CoCrMo will be discussed later in Section 8.1.2.

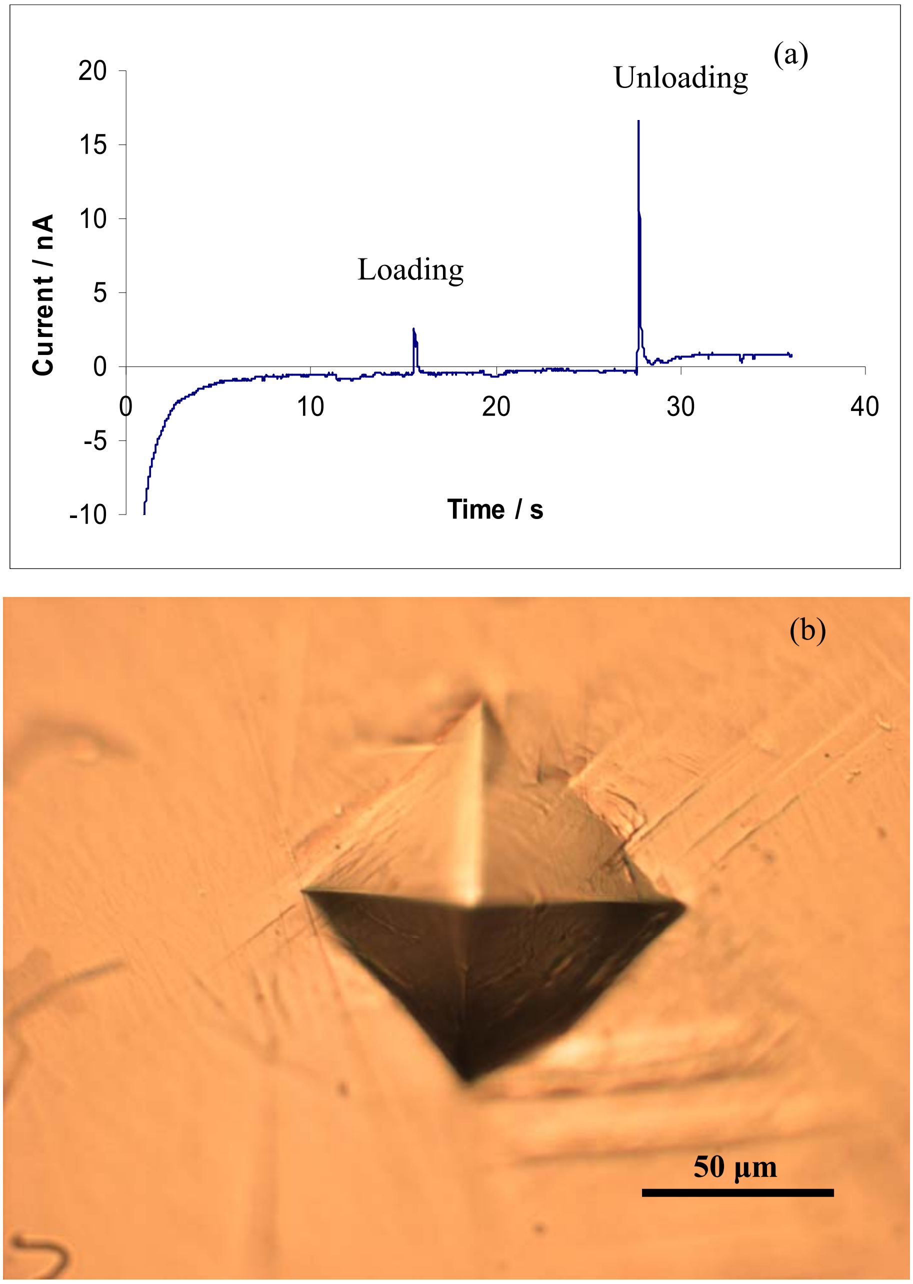

Figure 8.1: Vickers micro-indentation made in 0.9 wt.% NaCl under 9.8 N applied load. (a) in-situ electrochemical current noise and (b) optical image of the indent.

Figure 8.2 (a) shows the current noise collected during the multiple indentation process. The current peak and charge released are both significantly greater for the first indentation cycle as compared with those at the second and the following indentations. This could be due to the plastic deformation that takes place during the first indentation, while elastic deformation is predominant for the second and following indentations [260]. The indent size (~ 100 µm diagonally) and profile of a multiple indent appears to be similar to those seen for single indentation, Figure 8.2 (b).

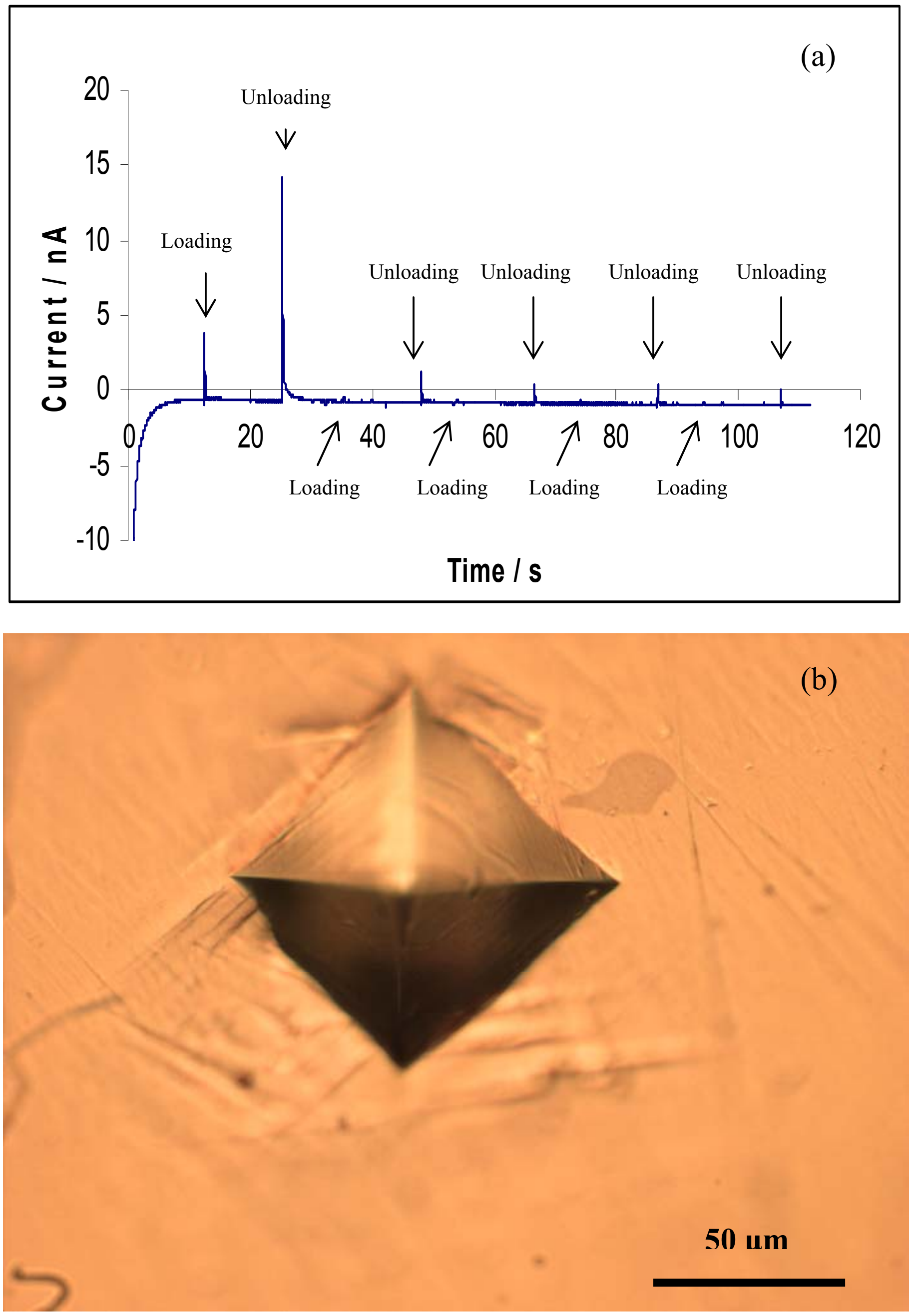

Figure 8.2: Multiple (×5) Vickers micro-indentation made in 0.9 wt.% NaCl under 9.8 N applied load. (a) in-situ electrochemical current noise and (b) optical image of the indent.

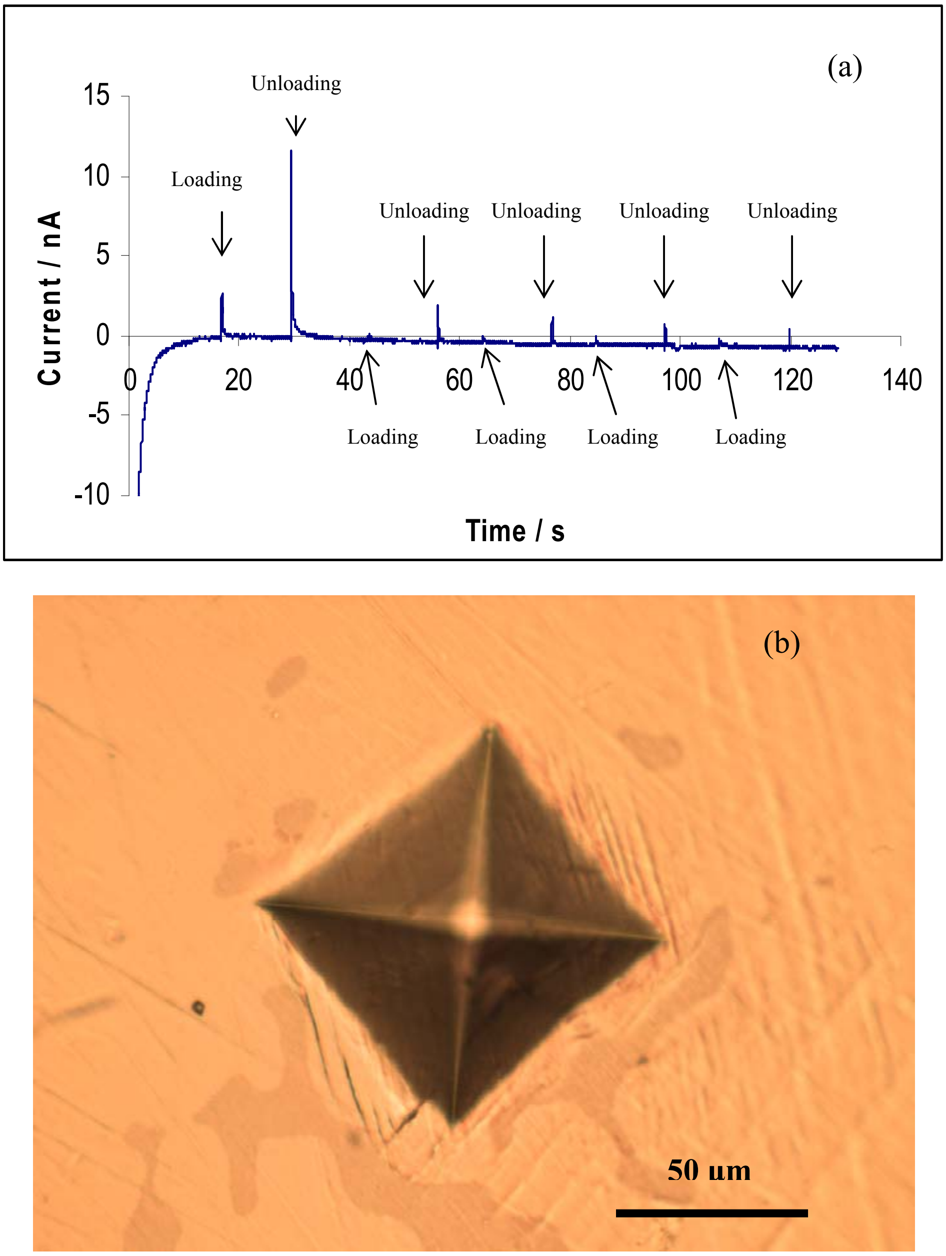

Figure 8.3: Multiple (×5) Vickers micro-indentation made in 25% BS under 9.8 N applied load. (a) in-situ electrochemical current noise and (b) optical image of the indent.

Figure 8.3 shows that the multiple indentation performed in 25% BS under the same indentation condition as in 0.9 wt.% NaCl tests gives rise to a similar indent profile and current pattern as in Figure 8.2. The current peak during unloading is always larger than that during the respective loading process. The current peak and the charge released are approximately constant for the second and following loading/unloading cycles, this might be because after the first loading/unloading cycle, no further plastic deformation takes place and the repassivation film is only partially damaged and recovers at much smaller current levels under an elastic deformation regime.

The intense current peak resulting from the unloading process of the first indentation cycle corresponds to the major current flow event throughout the multiple cycle test. The charge generated during the unloading process can be calculated by Faraday's law and the results show that the charge generated was at a similar level for both the 0.9 wt.% NaCl and 25% BS solutions, see Figure 8.4. According to the XPS analysis in Chapter 4, the surface oxide film thickness is about 0.88 nm. Assuming the current flow is for film repair (reformation of Cr_2O_3) only, the area of film being repaired during the first loading/unloading cycle is about 6 % of the total deformed area (detailed calculation refer to [193]). Therefore it can be suggested that the CoCrMo is only subject to minor surface oxide damage under the indented area during the indentation process.

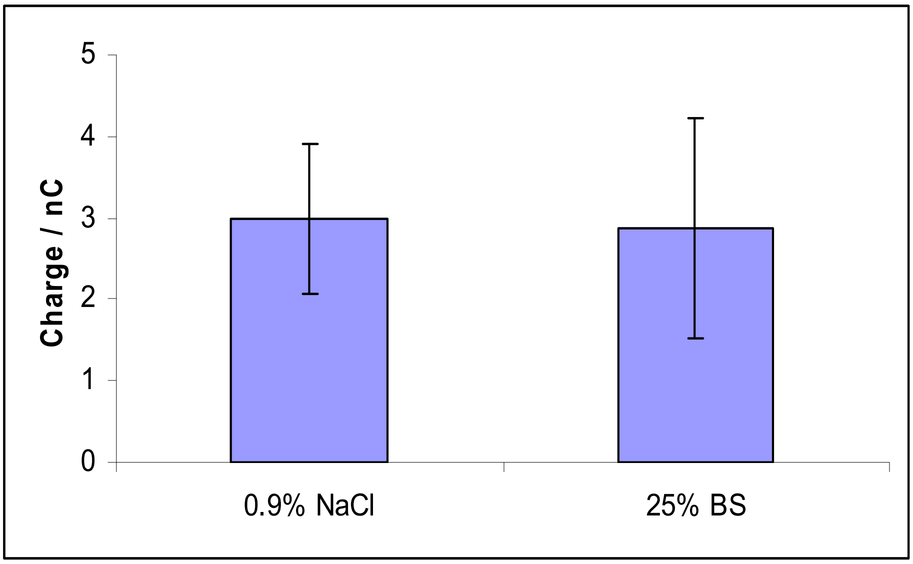

Figure 8.4: Charge generated in different test solutions during first unloading process.

8.1.2 Microstructure analysis

From Figures 8.1 (b), 8.2 (b) and 8.3 (b), slip lines have been identified within and around the periphery of the indent, this is the result of extensive plastic deformation during the indentation (loading) process. The resulting microstructual change could be a combination of a few processes including the formation of planar dislocation arrays, twins or martensite by a strain induced phase transformation (SIT, see Section 2.1.2.3) in the deformed grains [261].

In order to investigate whether SIT has occurred during this study, additional EBSD analysis has been carried out. For EBSD analysis, the surface polishing marks have to be removed prior to the scan as they may induce artefacts. The EBSD specimens were ground, polished and subsequently electro-polished using a solution of 7% perchloric acid and 93% acetic acid (volume %) at a temperature of 10 ºC and an applied voltage of 30 V for 60 seconds. An indentation test under the same test conditions mentioned previously in Section 8.1.1 was carried out in 0.9 wt.% NaCl at 37 ºC and the specimen was rinsed with distilled water and air dried. The indent was then studied under a JEOL FEB_SEM 6500F using an automated EBSD system (Channel 5 software from HKL, Denmark) at 15 kV and 10 nA.

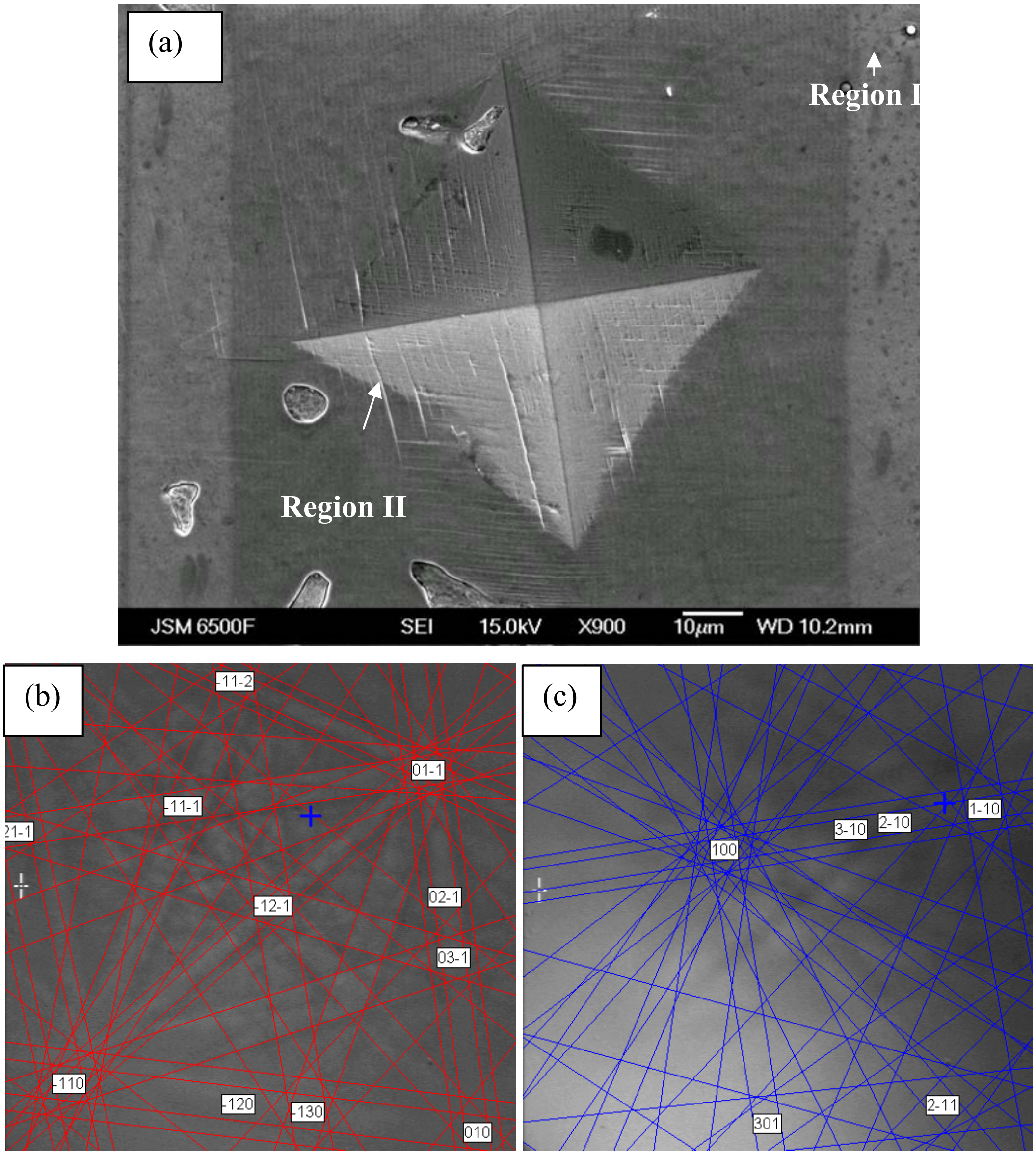

Figure 8.5: Microstructual change of CoCrMo due to micro-indentation. (a) SEM image of a micro-indent, (b) Kikuchi pattern for undamaged surface (Region I) and (c) Kikuchi pattern for deformed surface (Region II).

Figure 8.5 shows the profile of the microindent made on the CoCrMo and the associated Kikuchi pattern [208] obtained from EBSD analysis outside and on the boundary of the indent. According to EBSD phase mapping (see Figure 3.3), a FCC structure is the predominant crystal structure for the undeformed material (Region I), which is featured by the pattern centred at $[\bar{1}\,\bar{1}\,0]$. Although the specimen supplier suggested that there might be traces of martensite present in the 'as cast' samples due to the casting process, such martensite has not been indentified from the current EBSD analysis on the polished/etched surface. HCP phases (possibly as a result of SIT) were only found at the points where severe deformation has taken place (e.g., Region II). A martensitic transformation takes place, resulting in a HCP structure featured by the $[00\bar{1}]$ direction in the Kikuchi pattern. This also gives rise to the orientation relationship: $[111]_{FCC}$ // $[1]_{HCP}$ and $(2\bar{2}0)_{FCC}$ // $(\bar{2}110)_{HCP}$. This conforms with the crystallographic relationship between FCC and HCP as seen for pure cobalt [262].

For a FCC structure, the stacking fault is essentially a very thin layer of HCP, so that such a fault may be an effective coherent nucleus in transformations between these phases. One possibility is that at a sufficiently high driving force, the effective fault energy becomes negative so that spontaneous dissociation of existing dislocations into very wide faults takes places. A group of dislocations could then lead to a multilayer set of faults which, if suitably spaced, constitute a region of the new phase [263]. It is worth mentioning that the HCP phase has not been found within the whole deformed region of the indent (apart from region II), this might be due to the non-uniform force experienced by the material under the indent or due to the inhomogeneous nature of the crystal structure.

In order to study the effect of the hard carbide phase during micro-indentation process, a micro-indent has been made on a carbide. Figure 8.6 (a) shows the top view of the indent. FIB has been performed along a specific region (dashed line) to reveal the sub-surface structure. It has been shown that the relatively soft Co matrix has been smeared over the hard carbide during the indentation process, see Figure 8.6 (b). The carbide phase is also shown to be deformed under the applied load to conform to the shape of the indenter. This indicates that when the applied stress is sufficiently high (approaching/exceeding the yield strength of the alloy), both phases within the alloy undergo severe plastic deformation, and thus mechanically mixed layer may form within the deformed region under a repeated indentation process.

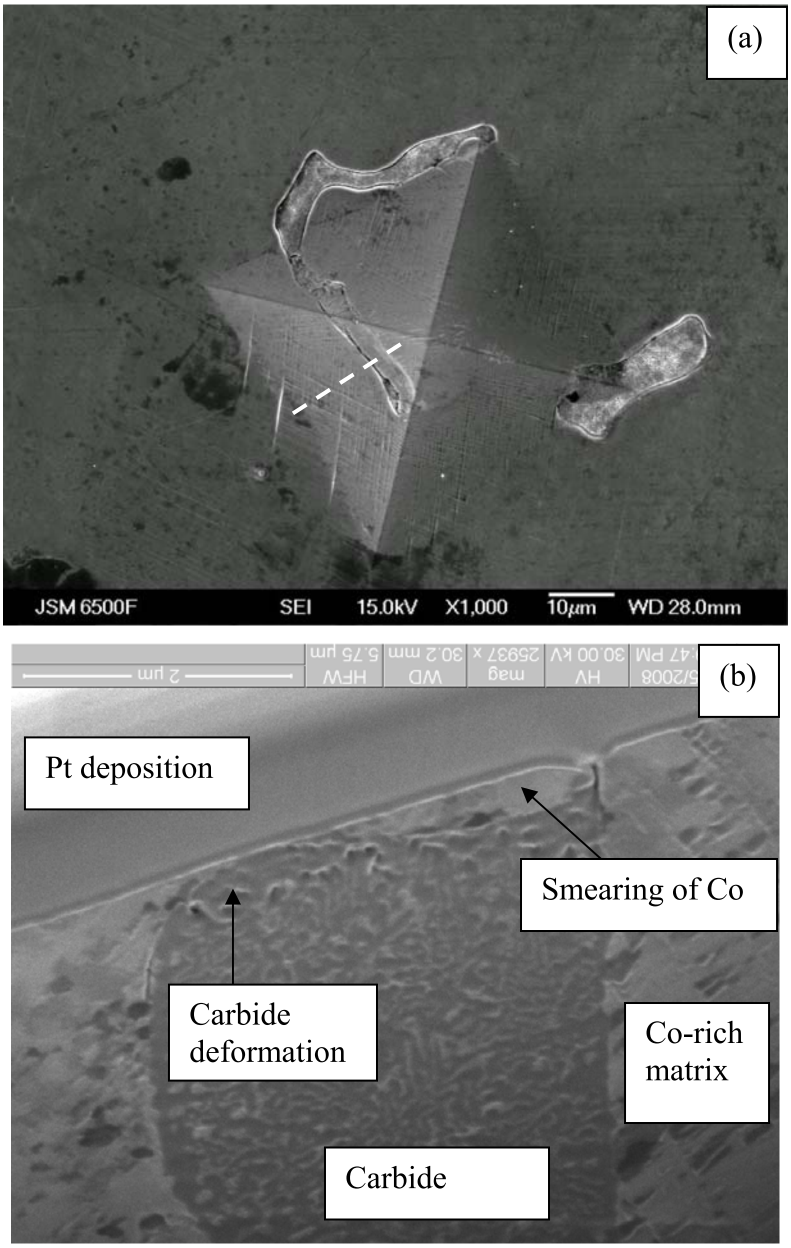

Figure 8.6: (a) SEM (b) FIB-SEM analysis showing surface and sub-surface structure of a micro-indent.

8.2 Nano –scratching

8.2.1 Wear mechanism evaluation

As previously shown in Figure 2.7, scratches with widths of microns were evident on the retrieved MoM joint surfaces. These scratches are likely to have been caused by third body particles generated *in vivo*. Scratching tests at nano-scales using diamond probe are well-established techniques for characterizing the tribological properties of

Co based alloys [263] and are therefore employed in this present study, the details of the experimental setup can be found in Section 3.5.2.

Figure 8.7 (a) shows the typical features seen for single/multiple scratches made on CoCrMo surfaces. The dominant features of the deformation microstructures were the development of numerous intersecting slip lines as shown in Figures 8.7 (b) to (d). These features were a result of the plastic deformation of the materials tested.

Figure 8.7 (b) shows that the cracking occurred along the coarse slip bands. According to Shetty *et al.* [263], the coarse slip bands are evidence of the planar slip character which should be expected in a FCC Co-rich matrix of low stacking fault energy. In their study, slip band cracking has also been observed in the scratch groove which was accompanied by SIT. This suggested that some HCP material has been formed in the coarse slip bands and leads to the observed cracking [263]. Crack formation on coarse slip bands was also suggested to contribute to detachment of material from the ploughed ridges and scratch edges [38].

It can be seen from Figure 8.7 (c) and (d) that the intersecting slip lines do not appear near the periphery of the carbides. The carbide inhibits the occurrence of a strain-induced phase transformation as well as the flow and hardening behaviour of the alloy due to the interactions between the strain-induced crystal defects and carbide phase present in the structure. This indicates that the carbide plays an important role for accommodating deformation caused by strain-induced phase transformation, and therefore higher carbide phase content could reduce the overall ductility of the alloy [19]. Varano *et al.* [263, 264] suggested that the increased carbon in the CoCrMo alloy solid solution caused reduction in volumetric wear (pin-on-disc) because carbon helped to stabilize a FCC crystal structure, limiting the amount of strain-induced transformation to a HCP structure.

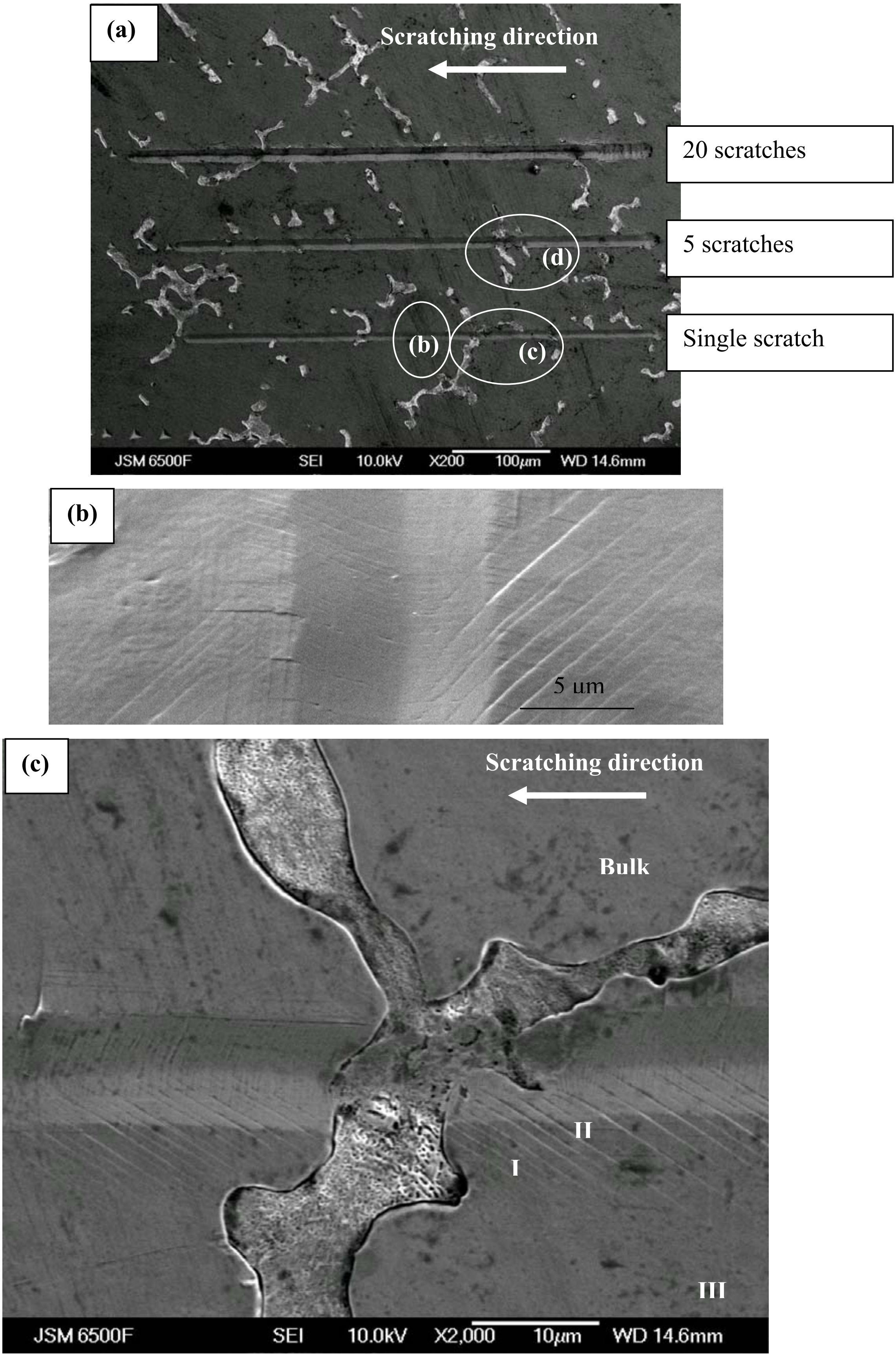
(a)
Scratching direction
20 scratches
5 scratches
Single scratch
(d)
(b)
(c)
JSM 6500F SEI 10.0kV X200 100μm WD 14.6mm
(b)
5 um
(c)
Scratching direction
Bulk
II
I
III
JSM 6500F SEI 10.0kV X2,000 10μm WD 14.6mm

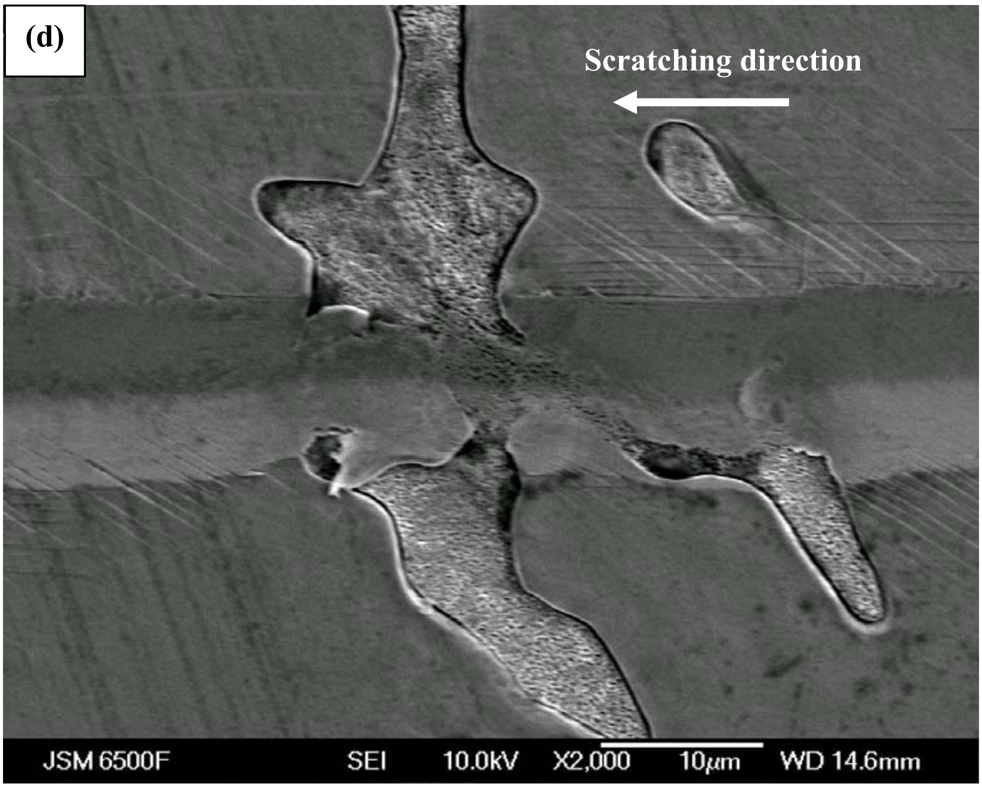

Figure 8.7: Single and multiple scratches made on CoCrMo in air. (a) Overall view (b) Close-up image for single scratch (c) high magnification image for single scratch and (d) high magnification image for 5-pass scratch.

The possible strain induced phase transformation has been investigated using EBSD for areas outside, near and on the boundary of the scratch shown in Figure 8.7 (c). Figure 8.8 shows the Kikuchi pattern obtained from the EBSD analysis. It can be seen that FCC structure is the predominant crystal structure for the bulk (Region III) material, which is featured by the pattern centred at $[\bar{1}\,\bar{1}\,0]$ (Figure 8.8 (a)). When the point being analysed is closer to the scratch (Region I), although there are slip lines present, the crystal structure remains identical to that of the bulk. SIT only occurs at the points where severe deformation has taken place (e.g., Region II). Martensitic transformation takes place, resulting in a HCP structure featured by the $[00\bar{1}]$ direction in the Kichuchi pattern (Figure 8.8 (b)). This gives rise to the same orientation relationship: $[111]_{FCC}$ // $[0001]_{HCP}$ and $(2\bar{2}0)_{FCC}$ // $(\bar{2}110)_{HCP}$ as was found in Section 8.1.

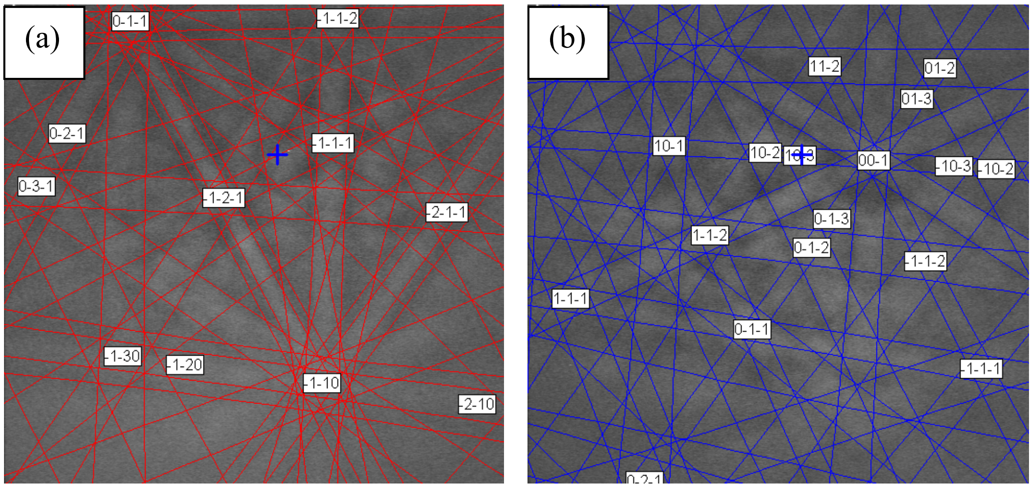

Figure 8.8: Kikuchi patterns for different regions shown in Figure 8.7 (c). (a) Region (I) and (III) FCC and (b) Region (II) HCP.

Besides the slip line formation and matrix/carbide deformation/fracture (Figure 8.9), other material deformation regimes have also been found at various locations of the scratched surface under the present investigation, which include: smearing of matrix material over the carbides (Figure 8.9 (a)), thin detached layers of matrix material inside the scratch groove (Figure 8.9 (b)), carbide cracking, pile-up of matrix material along the leading edge of the carbide (Figure 8.10, 8.13 (b)) and separation of carbides and matrix phases along the carbide-matrix interface. These results are consistent with Shetty *et al.* [40] in their study on powder metallurgy CoCrMo samples. No pile-up of material has been found at the end of the scratches, which indicates that no material has been removed by micro-cutting regime, see Figure 8.7 (a).

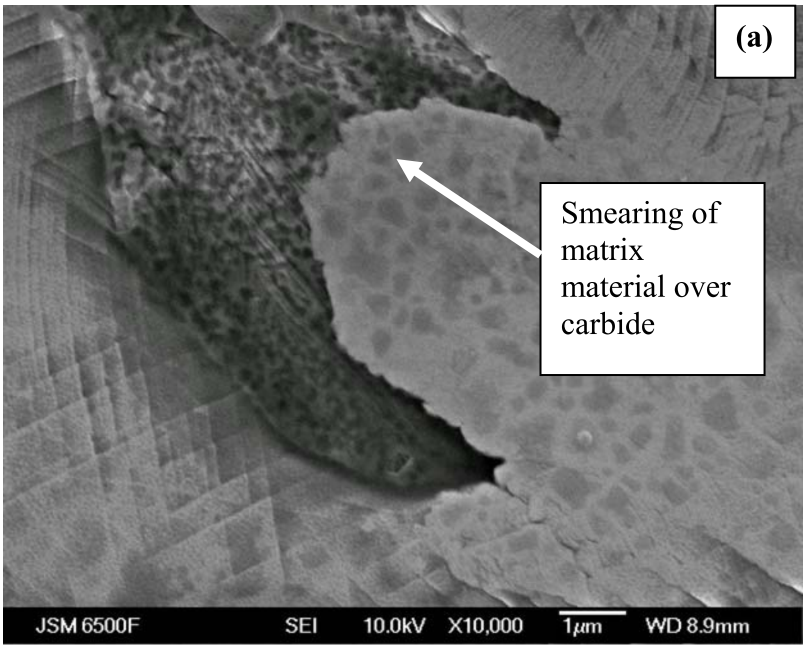

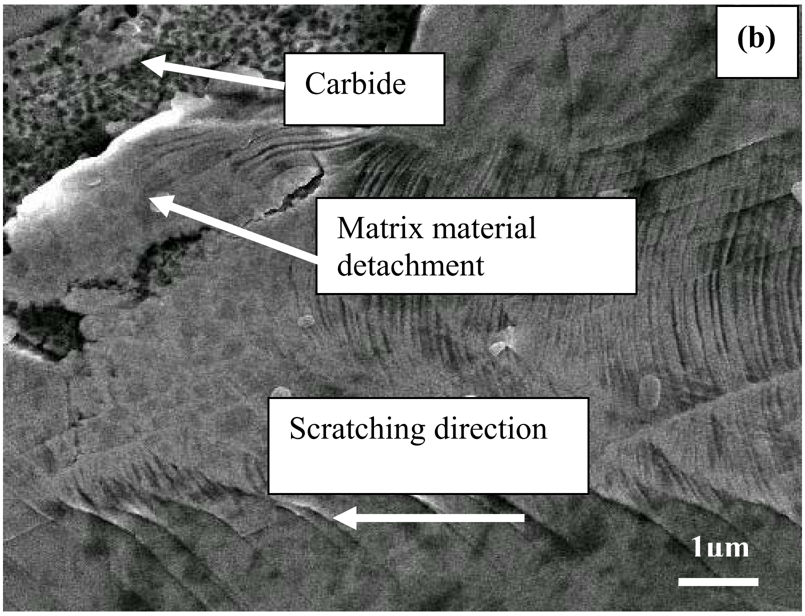

Figure 8.9: Other wear mechanisms seen in scratch tests (a) smearing of matrix material over carbide within a scratch, (b) detachment of matrix material.

Multiple scratches (×5 and ×20 along the same location) have only resulted in wider grooves and more material being pushed to both sides of the groove, (Figure 8.7). Figure 8.10 shows an example of multiple scratches made in 25% BS. In this case, the diamond probe was not aligned during repeated scratching, resulting in new scratches ploughing through the edge (pile-up region) of the previous ones. In this region (dashed circle), the plastically deformed material is subject to multiple cycles of plastic strain, which results in eventual rupture of the surface material and formation of wear debris. This observation is clinically relevant in terms of the wear pattern and the wear debris formation.

Figure 8.10: Multiple scratches made in 25% BS. Material detachment was found when new scratches ploughed along the edge of the previous scratches.

One distinct feature found at certain regions along the periphery of the scratches is the formation of triangular and/or rhombic grains with a size ranging from 100 to 500 nm, Figure 8.11. This feature has been identified along the scratches made in air, 0.9 wt.% NaCl and 25% BS. In Figure 3.3, it has been shown from the EBSD mapping that the polished/etched CoCrMo specimen surface is predominantly a FCC structure. Figure 8.12 shows typical slip systems for a FCC lattice structure. For FCC metal, deformation occurs primarily on the close-packed {111} planes and in the <110> close packed directions of which there are three in each {111} plane forming a triangle (the combination of a slip plane and a slip direction forms a slip system). The triangular structure shown in Figure 8.11 may indicate the direction of the crystallographic plane under observation is in the (111) direction. When not constrained, the material under stress might have been forced to slip along their slip systems forming a triangular and stepped structure. This process might also be accompanied by HCP formation due to SIT. Triangular and rhombic structures with similar dimensions have been found sub-surface (5 µm under the worn surfaces) of a retrieved MoM cup [40]. The feature seen in that study has been attributed to interactions between the stacking faults or HCP martensite on the sliding planes.

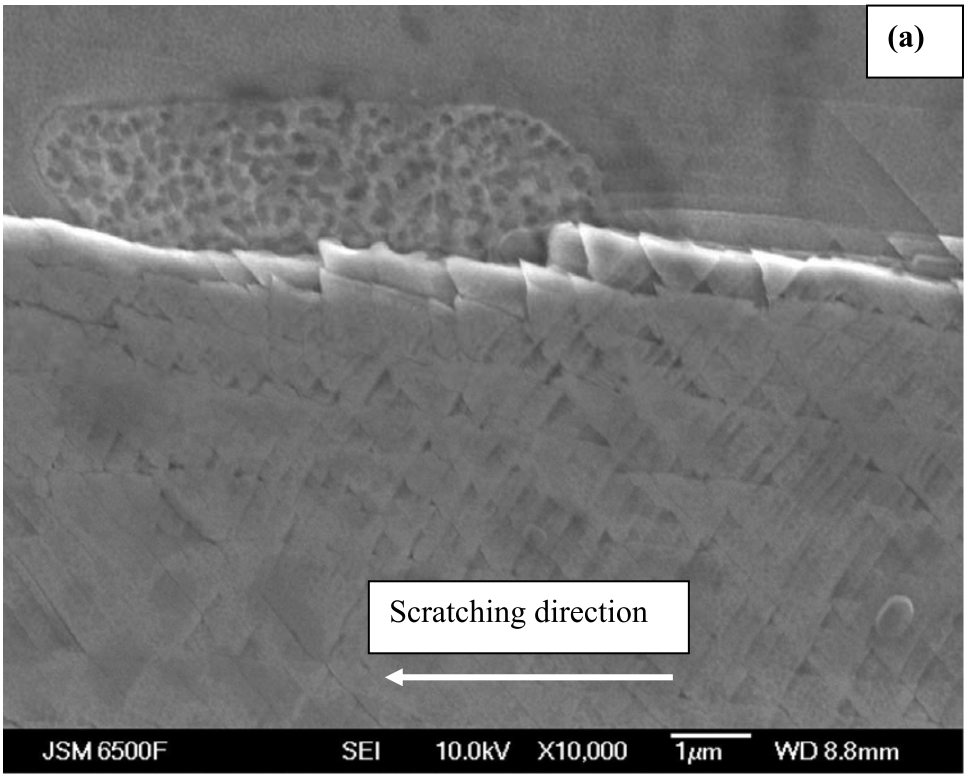

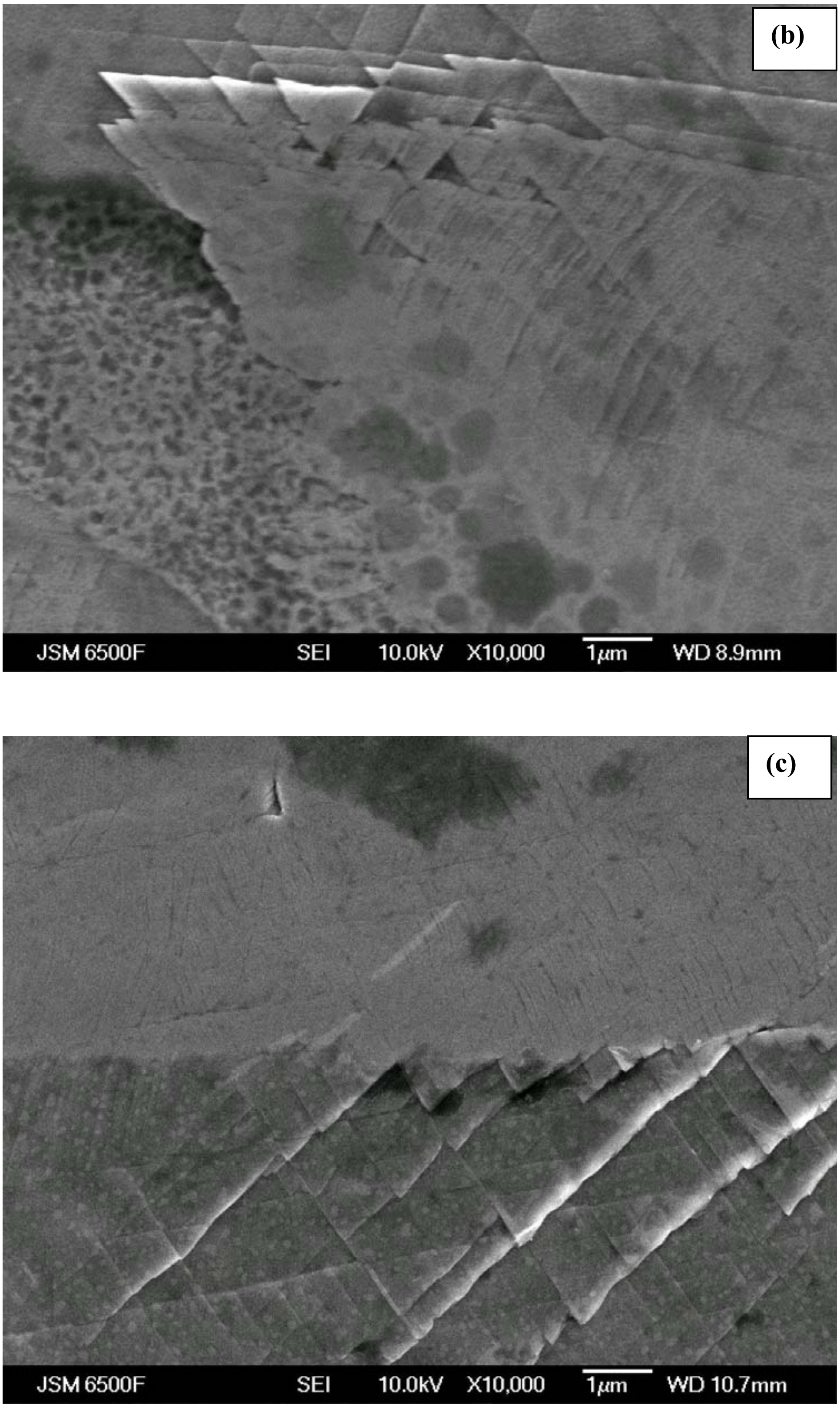

Figure 8.11: Sub-micron triangular and rhombic structure (facets) formed along the scratches. Single scratch made (a) in air, (b) 0.9 wt.% NaCl, and (c) in 25% BS.

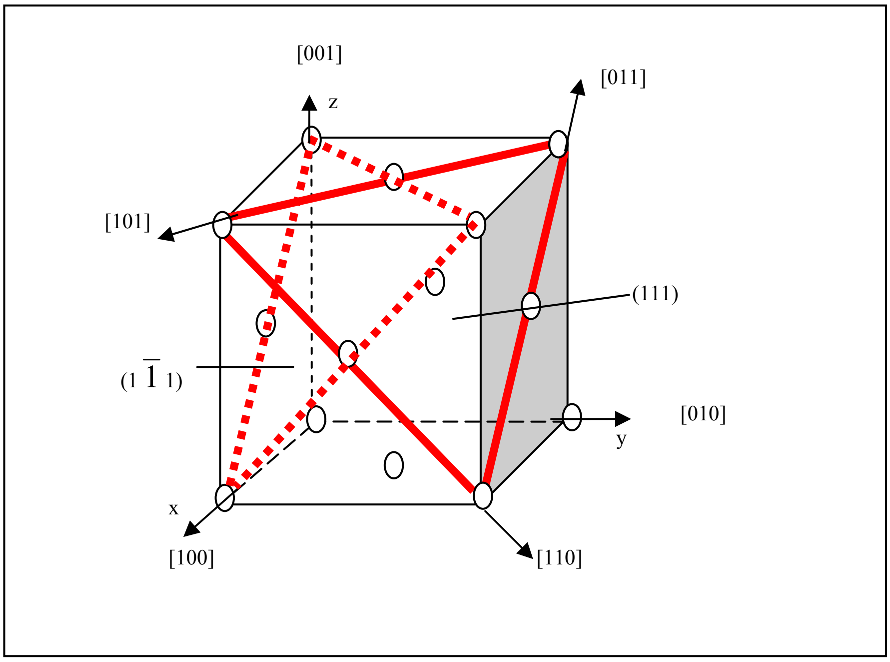

Figure 8.12: Typical slip systems for a FCC crystal, dashed triangle and solid triangle show the typical slip systems.

The effect of applied load on the initiation of the slip line formation has also been investigated. Figure 8.13 shows that slip lines emerge at applied load as low as 10 mN (mean contact pressure ~ 6 GPa), slip lines may not be visible below this load level although deformation may still take place. As the applied load increases, the slip lines extend further towards outside of the grooves and deeper grooves result.

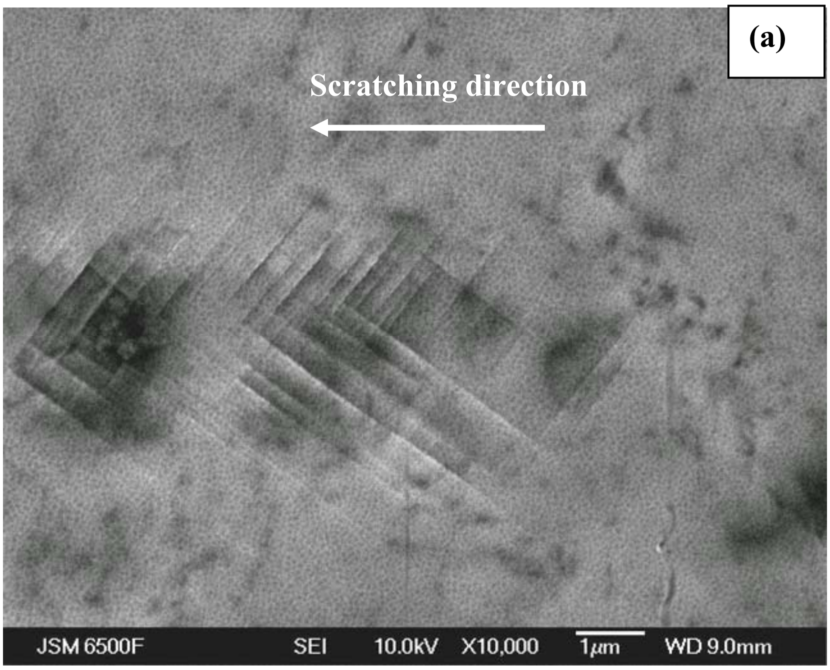

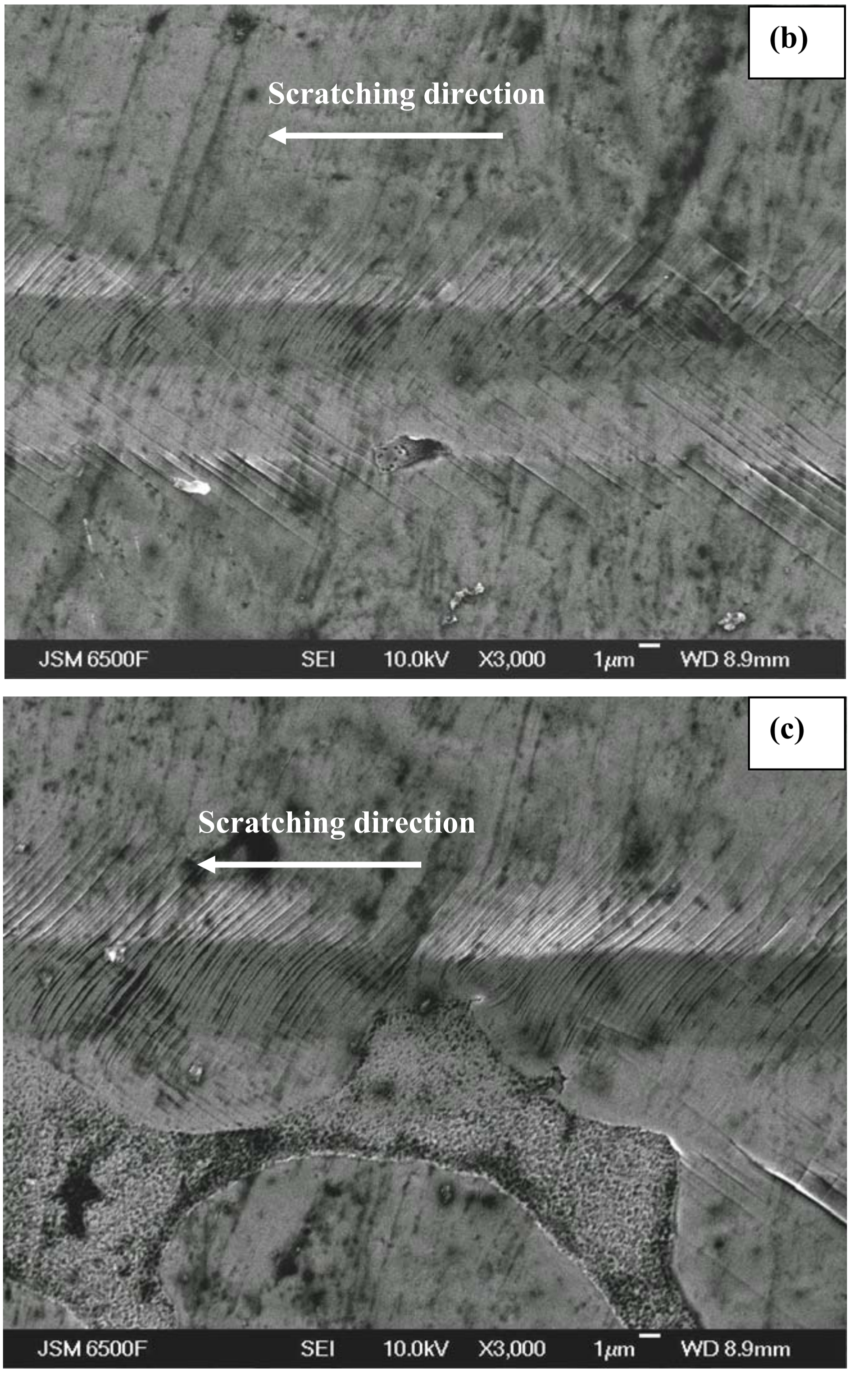

Figure 8.13: Effect of applied load on the single scratch made in 25%BS (a)10 mN, (b)100 mN, and (c) 200 mN.

From the SEM observations of the scratches made in air, 0.9 wt.% NaCl and 25% BS, it is found that the extent of material plastic deformation and the resulting surface microstructure are not dependent on the testing environments. Although the presence of corrosive testing solutions is expected to accelerate the metal-ion release through scratch-induced corrosion, the overall mechanical damage / microstructual change within the scratch are very similar for scratches made in various test solutions.

The sub-surface micro-structure of the scratches has been studied using FIB-SEM. For comparison purposes, a cross-section has been made on a polished and etched sample to reveal the sub-surface profile of a virgin surface, Figure 8.14. As can be seen from Figure 8.14 (b), the carbides are actually about 200 nm lower than the Co rich matrix after the etching procedure, indicating the carbide phase is less corrosion resistant to the etchant used.

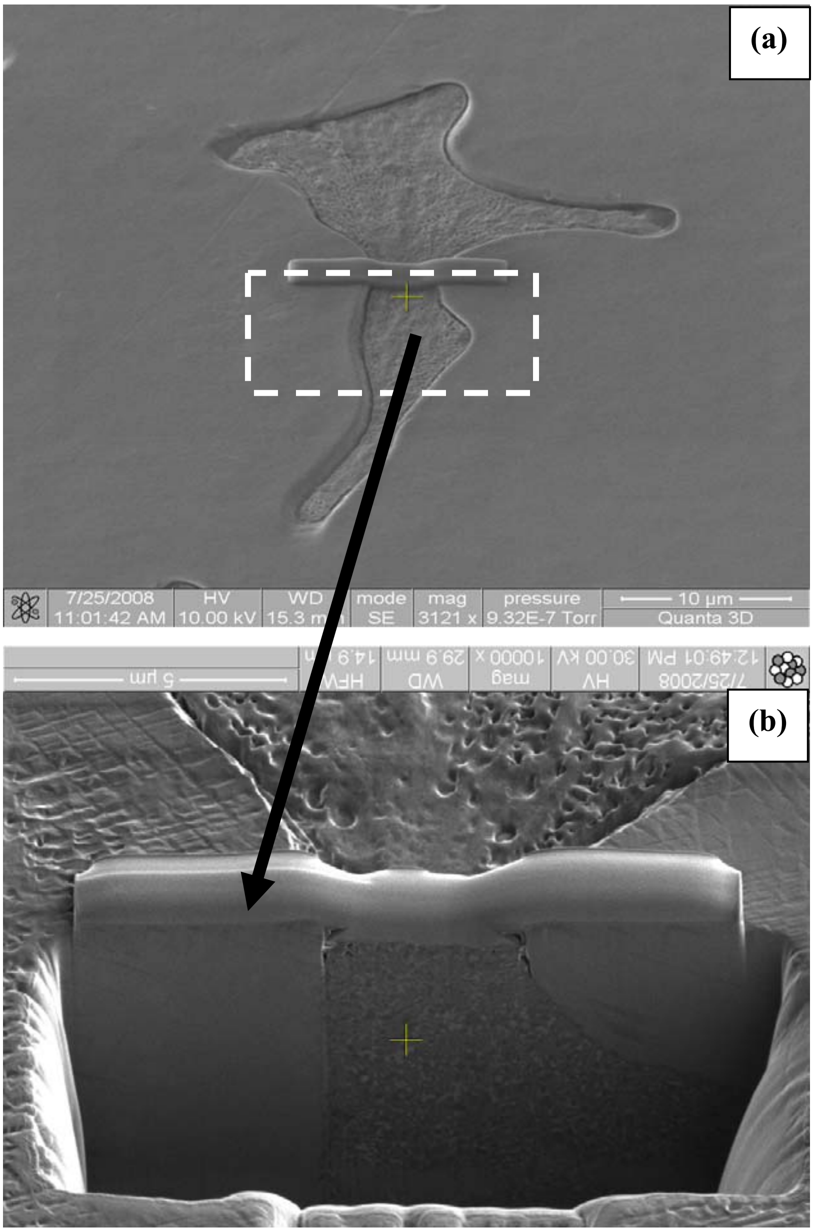

Figure 8.14: (a) Top view of the virgin surface before FIB cross-sectioning, (b) cross-section of the surface after FIBing showing sub-surface structure of the virgin surface.

Figure 8.15 (a)-(b) reveals the surface and sub-surface structure of a single scratch made on CoCrMo etched surface in air. Fracture lines and intersecting slip lines are visible along the edge of the scratch from Figure 8.15 (a). Figure 8.15 (b) shows that there is a nanocrystalline structure layer formed due to the scratching process and the grain size can be as small as 100 nm. A similar fine grain structure has been found in the sub-surface of retrieved joints and the grain refinement has been attributed to the cell formation/rotation under high strain field [261, 265-267].

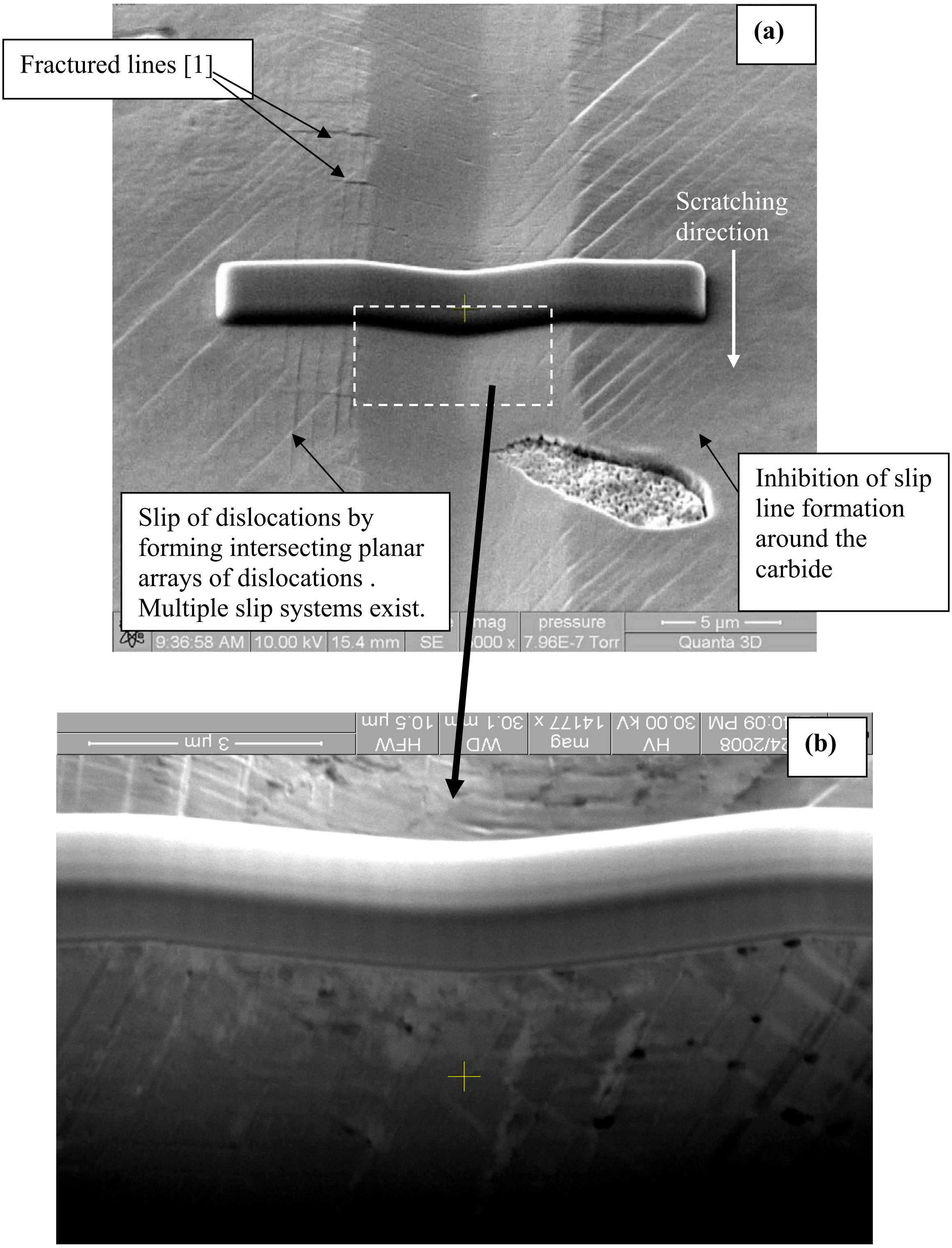

Figure 8.15: (a) SEM image of surface and (b) ion beam image of sub-surface structure of cast CoCrMo after a single scratch test in air.

Figure 8.16 shows the ion beam image of the sub-surface under a multiple-scratch sub-path made in air. The extent of the sub-surface microstructual change is more significant than that for a single scratch test. The depth of sub-surface microstructual change expands deeper underneath the multiple-scratch (>2 μm) (Figure 8.16 (b)) compared to 1 μm for a single scratch. A high magnification image in Figure 8.16 (b) shows sub-micron sized grain features directly underneath the scratch surface. Figure 8.16 (c) on the other hand reveals an entirely different microstructure for the sub-surface region outside the scratch. Striations extending from the near surface into the bulk were found which demonstrated a certain correlation to the surface slip lines. This might be due to the unconstrained condition (in contrast to constrained area right underneath the scratch, details see Figure 8.18) where the material tends to slip under preferential slip systems and form stepped structures on the top surface.

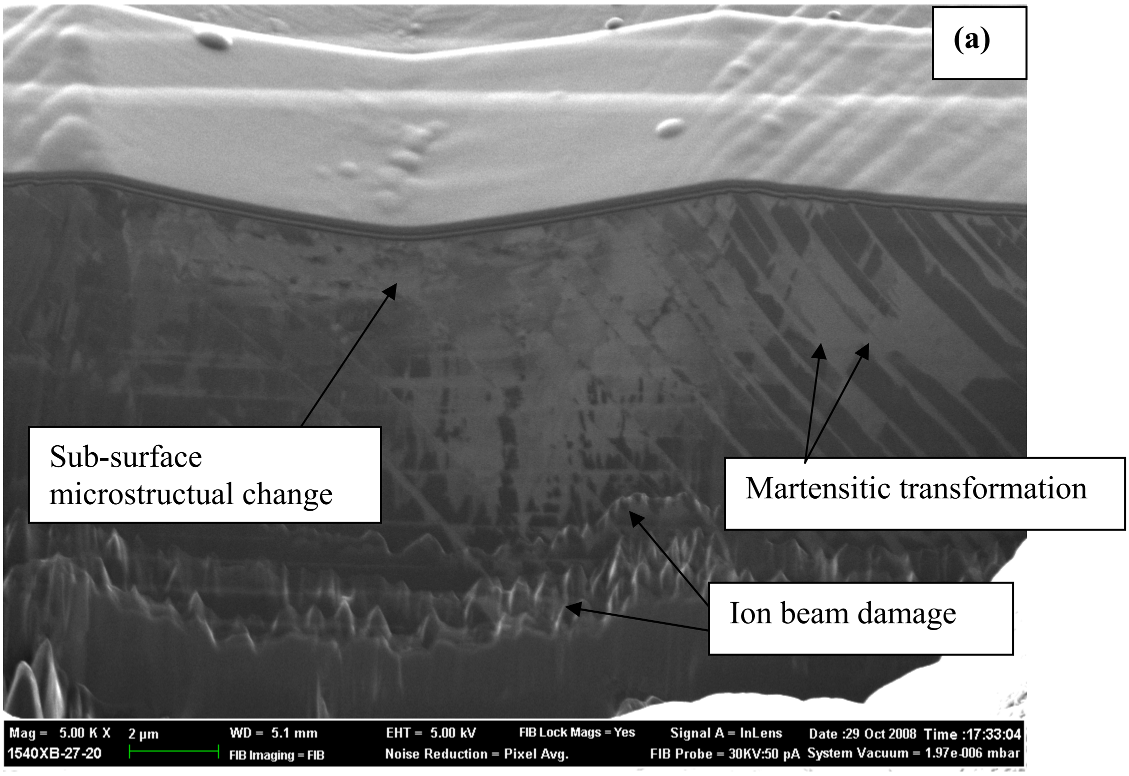

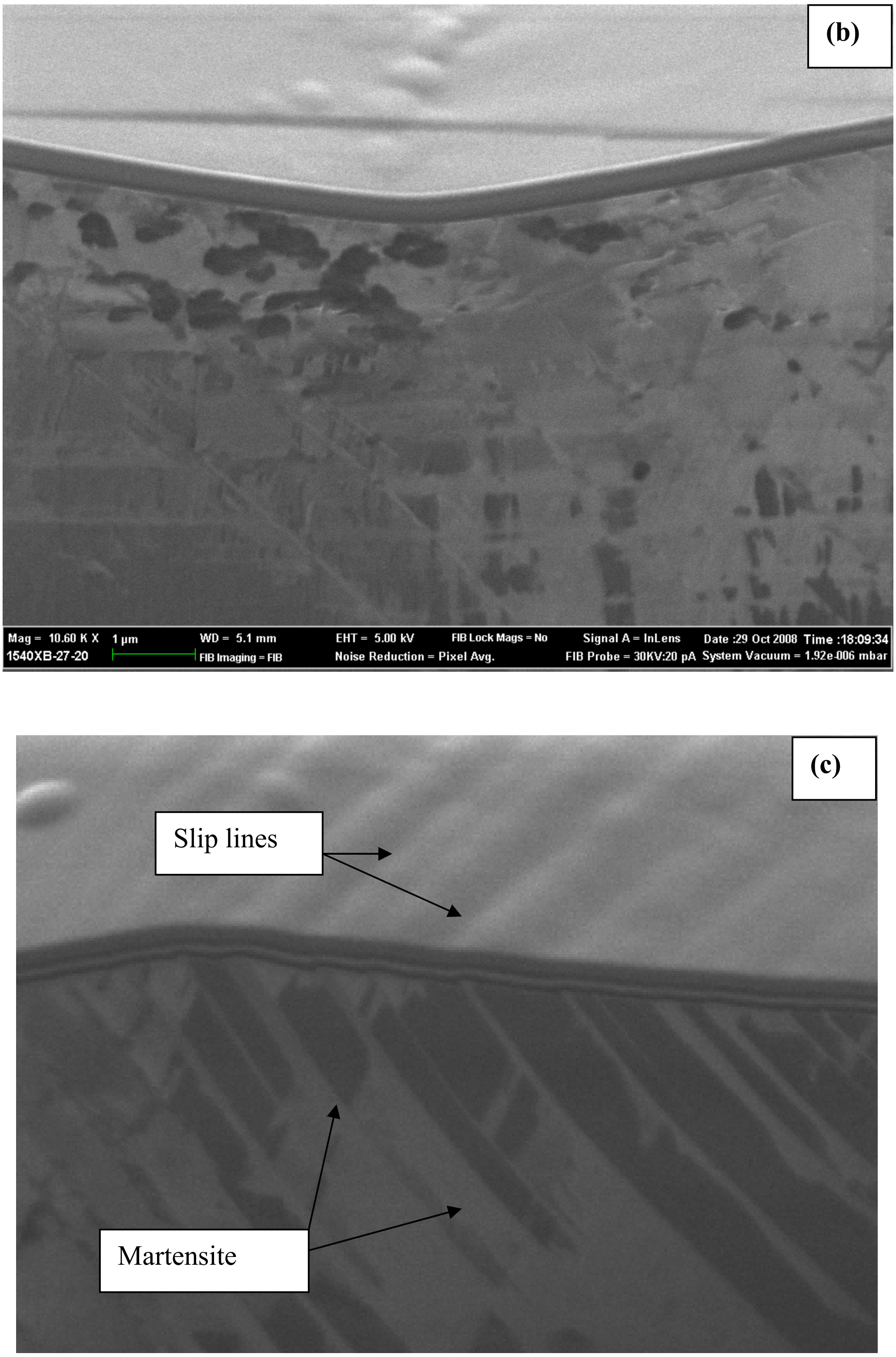

Figure 8.16: Ion beam image showing sub-surface of cast CoCrMo after a multiple-scratch (×20) test in air. (a) Overall view of sub-surface under the scratch, (b) high magnification image showing sub-grain formation right underneath the scratch, (c) Slip lines formed on the top surface on the periphery of the scratch and martensite formation sub-surface.

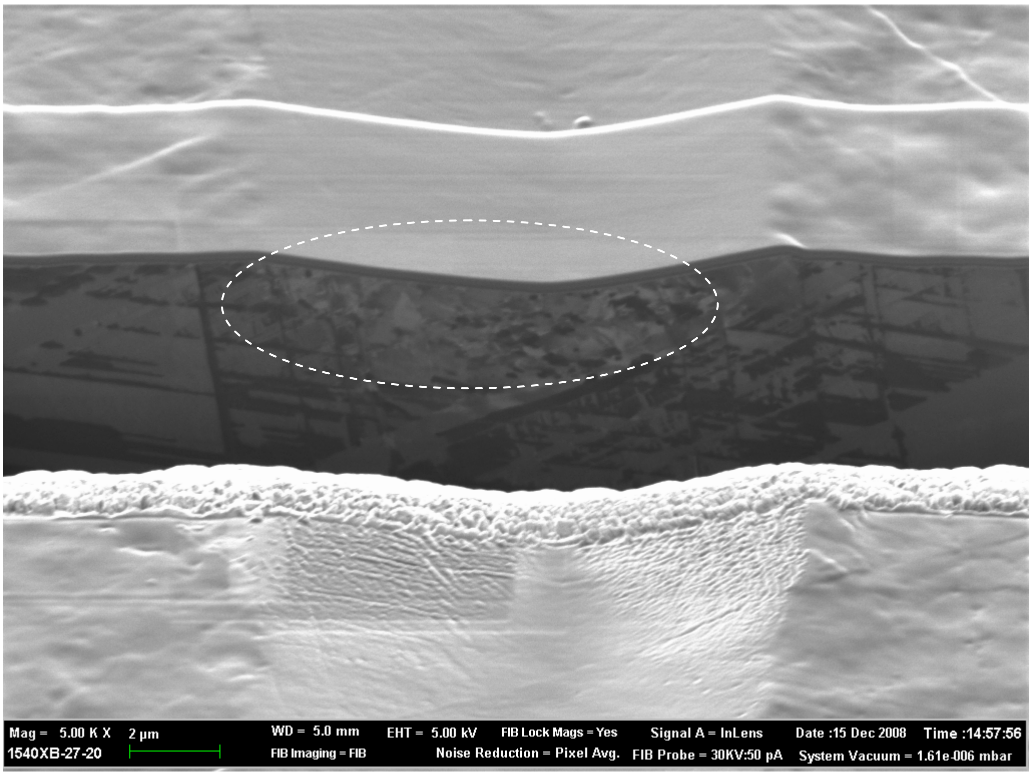

Figure 8.17: Ion beam image showing sub-surface of cast CoCrMo after a multiple-scratch (×20) test in 25% BS.

Figure 8.17 shows the ion beam image of the sub-surface under a multiple-scratch made in 25% BS. The extent of the sub-surface microstructual change (nanocrystalline structure in white circle) is similar to that seen for Figure 8.16(b). Although the presence of proteinaceous material may adsorb onto the diamond probe and CoCrMo and thus lubricate the interacting surfaces, the influence of the testing environment is considered to be negligible due to the high stress experienced by the material during scratching.

The sub-surface microstructure generated from plastic deformation has been discussed in the literature for Co-based alloy and pure cobalt [268]. A fine-grained polycrystalline or sub-grain structure has been reported to occur under many conditions for low stacking fault FCC metals under sliding contact when the stresses are high enough to produce plastic deformation [261]. Grain refinement of CoCrMo may occur by a heavily plastic deformation type process, involving formation of planar dislocation arrays, twins or martensite by SIT within deformed grains [265]. Olson *et al.* [266] suggested that presence of shear bands (mechanical twins or dense stacking-fault bundles, which are commonly present in the low-stacking fault FCC austenite), can effectively form the strain-induced martensite, which is featured by the non-continuous striations. Salinas-Rodriguez *et al.* [266], suggested that the low-stacking fault energy of Co-based alloys makes plastic deformation by dislocation slip in the FCC phase very difficult. Plastic deformation must be microscopically accommodated by alternative mechanisms such as formation of intrinsic stacking faults, twinning, and highly localised slip along pre-existing and strain-induced stacking faults. These interactions between moving dislocations and dissociated (partial) dislocations and/or twins are considered to be the major source for rapid and localized strain hardening, which eventually leads to cracking, if no additional strain-producing mechanisms become available to relieve the high stress required to maintain the plastic flow. Strain induced phase transformation from FCC to HCP can significantly increase the yield strength. The rate-controlling mechanism for the dynamic phase transformation is the evolution of shear band formation. This is characterized by the probability of shear band intersections and the probability of an intersection generating a martensitic embryo. The incremental increase in the number of embryos of the new phase during deformation is related to the increase in the number of shear band intersections [267]. According to Wu *et al.* [39, 267], the planar array of dislocations may reduce the ability to cross-slip, leading to enhanced strain hardening. Twinning on the other hand is highly effective in terms of enhancing the strain hardening, stemming from twin boundaries acting as strong barriers to dislocation motion. In addition, due to the development of either the lamellae or networks of martensite, the movement of dislocations over large distances would become extremely difficult and thus, slip occurs mainly in the FCC phase, providing strain hardening. All the above findings show consistency in the mechanisms of the changing microstructures, the outcome of which may be the significant work hardening during deformation of the material [264]. Such strengthening of the CoCrMo alloy may occur when the material is undergoing repeated articulation and subjected to abrasive wear *in vivo*. The grain refinement and formation of HCP phase may effectively strengthen the material and improve its tribological properties, which make it more resistant to abrasion under the subsequent wear process.

To better understand the correlation between sub-surface microstructual change and the contact mechanics, Hertzian analysis is performed for a simplified static loading condition (single spherical indentation) to find out the maximum shear stress and depth at which maximum shear stress occurs and the details can be found in Table 8.1. The details of the calculation can be found in the Appendix.

Table 8.1: Maximum shear stress calculated for static indentation condition.

Applied normal load	**Maximum shear stress**	**Depth of max shear stress**	**Mean contact pressure**	**Load for first yield**
200 mN	7.27 GPa	0.93 µm	16.4 GPa	185 mN

During scratching, the sub-surface stress field is skewed by frictional forces towards the trailing edge. The magnitude and location of the maximum shear stress moves towards the surfaces as friction increases. Assuming the frictional force does not significantly influence the stress field distribution in this case, the maximum shear stress during scratching is estimated to be within 0-0.93 µm depth sub-surface, which coincides with the depth of sub-surface microstructure change as is shown for the single scratch test. Figure 8.18 schematically illustrates the regions with maximum shear stress and microstructure features resulted within constrained and unconstrained areas underneath the scratching path.

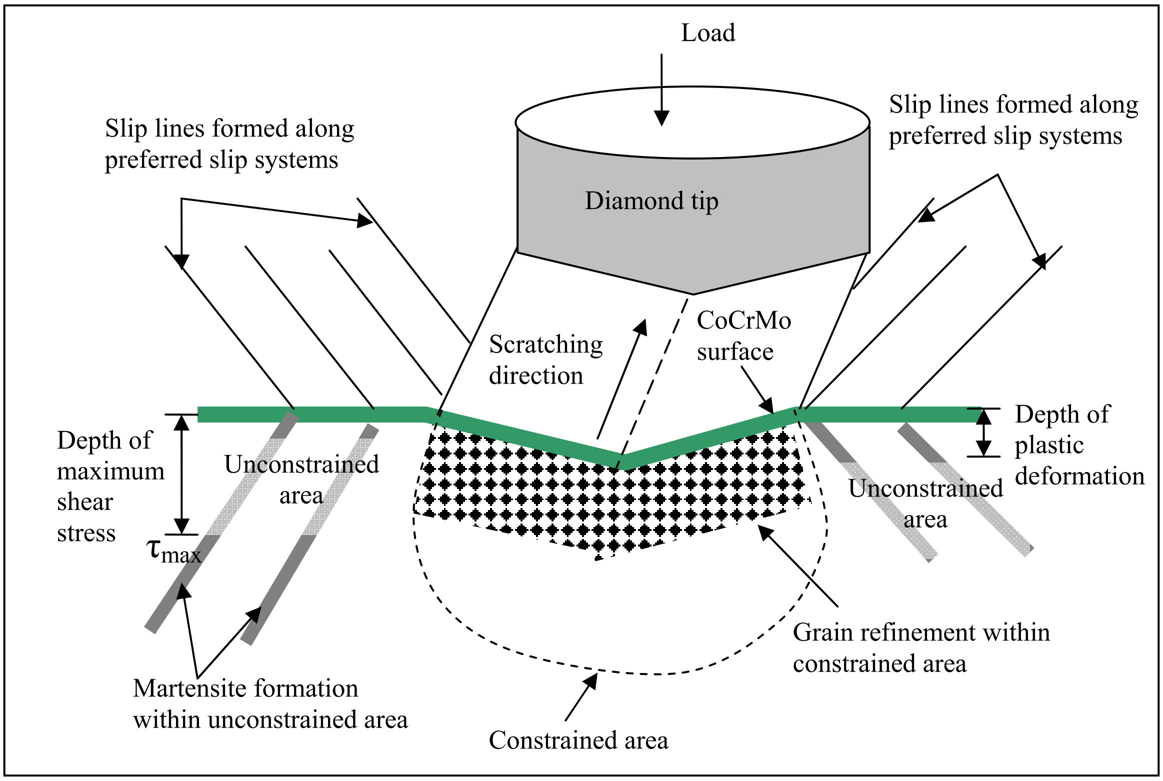

Figure 8.18: Schematic showing the surface/sub-surface microstructual features of a single scratch.

Plastic deformation of carbides has also been observed in the present study. Figure 8.19 shows the sub-surface of a multiple scratch ($\times 5$) made in air on a carbide, resulting in lip formation. This phenomenon may help explain the possible carbide detachment upon repeated wear processes which causes the release of third body hard particles.

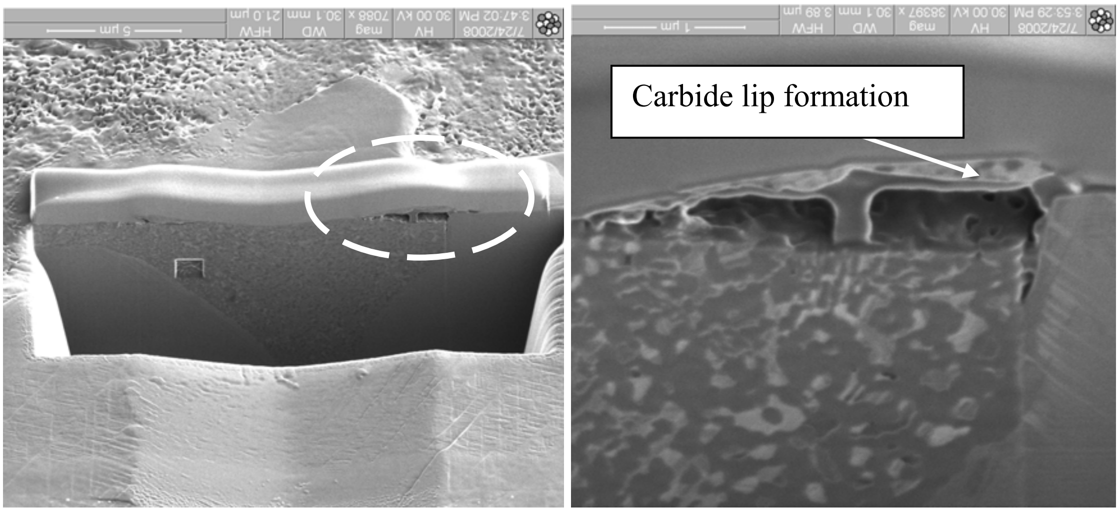

Figure 8.19: Multiple scratch made on carbide phase resulting in lip formation on carbide.

Linking the results obtained in the present chapter with wear scar profiles presented in Chapter 5-8, it may be suggested that although the abrasives used (SiC and Al_2O_3) are much softer than the diamond stylus used to scratch, they are of comparable hardness to the carbide phases present in the alloys and therefore can cause significant plastic deformation in the carbides [193] as well as the Co matrix. The material degradation under multiple abrasive wear may start with surface plastic deformation / local slip line formation. On repeated indentation/cutting action of the subsequent entrained abrasives, the material may be subject to work hardening (and sub-surface grain refinement) and a reduction in toughness. This may in turn cause material removal by fracture / fatigue. In addition, fatigue could also be one of the factors that contribute to the wear debris formation under micro-abrasion, although no phenomenological evidence has been found for fatigue under the microscopic observation of microabrasion wear scars.

8.2.2 Scratch-induced corrosion

In order to understand the effects of nano-scratching on the corrosion behaviour of the CoCrMo alloy and to compare the scratch-induced corrosion current levels generated under different test solutions, scratch-induced corrosion current was measured *in situ* during the single scratch test in both 0.9 wt.% NaCl and 25% BS test solutions. Figure 8.20 shows the typical examples for current caused by the scratching in both test solutions. The baseline current (I_{corr} - corrosion current under statically immersed condition) has been off-set for clarity.

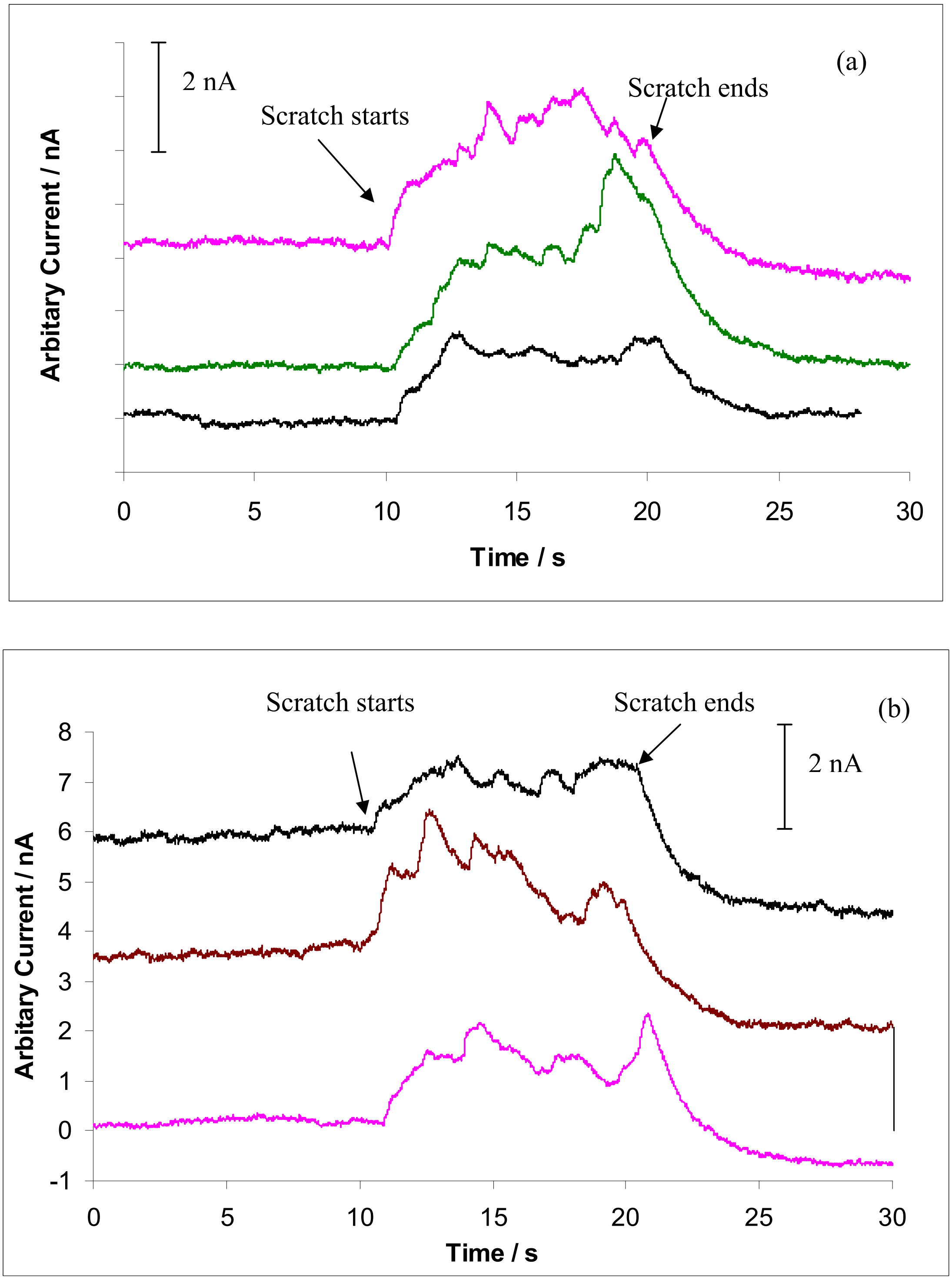

Figure 8.20: Current induced by three single scratch tests **(a)** 0.9 wt.% NaCl and **(b)** 25% BS at an applied OCP.

It can be seen from Figure 8.20 that there is an increase in the current level as the scratch starts corresponding to the rupture of the surface oxide film (depassivation). The gradual increase of current at the onset of the scratch may be due to the loading process (~1 s) of the diamond probe. The current level during scratching is generally 1-2 nA higher than the baseline current, although the current pattern (fluctuation) varies in different tests. As the scratch is completed, the current gradually recovers to its pre-scratching level indicating repassivation is taking place. The scratching speed employed in this study was 100 μm s^{-1} (which is the maximum speed allowed by the instrument). Such low scratching speed allows part of the damaged surface to repassivate as the diamond probe moves forward, leaving only a small portion of the bare surface (which is immediately behind the scratching probe) exposed during the scratching. It is likely that a higher scratching speed may result in higher scratch-induced current. No correlation has been found between the current pattern and the microstructure within the scratch. The total charge generated due to the scratch-induced current has been calculated using Faraday's law and the results plotted for different test solutions in Figure 8.21.

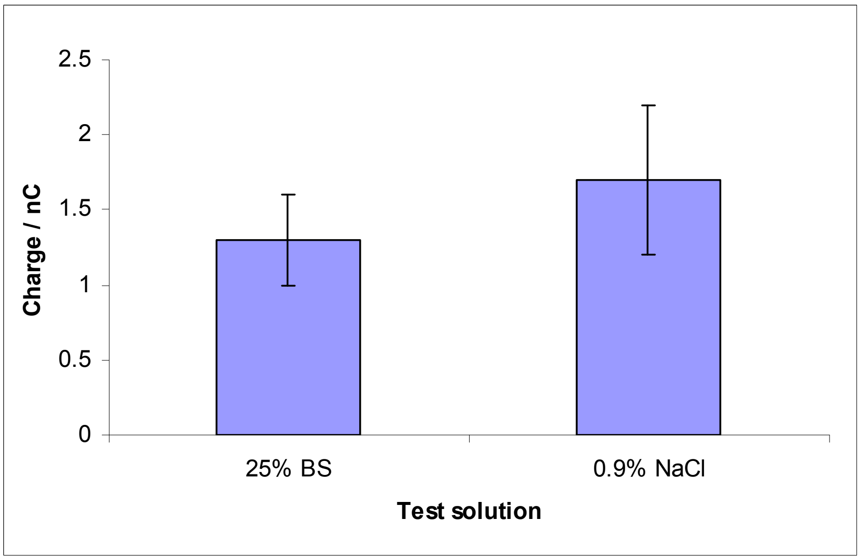

Figure 8.21: Charge generated in different test solutions during the course of scratching.

As is shown in Figure 8.21, the total amount of charge transferred during the scratching process (up to the point where indenter stopped moving, not including the repassivation period) is about 1.3×10^{-9} and 1.7×10^{-9} C for 25% BS and 0.9 wt.% NaCl, respectively. According to the XPS analysis in Chapter 4, the surface oxide film thickness is about 0.88 nm. Assuming the electrons transferred are only for the oxide reformation, the total repaired oxide film area is only about 15% and 20% of the total scratch area for scratches made in 25% BS and 0.9 wt.% NaCl, respectively (detailed calculation refer to [269]). Similar to the result seen for the microindent, this may suggest that the CoCrMo is only subject to partial surface oxide damage under the scratched area. Under plastic deformation, the local slip line formation causes the rupture of surface oxide film, which may in turn become the sites for repassivation and the associated current flow. Conversely, the majority of the oxide film (area in between slip lines and outside the scratch area) may remain intact. The relatively lower current seen for 25% BS may be due to a less damaged oxide film, which could be related to the surface lubrication effect of the adsorbed proteins or the charge transfer inhibition effect imposed by the adsorbed protein film.

8.3 Nanoindentation

To study the indentation type damage on the CoCrMo surface which may be caused by a single abrasive particle and to better understand the material deformation under a further reduced scale, nanoindentation was carried out on the electro-polished specimen surface in air and in a wet-cell. SEM analysis shows that the indent profile (size and morphology) was not influenced by the test conditions. Figure 8.22 shows the SEM and AFM images of the indent made in air at 200 mN applied load, loading rate 3 mN s^{-1}. Slip lines again emerged around the periphery of the indent. EBSD analysis (Figure 8.23) was performed on the deformed and undeformed region of the nanoindent (Region I and II in Figure 8.22), and again revealed that the strain induced phase transformation (FCC → HCP) has occurred during the indentation process.

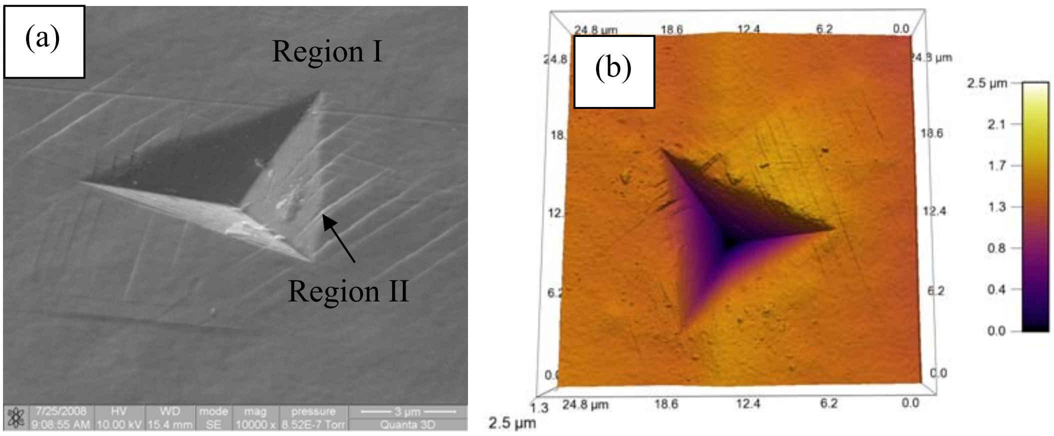

Figure 8.22: SEM (a) and AFM (b) image of a nanoindent made in air on a polished and etched specimen.

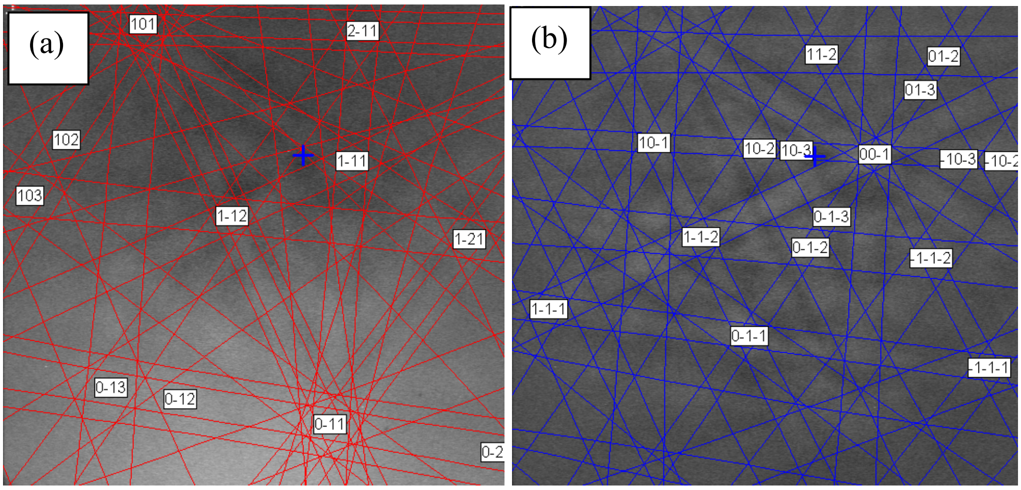

Figure 8.23: Kikuchi pattern showing the crystallography of (a) Region I (FCC) (b) Region II (HCP).

In contrast to the FIB analysis conducted for the micro-abrasion/scratch test samples, no apparent grain refinement has been seen under a single indentation from the ion beam image, (Figure 8.24), despite the plastic deformation induced by the indentation process.

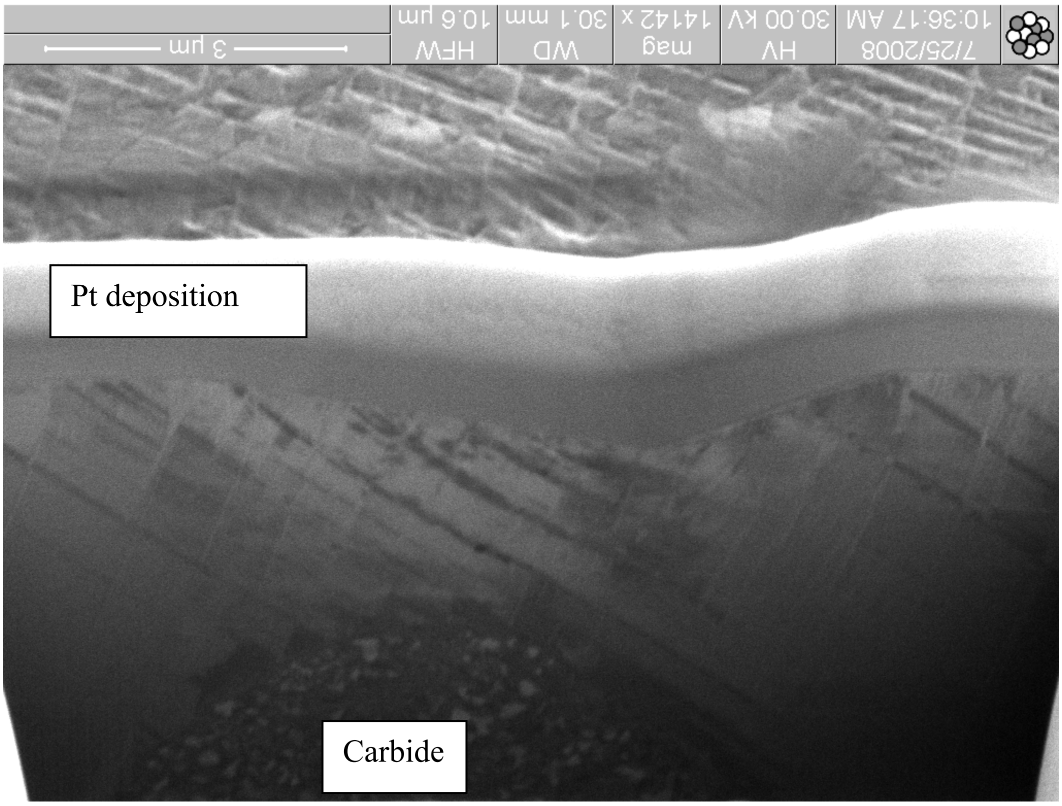

Figure 8.24: FIB image showing the sub-surface of a nano-indent.

Due to equipment limitations, the current noise (approximately in the order of 10^{-15} A) induced by the nano-indentation process cannot be detected above the background noise by the existing Gamry system in the laboratory. Improvements to signal/noise ratios are required.

8.4 Summary

This chapter has identified the micro-/nano-scale wear process that may occur at the hip joint surface *in vivo*, the tribo-corrosion behaviour of cast CoCrMo under micro- and nano-scales tribological tests simulating effects of a single abrasive have also been presented. This includes wet-cell microindentation, wet-cell nano-scratching and nanoindentation. Results show that these micro- and nano-scale tribological processes can produce significant surface deformation and sub-surface microstructual changes, which may be associated with the potential wear debris formation / metal ion release. The FIB analysis reveals the complexity of the sub-surface microstructual change resulted from single to multiple stress events, which may be related to origin of the sub-surface nano-crystalline structure seen for microabrasion wear scars and for retrieved MoM joints' sub-surfaces. This near surface nanostructure layer and phase transformation might offer better wear resistance through these inherent self-protecting mechanisms (i.e. increased hardness); conversely, it may become the precursors to debris ejection and enhanced ion-release into the CoCrMo joints. Both SEM and FIB analysis confirm that the surface and sub-surface microstructual changes resulting from the scratching are not dependent on the test environments. The current noise measurements show that surface damage caused by a micro-indentation/nano-scratch could cause detectable current flow as a result of partial surface oxide film damage. The results indicate that even surface damage caused by a single abrasive could potentially increase the metal ion release and the effect of multiple abrasives may be far more detrimental to the patient's health.

Chapter 9

General discussion

In Chapters 5 to 8, the effects of factors such as the test solution chemistry, abrasive size, single abrasive scratching, on the tribo-corrosion performance of cast CoCrMo have been discussed. This chapter overviews the entire data obtained from this study, and aims to link the effects of different parameters, and to discuss the mechanisms to provide an understanding of the tribo-corrosion behaviour of cast CoCrMo.

9.1 Wear mechanisms and factors influencing the wear scar morphology

9.1.1 Nature of abrasives

In the present study, relatively hard and large abrasives - SiC (4 μm) and Al_2O_3 (1 μm / 300 nm) in slurries have been entrained to abrade a cast CoCrMo alloy. The alloy contained chromium carbides (~ 25 μm) in a relatively soft Co-rich matrix. Although the hardness of SiC and Al_2O_3 is similar to that of the chromium carbides (~ 20 GPa), they still generated significant wear damage to the CoCrMo, including both the carbide phase and the Co matrix. Figures 9.1 and 9.2 give typical examples of the wear scars from tests using different sizes of abrasives. One distinct difference in wear scar profiles is the increase in the density of the indents (from rolling abrasion, see Figure 9.1) and of grooves (from grooving abrasion, see Figure 9.2) as the abrasive size decreases. Decreasing the size of the abrasives increases the number of abrasives entrained into the tribo-contact during testing.

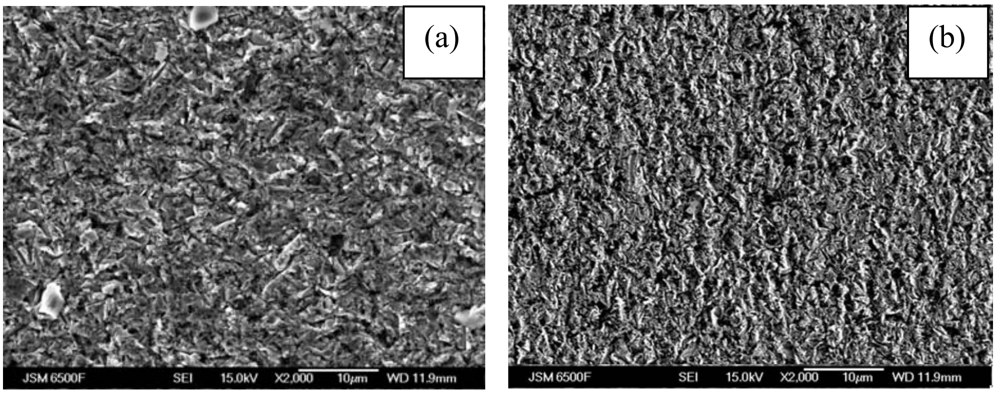

Figure 9.1: Wear scar produced by (a) 0.238 vol% SiC (b) 0.238 vol% 1 µm Al_2O_3 in 25% BS.

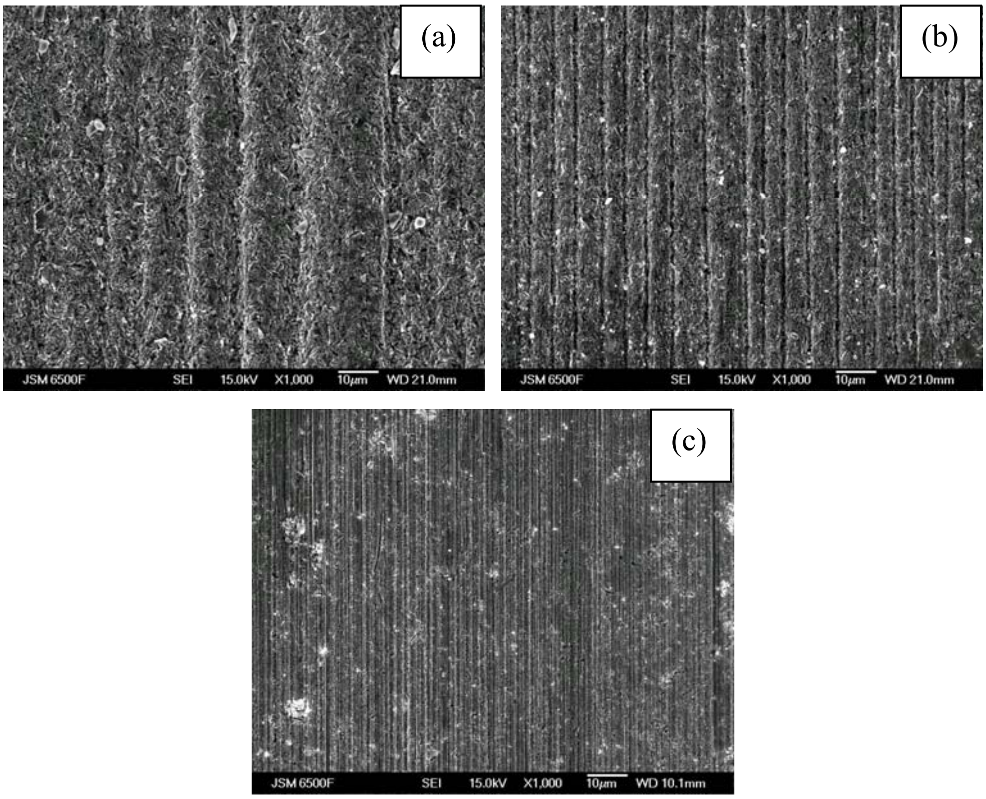

Figure 9.2: Wear scar produced by 0.072 vol% (a) SiC, (b) 1 µm Al_2O_3 and (c) 300 nm Al_2O_3 in 25% BS.

The entrainment of abrasive particles into the contact is approximately proportional to the grooving count within unit area of the wear scar. The total number of particles (N_p) within the interaction area between the ball and the specimen has been suggested by Adachi and Hutchings [270] and is given in Equation 9.1.

$$N_p = \frac{Acv}{\pi D_p^2} \qquad \text{......9.1}$$

Where A is the interaction area derived from the Hertzian elastic contact area and the size of the particle (m^2), c is a constant of proportionality, v is the volume fraction of abrasives within the slurry, and D_p is the diameter of the abrasive particle (m).

In the present study, the number of grooves (groove density) seen for the 1 µm Al_2O_3 wear scars is about 1.5 times that of the 4 µm SiC scars according to surface profilometry measurements. However, according to Equation 9.1, the groove density for the 1 µm Al_2O_3 abrasives is estimated to be twice that for SiC. It should to be noted that the friction between Al_2O_3 and CoCrMo may be different to SiC and CoCrMo. In addition, the differences in abrasive entrainment and metal removal within the scar could have complicated this simplistic model. For example, the slurries with different abrasives and concentrations have different viscosities, see Table 3.9. It has been suggested by Shipway et al. [185], that the number of particles entrained can be influenced by the slurry viscosity, which in turn is a function of abrasive volume fraction. The viscosity values of Al_2O_3 based slurries used in the present study are significantly lower (e.g., 4.87 mPa for 0.238 vol% Al_2O_3 in 25%BS, at 37 ºC and shear rate 24.5 s^{-1}) compared to those of SiC based slurries (e.g., 20.5 mPa for 0.238 vol% SiC in 25%BS, at 37 ºC and shear rate 24.5 s^{-1}) under similar conditions (detailed measurements can be found elsewhere [270]). The change in viscosity may be associated with the difference in electrostatic repulsion between particles within the slurry therefore influencing particle entrainment into the tribo-contact. The lower viscosity levels could result in a thinner slurry film formation between ball and test piece and therefore suppress particle entrainment [271], this could in turn lead to the reduced wear rates induced by Al_2O_3 slurries.

Reducing abrasive size is also associated with an increase in severity of contact (S_c) values for the same test conditions, see Figure 9.3, which helps to explain why smaller Al_2O_3 abrasives show a faster transition from rolling abrasion to grooving abrasion (as it crossed the S^* value earlier in Section 7.2).

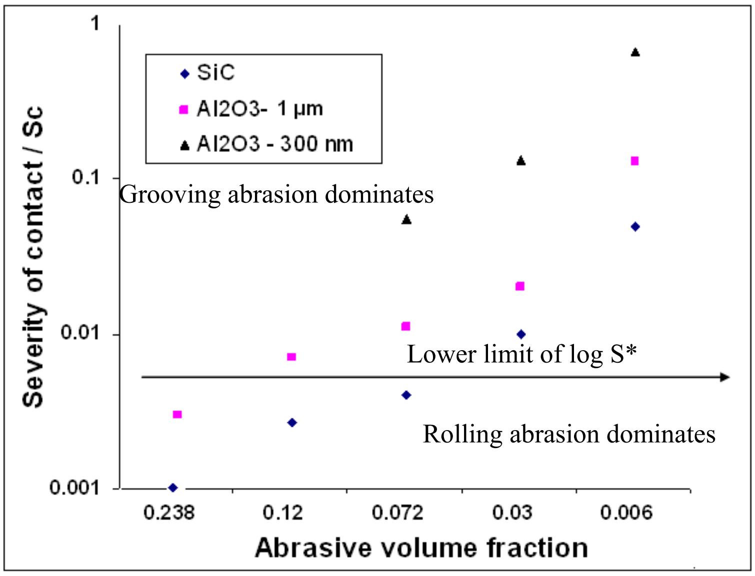

Figure 9.3: Change of severity of contact against abrasive volume fraction for different abrasives.

The SWRs, the wear-induced corrosion currents and the wear scar morphology vary significantly for each test abrasive as the abrasive volume fraction decreases. A quantitative analysis is presented in Table 9.1 using typical data obtained from tests with protein containing abrasive slurries at 0.072 vol% (wear scars without roll-ups) and 0.006 vol% (wear scar with roll-ups), respectively. Note that grooving abrasion is the dominant wear mechanism for the chosen test conditions in order to rule out the influence of different wear mechanisms.

Table 9.1: Comparison of specific wear rates (SWRs) and wear-induced current for protein containing test slurries at 0.072 vol% and 0.006 vol%.

	0.072 vol% (wear scar without roll-ups)				**0.006 vol% (wear scar with roll-ups)**			
Abrasives	**4 µm SiC**	**1 µm Al_2O_3**	**300 nm Al_2O_3**	**Sub-micron $BaSO_4$**	**4 µm SiC**	**1 µm Al_2O_3**	**300 nm Al_2O_3**	**Sub-micron $BaSO_4$**
SWRs /10^{-5} mm^3 N^{-1}m^{-1}	193 ± 7.4	98.6 ± 2.4	38.6 ± 14.6	6.8 ± 3.0	7.9 ± 3.0	16.8 ± 3.7	28.9 ± 16.9	3.6 ± 0.3
Current / µA	16.7± 0.8	16.8 ± 1.4	10.6 ± 1.4	2.5 ± 0.1	2.7± 0.1	3.3 ± 0.8	3.28 ± 0.8	1.9 ± 0.3

It can be seen from Table 9.1 that at 0.072 vol%, both SWRs and wear induced corrosion current decrease with decreasing abrasive size, with the relatively soft $BaSO_4$ giving the lowest SWRs and currents (5-10 times lower than those for 300 nm and 1 μm Al_2O_3. As the abrasive volume fraction drops to 0.006 vol%, the SWRs and current levels for each abrasive were appreciably lower than their corresponding values at 0.072 vol%. In addition, smaller Al_2O_3 abrasives give higher SWRs than the SiC abrasives and the SWR data shows significant increase in the scatter. This may be due to the increased difficulty in particle entrainment for larger SiC (less number of abrasives are introduced) and there is a lower test repeatability as the abrasive volume fraction decreases. Conversely, the current data appears to be less sensitive to changes of the SWRs.

9.1.2 Particle entrainment and particle motion within the tribo-contact

The abrasive entrainment process is governed by the fluid motion around the contact, until the particles are trapped in the entry region when the frictional forces cause their inevitable entrainment [272]. It has also been proposed that particle entrainment is a function of the properties of the test piece material (e.g., roughness) [273].

A mechanical model for particle motion in the microabrasion test has been proposed by Shipway [274], the behaviour of the particle has been mapped as a function of parameters such as applied load per particle, particle shape, hardness of the two surfaces and coefficient of sliding friction between the particle and the surface. When water is present, it lubricates the contact between the particle and the test piece, reducing deformation and consequently reduces the tendency of particles to roll (since the frictional toque required to maintain the rolling action is reduced) and indent the test piece [275]. Mishina et al. [276] claimed that the lubrication film formed by bovine serum albumin (BSA) solution is thicker but the friction coefficient between the contacts is higher. The higher friction was thought to be due to the higher viscosity of BSA solution which leads to higher shear force of the contact.

As is shown in Figures 7.1 (d2), 7.2 (e2), 7.3 (c2) and 7.4 (d), elongated protein conglomerates/roll-ups are seen on some of the worn surfaces with the largest dimensions ranging from a few hundred nanometres to a few microns. Wimmer *et al.* [46] also reported precipitates of denatured proteins which were adhered to the surfaces of both MoM simulator and retrieved joints. The shape of the precipitate varied widely from curved and compact to flat and elongated, with their sizes ranging from a few tens to a few hundred microns in size. The formation of these precipitates was believed to be due to tribochemical reactions that occur when surfaces in mechanical contact react with the interfacial medium and the environment. It was suggested that the mechanical and thermal activation of the surfaces due to friction leads to an increased flash temperature up to 80 ºC in conventional MoM bearing couples, which may decompose the proteins [46]. Figure 9.4 shows the 3-D morphology of the protein conglomerates in the centre regions of the wear scar (0.006vol% SiC in 25% BS). The conglomerates range from 1-10 μm in length and up to 0.5 μm in height and are consistent with the findings of Wimmer *et al.* [277]. The formation of these protein conglomerates could also be due to the thermally induced protein denaturation within the tribo-contact. These protein conglomerates are likely to reduce the abrasivity of the particles and reduce the damage to the CoCrMo surface. The proteins might form an organo-metallic complex with the metallic elements from the CoCrMo, hence it is likely that these protein-debris conglomerates polish the CoCrMo surface via a 'chemical-mechanical polishing' regime. Figure 9.5 further illustrates the schematic of the load sharing between protein conglomerates and the abrasives in the tribo-contact, which helps to understand the polishing effect seen in Figures 7.1 (d2), 7.2 (e2), 7.3 (c2) and 7.4 (d). The dimension of the protein conglomerates is normally greater than the theoretical film thickness (~ 200 nm for CoCrMo/ZrO_2 contact), and some times comparable in size with the entrained abrasives. It is likely the load applied is partially transmitted through the protein conglomerates and therefore the less abrasive wear damage results. Such precipitates are not visible at higher abrasive volume fraction, which could be due to the increased difficulty for the denatured protein to retain its intactness under a more severe abrasive damage.

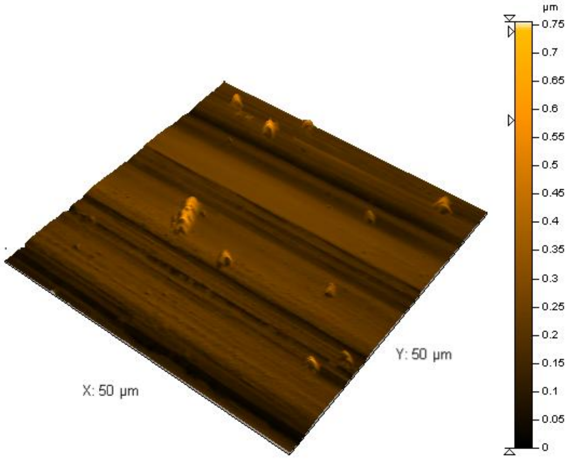

Figure 9.4: AFM image of the protein conglomerates found on worn CoCrMo in the present study after ball cratering test with 0.006vol% SiC in 25% BS.

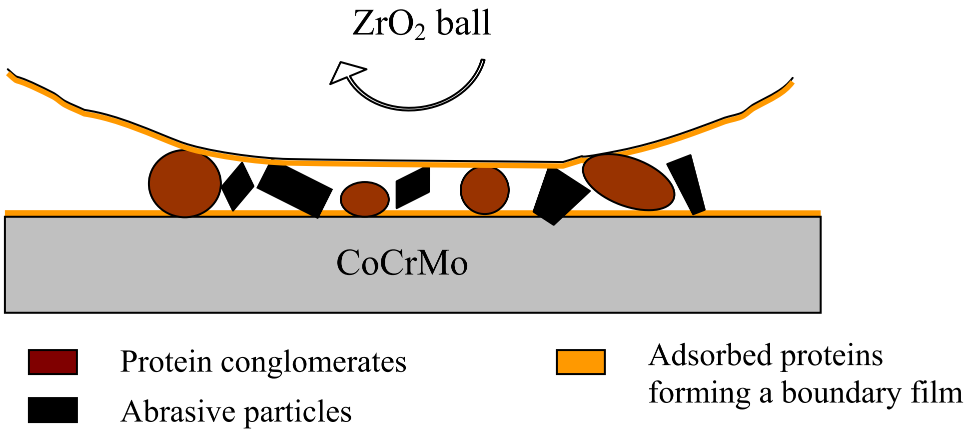

Figure 9.5: Schematic of the load sharing between protein conglomerates and abrasive particles within the tribo-contact during microabrasion.

In summary, the possible mechanisms generating the lower wear rates resulting from the protein containing solutions at low abrasion volume fractions (e.g., 0.006 vol%) are listed below:

- Adsorbed protein (possibly a few tens of nanometers) acting as tribo-layers under boundary lubrication.
- The denatured proteins mixed with metal debris forming conglomerates with micron and sub-micron dimension, which roll between the contacts, reducing asperity contact between surfaces and separate/polish the surfaces.
- The adsorption of proteins onto the abrasives may influence the contact mechanics /entrainment, and reduces the abrasivity of the particles.

9.1.3 Effect of particle hardness

Another distinct difference between the abrasives employed in this study is the hardness values. The hardness of $BaSO_4$ is significantly lower (20-fold less hard than the carbides) than that of SiC or Al_2O_3. The size of the particles employed in this study are all greater than the theoretical lubricant film thickness (e.g., ~ 200 nm for 25%BS solution before entrainment of abrasives), therefore the load applied is transmitted through particles rather than the lubricant film. Despite the difference in the wear scar morphology resulting from the different test conditions, the carbide phase in the alloy shows little wear resistance to SiC and Al_2O_3. $BaSO_4$ only caused limited wear damage to the softer Co-rich matrix (no visible damage seen on carbides) as is shown in chapter 7. The total wear loss resulted in 0.072 vol% $BaSO_4$/25% BS is almost 10-fold less than that of 1 μm Al_2O_3 under the same condition. Therefore it is reasonable to assume that *in vivo* the CoCrMo is more susceptible to wear in the presence of harder abrasive particles such as the broken carbides, but even relatively softer particles such as bone debris or bone cement may cause wear damage to the Co matrix and therefore may result in elevated metal-ion release.

One distinct feature shown by $BaSO_4$ wear scars was the formation of truncated grooves, which was not seen in any of the SiC or Al_2O_3 wear scars. This may be attributed to the sudden fracture of the relatively soft (or weakly bonded) $BaSO_4$ particles and/or agglomerates when they travel through the contact. The much smaller broken pieces could tumble through the contact without causing substantial wear damage to the CoCrMo surface. The truncated grooves may also be due to some of the soft particles loosing their sharp edges when travelling through the tribo-contact and therefore were not able to form continuous grooves. Figure 9.6 illustrates schematically the possible formation mechanism of the truncated grooves.

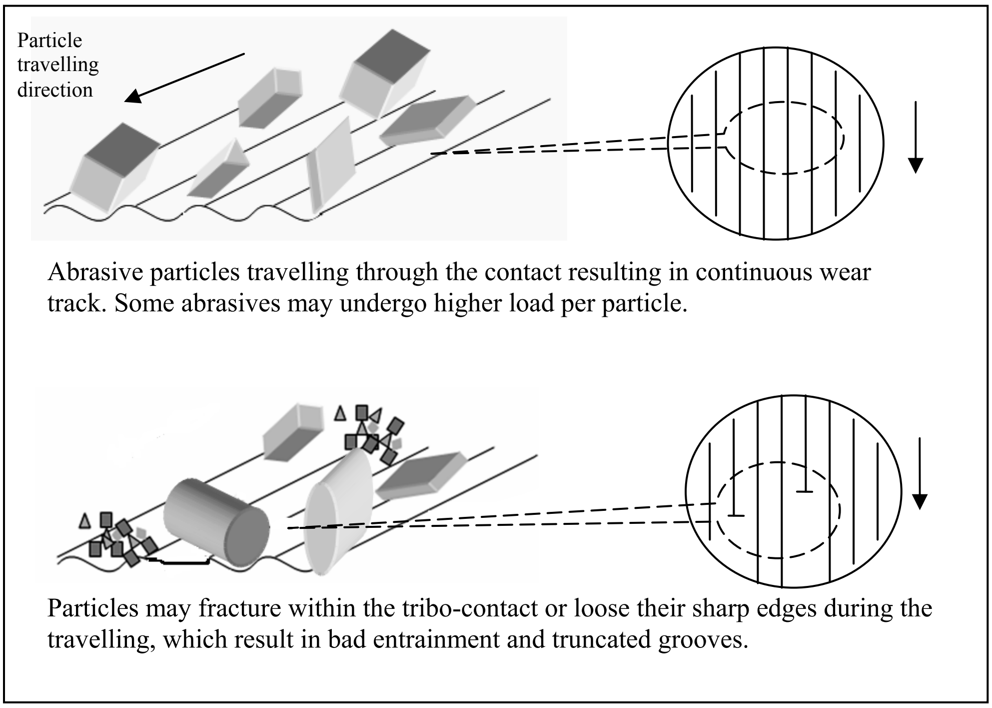

Abrasive particles travelling through the contact resulting in continuous wear track. Some abrasives may undergo higher load per particle.

Particles may fracture within the tribo-contact or loose their sharp edges during the travelling, which result in bad entrainment and truncated grooves.

Figure 9.6: Formation of the truncated grooves in BaSO$_4$ wear scars.

The influence of relatively soft third body particles on the wear of CoCrMo alloy surface has been studied for metal-on-polymer bearings using PMMA bone cement particles with and without BaSO$_4$, as well as bone debris [277]. In that study, surface damage of CoCrMo (scratch) has been observed for all test conditions, with PMMA + BaSO$_4$ giving the most scratches and bone particles giving the least surface damage. The findings in [243] are consistent with the results of the present study and it suggests that scratches may result when particles create stress concentrations large enough to cause plastic deformation of the articulating surface. It has been shown from Chapter 7 (Figure 7.15) that the SWRs resulted from BaSO$_4$ tests are even lower than the SWRs from the pure sliding condition (CoCrMo against CoCrMo).

9.2 Surface deformation and sub-surface microstructual change

9.2.1 Effects of multiple abrasives

The sub-surface microstructual change produced during micro-abrasion-corrosion with and without multiple abrasives has been presented in Figures 5.14-5.18. It is evident that the sub-surface nanocrystalline formation can be influenced by the presence of abrasives as well as the proteinaceous material present within BS solutions.

Figure 9.7 shows schematically the subsurface nanocrystalline (NC) layer evolution under the SC conditions (without abrasives) in 0.9 wt.% NaCl and 25% BS solutions, respectively. For both cases, it is the asperity contact between the ball and the specimen that causes surface damage (deformed junctions/lips, etc) on the CoCrMo, which subsequently forms the mechanically mixed nanocrystalline layer during repeated ploughing actions. This process is also likely to be accompanied by a strain induced phase transformation. In the presence of proteinaceous material, Figure 9.7 (b), wear debris from the CoCrMo mixes to form organo-metallic agglomerates that roll in between the bearing surfaces, reducing the abrasive damage. This results in a much more polished wear scar surface and thinner sub-surface NC layer (less than 1 μm).

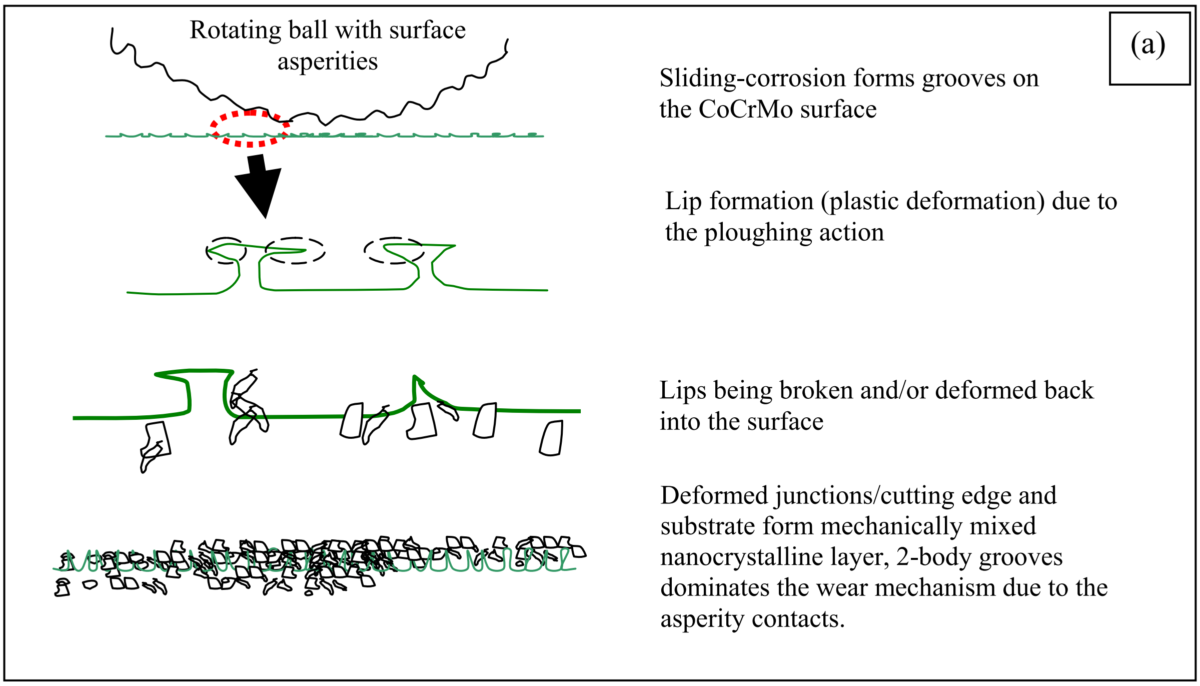

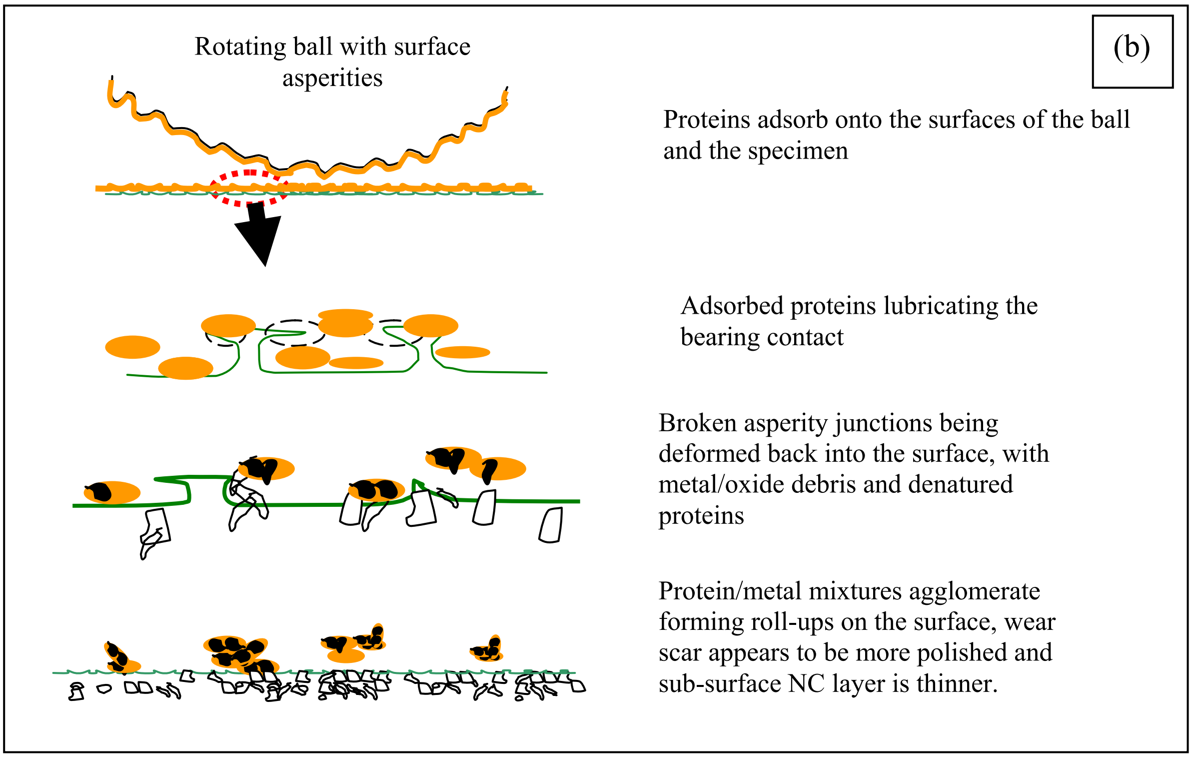

Figure 9.7: Schematic of the subsurface nanocrystalline layer formation during sliding-corrosion tests in (a) 0.9 wt.% NaCl and (b) 25% BS solutions.

Figure 9.8 shows, schematically, the NC layer formation mechanism for the AC test condition involving multiple abrasives in 0.9 wt.% NaCl and 25% BS, respectively. Repetitive formation and breaking of asperity junctions during micro-ploughing/micro-cutting processes caused by abrasives results in surface damage and wear debris formation. These debris and/or unbroken junctions can be further deformed and incorporated into the CoCrMo surface layers. The distinct sub-surface structure is likely to be a mixture of the wear debris, substrate metal, oxide layers, martensite from strain induced phase transformation and possibly the surrounding biological species forming a mechanically mixed layer [242].

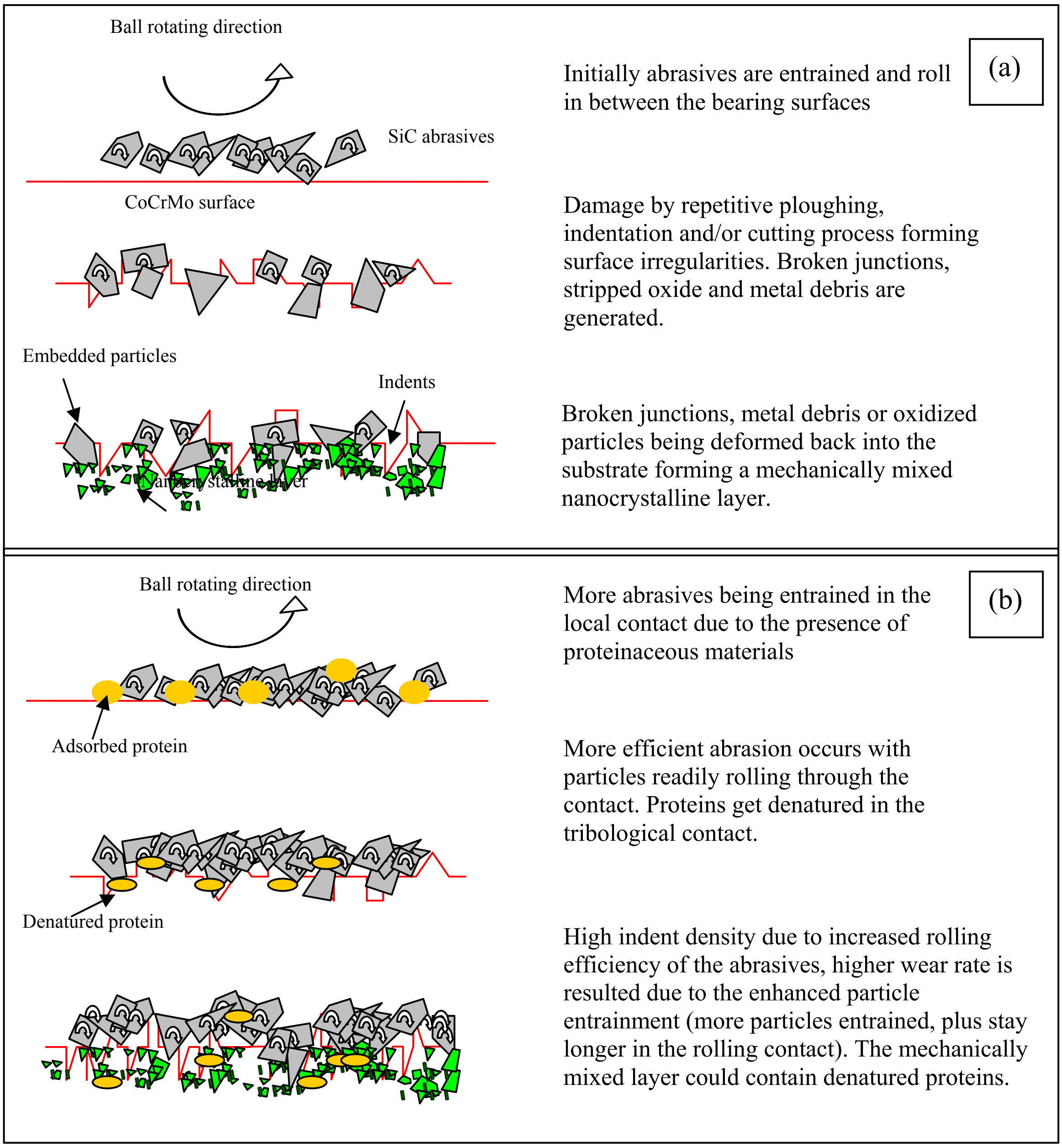

Initially abrasives are entrained and roll in between the bearing surfaces

Damage by repetitive ploughing, indentation and/or cutting process forming surface irregularities. Broken junctions, stripped oxide and metal debris are generated.

Broken junctions, metal debris or oxidized particles being deformed back into the substrate forming a mechanically mixed nanocrystalline layer.

More abrasives being entrained in the local contact due to the presence of proteinaceous materials

More efficient abrasion occurs with particles readily rolling through the contact. Proteins get denatured in the tribological contact.

High indent density due to increased rolling efficiency of the abrasives, higher wear rate is resulted due to the enhanced particle entrainment (more particles entrained, plus stay longer in the rolling contact). The mechanically mixed layer could contain denatured proteins.

Figure 9.8: Schematic of the subsurface nanocrystalline layer formation under abrasion-corrosion conditions in (a) 0.9 wt% NaCl and (b) 25% BS solutions.

As can be seen from Figure 9.7, for the SC condition the presence of protein helps the lubrication and reduces the surface damage, which in turn results in thinner sub-surface nanocrystalline layer. However, for AC conditions (Figures 9.8), the presence of protein enhances the particle entrainment and aggravates the surface wear and subsequently leads to a more pronounced sub-surface microstructual change.

9.2.2 Effects of a single abrasive

In order to investigate the effects of a single abrasive on the wear mechanism of CoCrMo, single and multiple scratch tests have been carried out and results were presented in Chapter 8. FIB analysis (Figures 8.15-8.17) shows that the extent of the sub-surface microstructual change resulted from multiple scratch is more significant than that for a single scratch. The sub-surface microstructual change expands to ~ 2 μm underneath the multiple-scratch as compared to ~ 1 μm for a single scratch. During scratching, the sub-surface stress field is skewed by frictional forces towards the leading edge. The magnitude and location of the maximum shear stress moves towards the surfaces as friction increases. For the present scratch test, the frictional force can be measured *in situ* during the test process (Figure 9.9 (a)), and the average coefficient of friction μ (Equation 9.2) was calculated to be ~ 0.15 for a single scratch. The effect of frictional force on the stress field distribution can be neglected in this case.

$$\mu = \frac{F}{N} \qquad \ldots\ldots 9.2$$

Where F is the frictional force measured in situ and N is the normal applied force (200 mN in this study).

From Table 9.1, it can be estimated that the maximum shear stress (~ 7.27 GPa, see Appendix A) during scratching is within 0- 0.93 μm depth sub-surface, which coincides with the depth of sub-surface microstructual changes. Such a shear stress level is well beyond the CoCrMo yield strength (~ 450 MPa) and will cause yielding of the material. It has also been found that multiple scratches (x 20) result in a larger extent of sub-surface microstructual change (i.e., grain refinement found down to ~ 2 μm sub-surface) compared to that of a single scratch (~1 μm sub-surface). The depth of sub-surface microstructual change was not proportional to the number of stress cycles, which may be because the grain refinement has strengthened the material, making it more resistant to the subsequent abrasive wear. The average grain size of as cast CoCrMo is about 400 μm, whereas the typical sub-surface grain size after scratching is of the order of 100 nm. According to the Hall-Petch relationship [266] (Equation 5.1), this reduction in the grain size could result in the yield strength of the material being higher than the theoretical maximum shear stress and hence make the material more resistant to the further mechanically induced plastic deformation. This may to a certain extent, explain the reduced wear rate of the CoCrMo hip implants as their service life increases. However, as the material hardens, it may be more prone to fracture and debris formation due to its reduced fracture toughness.

The understanding of the sub-surface stress field, the correlation between the sub-surface microstructual change and the local stress, as well as how the material responds under repeated stress can only be obtained with the aid of more sophisticated methods such as finite element analysis (FEA). FEA is beyond the scope of this study but will be discussed in the future work section of this thesis (Chapter 10).

From the SEM image of the multiple scratch, Figure 9.9 (b), it has also been found that the presence of the carbide phase resulted in a drop in the frictional force during the course of measurements. This may be associated to the surface roughness effect as the carbide phase in the specimen is lower than the matrix after etching. During the first scratch, the strain gauge connected to the frictional probe may experience a temporary drop of force when the probe goes though a valley. However, according to Figure 8.19, it is evident that the carbide phase has also been subjected to damage after multiple scratching cycles, indicating the carbide phase is levelled with the matrix. The lower frictional force found for the subsequent scratches (> 5 passes) could actually be due to the lower coefficient of friction from the carbide phase.

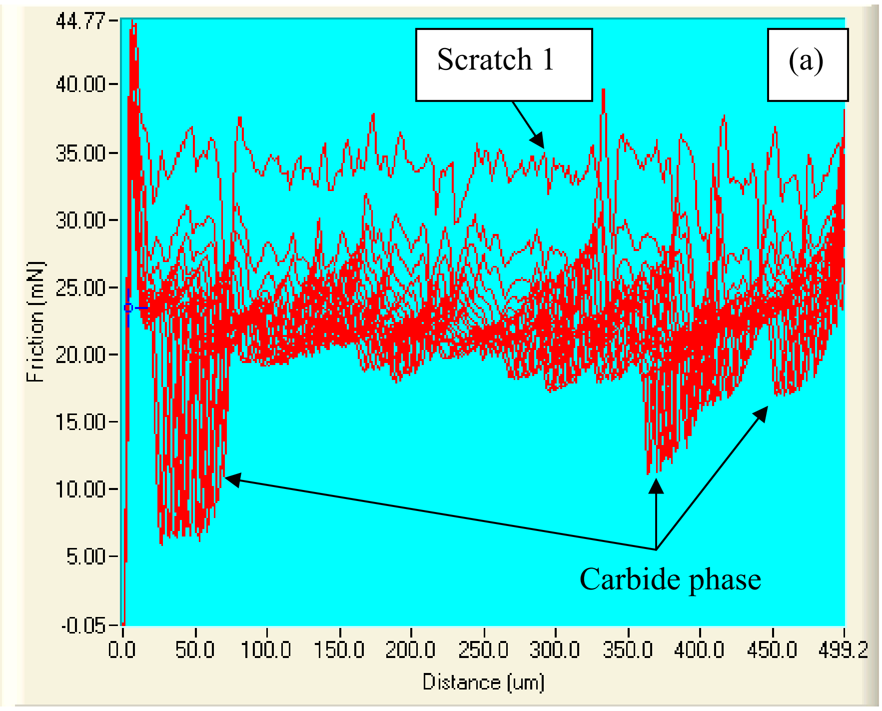

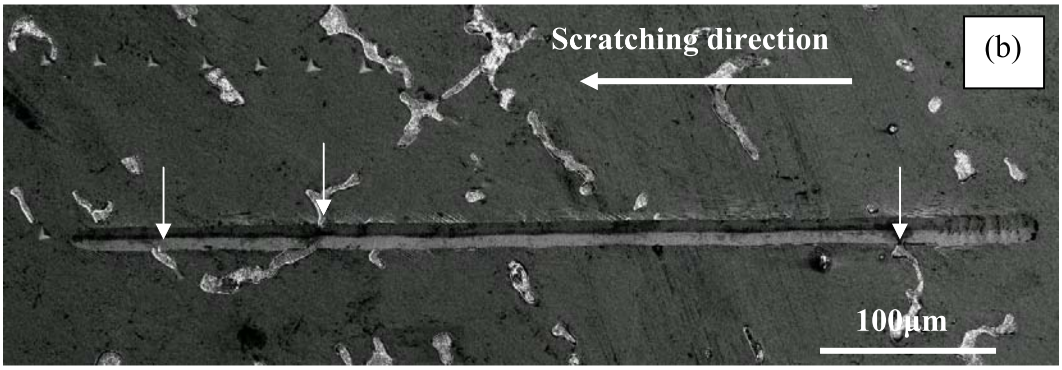

Figure 9.9: (a) Frictional force measured during multiple scratch test (×20) in air. (b) SEM image of the multiple-scratch showing the correlation between carbide phase (labelled by white arrows) and the drop in frictional force.

From Figure 9.9 (a) and Equation 9.2, μ is found to be highest during the first pass scratch and gradually decreases with repeated scratching action until it stabilizes at about 0.1. This reduction may be associated the removal of the surface roughness under repeated scratching action. Some other researchers [261] suggest that the HCP crystal structure that forms during plastic deformation contributes to a lower friction coefficient and this could result in lower wear rates than metals which possess a FCC structure. Unfortunately, the amount of HCP martensite formation caused by the plastic deformation process could not be quantified by the available equipment at University of Southampton, however, this issue has been raised in the Future Work section.

The sub-micron sized grains observed under single/multiple scratch sub-surface (Figures 8.15-8.17) may explain the origin of the sub-surface nanocrystallined structure seen for micro-abrasion wear scars in Section 5.3.2. These 100-500 nm grains undergo repeated shear stress by the entrained multiple abrasive particles, the increasing degree of plastic deformation leads to displacement in the lattice defects, which may form new grain boundaries and subsequently a highly textured microstructure with even smaller grain sizes (e.g., less than 100 nm). However, closer to the surface of the micro-abrasion wear scars, the high density of grains start to rotate, which destroys the texture and makes any distinct grain feature unidentifiable. In the present study the average grain size for the cast CoCr alloys was ~ 400 µm (but never precisely defined because of the dendritic structure [242]), whereas the grain refinement resulted from the heavy plastic deformation from micro-abrasion resulted in a grain size of as small as 100 nm. According to Hall-Petch relationship [118], the yield strength of the material can be increased by up to 60 fold due to a decrease in the grain size. Such an improvement in the mechanical property is certainly desirable in terms of the material wear resistance, however, the nanocrystalline structure might become the source of nano-sized wear debris formation [278] and disruption of the passive film on the surface.

In Chapter 8, slip line formation has been found along the periphery of scratches / indents at the nano-scale as a result of nano-scratching / nano-indentation action. For most of the wear scars produced by micro-abrasion-corrosion, slip lines are not visible as they have been removed due to the repeated wear damage. However, such events do take place at the nano-scale as highlighted in Figure 9.10. The slip line formation together with more severe surface damage caused by the surface asperity / abrasives may result in rupture of the surface oxide film, and exposure of bare alloy with possible strain induced phase transformation. This may lead to a localised change in the alloy corrosion potential and corrosion current and subsequently potential increase in the metal-ion release.

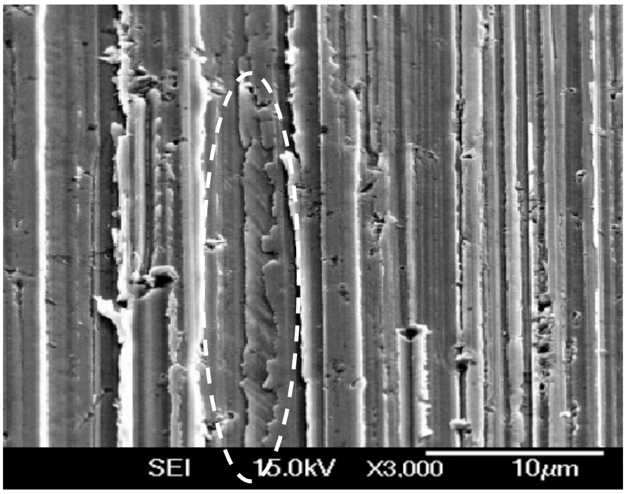

Figure 9.10: Slip lines (in dashed circle) seen in sliding-corrosion wear scar produced 0.9 wt.% NaCl.

Figure 9.11 schematically illustrates accelerated corrosion caused by the slip line formation. The oxide film formed on the CoCrMo surface ruptures under the shear stress / plastic deformation. The plastic deformation process may be accompanied by the local strain induced phase transformation, at the same time, sub-surface bare alloy is being exposed to the external corrosive environment. The exposed bare alloy is of different work function / corrosion potential to the oxide film and therefore a local micro-galvanic cell may form. This may subsequently lead to accelerated metal dissolution and metal-ion release.

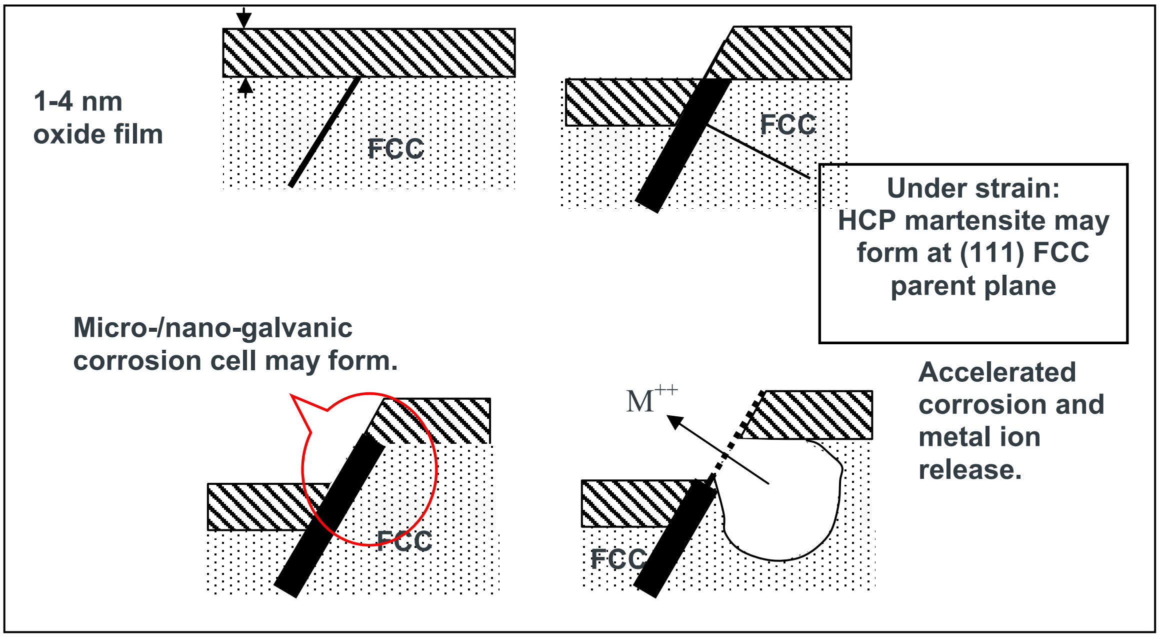

Figure 9.11: Slip line formation results in corrosion cell which induces accelerated corrosion and metal-ion release [278].

9.3 Mechanical depassivation and electrochemical repassivation

9.3.1 Electrochemical and mechanical interactions

As discussed in Section 9.1, the decrease in abrasive size results in different wear scar morphology. It was also discussed in Chapter 7 that a linear correlation is present between the mechanical processes and the electrochemical process for micro-abrasion-corrosion process involving 4 µm SiC and / or 1 µm Al_2O_3. Figure 9.12 combines the data for 4 µm SiC, 1 µm Al_2O_3 and 300 nm Al_2O_3 and replots the slopes ($\frac{\Delta Current}{\Delta SWR}$) from the electrochemical and mechanical interactions graphs (Figures 7.13 and 7.14). Only tests involving the grooving abrasion regime have been considered in this replot in order to rule out any influence due to change of wear mechanisms. It can be seen from Figure 9.12 that as the particle size increases, the slope decreases, which indicates that for the same volume of material removed, smaller abrasives generate higher corrosion currents. This can also be supported by Figure 9.1, where the wear scars generated by smaller abrasives featured more numerous and finer indents/grooves, hence for the same volume of material removal, a greater area of bare alloy has been generated which is exposed to the corrosive environment. For test solutions containing BS, the slopes are generally lower, which means the current generation during the same wear process has been impeded. The adsorption of proteins which may act as a charge transfer barrier may explain this phenomenon. The discussion above shows that the sensitivity of the tribo-corrosion response is dependent on the nature of the abrasives, test solution, as well as the wear mechanisms.

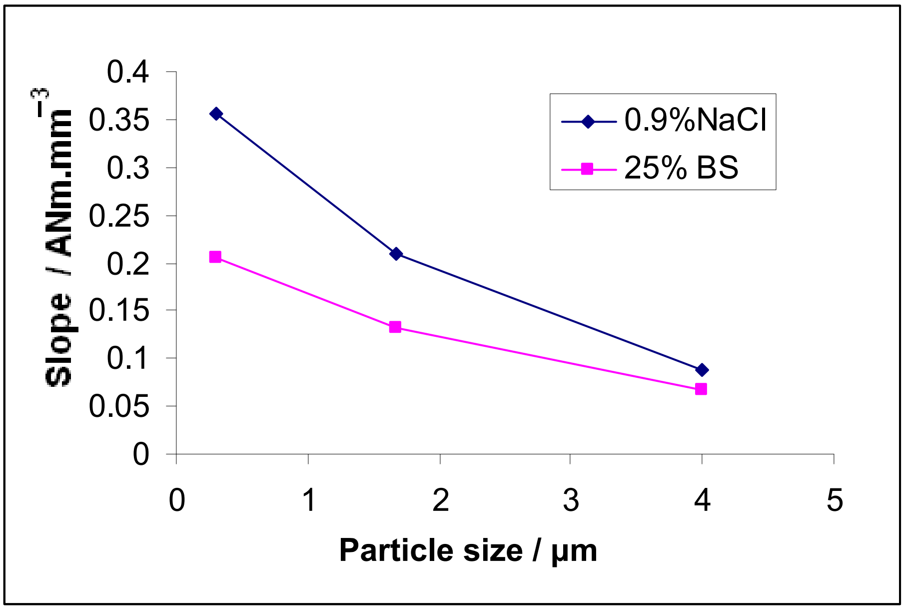

Figure 9.12: Relationship between $\frac{\Delta Current}{\Delta SWR}$ and the abrasive size under grooving abrasion regime.

9.3.2. The repassivation kinetics

When *in vivo*, the surface oxide (passive) film on CoCrMo hips joints may frequently be ruptured (depassivated) under mechanical loads and/or articulation due to abrasion and sliding wear. This will potentially expose the bare metal to the corrosive body fluids, and result in elevated metal-ion dissolution before repassivation is complete. The repassivation process will take place after the initial passive film damage due to the oxide (primarily Cr_2O_3) reformation, Equation 9.3, which will suppress the corrosion process. The rate of repassivation is dependent on the reaction kinetics.

$$4Cr^{3+} + 3O_2 + 12\ e^- = 2Cr_2O_3 \qquad ......9.3$$

The rate at which the repassivation (oxide film reformation) takes place is important as it is directly related to the amount of corrosion product (i.e., metal-ions) released into the surrounding environment. There have been a number of models developed for the depassivation and / or repassivation of metals/alloys in tribo-corrosion systems [161]. In the present study, the current noise immediately after the microabrasion-corrosion can be closely described by a second order exponential decay function (Equation 7.5).

For microabrasion carried out in all 0.238 vol% slurries, the repassivation time is dominated by the first time constant τ_1. The repassivation time appears to be similar (~1 s) as shown in Figure 9.13, and the presence of protein does not influence the repassivation kinetics significantly. This may be associated with the relatively high level of current noise resulting from both test solutions.

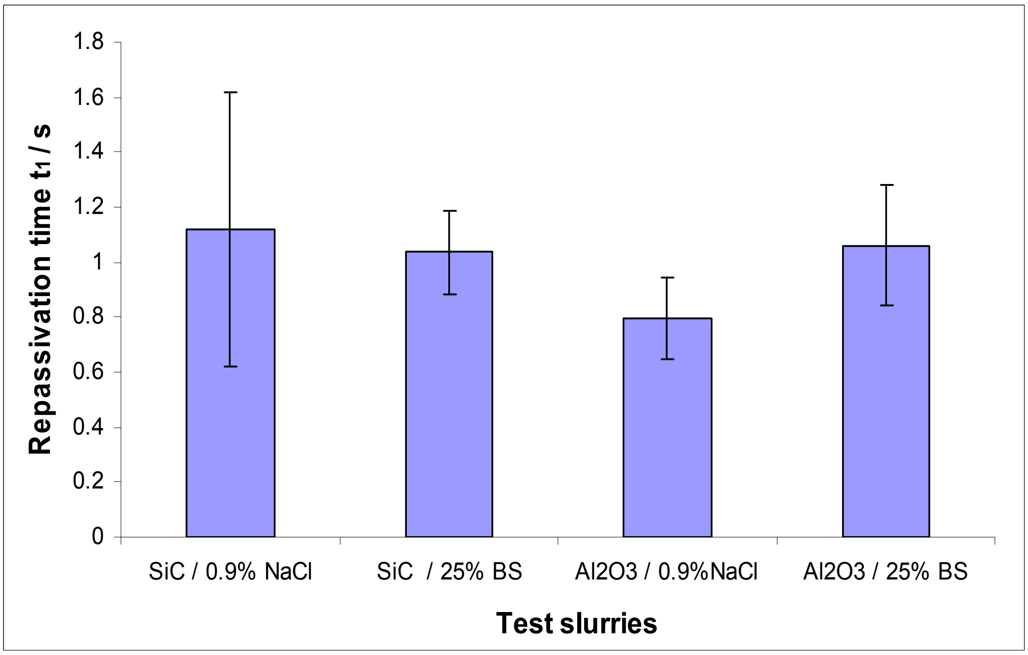

Figure 9.13: Repassivation time under different abrasion-corrosion conditions (0.238 vol% abrasive slurry).

The model proposed in the present study differs from that by Goldberg et al. [161] from a single scratch test (a first order exponential decay function, with time constant of about 30 ms). The second order exponential decay model may reflect the complexity of the damaged area resulting from the abrasion-corrosion tests and the potential hindrance of the oxygen diffusion due to the experimental conditions.

Firstly, the area of damage in the present study is much greater than the single scratch in [279]. Secondly, the plastically deformed surface/subsurface region may have a different corrosion potential [161] due to different severity of damage compared to the single scratch test in [280]. On the other hand, repassivation of the damaged surface is through reformation of the surface oxide film, and the repassivation kinetics are dependent on the diffusion process of the oxidizing agent (oxygen in this case) [161]. The damaged surface is still loaded against the ZrO_2 ball in the presence of abrasives while repassivation takes place, thus the oxygen diffusion process could be hindered in the present test setup. Therefore, the presence of the second time constant could be a collective result of both the extensively damaged/deformed scar area and the difficulty in oxygen diffusion within the contact area which limits the repassivation process.

The electrochemical process (wear-induced corrosion current) involved in microindentaion has been discussed in Chapter 8. From Figures 8.1 to 8.3, the repassivation process corresponding to the intense current peak after first loading/unloading cycle can be closely described by a 1st order exponential decay function (Equation 9.4) for tests done in 0.9 wt.% NaCl and 25% BS solution, Figure 9.14. The repassivation time constant τ can be extracted from the fitted curve and the value has been found to be greater for the 25% BS test than that for the 0.9 wt.% NaCl test, Figure 9.15. These results are comparable with [281], and the greater time constant found for 25% BS solution has been attributed to the protein physical barrier (charge inhibiting) effect, which slows down the charge transfer required for the repassivation process. In addition, on CoCrMo alloys, the diffusion limiting current for the oxygen reduction is lower, possibly because of a lower diffusion coefficient of oxygen in the serum and an inhibiting effect of proteins adsorbed on metal surface [161]. The gradual re-establishment of the electric double layer across the metal/electrolyte interface may also contribute to the slow recovery of current.

$$I = I_0 + A_1 \exp\left(-\frac{t - t_0}{\tau_1} \right) \qquad \text{……9.4}$$

Where I is the current generated during the indentation process, I_0 is the baseline current, A_1 is a current-related constant, τ_1 is the time constant.

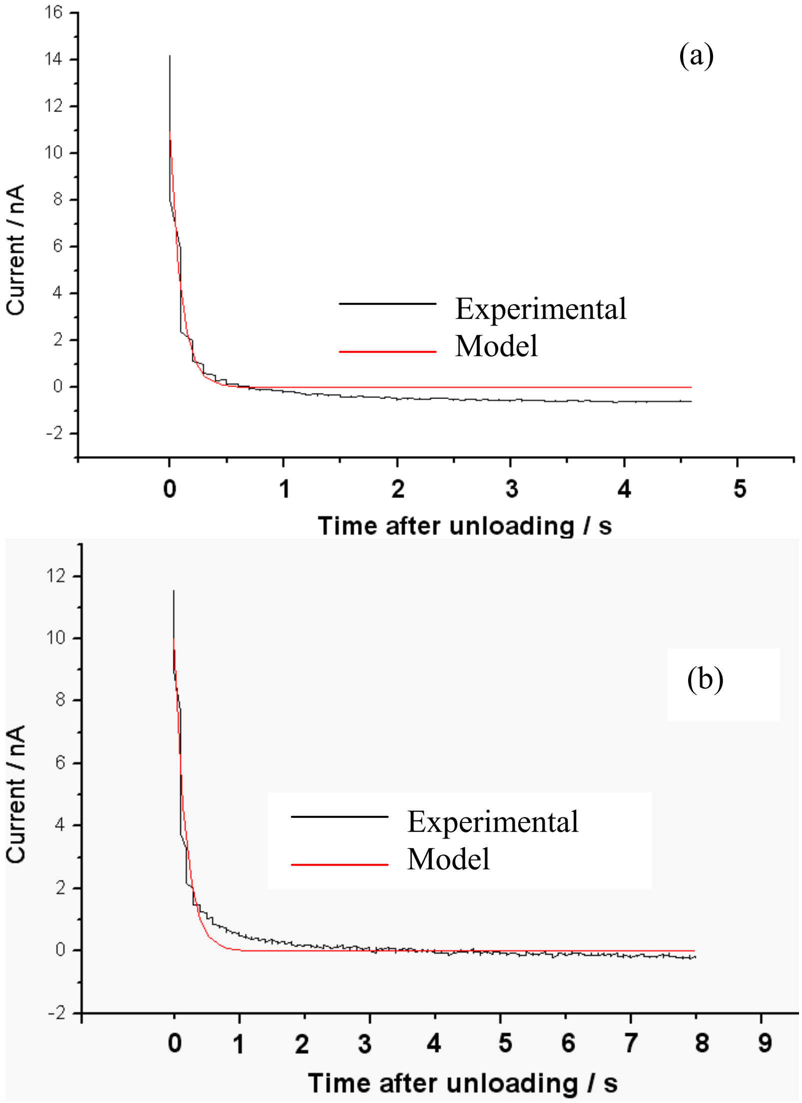

Figure 9.14: Curve fitting for the repassivation process after wet-cell microindentaion (1st unloading) (a) 0.9 wt.% NaCl and (b) 25% BS.

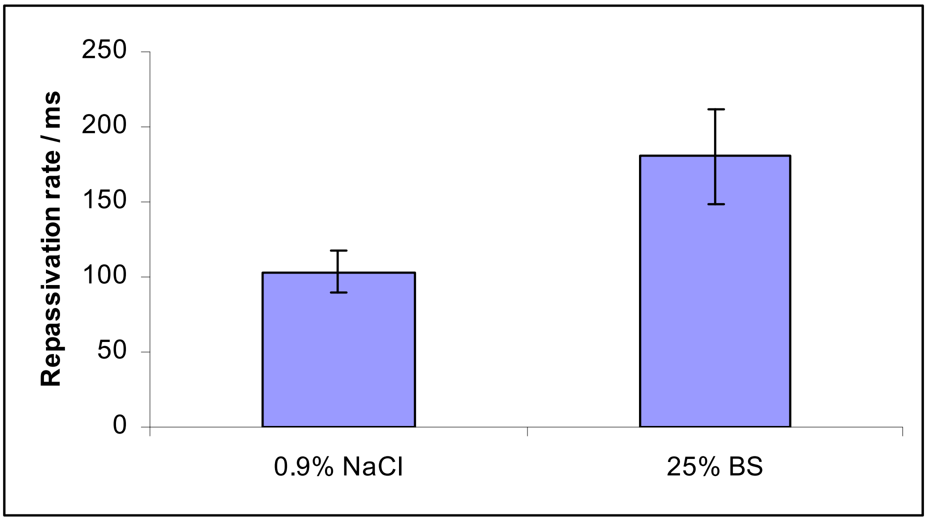

Figure 9.15: Repassivation time for 0.9 wt.% NaCl and 25% BS resulted from the first unloaded microindentaion.

The repassivation kinetics resulting from a single scratching test has been plotted in Figure 9.16, which follows a first order exponential decay (Equation 9.4), which agrees with [266]. The current repassivation takes a significantly longer time (~ 1.5 s), Figure 9.17, compared to the wet-cell micro-indentation results.

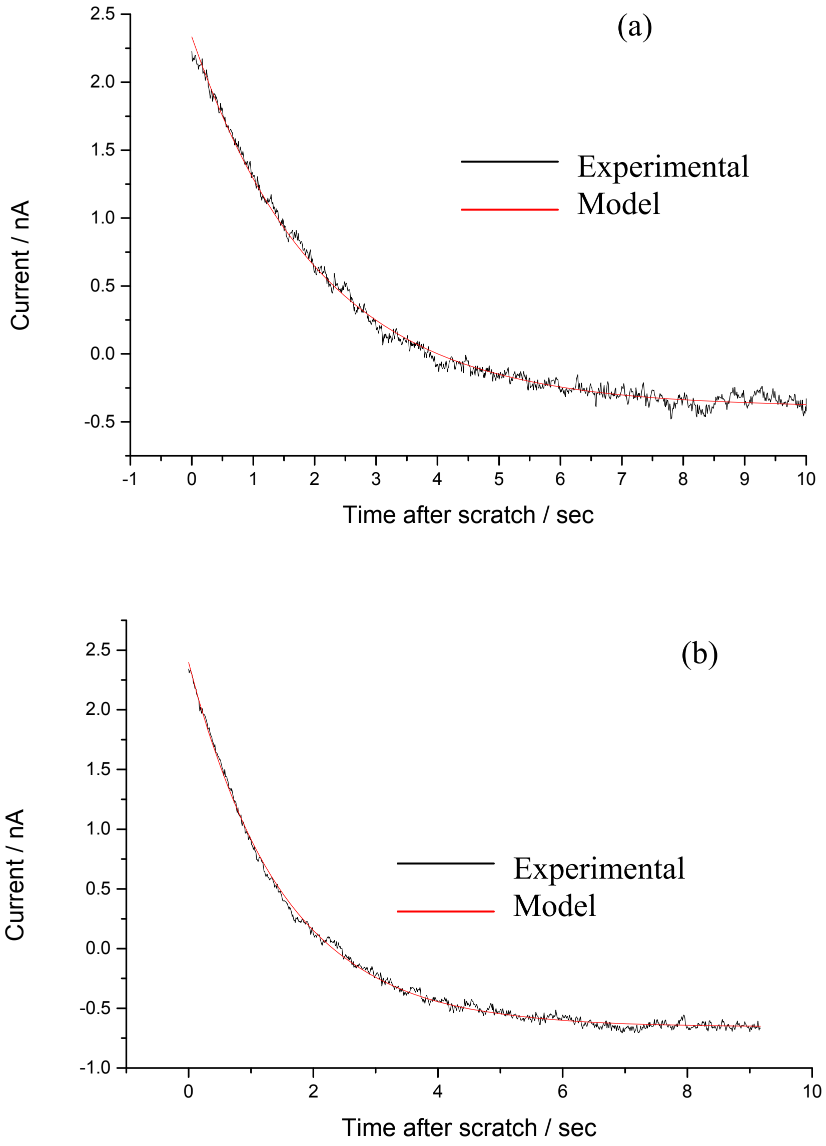

Figure 9.16: Curve fitting for the repassivation process after a single scratch (a) 0.9 wt.% NaCl and (b) 25% BS.

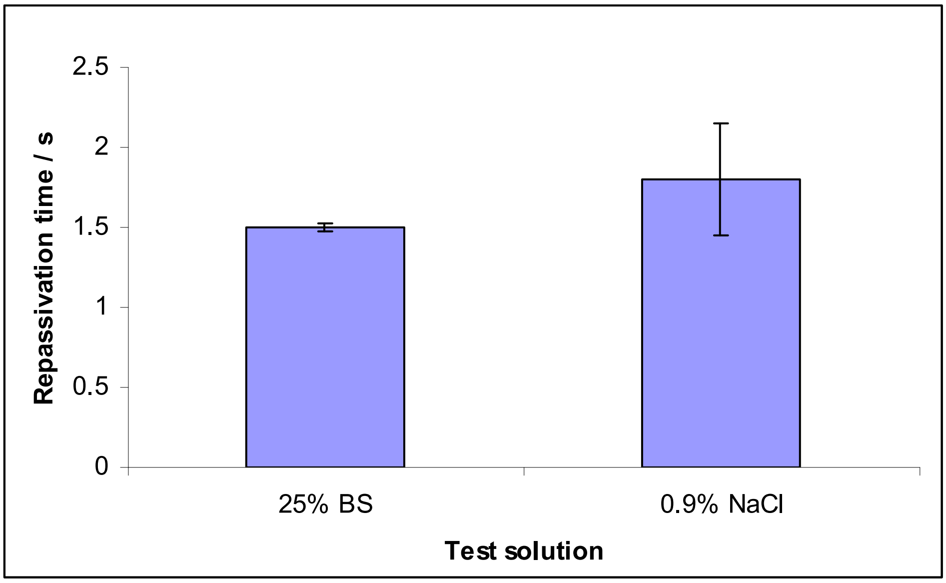

Figure 9.17: Repassivation time for 0.9 wt.% NaCl and 25% BS in single scratch tests.

From Figures 9.13, 9.15 and 9.17, it can be seen that the repassivation rate of the cast CoCrMo is very much dependent on the nature of the wear process, and the extent of the surface oxide damage and the rate at which the surface damage is taking place. In Sections 8.1.1 and 8.2.2, it has been estimated that the area of the damaged surface oxide resulted from single microindentation is about 6% and nano-scratching about 15-20% of the total worn area. These both indicate that the oxide film formed on the CoCrMo is quite tenacious and will largely remain intact even under severe plastic deformation. The damaged oxide area under micro-abrasion wear scar is hard to estimate due to the complexity of the wear morphology and the complicated test system/environment, however it can be assumed that only partial oxide film damage contribute to the wear-induced corrosion current even under a much more severe abrasion process.

9.4 Summary

This chapter compares the several aspects of the tribo-corrosion results obtained from various experimental conditions ranging from micro-abrasion-corrosion, wet-cell micro-indentation and nano-indentation/scratching. The mapping of the CoCrMo tribo-corrosion performance has been scaled down from multiple to single, hard to soft, micron to sub-micron abrasives. This is relevant to the MoM wear life cycle, i.e., running-in phase where hard carbides are mostly likely to be generated, and during the steady-state where relatively soft metal debris are more likely to be generated. It has been found that the surface wear damage and sub-surface microstructual change generated by microscopic tribological process can be closely related to the nano-scale material degradation process. The specific wear rates, and the interaction between mechanical and electrochemical processes have been found to be dependent on the abrasive size. The material depassivation/repassivation kinetics have been discussed for micro-abrasion-corrosion, wet-cell microindentation and nanoscratching, and the results show that the repassivation kinetics of the CoCrMo is dependent on the test conditions.

The process of tribo-corrosion results in both geometrical and micro-structural changes of the wearing material surface. These changes will influence the future contact conditions and wear generated in the same contact. At the nano-scale, the interaction of dislocation/stacking faults results in martensitic phase formation and a nano-crystalline structure formation. Microscopically, material is found to be plastically deformed by various mechanisms, some of which may lead to wear debris formation. At the macro-scale, wear scars generated by the tribo-corrosion process can be observed by the naked eye.

Both hard and relatively soft abrasives can cause surface damage and accelerated corrosion of CoCrMo; the wear processes by single/multiple abrasive particles could actually induce sub-surface grain refinement (work hardening) of CoCrMo, which will lead to a substantial increase in the material yield strength and hence potentially reduce the wear rates. Understanding of such nanocrystalline behaviour under abrasion processes could lead to improved material design in microstructure/composition of the cast CoCrMo.

Chapter 10

Conclusions and future work

10.1 Conclusions

This study has conducted a fundamental investigation into the abrasion-corrosion behaviour of cast CoCrMo alloy involving third body abrasive particles. Progress has been made towards establishing a fundamental understanding of cast CoCrMo tribo-corrosion performance and surface degradation mechanisms in abrasion-corrosion systems. The mechanical and electrochemical behaviour resulting from micro- to nano-scale tribological processes under various test environments, as well as their corresponding surface / sub-surface microstructures have been addressed. The link between multi-scale wear processes have been identified and discussed. Some important findings are summarized in the following sections.

10.1.1 Effects of test solution composition and presence of proteins on CoCrMo tribo-corrosion

- Under the static condition, the presence of proteinaceous material affects the corrosion rate of the cast CoCrMo. For 25% and 50% BS solutions, the corrosion rate was higher compared to those in the 0.9 wt.% NaCl or PBS solutions. The proteinaceous material influences the cathodic reaction kinetics, depending on the BS concentration, while the presence of phosphate has little effect on the cathodic reaction. The enhanced corrosion rate in BS solutions has been attributed to the formation of metal-protein complexes which can be transported away via diffusion under the static condition.

- Under both sliding-corrosion and abrasion-corrosion conditions, the presence of protein lowers the *in situ* electrochemical current noise, and also gives a generally lower current density compared to inorganic solutions. The adsorbed proteins could play a role in reducing the current by acting as a charge transport barrier during the wear-corrosion process.

- For abrasion-corrosion condition, the presence of proteins increased the corrosion-enhanced wear, more appropriately, protein-enhanced wear component in the synergy. This could be due to the adsorption of protein enhancing the particle entrainment as well as the rolling efficiency of the abrasives.

10.1.2 Effects of pH on cast CoCrMo tribo-corrosion

- A decrease in pH resulted in greater protein adsorption onto the CoCrMo surface under static conditions. The extent of the protein adsorption subsequently affects the tribo-corrosion (wear rates and wear-induced current noise levels) behaviour of the alloy under the dynamic conditions (sliding-corrosion and abrasion-corrosion).

- The presence of proteinaceous material on the CoCrMo surface is essential for improving surface separation between the MoM bearing surfaces and thereby minimizes wear-corrosion rates. Under a sliding-corrosion condition at pH 7.4, the presence of 50% bovine serum protein can effectively reduce the SWRs by 75%.

- Although acidic pH conditions representing infected joint environments may not significantly affect the wear rates of the MoM components, it has been shown to increase wear-induced corrosion current (by up to 67%) and therefore accelerated metal-ion release rates.

- Generation and entrainment of third body particles (from the wear debris) aggravate both the wear rate and metal-ion release. The co-existence of third body particles and acidic pH are especially detrimental to the abrasion-corrosion performance of the CoCrMo alloy by significantly increasing both wear and corrosion. Therefore, the presence of infection and hard particles could both impose potential risk to the patients’ health and potentially shorten the life span of the MoM orthopaedic implants.

10.1.3 Effects of abrasive size, concentration and hardness on cast CoCrMo tribo-corrosion

- A linear correlation was found between the specific wear rates and the wear-induced corrosion current for abrasives with different sizes (e.g., 1 μm and 4 μm) and at different volume fractions. Reducing the size of the particles was found to be more effective in producing a wear-induced corrosion current for the same amount of material removal, which implies a potentially higher metal ion release rate.

- The presence of protein encourages a negative synergy especially at low abrasive volume fractions by forming protein/metal debris conglomerates that lubricate/separate the surfaces. This is beneficial to the wear-corrosion performance of the CoCrMo as it could significantly reduce the wear and subsequently the wear-induced corrosion.

- Even small (300 nm Al_2O_3) and relatively soft ($BaSO_4$) particles can induce significant material deterioration by means of mechanical damage and corrosion, although the test reproducibility decreases with smaller and softer particles being used. The specific wear rates with $BaSO_4$ abrasives approaches the clinical wear rate levels, which helps to underline the possible effects of sub-micron sized soft particles that are likely to be seen *in vivo.*

10.1.4 Multi-scale wear-corrosion mechanisms and material science

- Micro- and nano-scale tribological processes simulating surface damage caused by a single abrasive can produce significant surface/sub-surface material deformation, which may be associated with the potential wear debris formation / metal-ion release. These micro-/nano-scale wear mechanisms include: local slip line formation, strain induced phase transformation (HCP martensite formation), smearing/fracture of Co matrix material, deformation/detachment of carbides, lipping, matrix material detachment (debris formation), formation of sub-micron scale structure along periphery of the scratch, formation of nano-crystalline structure/twinning/martensite sub-surface.

- The process of tribo-corrosion due to single/multiple abrasives resulting in both geometrical and micro-structural changes of the wearing material surface. These changes will influence the future contact conditions and wear generated in the same contact. At the nano-scale, the interaction of atoms/stacking faults result in martensitic phase formation and / or twinning, which subsequently contribute to the sub-surface nano-crystalline structure formation. Microscopically, material is found to be plastically deformed by various mechanisms, some of which may lead to wear debris formation. At the macro-scale, wear scars generated by the tribo-corrosion process can be observed by the naked eyes.

- FIB analysis shows that the sub-surface microstructual change resulting from single and multiple stress events have induced strain induced phase transformation and grain refinement; both phenomena could contribute to the origin of the sub-surface nano-crystalline structure seen for microabrasion wear scars and that seen for retrieved implants. Various mechanisms have been suggested to contribute to the sub-surface grain refinement and the strengthening of CoCrMo under tribological processes. The major mechanisms include: formation of planar dislocation arrays, twinning, and strain induced martensite (HCP) formation.

- The current noise measurements show that surface damage caused by a micro-indentation / nano-scratch could still cause detectable (order of nA) current flow. This indicates that the accumulated current flow due to damage by multiple abrasives could result in significant increase in the corrosion level and metal-ion release.

- Although a single abrasive is more likely to cause surface plastic deformation rather than material removal, the accumulated effect of multiple abrasives may cause repeated damage to the surface and work hardening of the alloy. This in turn could give rise to significant material removal through cutting/fracture/fatigue, all of which could contribute to the wear debris formation.

10.1.5 Summary

In this study, the tribo-corrosion performance of cast CoCrMo alloy, more particularly, the abrasion-corrosion of the alloy in the presence of third body particles have been studied extensively. It has been found that the wear-corrosion mechanism of the cast CoCrMo is multi-factorial; it not only depends on the local biological environments, the patient's health, but also the nature of the particles that are involved in the tribo-corrosion process.

For the first time, studies on the effects of single/multiple abrasive particles on cast CoCrMo have been conducted employing wet-cell micro-/nano-indentation, nano-scratching and micro-abrasion-corrosion, incorporating electrochemical cells. A link between single abrasive wear and wear induced by multiple abrasives has been established, which provided an insight into the evolution of the material surface wear pattern, sub-surface microstructual change, as well as the possible origin of wear debris formation. The sub-surface grain refinement due to a single scratch was found to occur at a depth that is conincident with the theoretical value. Various mechanisms (grain refinement, twinning, strain-induced phase transformation) have been suggested to contribute to the material strengthening (hardness / yield strength), which may improve the material wear resistance.

This study has revealed the inter-relation between the local hip joint environments on the tribo-corrosion behaviours of cast CoCrMo, therefore providing some important implications as to the MoM components' performance *in vivo* (e.g., generation of wear debris / accelerated metal-ion release, etc) and its potential effects on the patient's health. Mechanistic commonality between the wear seen from the retrieved joints and the present laboratory studies has been indentified in this study, leading to the establishment of a series of techniques that may be related to the clinical MoM abrasion-corrosion process. The findings of this study may give some future directions as to the improvements of MoM component design, modelling as well as material selection, some of which will be discussed in the Future work section.

10.2 Future work

10.2.1 Further tribological testing and analysis

From Chapter 9, it has been suggested that the surface wear process may induce sub-surface grain refinement as a result of work hardening. This process is accompanied by various mechanisms such as strain induced phase transformation. The material surface may be strengthened and become more wear resistant due to this strengthening process. However, such a work hardening process may result in the reduction of material ductility and make it more prone to fracture due to the lower fracture toughness. The sub-surface nano-crystalline layer is also thought to be a potential source of the nano-sized wear debris.

More extensive experimental work may be carried out in the future to look at the potential factors that may influence the sub-surface microstructure, especially the extent of grain refinement. For example, micro-abrasion-corrosion can be conducted at different sliding distances and/or different applied load; scratching tests at different applied load and scratch cycles may also be conducted. The sub-surface of the worn samples can be examined to using FIB / TEM to provide greater detail of the sub-surface microstructure. These experiments can also be extended to the sub-surface examination of MoM components obtained from simulator tests and retrievals. The correlation between test parameters and the extent of sub-surface microstructual change is yet to be established. The cross comparison of CoCrMo sub-surface obtained from different sources may provide a more in-depth understanding of the role and function of the sub-surface micro-structural change. The question of whether the strengthening of material by mechanical means can outweigh the side effects of nano-sized debris generation needs to be answered. Such information may provide important indications to the MoM performance *in vivo* and provide future directions as to improvements in the MoM design and manufacturing.

In addition, multi-directional motion of the MoM components *in vivo* may give rise to different wear patterns and wear mechanisms on the MoM surfaces/sub-surface as compared to the unidirectional damage caused by the present laboratory tests. Multi-directional wear tests may be considered in the future, where cross-shear motion of diamond probe in the nano-scratch instrument may be explored. Further collaboration with MicroMaterials Ltd is needed in terms of the nanoindenter software upgrade and hardware modification in order for the nanoindenter to achieve such functionality.

10.2.2 Effects of martensite formation

As discussed in Chapter 9, the severe local plastic deformation is normally accompanied by strain induced phase transformation (FCC → HCP). Although for low carbon wrought CoCrMo, the HCP phase gave rise to a lower coefficient of friction and this could result in lower wear rate than metals which originally possess the FCC structure [40], the validity of this statement for high carbon cast CoCrMo is still subject to further verification. On the other hand, the HCP phase is less ductile than the FCC phase and may cause cracking of the material surface under high stress, therefore the effects of HCP phase need to be studied very carefully. Systemic tribological testing with in-situ friction measurements (such as scratching, pin-on-disc) need to be conducted under controlled conditions in order to find out the correlation between the test parameters (applied load, stress cycles etc) and the degree of phase transformation. Greater understanding also needs to be established in terms of the potential surface damage / debris formation that may be caused by such a phase transformation.

10.2.3 Advanced microstructual analysis using TEM/EBSD

A detailed knowledge of the microstructure of mechanically deformed cast CoCrMo is essential for understanding its mechanical properties and tribological behaviour. The main technique available to researchers for qualitative and quantitative analysis of deformation substructure in metals is transmission electron microscopy (TEM) and this has been successfully used for the detailed characterization of microstructures in Co based alloys. Buscher *et al.*[253] have studied the sub-surface microstructure of retrieved worn MoM joint surfaces using TEM. Their technique involves cross-sectional imaging of the worn surface and different microstructures emerging as a function of depth have been observed. A similar technique can be applied in the future to look at the detailed sub-surface grain structure of the worn cast CoCrMo from laboratory studies. The dislocation pattern, stacking faults, cell formation and grain refinement can be observed at a greater resolution.

In addition, as TEM is only capable of studying small areas of a sample, high-resolution electron backscattered diffraction (EBSD) can be employed to allow complete characterization of dislocation cell and sub-grain structure. EBSD is capable of obtaining orientation data of a specific sample area and larger areas of the worn surface may be examined. Local EBSD mapping may find out the strain induced phase transformation but it requests a flat/smooth sample surface. By polishing the worn surface electrochemically (removal the surface roughness), the wear-induced strain in the sub-surface can be retained while not imposing further mechanical work to the material surface.

10.2.4 Finite element modelling and analysis

According to the simplified Herzian analysis conducted in Section 8.2, compressive stress is present right beneath the scratch with the maximum shear stress at the depth of ~ 1.2 μm. This seems to coincide to the depth of the sub-surface NC layer formation. However, to determine the exact relationship between local stress field and the sub-surface microstructual change during a tribological event, finite element (FE) modelling and analysis could be carried out.

FE modelling of the sub-surface stress field developed under static/dynamic mode for scratch and indentation conditions as well as the multiple dynamic wear process – microabrasion may be performed in the future. The modelling results may be related to the FIB observations. The gradient strain field may provide an indication about the step-wise microstructual change seen for the material sub-surface both *in vivo* and *in vitro*.

Additionally, the finite element method can be used to investigate the resistance of the CoCrMo alloy bearing surface to plastic deformation due to various entrapped hard (e.g., carbide) and soft (e.g, bone) debris in the MoM contact. Mirghany and Jin [19] modelled CoCrMo deformation caused by rigid particles (ZrO_2, CoCrMo) in a metal-on-polymer joint using a simple axisymmetric micro-contact mechanics model, where the deformation of both the wear particle and the bearing surfaces was modelled and was treated as elastic-plastic. However, the effects of hard and soft particles on the deformation and scratch resistance of cast CoCrMo in a metal/metal contact is still lacking.

For an accurate FE modelling, one needs to establish a 3D model with proper material property input. For multiphase materials such as cast CoCrMo (Co-rich matrix incorporating hard carbide phase), an accurate model needs to take into consideration of the effect of the 2nd phase, their size, geometry and distribution. A high power computer tomography (synchrotron source) scan will be necessary for a high density alloy such as cast CoCrMo. Once the distribution of carbides is confirmed, one may be able to incorporate the 2nd phase into the FE model.

10.2.5 Corrosion monitoring

In Section 9.1 to 9.3, slip lines have been found on the damaged surface during the scratch / indentation tests, which may render the material being more susceptible to corrosion and therefore a higher metal-ion release level. Scanning electrochemistry workstation with high resolution capability by using a Scanning Kelvin Probe (SKP) may be employed for a local micro-/nano-scale surface damage scan (e.g., wear scar, scratches, carbides/matrix interface, slip lines). The technique operates using a vibrating capacitance probe, and through a swept backing potential, the work function difference is measured between the scanning probe reference tip and sample surface. The work function can be directly correlated to the surface condition. A corrosion current mapping which may indicate the difference in corrosion level at a specified location of wear damage can be established and therefore more insightful information regarding the change of surface corrosion properties due to micro-/nano-scale tribological processes can be obtained.

1. Wu, X., Tao, N., Hong, Y., Liu, G., Xu, B., Lu, J., Lu, K., *Strain-induced grain refinement of cobalt during surface mechanical attrition treatment.* Acta Materialia, 2005. **53**(3): p. 681-691.
2. Williams, S., Tipper, J.L., Ingham, E., Stone, M.H., Fisher, J., *In vitro analysis of the wear, wear debris and biological activity of surface-engineered coatings for use in metal-on-metal total hip replacements.* Proc Inst Mech Eng, 2003. **217**(H): p. 155-163.
3. http://ortho.muhealth.org/hipandknee/images/HipReplace.jpg.
4. http://www.hipsforyou.com/strykerceramichip.php.
5. Dowson, D., *New joints for the millennium: wear control in total replacement hip joints.* Proc I Mech E (H), 2001. **215**(H4): p. 335-358.
6. Buford, A., Goswami, T., *Review of wear mechanisms in hip implants: Paper I - General.* Materials and Design, 2004. **25**(5): p. 385-393.
7. Dowson, D., Hardaker, C., Flett, M., Issac, G.H., *A hip joint simulator study of the performance of metal-on-metal joints. Part I: The role of materials.* The Journal of Arthroplasty, 2004. **19**(8): p. 118-123.
8. Jin, Z.M., Stone, M.H., Ingham, E., Fisher, J, *Biotribology.* Current Orthopaedics, 2006. **20**: p. 32-40.
9. Roberts, P., Grigoris, P., Bosch, H., Talwaker, N, *Resurfacing arthroplasty of the hip.* Current Orthopaedics, 2005. **19**: p. 263-279.
10. Hughs, D., *Hip resurfacing versus hip replacement - What, Why, Who and When? http://personal.strath.ac.uk/david.hughes/Papers/Hip_replacement_versus_hip_resurfacing.pdf*.
11. Adams, D., Quigley, S., *Hip resurfacing: Past, present and future.* Journal of Orthopaedic Nursing, 2005. **9**: p. 87-94.
12. Wang, A., Yue, S., Bobyn, J.D., Chan, F.W., and Medley, J.B., *Surface characterization of metal-on-metal hip implants tested in a hip simulator.* Wear, 1999. **225-229**(pt.2): p. 708-715.
13. Catelas, I., Bobyn, J.D., Medley, J.B., Krygier, J.J., Zukor, D.J., Huk, O.L., *Size, shape, and composition of wear particles from metal-metal hip simulator testing: Effects of alloy and number of loading cycles.* Journal of Biomedical Materials Research - Part A, 2003. **67**(1): p. 312-327.
14. Goldsmith, A.A.J., Dowson, D., Isaac, G.H., and Lanscaster, J.G., *A Comparative Joint Simulator Study of the Wear of Metal-On-Metal and Alternative Material Combinations in Hip Replacements.* Proceedings of the I MECH E Part H Journal of Engineering in Medicine, 2000. **214**: p. 39-47.
15. Walker, P.S., Erkman, M. J., *Metal-on-metal lubrication in artificial human joints.* Wear, 1972. **21**(2): p. 377-392.
16. Liu, F., Jin, Z. M., Hirt, F., Rieker, C., Roberts, P., Grigoris, P., *Effect of wear of bearing surfaces on elastohydrodynamic lubrication of metal-on-metal hip implants.* Proceedings of the Institution of Mechanical Engineers, Part H: Journal of Engineering in Medicine, 2005. **219**(5): p. 319-328.
17. Dowson, D., Jin, Z.M., *Metal-on-metal hip joint tribology.* Proc. IMechE, Part H: J. Engineering in Medicine, 2005. **220**: p. 107-118.
18. Medley, J.B., Bobyn, J.D., Krygler, J.J., Chan, F.W., Tanzer, M., Roter, G.E. *Elastohydrodynamic lubrication and wear of metal-on-metal hip implant.* in *World Tribology Forum in Arthroplasty*. 2001. Bern: Hans Huber.

19. Varano, R., Bobyn, D., Medley, J.B., Yue, S., *The effect of microstructure on the wear of cobalt-based alloys used in metal-on-metal hip implants* Proc I Mech E (H), 2006. **220**: p. 145-159.
20. Chan, F.W., Bobyn, J.D., Medley, J.B., Krygier, J.J., Yue, S., Tanzer, M., *Engineering issues and wear performance of metal on metal hip implants.* Clinical orthopaedics and related research 1996(333): p. 96-107.
21. Chan, F.W., Bobyn, J.D., Medley, J.B., Krygier, J.J., Tanzer, M., *Wear and lubrication of metal-on-metal hip implants.* Clin Orthop, 1999. **369**: p. 10-24.
22. Walker, P.S. and B.L. Gold, *Tribology (friction, lubrication and wear) of all-metal artificial hip joints.* Wear, 1971. **17**(4): p. 285-299.
23. Hernandez-Rodriguez, M.A.L., Mercado-Solis, R. D., Perez-Unzueta, A. J., Martinez-Delgado, D. I., Cantu-Sifuentes, M., *Wear of cast metal-metal pairs for total replacement hip prostheses.* Wear, 2005. **259**(7-12): p. 958-963.
24. Hallab, N.J. and J.J. Jacobs, *Orthopedic implant fretting corrosion.* Corrosion Reviews, 2003. **21**(2-3): p. 183-213.
25. Hallab, N.J., Messina, C., Skipor, A., Jacobs, J.J., *Difference in the fretting corrosion of metal-metal and ceramic-metal modular junctions of total hip replacements.* Journal of Orthopaedic Research, 2004. **22**: p. 250-259.
26. Gilbert, J.L., Buckley, C.A., and Jacobs, J.J., *In-Vivo Corrosion of Modular Hip Prosthesis Components in Mixed and Similar Metal Combinations: The Effect of Crevice, Stress, Motion and Alloy Coupling.* J Biomed Mater Res, 1993. **27**(12): p. 1533–1544.
27. Ratzer-Schiebe, H.J., *The relationship between repassivation behavior and pitting corrosion for ti and Ti-6Al-4V.* Corrosion 1978. **34**: p. 437-442.
28. Dumbleton, J.H., *Tribology of natural and artificial joints*. 1981, Amsterdam: Elsevier.
29. Tipper, J.L., Ingham, E., Jin, Z.M., Fisher, J., *The science of metal-on-metal articulation.* Current Orthopaedics, 2005. **19**: p. 280-287.
30. Callister, W.D., *Materials science and engineering: an introduction*. 5th ed. 1999: John Wiley & Sons Inc. p.579.
31. Venugopalan, R., Gaydon, J. , *A review of corrosion behaviour of surgical implant alloys.* Technical Review Note, Perkin Elmer Instruments, Princeton Applied Research, 1999-2001: p. 1-10.
32. Dearnley, P.A., *A review of metallic, ceramic and surface treated materials used for bearing surfaces in human joint replacements.* Proc Inst Mech Eng, 1999. **3**(H): p. 107-135.
33. Mckee, G.K., Watson-Farrar, J., *Replacement of arthritic hips by the Mckee-Farrar prosthsis.* J Bone & Joint Surgery, 1966. **48**(B): p. 245-259.
34. Marti, A., *Cobalt-base alloys used in bone surgery.* Injury, Int J. Care Injured, 2000. **31**: p. S-D 18-21.
35. Park, J.B., Kon Kim, Y., *Metallic Biomaterials*, in *The Biomedical Engineering Handbook, 2nd Ed.*, J.D. Bronzino, Editor. 2000, CRC Press LLC: Boca Raton.
36. Yan, Y., Neville, A., Dowson, D., Williams, S., *Tribocorrosion in implants-assessing high carbon and low carbon Co-Cr-Mo alloys by in situ electrochemical measurements.* Tribology International, 2006. **39**(12): p. 1509-1517.
37. Metcalf, J.E.P., Cawley, J., Band, T.J., *Cobalt Chromium Molybdenum metal-on-metal resurfacing orthopaedic hip devices.* Business briefing: medical device manufacturing & technology, 2004: p. 1-7.
38. Salinas-Rodriguez, A., *The Role of the FCC-HCP phase transformation during the plastic deformation of Co-Cr-Mo-C alloys for biomedical applications*, in *ASTM Special Technical Publication 1365*, R.L.K. J.A. Disegi, R. Pilliar, Editor.

1999, American Society for Testing and Materials: West Conshokochen, PA. p. 108-121.

39. Lopez, H.F., Saldivar, A. Huang, P. *Development and properties of ε-martensite in CoCrMo alloys for biomaterials applications*. in *the Proceedings of 2nd International Alloy Conference*. 1999. Davos, Switzerland: Kluwer Academic/Plenum Publishers, New York.
40. Büscher, R., Fischer, A., *The pathways of dynamic recrystallization in all-metal hip joints.* Wear 2005. **259**: p. 887-897.
41. Weber, B.G., *Experience with the Metasul total hip bearing system.* Clin Orthop, 1996. **3295**: p. S78-88.
42. Harlan, C.A., M.D., *History of Hip Resurfacing*, http://www.jri-oh.com/jri_hip_surface.php. Access date: 01.Dec 2007.
43. Wagner, M., Wagner, H., *Prelinimary results of uncemented metal-on-metal stemmed and resrfacing hip replacement arthroplasty.* clin Orthop, 1996. **329S**: p. S89-98.
44. Jin, Z.M., Tipper, J.L., Stone, M.H., Ingham, E., Fisher, J, *Hip joints, aritificial*, in *Encyclopedia of Medical Devices and Instrumentation*, J.G. Webster, Editor. 2006, John Wiley & Sons, Inc.
45. Cawley, J., Metcalf, J.E.P., Jones, A.H., Band, T.J., Skupien, D.S., *A tribological study of cobalt chromium molybdenum alloys used in metal-on-metal resurfacing hip arthroplasty.* Wear, 2003. **255**(pt.2): p. 999-1006.
46. Wimmer, M.A., Loos, J., Nassutt, R., Heitkemper, M., Fischer, A., *The acting wear mechanisms on metal-on-metal hip joint bearings: in vitro results.* Wear, 2001. **250**: p. 129-139.
47. http://www.wheelessonline.com/ortho/gait. Access date 01-01-2009.
48. Paul, J.P., *Force actions transmitted by joints in the human body.* Proceedings of the Royal Society of London. Series B, Biological Sciences, 1976. **192**(1107): p. 163-172.
49. Litsky, A.S., Spector, M., *Biomaterials*, in *Orthopaedic basic science*, S.R. Simon, Editor. 1994, American academy of orthopaedic surgeons. p. 470-473.
50. Bergmann, G., Graichen, F., Rohlmann, A., *Hip joint loading during walking and running, measured in two patients.* J. Biomech, 1993. **26**: p. 969.
51. Bergmann, G., Graichen, F., Rohlmann, A., *Is staircase walking a risk for the fixation of hip implants?* Journal of Biomechanics, 1995. **28**(5): p. 535-53.
52. Jin, Z.M., Dowson, D., Fisher, J., *Analysis of fluid film lubrication in artificial hip joint replacements with surfaces of high elastic modulus.* Proceedings of the Institution of Mechanical Engineers, Part H: Journal of Engineering in Medicine, 1997. **211**(3): p. 247-256.
53. Semlitsch, M., Willert H.G., *Clinical wear behavior of ultra-high molecular weight polyethylene cups paired with metal and ceramic ball heads in comparison to metal-on-metal pairings of hip joint replacements.* Proc Inst Mech Eng, 1997. **211**(H): p. 73-88.
54. Doorn, P.F., Campbell, P.A., Worrall, J., Benya, P.D., McKellop, H.A., Amstutz, H.C., *Metal wear particle characterization from metal on metal total hip replacements: transimission electron microscopy study of periprosthetic tissues and isolated particles.* J. Biomed. Mater. Res, 1998. **42**: p. 103-111.
55. Hanawa, T., *Metal ion release from metal implants.* Materials Science and Engineering C, 2004. **24**(6-8 SPEC ISS): p. 745-752.
56. Peters, T.J., *Serum Albumin.* Advances in Protein Chemistry, 1985. **37**: p. 161-245.
57. Van Oss, C.J., Good, R.J., *Orientation of the water molecules of hydration of human serum albumin* Jounral of Protein Chemistry, 1988. **7**(2): p. 179-183.

58. Burnstock, G., *Purine-mediated signalling in pain and visceral perception.* Trends Pharmacol. Sci., 2001. **22** p. 182-188.

59. Wood, D.J., *The characterization of particulate debris obtained from failed orthopedic implants*. 1993, San Jose State University, College of Material Engineering.

60. Steen, K.H., Reeh, P.W., *Sustained graded pain and hyperalgesia from harmless experimental tissue acidosis in human skin.* Neuroscience letter, 1993. **154**: p. 113-116.

61. Ratner, B.D., Hoffman, A. S., Schoen, F.J., Lemons, J.E., *Biomaterials Science, an Introduction to Materials in Medicine, 2nd*. 2004: Elsevier Academic Press.

62. Moulton, S.E., Barisci , J.N., Bath, A., Stella, R. , Wallace, G.G. , *Investigation of protein adsorption and electrochemical behavior at a gold electrode.* J Colloid Interface Sci. , 2003. **15**(261(2)): p. 312-319.

63. Hiromoto, S., K. Noda, and T. Hanawa, *Electrochemical properties of an interface between titanium and fibroblasts L929.* Electrochimica Acta, 2002. **48**(4): p. 387-396.

64. Gettens, R.T.T., Gettens, R. T. T., Gilbert, J. L. *Fibrinogen Adsorption onto 316L Stainless Steel: Voltage Effects*. in *Bioengineering Conference, 2006. Proceedings of the IEEE 32nd Annual Northeast*. 2006.

65. de Ficquelmont-Loizos, M.M., Takenouti, H., Kante, W., *Long-time and short-time investigation of the electrode interface through electrochemical impedance measurements. Application to adsorption of human serum albumin onto glassy carbon rotating disc electrode.* Journal of Electroanalytical Chemistry, 1997. **428**(1-2): p. 129-140.

66. Kleijn, J.M., Barten, Desiree, Stuart, Martien A. Cohen, *Adsorption of charged macromolecules at a gold electrode.* Langmuir, 2004. **20**(22): p. 9703-9713.

67. Serro, A.P., Gispert, M. P., Martins, M. C. L., Brogueira, P., Colaco, R., Saramago, B., *Adsorption of albumin on prosthetic materials: Implication for tribological behavior.* J Bio Mat Res - Part A, 2006. **78**(3): p. 581-589.

68. Sharma., C.P., Clark, G.C.F., Williams, D.F., *The adsorption of proteins on metal surfaces.* Engineering in medicine, 1981. **10**(1): p. 11-16.

69. Bernabeu, P., Tamisier, L., de Cesare, A., Caprani, A., *Study of the adsorption of albumin on a platinum rotating disk electrode using impedance measurements.* Electrochimica Acta, 1988. **33**(8): p. 1129-1136.

70. Choi, K.H., Friedt, J. M., Laureyn, W., Frederix, F., Campitelli, A., Borghs, G., *Investigation of protein adsorption with simultaneous measurements of atomic force microscope and quartz crystal microbalance.* Journal of Vacuum Science & Technology B (Microelectronics and Nanometer Structures), 2003. **21**(4): p. 1433-6.

71. Ying, P., Viana, A. S., Abrantes, L. M., Jin, G., *Adsorption of human serum albumin onto gold: A combined electrochemical and ellipsometric study.* Journal of Colloid and Interface Science, 2004. **279**(1): p. 95-99.

72. Malmsten, M., *Formation of adsorbed protein layers.* Journal of Colloid and Interface Science, 1998. **207**: p. 186-199.

73. Merritt, K., Brown, S. A., *Effect of proteins and pH on fretting corrosion and metal ion release.* Journal of Biomedical Materials Research, 1988. **22**(2): p. 111-120.

74. Sven, P., *Determination of transferrin isoproteins in human cerebrospinal fluid using isoelectric focusing and zone immunoelectrophoresis assay.* Electrophoresis, 1987. **8**(11): p. 515-517.

75. Salim, M., O'Sullivan, B., McArthur, S. L.,Wright, P.C., *Characterization of fibrinogen adsorption onto glass microcapillary surfaces by ELISA.* Lab Chip, 2007. **7**: p. 64 - 70.

76. Geborek, P., Wollheim, F.A., *Synovial fluid*, in *Mechanics of Human Joints, Physiology, Pathophysiology and Treatment*, Verna Wright and E.L. Radin, Editors. 1993, Marcel Dekker: New York. p. 117-136.

77. Jones, K.L., O'Melia, C. R., *Protein and humic acid adsorption onto hydrophilic membrane surfaces: Effects of pH and ionic strength.* Journal of Membrane Science, 2000. **165**(1): p. 31-46.

78. Cabilio, N.R., Omanovic, S., Roscoe, S.G., *Electrochemical studies of the effect of temperature and pH on the adsorption of alpha-lactalbumin at Pt.* Langmuir, 2000. **16**(22): p. 8480-8488.

79. Hughes Wassell, D.T., Embery, G., *Adsorption of bovine serum albumin on to titanium powder.* Biomaterials, 1996. **17**(9): p. 859-864.

80. Malmsten, M., *Biopolymers at Interfaces*. 1998, New York: Marcel Dekker.

81. Okazaki, Y., Tateishi, T., Ito, Y., *Corrosion resistance of implant alloys in pseudo physiological solution and role of alloying elements in passive films.* Materials Transactions, JIM, 1997. **38**(1): p. 78-84.

82. Lacour, F., Torresi, R., Gabrielli, C., Caprani, A., *Comparison of the quarz-crystal microbalance and the double-layer capacitance methods for measuring the kinetics of the adsorption of bovine serum albumin onto a gold electrode.* Journal of the Electrochemical Society, 1992. **139**(6): p. 1619-1622.

83. Omanovic, S., Roscoe, S. G., *Electrochemical studies of the adsorption behavior of bovine serum albumin on stainless steel.* Langmuir, 1999. **15**(23): p. 8315-8321.

84. Moulton, S.E., Barisci, J. N., Bath, A., Stella, R., Wallace, G. G., *Studies of double layer capacitance and electron transfer at a gold electrode exposed to protein solutions.* Electrochimica Acta, 2004. **49**(24): p. 4223-4230.

85. Gassa, L., De Mele, Monica Fernandez Lorenzo. *Influence of the composition of the biological media on the electrochemical response of the metallic components of biomaterials*. 2005. Lisbon, Portugal.

86. Tang, Q., Xu, C.H., Shi S. Q., Zhou, L M., *Formation and characterization of protein patterns on the surfaces with different properties.* Synthetic Metals, 2004. **147**(1-3): p. 247-52.

87. Tuemmler, H.P., Thull, R., *Model of the metal/tissue connection of implants made of titanium or tantalum*. Biological and Biomechanical Performance of Biomaterials. 1986, Paris, Fr: Elsevier, Amsterdam, Neth. 403-408.

88. Gilbert, J.L., Bai, Zhijun, Bearinger, Jane, Megremis, Spiro. *The dynamics of oxide films on metallic biomaterials*. 2003. Anaheim, CA., United States: ASM International.

89. Lacour, F., Frayret, J. P., Caprani, A., *Effect of the electrode roughness on the kinetics of albumin adsorption at a rotating disk electrode investigated by double-layer capacitance measurements.* Journal of the Electrochemical Society, 1992. **139**(1): p. 153-159.

90. Contu, F., Elsener, B., Bohni, H., *Serum effect on the electrochemical behaviour of titanium, Ti6Al4V and Ti6Al7Nb alloys in sulphuric acid and sodium hydroxide.* Corrosion Science, 2004. **46**(9): p. 2241-2254.

91. Jost, H.P., *Lubrication, Education and Research – A report on the Present Position and Industry's Needs.* . Her Majesty's Stationery Office. London, 1966.

92. Hutchings, I.M., *Tribology: friction and wear of engineering materials.* 1992, London: Edward Arnold.

93. Williams, J.A., *Engineering Tribology*. 1998, Oxford: Oxford University Press.

94. Dowson, D., *A comparative study of the performance of metallic and ceramic femoral head components in total replacement hip joints.* Wear, 1995. **190**(2): p. 171-183.
95. Unsworth, A., *The effects of lubrication in hip prostheses.* Physics in Medicine and Biology, 1978. **23**(2): p. 253-268.
96. Black, J., *Orthopaedic Biomaterials in Research and Practice*. 1988, New York: Churchill Livingstone Inc.
97. Smith, S.L., Dowson, D., Goldsmith, A. A. J., *The lubrication of metal-on-metal total hip joints: A slidedown the Stribeck curve.* Proceedings of the Institution of Mechanical Engineers, Part J: Journal of Engineering Tribology, 2001. **215**(5): p. 483-493.
98. Hamrock, B.J., Dowson, D., *Elastohydrodynamic lubrication of elliptical contacts for materials of low elastic modulus. I:fill flooded conjunction.* Trans. ASME, J. Lubrication Technol., 1978. **100**(2): p. 236-245.
99. Tanner, R.I., *An alternative mechanism for the lubrication of synovial joints.* Physics in Medicine and Biology, 1966. **11**: p. 119-127.
100. Jones, H.P., Walker, P.S., *Casting techniques applied to the study of human joints.* J Inst Sci Technol, 1968. **14**: p. 57.
101. Linn, F.C., *Lubrication of animal joint II- the mechanism.* J. Biomech, 1968. **1**: p. 193-205.
102. Linn, F.C., Radin, E.L., *Lubrication of animal joints III - the effect of certain chemical alteration of the cartilage and lubricant.* Arth. Rheum, 1968. **11**: p. 674-682.
103. Dowson, D., Jin, Z. M., *Microelastohydrodynamic lubrication of low-elastic-modulus solids on rigid substrates.* Journal of Physics D: Applied Physics, 1992. **25**(1A): p. 116-123.
104. Dowson, D., Jin, Z. M., *Micro-elastohydrodynamic lubrication of synovial joints.* Engineering in Medicine, 1986. **15**: p. 63-5.
105. Roberts, B.J., Unsworth, A., Mian, N., *Modes of lubrication in human hip joints.* Ann. Rheum. Dis., 1982. **41**: p. 221-224.
106. Scholes, S.C., Unsworth, A., *Comparison of friction and lubrication of different hip prostheses.* Proceedings of the Institution of Mechanical Engineers, Part H: Journal of Engineering in Medicine, 2000. **214**(1): p. 49-57.
107. Jin, Z.M., Dowson, D., Fisher, J. *Lubrication mechanisms in metal-on-metal hip joint replacements*. 1996. Toronto, Can: Soc for Biomaterials, St. Louis Park, MN, USA.
108. Vassiliou, K., Elfick, A. P. D., Scholes, S. C., Unsworth, A., *The effect of 'running-in' on the tribology and surface morphology of metal-on-metal Birmingham hip resurfacing device in simulator studies.* Proceedings of the Institution of Mechanical Engineers, Part H: Journal of Engineering in Medicine, 2006. **220**(2): p. 269-277.
109. Jacobs, J.J., Skipor, K.A., Campbell, P.A., Hallab, N.J., Urban, R.M., Amstutz, H.C., *Can Metal Levels Be Used to Monitor Metal-on-Metal Hip Arthroplasties?* The Journal of Arthroplasty 2004. **19**(8): p. 59-65.
110. Dowson, D., *Tribological principles in metal-on-metal hip joint design.* Proceeding of IMechE, part H: J. Engineering in Medicine, 2006. **220**: p. 161-170.
111. Wang, A., Bobyn, J. D., Yue, S., Medley, J. B., Chan, F. W., *Residual abrasive material from surface grinding of metal-metal hip implants: A source of third-body wear?*, in *ASTM Special Technical Publication 1365*. 1999, American Society for Testing and Materials, USA. p. 125-134.

112. Howie, D.W., McCalden, R.W., Nawana, N.S. , Costi, K., Pearcy, M.J., Subramanian, C., *The Long-Term Wear of Retrieved McKee-Farrar Metal-on-Metal Total Hip Prostheses.* The Journal of Arthroplasty, 2005. **20**(3): p. 350-357.

113. Lippincott, A.L.I., Dowling, J.M., Medley, J.B., Christensen, R.W., *Temporomandibular joint arthroplasty using metal-on-metal and acrylic-on-metal configurations : Wear in laboratory tests and in retrievals.* Surg Technol Int. , 2000. **VIII**: p. 321-330.

114. Reinisch, G., , Judmann, K.P., Lhotka, C., Lintner, F., Zweymuller, K.A., *Retrieval study of uncemented metal-metal hip prostheses revised for early loosening.* Biomaterials, 2003. **24**(6): p. 1081-1091.

115. Rieker, C., Shen, M., Kottig, P. *In-vivo tribological performance of 177 metal-on-metal hip articulations*. in *World Tribology Forum in Arthroplasty*. 2001. Bern: Hans Huber.

116. Schmalzried, T.P., Callaghan, J.J., *Current concept review - wear in total hip and knee replacements.* J Bone Joint Surg Am, 1999. **81**: p. 115-136.

117. Davidson, J.A., *Characteristics of metal and ceramic total hip bearing surfaces and their effect on long-term ultra molecular weight polyethylene wear.* Clin orthop Rel Res, 1993. **294**: p. 361-378.

118. Büscher, R., Tager, G., Dudzinski, W., Gleising, B., Wimmer, M. A., Fischer, A., *Subsurface microstructure of metal-on-metal hip joints and its relationship to wear particle generation.* J Biomed Mat Res Part B 2005. **72**(1): p. 206-214.

119. Silva, M., Heisel, C., Schmalzried, T.P., *Metal-on-metal total hip replacement.* Clin orthop Rel Res, 2005. **430**: p. 53-61.

120. Jin, Z.M., Medley, J.B., Dowson, D. *Fluid film lubrication in artificial hip joints*. in *Proc 29 th Leeds-Lyon symp Tribology*. 2003.

121. Tipper, J.L., Ingham, E., Hailey, J.L., Besong, A.A., Fisher, J., Wroblewsky, B.S., Stone, M.H., *Quantitative analysis of polyelthylene wear debris, wear rate and head damage in retrienved Charnley hip protheses.* J Mat Sci, Mat Med, 2000. **11**: p. 117-124.

122. Tipper, J.L., Firkins, P. J., Ingham, E., Fisher, J., Stone, M. H., Farrar, R., *Quantitative analysis of the wear and wear debris from low and high carbon content cobalt chrome alloys used in metal on metal total hip replacements.* Journal of Materials Science: Materials in Medicine, 1999. **10**(6): p. 353-362.

123. Green, T.R., Fisher, J., Matthews, J.B., Stone, M.H., Ingham, E., *Effect of size and dose on bone resorption activity of macrophages in vitro by clinically relevant ultra high molecular weight polyethylene particles.* J Biomed Mater Res Appl Biomat, 2000. **53**(490-497).

124. Germain, M.A., *Biological reactions to cobalt chrome wear particles. PhD dissertation*. 2002, University of Leeds: Leeds.

125. Germain, M.A., Hatton, A., Williams, S., Matthews, J.B., Stone, M.H., Fisher, J., Ingham, E., *Comparison of the cytotoxicity of clinically relevant cobalt-chromium and alumina ceramic wear particles in vitro.* Biomaterials, 2003. **24**: p. 469-479.

126. Lewis, C.G., Sunderman, F.W. Jr., *Metal carcinogenesis in total joint arthroplasty. Animal models.* Clin Orthop, 1996. **329**(S): p. S264-S268.

127. Galvin, A.L., Endo, M.M., Tipper, J.L., ingham, E., Fisher, J. *Functional biological activity and osterolytic potential of non-crosslinked and cross-linked UHMWPE hip joint prostheses*. in *Trans 7th World Biomat Cong*. 2004.

128. Yao, J.Q., Laurent, M. P., Johnson, T. S., Blanchard, C. R., Crowninshield, R. D., *The influences of lubricant and material on polymer/CoCr sliding friction.* Wear, 2003. **255**(1-6): p. 780-784.
129. Ahlroos, T., *Effect of lubricant on the wear of prosthetic joint materials. Dissertation for the degree of Doctor of Science in Technology*. 2001, Helsinki University of Technology: Espoo.
130. Zhou, B., Shi, S., Wang, X., *Microstructures and wear resistance of medical CoCrMoC alloys.* Xiyou Jinshu Cailiao Yu Gongcheng/Rare Metal Materials and Engineering, 2006. **35**(1): p. 105-109.
131. Huang, P., Salinas-Rodriguez, A., Lopez, H. F., *Tribological behaviour of cast and wrought Co-Cr-Mo implant alloys.* Materials Science and Technology, 1999. **15**(11): p. 1324-30.
132. Bowsher, J.G., Nevelos, J., Williams, P. A., Shelton, J. C., *'Severe' wear challenge to 'as-cast' and 'double heat-treated' large-diameter metal-on-metal hip bearings.* Proceedings of the Institution of Mechanical Engineers, Part H: Journal of Engineering in Medicine, 2006. **220**(2): p. 135-143.
133. Yan, Y., *PhD Thesis: Corrosion and tribo-corrosion behaviour of metallic orthopaedic implant materials*, in *School of Mechanical Engineering*. 2006, University of Leeds: Leeds.
134. Sinnett-Jones, P.E., Wharton, J.A., Wood, R.J.K., *Micro-abrasion-corrosion of a CoCrMo alloy in simulated artificial hip joint environments.* Wear, 2005. **259**(7-12): p. 898-909.
135. Sun, D., Wharton, J. A., Wood, R. J. K., Ma, L., Rainforth, W. M., *Microabrasion-corrosion of cast CoCrMo alloy in simulated body fluids.* Tribology International, 2009. **42**(1): p. 99-110.
136. T. D. Warner, I.V., D. Bishop-Bailey, J.A. Mitchell, *Influence of plasma protein on the potencies of inhibitors of cyclooxygenase-1 and -2* The FASEB Journal, 2006. **20**: p. 542-544.
137. Landolt, D., *Corrosion and surface chemistry of metals*. 2007: EPFL-Press.
138. *Impedance Spectroscopy: Theory, Experiment, and Applications*, ed. E. Barsoukov and J.R. Macdonald. 2005: Published by Wiley-IEEE.
139. Jacobs, J.J., Gilbert, J.L., Urban, R.M., *Current concepts review: Corrosion of metal orthopaedic implants.* J Bone Joint Surg Am, 1998. **80**: p. 268-282.
140. Fontana, M.G., *Corrosion engineering* 2nd ed. 1978, New York McGraw-Hill.
141. Contu, F., Elsener, B., Bohni, H., *Electrochemical behavior of CoCrMo alloy in the active state in acidic and alkaline buffered solutions.* Journal of Electrochemistry Society, 2003. **150**(9): p. B419-B424.
142. Park, J.B., Lakes, R.S., *Metallic Implant Materials*, in *Biomaterials - an Introduction*. 1992, Plenum Press: New York. p. 75-115.
143. Urban, R.M., Jacobs, J.J., Gilbert, J.L., Galante, J.O., *Migration of corrosion products from modular hip prostheses. Particle microanalysis and histrophathological findings.* J Bone Joint Surg, 1994. **76**(A): p. 1345-1359.
144. MacDonald, S.J., McCalden, R.W., Chess, D.G., Bourne, R.B., Rorabeck, C.H., Cleland, D., Leung, F., *Metal-on-metal versus polyethylene in hip arthroplasty: a randomized clinical trial.* . Clin Orthop, 2003. **406**: p. 282-296.
145. Jones, D., Lucas, H., O'Driscoll, M., Price, C., Wibberley, B., *Cobalt toxicity after McKee hip arthroplasty.* J Bone Joint Surg Br, 1975. **57**(3): p. 389-396.
146. Merritt, K., Brown, S. A., *Release of hexavalent chromium from corrosion of stainless steel and cobalt-chromium alloys.* Journal of biomechanical Materials Research, 1995. **29**: p. 627-633.
147. Sargeant, A., Goswami, T., *Hip implants- Paper VI- Ion Concentrations.* Materials & Design, 2005. **28**(1): p. 155-171.

148. Clarke, M.T., Lee, P. T. H., Arora, A., Villar, R. N. , *Levels of metal ions after small- and largediameter metal-on-metal hip arthroplasty.* Journal of Bone & Joint Surgery, 2003. **85-B,** (6): p. 913-917.
149. Montero-Ocampo, C., Rodriguez, A. S., *Effect of carbon content on the resistance to localized corrosion of as-cast cobalt-based alloys in an aqueous chloride solution.* Journal of Biomedical Material Research, 1995. **29**(4): p. 441-453.
150. Igual Munoz, A., Mischler, S., *Interactive effects of albumin and phosphate ions on the corrosion of a CoCrMo implant alloy.* J Electrochem Soc, 2007. **154**(10): p. C562-C570.
151. Kurz, S., Hodgson, A.W., Virtanen, S., Fervel, V., Mischler, S, *Corrosion characterisation of passive films on CoCrMo with electrochemical techniques in saline and simulated biological solutions.* European Cells & Materials, 2002. **3**(1): p. 26-27.
152. Fagan, G.J., Wayment ,H., Morris, D.L., Crosby, P.A., *The Albumin Cobalt Binding Test: Analytical Performance of a New Automated Chemistry Assay for the Detection of Ischemia Modified Albumin (IMA™).* Journal of Clinical Ligand Assay, 2002. **25**(2): p. 178-187.
153. Lassac, J.P., Sakar, B, *Characterization of the copper (II) and nickel (II) transport site of human serum albumin. studies of copper (II) and nickel (II) binding to peptide 1-24 of human serum albumin by 13 C and 1 H NMR spectroscopy.* Biochemistry, 1984: p. 2831-2838.
154. Bal, W., Christodoulou, J., Sadler, P., Tucker, A., *Multi-metal binding site of serum albumin.* J Inorganic Biochem, 1998. **70**: p. 33-39.
155. http://commons.wikimedia.org/wiki/File:Vitamin_B12.png. Access date: 01.01.2009.
156. Jacobs, J.J., Hallab, N.J., Skipor, A.K., Urban, R.M. , *Metal degradation products: a cause for concern in metal-metal bearings?* Clin Orthop Relat Res, 2003. **417**: p. 139-147.
157. Williams, D.F., Clark, G. C. F., *The corrosion of pure cobalt in physiological media.* Journal of Materials Science, 1982. **17**(6): p. 1675-1682.
158. Williams, R.L., Brown, S.A., Merritt, K., *Electrochemical studies on the influence of proteins on the corrosion of implant alloys.* Biomaterials, 1988. **9**: p. 181-186.
159. Lewis, A.C., Kilburn, M. R., Papageorgiou, I., Allen, G. C., Case, C. P., *Effect of synovial fluid, phosphate-buffered saline solution, and water on the dissolution and corrosion properties of CoCrMo alloys as used in orthopedic implants.* J Biomed Mat Res - Part A, 2005. **73**(4): p. 456-467.
160. Contu, F., Elsener, B., Bohni, H., *Corrosion behaviour of CoCrMo implant alloy during fretting in bovine serum.* Corrosion Science, 2005. **47**: p. 1863-1875.
161. Goldberg, J.R., Gilbert, J. L., *Electrochemical response of CoCrMo to high-speed fracture of its metal oxide using an electrochemical scratch test method.* Journal of Biomedical Materials Research, 1997. **37**(3): p. 421-431.
162. Jones, D., *Principals and Prevention of Corrosion.* 2 ed. 1996: Prentice-Hall. 84-86.
163. Cottis, R., Turgoose, S., *Electrochemical Impedance and Noise*, ed. B.C. Syrett. 1999, USA: NACE International.
164. Dawson, J.L., *Electrochemical Noise Measurement* Electrochemical noise measurement for corrosion applications, ASTM STP 1277. Annual Book of ASTM Standards, ed. J.R. Kearns and J.R. Scully. 1996. p.3-35.

165. Mischler, S., *Triboelectrochemical techniques and interpretation methods in tribocorrosion: A comparative evaluation.* Tribology International, 2008. **41**(7): p. 573-583.

166. Landolt, D., Mischler, S., Stemp, M., *Electrochemical methods in tribocorrosion: a critical appraisal.* Electrochimica Acta, 2001. **46**: p. 3913-3929.

167. Sun, D., Wharton, J., Wood, R.J.K. *Effect of protein adsorption on the wear-corrosion behaviour of cast CoCrMo alloy in simulated healthy and infected joint environments*. in *the Proceedings of 16th International Colloquium of Tribology*. 2008. Stuttgart/Ostfildern, Germany.

168. Tan, K.S., Wharton, J. A., Wood, R. J. K., *Solid particle erosion-corrosion behaviour of a novel HVOF nickel aluminium bronze coating for marine applications - Correlation between mass loss and electrochemical measurements.* Wear, 2005. **258**(1-4 SPEC ISS): p. 629-640.

169. Wood, R.J.K., Wharton, J. A., Speyer, A. J., Tan, K. S., *Investigation of erosion-corrosion processes using electrochemical noise measurements.* Tribology International, 2002. **35**(10): p. 631-641.

170. Wood, R.J.K., Speyer, A. J., *Erosion-corrosion of candidate HVOF aluminium-based marine coatings.* Wear, 2004. **256**(5): p. 545-556.

171. Yan, Y., Neville, A., Dowson, D. *Understanding the role of corrosion in the degradation of metal-on-metal implants*. in *Proc. IMechE, Part H: J. Engineering in Medicine*. 2006.

172. Watson, S.W., Friedersdorf, F. J., Madsen, B. W., Cramer, S. D., *Methods of measuring wear-corrosion synergism.* Wear, 1995. **181-183**(2): p. 476-484.

173. *ASTM G119-93 Standard guide for determining synergism between wear and corrosion*, in *ASTM handbook*. 1993. p. 502-507.

174. Wang, X.Y., Li, D. Y., *Application of an electrochemical scratch technique to evaluate contributions of mechanical and electrochemical attacks to corrosive wear of materials.* Wear, 2005. **259**(7-12): p. 1490-1496.

175. Wu, P.Q., Celis, J. P., *Electrochemical noise measurements on stainless steel during corrosion-wear in sliding contacts.* Wear, 2004. **256**(5): p. 480-490.

176. Ponthiaux, P., Wenger, F., Drees, D., Celis, J. P., *Electrochemical techniques for studying tribocorrosion processes.* Wear, 2004. **256**(5): p. 459-468.

177. Gilbert, J.L., and Jacobs, J.J., *The Mechanical and Electrochemical Processes Associated with Taper Fretting Crevice Corrosion.*, in *Modularity of Orthopedic Implants, ASTM STP 1301* J.E. Parr, M.B. Mayor, and D.E. Marlow, Editors. 1997, ASTM: Philadelphia. p. 45-49.

178. Gilbert, J.L., Buckley, C.A., Lautenschlager, E.P., *Titamium oxide film fracture and repassivation: The effect of potential, pH, and aeration*, in *Medical Applications of Titanium and Its Alloys: The Materials and Biological Issues, ASTM STP 1272, American Society for Testing and Materials*, S.A. Brown and J.E. Lemons, Editors. 1996: Philadelphia. p. 199-218.

179. Gilbert , J., *Novel Electrochemical Techniques for Analysis of Metallic Biomaterials Surfaces.* Medical Plastics and Biomaterials, Category: surface analysis, 1998: p. 16.

180. Garcia, I., Drees, D., Celis, J. P., *Corrosion-wear of passivating materials in sliding contacts based on a concept of active wear track area.* Wear, 2001. **249**(5-6): p. 452-460.

181. Stemp, M., Mischler, S., Landolt, D., *The effect of mechanical and electrochemical parameters on the tribocorrosion rate of stainless steel in sulphuric acid.* Wear, 2003. **255**(1-6): p. 466-475.

182. Hiromoto, S., Mischler, S., *The influence of proteins on the fretting-corrosion behaviour of a Ti6Al4V.* Wear, 2006. **261**(9): p. 1002-1011.

183. Iwabuchi, A., Lee, J.W., Uchidate, M., *Synergistic effect of fretting wear and sliding wear of Cr-alloy and Ti alloy in Hanks' solution.* Wear, 2007. **263**(1-6): p. 492-500.
184. Oltra, R., Chapey, B., Renaud, L., *Abrasion-corrosion studies of passive stainless steels in acidic media: combination of acoustic emission and electrochemical techniques.* Wear, 1995. **186-187**(2): p. 533-541.
185. Sun, D., Wharton, J., Wood, R. *Tribo-Corrosion of cast CoCrMo alloy - abrasive size and concentration effects*. in *the 35th Leeds-Lyon Tribology Symposium*. 2008. Leeds. Tribology International (2009), doi:10.1016/j.triboint.2009.03.018.
186. Sun, D., Wharton, J., Wood, R. *The Effects of Proteins and pH on Tribo-Corrosion Performance of Cast CoCrMo – a Combined Electrochemical and Tribological Study*. in *5th China International symposium on Tribology.* . 2008. Beijing. Full paper accepted by Tribology - Materials, Surfaces & Interfaces.
187. Sun, D., Wharton, J.A., Wood, R.J.K. . *Microabrasion mechanisms of cast CoCrMo in simulated body fluids*. in *1st International Conference on Abrasion Processes and in Wear,* . 2008. Cambridge. Wear (2009), doi: 10.1016/j.wear.2009.03.005.
188. Sun, D., Wharton, J.A., Wood, R.J.K. *Microabrasion-corrosion of cast CoCrMo-Effects of micron and sub-micron sized abrasives*. in *the 17th International Conference on Wear of Materials* 2009. Las Vegas, USA: and in Wear, doi:10.1016/j.wear.2009.01.011.
189. Neville, A., Reyes, M., Xu, H., *Examining corrosion effects and corrosion/erosion interactions on metallic materials in aqueous slurries.* Tribology International, 2002. **35**(10): p. 643-650.
190. Rubin, B.T., *Kinetics of oxide film repair on titanium.* Electroanalyt. Interfac. Electrochem., 1975. **58**: p. 323-337.
191. Seo, M., Chiba, M., Suzuki, K., *Nano-mechano-electrochemistry of the iron (100) surface in solution.* Journal of Electroanalytical Chemistry, 1999. **473**(1): p. 49-53.
192. Seo, M., Chiba, M., *Nano-mechano-electrochemistry of passive metal surfaces.* Electrochimica Acta, 2001. **47**(1): p. 319-325.
193. Fushimi, K., Takase, K.i, Azumi, K., Seo, M., *Current transients of passive iron observed during micro-indentation in pH 8.4 borate buffer solution.* Electrochimica Acta, 2006. **51**(7): p. 1255-1263.
194. Landolt, D., *Electrochemical and materials aspects of tribocorrosion systems.* J. Phys. D: Appl. Phys., 2006. **39**: p. 3121-3127.
195. Yan, Y., A. Neville, and D. Dowson, *Biotribocorrosion of CoCrMo orthopaedic implant materials--Assessing the formation and effect of the biofilm.* Tribology International, 2007. **40**(10-12): p. 1492-1499.
196. Yan, Y., Neville, A., Dowson, D., *Biotribocorrosion - an appraisal of the time dependence of wear and corrosion interactions: II. Surface analysis.* Journal of Physics D (Applied Physics), 2006. **39**(15): p. 3206-3212.
197. Yan, Y., Neville, A., Dowson, D., Williams, S., Fisher, J., *Tribo-corrosion analysis of wear and metal ion release interactions from metal-on-metal and ceramic-on-metal contacts for the application in artificial hip prostheses.* Proc. IMechE, Part J: J. Engineering Tribology, 2008. **222**: p. 483-492.
198. Yan, Y.N., A., Dowson, D., Williams, S., Fisher, J., *The influence of swing phase load on the electrochemical response, friction and ion release of metal-on-metal hip prostheses in a friction simulator.* Proc. IMechE Part J: J. Engineering Tribology, 2009. **223**: p. 1-8.

199. Lucas Anissian, H., Stark, A., Good, V., Dahlstrand, H., Clarke, I.C., *The wear pattern in metal-on-metal hip prostheses.* Journal of Biomedical Materials Research, 2001. **58**(6): p. 673-678.

200. Gee, M.G., Gant, A.J., Hutchings, M., Kusano, Y., Schiffman, K., Van Acker, K., Poulat,S., Gachon, Y., von Stebut, J., Hatto, P., Plint, G., *Results from an interlaboratory exercise to validate the micro-scale abrasion test.* Wear, 2005. **259**: p. 27-35.

201. Rutherford, K.L., Hutchings, I. M., *A micro-abrasive wear test, with particular application to coated systems.* Surface and Coatings Technology, 1996. **79**(1-3): p. 231-239.

202. Mersmann, A., *Crystallization Technology Handbook*. 2001: CRC Press.

203. Trezona, R.I., Allsopp, D.N., Hutchings, I.M., *Transitions between two-body and three-body abrasive wear: Influence of test conditions in the microscale abrasive wear test.* Wear, 1999. **225-229**(I): p. 205-214.

204. Stack, M.M., *Bridging the gap between tribology and corrosion: From wear maps to Pourbaix diagrams.* International Materials Reviews, 2005. **50**(1): p. 1-17.

205. *NanoTest TM user manual. MicroMaterials Ltd. 2001.*

206. Newey, D., Wilkins, M. A., Pollock, H. M., *An ultra-low-load penetration hardness tester.* Journal of Physics E (Scientific Instruments), 1982. **15**(1): p. 119-122.

207. Bello, J.O., Wood, R. J. K., Wharton, J.A. *Micro abrasion-corrosion of AISI 316L stainless steel*. in *Proceedings of the IRG-OEDC on Wear of Engineering Materials, June 2005, Uppsala, Sweden.* 2005.

208. Zhao, J.-C., *Methods for Phase Diagram Determination*. 2007: Elsevier.

209. Contu, F., Elsener, B., Bohni, H., *Characterization of implant materials in fetal bovine serum and sodium sulfate by electrochemical impedance spectroscopy. I. Mechanically polished samples.* Journal of Biomedical Materials Research, 2002. **62**(3): p. 412-421.

210. Hodgson, A.W.E., Kurz, S., Virtanen, S., Fervel, V., Olsson, C. O. A., Mischler, S., *Passive and transpassive behaviour of CoCrMo in simulated biological solutions.* Electrochimica Acta, 2004. **49**(13): p. 2167-2178.

211. Ouerd, A., Alemany-Dumont, C., Normand, B., Szunerits, S., *Reactivity of CoCrMo alloy in physiological medium: Electrochemical characterization of the metal/protein interface.* Electrochimica Acta, 2008. **53**(13): p. 4461-4469.

212. Igual-Muñoz, A., Mischler, S. *Influence of proteins and phosphates on the tribocorrosion behaviour of High Carbon and Low Carbon CoCrMo biomedical alloys*. in *211th ECS Meeting*. 2007. Chicago, Illinois

213. Contu, F., Elsener, B., Bohni, H., *Stability and repassivation of metallic implants in serum bovine.* European Cells and Materials, 2001. **1**(1): p. 14-15.

214. Zitter, H., Plenk, H. Jr. , *The electrochemical behavior of metallic implant materials as an indicator of their biocompatibility.* Journal of Biomedical Materials Research, 1987. **21**(7): p. 881-896.

215. Metikos-Hukovic, M., Pilic, Z., Babic, R., Omanovic, D., *Influence of alloying elements on the corrosion stability of CoCrMo implant alloy in Hank's solution.* Acta Biomaterialia, 2006. **2**(6): p. 693-700.

216. Growcock, F.B., Jasinski, R. J., *Time-Resolved Impedance Spectroscopy of Mild Steel in Concentrated Hydrochloric Acid.* Journal of The Electrochemical Society, 1989. **136**(8): p. 2310-2314.

217. Jackson, D.R., Omanovic, S., Roscoe, S.G., *Electrochemical studies of the adsorption behaviour of serum proteins on titanium.* Langmuir, 2000. **16**: p. 5449-5457.

218. Hubrecht, J., *Electrochemical impedance spectroscopy as a surface analytical technique for biomaterials*, in *Metals as biomaterials*, J.A. Helsen and J. Breme, Editors. 1988, John Wiley & Sons: New York. p. 405-466.
219. *Dekker Encyclopedia of Nanoscience and Nanotechnology*, ed. J.A. Schwarz, C. I. Contescu, and K.Putyera. Vol. 4. 2004: CRC Press.
220. Xiao, S., Wieland, M., Brunner, S., *Surface reactions of 4-aminothiophenol with heterobifunctional crosslinkers bearing both succinimidyl ester and maleimide for biomolecular immobilization.* Journal of Colloid and Interface Science, 2005. **290**(1): p. 172-183.
221. Jermakowicz-Bartkowiak, D., Kolarz, B. N., Tylus, W., *Sorption of aurocyanide and tetrachloroaurate onto resin with guanidine ligand--an XPS approach.* Polymer, 2003. **44**(19): p. 5797-5802.
222. Salavati-Niasari, M., *Nanoscale microreactor-encapsulation 14-membered nickel(II) hexamethyl tetraaza: synthesis, characterization and catalytic activity.* Journal of Molecular Catalysis A: Chemical, 2005. **229**(1-2): p. 159-164.
223. Wang, H., Ho, H.P., Lo, K.C, Cheah, K.W., *Growth of p-type ZnO thin films by (N, Ga) co-doping using DMHy dopant.* J. Phys. D: Appl. Phys. , 2007. **40** p. 4682-4685.
224. Marton, D., Boyd, K. J., Al-Bayati, A. H., Todorov, S. S., Rabalais, J. W., *Carbon Nitride Deposited Using Energetic Species: A Two-Phase System.* Physical Review Letters, 1994. **73**(1): p. 118-121.
225. Ton-That, C., Shard, A.G., Bradley, R.H., *Thickness of spin-cast polymer thin films determined by angle-resolved XPS and AFM tip-scratch methods.* Langmuir, 2000. **16**: p. 2281-2284.
226. Sainio, J., *PhD thesis: Electron spectroscopy studies of vacuum deposited chromium and cobalt layers*, in *Department of Engineering Physics and Mathematics*. 2005, Helsinki University of Technology: Espoo.
227. Jablonski, A., Powell, C. J., *Comparisons of practical attenuation lengths obtained from different algorithms for application in XPS.* Surface Science, 2002. **520**(1-2): p. 78-96.
228. Buchanan, R.A., Rigney, E.D. Jr, Williams, J.M., *Ion implantation of surgical Ti-6Al-4V for improved resistance to wear-accelerated corrosion.* J Biomed Mater Res, 1987 **21**(3): p. 355-366.
229. Leinenbach, C., Fleck, C., Eifler, D., *Characterization of mechanically induced surface damage on the implant alloy TiAl6Nb7 in quasi-physiological media.* Materialwissenschaft und Werkstofftechnik, 2002. **33**(8): p. 442-447.
230. Isaacs, G.H., *The localized breakdown and repair of passive surfaces during pitting.* Corrosion Science, 1989. **29**(2/3): p. 313-323.
231. Isaac, G.H., *Comments.* Corrosion Science, 1993. **34**(3): p. 525-528.
232. Lewis, A.C., Heard, P. J., *The effects of calcium phosphate deposition upon corrosion of CoCr alloys and the potential for implant failure.* J Biomed Mat Res - Part A, 2005. **75**(2): p. 365-373.
233. Ishida, K.P., Griffiths, P.R., *Investigation of Polysaccharide Adsorption on Protein Conditioning Films by Attenuated Total Reflection Infrared Spectrometry II. Thin Copper Films.* J Colloid &Interface Sci 1999. **213**(2): p. 513-524(12).
234. Georges-Louis, F., *Interaction of deamidated soluble wheat protein (SWP) with other food proteins and metals.* 1996, A Thesis presented for the Award of Doctor of Philosophy to the University of Surrey
235. Galazka, V.B., Ledward, D. A., Sumner, I. G., Dickinson, E., *Influence of High Pressure on Bovine Serum Albumin and Its Complex with Dextran Sulfate.* J. Agric. Food Chem., 1997. **45**(9): p. 3465-3471.

236. Yang, X.F., Wang, D.S., Sun, Z.X., Tang. H.X, *Adsorption of phosphate at the aluminum (hydr)oxides–water interface: Role of the surface acid–base properties* Colloids & Surfaces A: Physicochemical and Engineering Aspects 2007. **297**(1-3): p. 84-90.
237. Band, T., Metcalf, J.,Jones, H. , *Metal on metal bearing wear of femoral hip orthopaedic implants produced in cobalt chromium molybdnum alloy.* J Bone &Joint Surgery 2001. **86B**: p. 402-403.
238. Kasemo, B., Gold, J, *Implant surfaces and interface process.* Adv Dent Res 1999. **13**: p. 8-20.
239. Murakami, T., Sawae, Y., Nakashima, K., Yarimitsu, S., Sato, T., *Micro- and nanoscopic biotribological behaviours in natural synovial joints and artificial joints.* Proceedings of the Institution of Mechanical Engineers, Part J: Journal of Engineering Tribology, 2007. **221**(3): p. 237-245.
240. Wimmer, M.A., Sprecher, C., Hauert, R., Tager, G., Fischer, A., *Tribochemical reaction on metal-on-metal hip joint bearings: a comparison between in-vitro and in-vivo results.* Wear, 2003. **255**: p. 1007-1014.
241. Takami, Y., Yamane,S., Makinouchi,K., Otsuka, G., Glueck, J., Benkowski, R., Nos, Y., *Protein adsorption onto ceramic surfaces.* Journal of Biomedical Materials Research, 1998. **40**(1): p. 24-30.
242. Callister, W.D., *Materials science and engineering: an introduction*. 5th ed. 1999: John Wiley & Sons Inc.
243. Büscher, R., Fischer, A. , *Metallurgical Aspects of Sliding Wear of fcc Materials for Medical Applications.* Materialwissenschaft und Werkstofftechnik, 2003. **34**(10-11): p. 966 - 975.
244. Swanson, S.A.V., Freeman, M. A. R., *The Scientific Basis of Joint Replacement.* 1977: Wiley, New York.
245. Levitas, V.I., *A microscale model for strain-induced phase transformations and chemical reactions under high pressure.* Europhys. Lett., 2004. **66**(5): p. 687-693.
246. Lu, Z., McKellop, H., *Frictional heating of bearing materials tested in a hip joint wear simulator.* Proceedings of the Institution of Mechanical Engineers, Part H (Journal of Engineering in Medicine), 1997. **211**(H1): p. 101-108.
247. Galazka, V.B., Sumner, I.G., Ledward, D.A., *Changes in protein-protein and protein-polysaccharide interactions induced by high pressure.* Food Chem., 1996. **57**: p. 393-398.
248. Liao, Y.S., Benya, P. D., McKellop, H. A., *Effect of protein lubrication on the wear properties of materials for prosthetic joints.* Journal of Biomedical Materials Research, 1999. **48**(4): p. 465-473.
249. Suzuki, C., Suzuki, K., Kitamura, K., Osvgi, J., *The protein denaturation under high pressure- Effects of pH and Some Substances on the Pressure Denaturation of Ovalbumin Solution.* The review of physical chemistry of Japan, 1962. **32**(1&2): p. 37-42.
250. Lu, B., Marti, A., McKellop, H. *Wear of a second-generation metal-on-metal hip replacement effect of third-body abrasive particles* in *Sixth World Biomaterials Congress*. 2000. USA.
251. Brown, S.S., Clarke, Ian C. *Lubrication conditions for wear simulation in artificial hip replacements*. 2004. Long Beach, CA, United States: American Society of Mechanical Engineers, New York, NY 10016-5990, United States.
252. Hamer, J.C., Sayles, R. S., Ioannides, E., , *Deformation mechanisms and stresses created by 3rd body debris contacts and their effects on rolling bearing fatigue*, in *Tribology Series*, D. Dowson, et al., Editors. 1987, Elsevier. p. 201-208.

253. Mirghany, M., Jin, Z. M., *Prediction of scratch resistance of cobalt chromium alloy bearing surface, articulating against ultra-high molecular weight polyethylene, due to third-body wear particles.* Proceedings of the Institution of Mechanical Engineers, Part H (Journal of Engineering in Medicine), 2004. **218**(H1): p. 41-50.
254. Sayles, R.S., Ioannides, E. , *Debris damage in rolling bearings and its effects on fatigue life.* Trans. ASME, J. Tribology, 1988. **110**: p. 26-31.
255. Fisher, J., Hu, X. Q., Tipper, J. L., Stewart, T. D., Williams, S., Stone, M. H., Davies, C., Hatto, P., Bolton, J., Riley, M., Hardaker, C., Isaac, G. H., Berry, G., Ingham, E., *An in vitro study of the reduction in wear of metal-on-metal hip prostheses using surface-engineered femoral heads.* Proceedings of the Institution of Mechanical Engineers, Part H (Journal of Engineering in Medicine), 2002. **216**(H4): p. 219-230.
256. Adachi, K., Hutchings, I.M., *Sensitivity of wear rates in the micro-scale abrasion test to test conditions and material hardness.* Wear, 2005. **258**: p. 318-321.
257. Landolt, D., Mischler, S., Stemp, M., Barril, S., *Third body effects and material fluxes in tribocorrosion systems involving a sliding contact.* Wear, 2003. **256**: p. 517-524.
258. Wright, L.G., Sethi, V.K. *Some thoughts on the contributions of bed particle properties to the FBC tube wastage problem.* in *Proceedings of the Symposium on Corrosion and Particle Erosion at Elevated Temepratures*. 1989. Las Vegas: TMS-ASM.
259. Bello, J.O., Wood, R.J.K., Wharton, J.A., *Synergistic effects of micro-abrasion-corrosion of UNS S30403, S31603 and S32760 stainless steels.* Wear, 2007. **263**: p. 149-159.
260. Yamamoto, T., Fushimi, K., Seo, M., Tsuri, S., Adachi, T., Habazaki, H., *Current transient during repeated micro-indentation test of passive iron surface in pH 8.4 borate buffer solution.* Electrochemistry Communications, 2007. **9**: p. 1672-1676.
261. Chiba, A., Kumagai, K., Nomura, N., Miyakawa, S., *Pin-on-disk wear behavior in a like-on-like configuration in a biological environment of high carbon cast and low carbon forged Co-29Cr-6Mo alloys.* Acta Materialia, 2007. **55**(4): p. 1309-1318.
262. *Dislocations and proerties of real materials*. in *Proceedings of the conference to celebrate the fiftieth anniversary of the concept of dislocation in crystals*. 1984. London: The Institute of Metals.
263. Shetty, H.R., Kosel, T. H., Fiore, N. F., *A study of abrasive wear mechanisms in cobalt-base alloys.* Wear, 1983. **84**(3): p. 327-343.
264. Shetty, H.R., Kosel, T. H., Fiore, N. F., *A study of abrasive wear mechanisms using diamond and alumina scratch tests.* Wear, 1982. **80**: p. 347-376.
265. Olson, G.B., Cohen, M., *Kinetics of strain-induced martensitic nucleation.* Metallurgical Transactions A, 1975. **6A**: p. 791-795.
266. Salinas-Rodriguez, A., Rodriguez-Galicia, J.L., *Deformation behavior of low-carbon CoCrMo alloys for low-friction implant applications.* Journal of Biomedical Material Research, 1996. **31**: p. 409-419.
267. Wu, X., Tao, N., Hong, Y., Lu, J., Lu., K., $\gamma \rightarrow \xi$ *martensite transformation and twinning deformation in fcc cobalt during surface mechanical attrition treatment.* Scripta Materialia, 2005. **52**: p. 547-551.
268. Walker, J.C., Ross, I. M. Rainforth, W. M., Lieblich, M., *TEM characterisation of near surface deformation resulting from lubricated sliding wear of aluminium alloy and composites.* Wear, 2007. **263**(1-6): p. 707-718.

269. Adachi, K., Hutchings, I.M., *Wear Mode Mapping for the Micro-scale Abrasion Test.* Wear, 2003. **255**: p. 23-29.
270. Shipway, P.H., Hodge, C.J.B., *Microabrasion of glass - the critical role of ridge formation.* Wear, 2000. **237**: p. 90-97.
271. Dwyer-Joyce, R.S., Heymer, J. *The entrainment of solid particles into rolling elastohydrodynamic contacts*. in *Proceedings of the 22nd Leeds-Lyon Symposium on Tribology, Lyon, France, 1995, D. Dowson et al., ed., Elsevier, Amsterdam, Tribology Series, 33, pp. 135–140.* 1996.
272. Shipway, P.H., Hogg, J.J., *Dependence of microscale abrasion mechanisms of WC-Co hardmetals on abrasive type.* Wear, 2005. **259**: p. 44-51.
273. Shipway, P.H., *A mechanical model for particle motion in the micro-scale abrasion wear test.* Wear, 2004. **257**: p. 984-991.
274. Shipway, P.H., Wirojanupatump, S., *The role of lubrication and corrosion in abrasion of materials in aqueous environments.* Tribology International, 2002. **35**(10): p. 661-667.
275. Mishina, H., Kojima, M., *Changes in human serum albumin on arthroplasty frictional surfaces.* Wear, 2008. **265**(5-6): p. 655-663.
276. Wimmer, M.A., Nassutt, R., Sprecher, C., Loos, J., Fischer, A., *Investigation on stick phemomena in metal-on-metal hip joints after resting period.* Proc Inst Mech Eng, 2006. **220**(Part: H. Engineering in Medicine): p. 219-227.
277. Que, L., Topoleski, D.T., *Third-body wear of cobalt-chromium-molybdenum implant alloys initiated by bone and poly(methyl methacrylate) particles.* Journal of biomedical materials research 2000. **50**(3): p. 322-330
278. *Shreir's Corrosion*. In Print, ed. Tony Richardson, Bob Cottis, and S.L. Rob Lindsay, David Scantlebury, Howard Stott, Mike Graham.
279. Lia, W., Li, D.Y., *Variations of work function and corrosion behaviors of deformed copper surfaces.* Applied Surface Science, 2005. **240**(1-4): p. 388-395
280. Enerhaug, J., Steinsmo, U., Grong, O., Hellevik, L.R., *Dissolution and Repassivation Kinetics of a 12.3Cr-2.6Mo-6.5Ni Super Martensitic Stainless Steel.* J Electrochem Soc, 2002. **149**(6): p. B256-B264.
281. Contu, F., Elsener, B., Assi, F. Bohini, H., *Repassivation Behavior of Metallic Implants in Inorganic and Physiological Electrolytes*, in *Materials for Medical Engineering*, H. Stallforth and P. Revell, Editors. 2005. p. 236-242.

References

1. X. Wu, N. Tao, Y. Hong, G. Liu, B. Xu, J. Lu, K. Lu, *Strain-induced grain refinement of cobalt during surface mechanical attrition treatmen*t, Acta Materialia 53 (3) (2005) 681-691.

2. S. Williams, J.L. Tipper, E. Ingham, M.H. Stone, J. Fisher, *In vitro analysis of the wear, wear debris and biological activity of surface-engineered coatings for use in metal-on-metal total hip replacements*, In Proceedings of Institution of Mechanical Engineers 217(H) (2003) 155-163.

3. http://ortho.muhealth.org/hipandknee/images/HipReplace.jpg.

4. http://www.hipsforyou.com/strykerceramichip.php.

5. D. Dowson, *New joints for the millennium: wear control in total replacement hip joints*, In Proceedings of Institution of Mechanical Engineers (H) 215 (4) (2001) 335-358.

6. A. Buford, T. Goswami, *Review of wear mechanisms in hip implants: Paper I – General*, Materials and Design 25(5) (2004) 385-393.

7. D. Dowson, C. Hardaker, M. Flett, G.H. Issac, *A hip joint simulator study of the performance of metal-on-metal joints. Part I: The role of materials*, The Journal of Arthroplasty 19(8) (2004) 118-123.

8. Z.M. Jin, M.H. Stone, E. Ingham, J. Fisher, *Biotribology*, Current Orthopaedics 20 (2006) 32-40.

9. P. Roberts, P. Grigoris, H. Bosch, N. Talwaker, *Resurfacing arthroplasty of the hip*, Current Orthopaedics 19 (2005) 263-279.

10. Hughs, D., *Hip resurfacing versus hip replacement - What, Why, Who and When? http://personal.strath.ac.uk/david.hughes/Papers/Hip_replacement_versus_hip_resurfacing.pdf*

11. D. Adams, S. Quigley, S., *Hip resurfacing: Past, present and future*, Journal of Orthopaedic Nursing 9 (2005) 87-94.

12. A. Wang, S. Yue, S., J.D. Bobyn, F.W. Chan, J.B. Medley, *Surface characterization of metal-on-metal hip implants tested in a hip simulator*, Wear 225-229 (pt.2) (1999) 708-715.

13. I. Catelas, J.D. Bobyn, J.B. Medley, J.J. Krygier, D.J. Zukor, O.L. Huk, *Size, shape, and composition of wear particles from metal-metal hip simulator testing:*

Effects of alloy and number of loading cycles, Journal of Biomedical Materials Research (A) 67 (1) (2003) 312-327.

14. A.A.J. Goldsmith, D. Dowson, G.H. Isaac, J.G. Lanscaster, *A Comparative Joint Simulator Study of the Wear of Metal-On-Metal and Alternative Material Combinations in Hip Replacements*, In Proceedings of the Institution of Mechanical Engineers (H) 214 (2000) 39-47.

15. P.S. Walker, M.J. Erkman, *Metal-on-metal lubrication in artificial human joints*, Wear 21(2) (1972) 377-392.

16. F. Liu, Z.M. Jin, F. Hirt, C. Rieker, P. Roberts, P. Grigoris, *Effect of wear of bearing surfaces on elastohydrodynamic lubrication of metal-on-metal hip implants.* In Proceedings of the Institution of Mechanical Engineers (H) 219 (5) (2005) 319-328.

17. D. Dowson, Z.M. Jin, *Metal-on-metal hip joint tribology*, In Proceedings of the Institution of Mechanical Engineers (H) 220 (2005) 107-118.

18. J.B. Medley, J.D. Bobyn, J.J. Krygler, F.W. Chan, M. Tanzer, G.E. Roter, *Elastohydrodynamic lubrication and wear of metal-on-metal hip implant*, In World Tribology Forum in Arthroplasty. 2001 Bern: Hans Huber.

18. F.W. Chan, J.D. Bobyn, J.B. Medley, J.J. Krygier, S.Yue, M. Tanzer, *Engineering issues and wear performance of metal on metal hip implants*, Clinical orthopaedics and related research 333(1996) 96-107.

19. Varano, R., Bobyn, D., Medley, J.B., Yue, S., *The effect of microstructure on the wear of cobalt-based alloys used in metal-on-metal hip implants* Proc I Mech E (H), 2006. **220**: p. 145-159.

20. Chan, F.W., Bobyn, J.D., Medley, J.B., Krygier, J.J., Yue, S., Tanzer, M., *Engineering issues and wear performance of metal on metal hip implants.* Clinical orthopaedics and related research 1996(333): p. 96-107.

21. Chan, F.W., Bobyn, J.D., Medley, J.B., Krygier, J.J., Tanzer, M., *Wear and lubrication of metal-on-metal hip implants.* Clin Orthop, 1999. **369**: p. 10-24.

22. P.S. Walker, B.L. Gold, *Tribology (friction, lubrication and wear) of all- metal artificial hip joints*, Wear 17 (4) (1971) 285-299.

23. M.A.L. Hernandez-Rodriguez, R. D. Mercado-Solis, A.J. Perez-Unzueta, D.I. Martinez-Delgado, M. Cantu-Sifuentes, *Wear of cast metal-metal pairs for total replacement hip prostheses*, Wear 259(7-12) (2005) 958-963.

24. N.J. Hallab, J.J. Jacobs, *Orthopedic implant fretting corrosion*, Corrosion Reviews 21(2-3) (2003) 183-213.

25. N.J. Hallab, C. Messina, A. Skipor, J.J. Jacobs, *Difference in the fretting corrosion of metal-metal and ceramic-metal modular junctions of total hip replacements*, Journal of Orthopaedic Research 22 (2004) 250-259.

26. J.L. Gilbert, C.A. Buckley, J.J. Jacobs, *In-Vivo Corrosion of Modular Hip Prosthesis Components in Mixed and Similar Metal Combinations: The Effect of Crevice, Stress, Motion and Alloy Coupling*, Journal of Biomedical Material Research 27 (12) (1993) 1533–1544.

27. H.J. Ratzer-Schiebe, *The relationship between repassivation behavior and pitting corrosion for ti and Ti-6Al-4V*, Corrosion 34 (1978) 437-442.

28. J.H. Dumbleton, *Tribology of natural and artificial joints* 1981 Elsevier, Amsterdam.

29. J.L. Tipper, E. Ingham, Z. M. Jin, J. Fisher, *The science of metal-on-metal articulation*, Current Orthopaedics 19 (2005) 280-287.

30. W.D. Callister, *Materials science and engineering: an introduction*, 5th ed. 1999 John Wiley & Sons Inc. p.579.

31. R. Venugopalan, J. Gaydon, *A review of corrosion behaviour of surgical implant alloys*, Technical Review Note 1999-2001 Perkin Elmer Instruments, Princeton Applied Research. p. 1-10.

32. P.A. Dearnley, *A review of metallic, ceramic and surface treated materials used for bearing surfaces in human joint replacements.* In Proceedings of the Institution of Mechanical Engineers (H) 3(1999) 107-135.

33. G.K. Mckee, J. Watson-Farrar, *Replacement of arthritic hips by the Mckee-Farrar prosthsis*, Journal of Bone & Joint Surgery 48 (B) (1966) 245-259.

34. A. Marti, *Cobalt-base alloys used in bone surgery*, Injury 31 (2000) S-D18-21.

35. Park, J.B., Kon Kim, Y., *Metallic Biomaterials*, in *The Biomedical Engineering Handbook, 2nd Ed.*, J.D. Bronzino, Editor. 2000, CRC Press LLC: Boca Raton.

36. Y. Yan, A. Neville, D. Dowson, S. Williams, *Tribocorrosion in implants-assessing high carbon and low carbon Co-Cr-Mo alloys by in situ electrochemical measurements* , Tribology International 39 (12) (2006) 1509-1517.

37. J.E.P. Metcalf, J. Cawley, T.J. Band, *Cobalt Chromium Molybdenum metal-on-metal resurfacing orthopaedic hip devices*, Business briefing: medical device manufacturing & technology (2004) 1-7.

38. A. Salinas-Rodriguez, *The Role of the FCC-HCP phase transformation during the plastic deformation of Co-Cr-Mo-C alloys for biomedical applications,* in *ASTM Special Technical Publication 1365*, R.L.K. J.A. Disegi, R. Pilliar, Editors. 1999 American Society for Testing and Materials, West Conshokochen, PA. p. 108-121.

39. H.F. Lopez, A. Saldivar, P. Huang, P. *Development and properties of ε-martensite in CoCrMo alloys for biomaterials applications*. in Proceedings of 2nd International Alloy Conference, 1999, Davos, Switzerland: Kluwer Academic/Plenum Publishers, New York.

40. R. Büscher, A. Fischer, *The pathways of dynamic recrystallization in all-metal hip joints*, Wear 259 (2005) 887-897.

41. B.G. Weber, *Experience with the Metasul total hip bearing system,* Clinical Orthopaedics 3295 (1996) S78-88.

42. C. Harlan, M.D. Amstutz, *History of Hip Resurfacing*, http://www.jri-oh.com/jri_hip_surface.php. Access date: 01.Dec 2007.

43. M. Wagner, H. Wagner, *Prelinimary results of uncemented metal-on-metal stemmed and resrfacing hip replacement arthroplasty,* Clinical Orthopaedics 329 (S) (1996) S89-98.

44. Z.M. Jin, J.L. Tipper, M.H. Stone, E. Ingham, J. Fisher, *Hip joints, artificial,* in *Encyclopedia of Medical Devices and Instrumentation*, J.G. Webster, Editor. 2006 John Wiley & Sons, Inc.

45. J. Cawley, J.E.P. Metcalf, A.H., Jones, T.J. Band, D.S. Skupien, *A tribological study of cobalt chromium molybdenum alloys used in metal-on-metal resurfacing hip arthroplasty,* Wear 255 (pt.2) (2003) 999-1006.

46. M.A. Wimmer, J. Loos, R. Nassutt, M. Heitkemper, A. Fischer, *The acting wear mechanisms on metal-on-metal hip joint bearings: in vitro results*, Wear (250) (2001) 129-139.

47. http://www.wheelessonline.com/ortho/gait. Access date 01-01-2009.

48. J.P. Paul, *Force actions transmitted by joints in the human body.* In Proceedings of the Royal Society of London (Series B) Biological Sciences 192(1107) (1976) 163-172.

49. A.S. Litsky, M. Spector, *Biomaterials*, in *Orthopaedic basic science*, S.R. Simon, Editor. 1994 American academy of orthopaedic surgeons. p. 470-473.

50. G. Bergmann, F. Graichen, A. Rohlmann, *Hip joint loading during walking and running, measured in two patients*, Journal of Biomechanics 26(1993) 969.

51. G. Bergmann, F. Graichen, A. Rohlmann, *Is staircase walking a risk for the fixation of hip implants?* Journal of Biomechanics 28(5) (1995)535-53.

52. Jin, Z.M., Dowson, D., Fisher, J., *Analysis of fluid film lubrication in artificial hip joint replacements with surfaces of high elastic modulus.* Proceedings of the Institution of Mechanical Engineers, Part H: Journal of Engineering in Medicine, 1997. **211**(3): p. 247-256.

53. M. Semlitsch, H.G. Willert, *Clinical wear behavior of ultra-high molecular weight polyethylene cups paired with metal and ceramic ball heads in comparison to metal-on-metal pairings of hip joint replacements.* In Proceedings of Institution of Mechanical Engineers 211(H) (1997) 73-88.

54. P.F. Doorn, P.A. Campbell, J. Worrall, P.D. Benya, H.A. McKellop, H.C. Amstutz, *Metal wear particle characterization from metal on metal total hip*

replacements: transmission electron microscopy study of periprosthetic tissues and isolated particles, Journal of Biomedical Materials Research 42 (1998) 103-111.

55. T. Hanawa, *Metal ion release from metal implants*, Materials Science and Engineering C 24(6-8 SPEC ISS) (2004) 745-752.

56. T.J. Peters, *Serum Albumin,* Advances in Protein Chemistry, 37 (1985) 161-245.

57. C.J. Van Oss, R.J. Good, *Orientation of the water molecules of hydration of human serum albumin*, Journal of Protein Chemistry 7(2) (1988) 179-183.

58. G. Burnstock, *Purine-mediated signalling in pain and visceral perception.* Trends Pharmacological Science 22 (2001) 182-188.

59. D.J. Wood, *The characterization of particulate debris obtained from failed orthopedic implants*. 1993, San Jose State University, College of Material Engineering.

60. K.H. Steen, P.W. Reeh, *Sustained graded pain and hyperalgesia from harmless experimental tissue acidosis in human skin*, Neuroscience letter 154 (1993) 113-116.

61. B.D. Ratner, A.S. Hoffman, F.J. Schoen, J.E. Lemons, *Biomaterials Science, an Introduction to Materials in Medicine*, 2nd Ed. 2004 Elsevier Academic Press.

62. S.E. Moulton, J.N. Barisci, A. Bath, R. Stella, G.G. Wallace, *Investigation of protein adsorption and electrochemical behavior at a gold electrode*, Journal of Colloid Interface Science 15 (261-2) (2003) 312-319.

63. S. Hiromoto, K. Noda, T. Hanawa, *Electrochemical properties of an interface between titanium and fibroblasts L929.* Electrochimica Acta 48 (4) (2002) 387-396.

64. R.T.T. Gettens, Gilbert, J. L. *Fibrinogen Adsorption onto 316L Stainless Steel: Voltage Effects*. in Proceedings of the IEEE 32nd Annual Northeast Bioengineering Conference, 2006.

65. M.M. de Ficquelmont-Loizos, H. Takenouti, W. Kante, *Long-time and short-time investigation of the electrode interface through electrochemical impedance measurements. Application to adsorption of human serum albumin onto glassy carbon rotating disc electrode*, Journal of Electroanalytical Chemistry 428 (1-2) (1997) 129-140.

66. J.M. Kleijn, D. Barten, M.A.C. Stuart, *Adsorption of charged macromolecules at a gold electrode*, Langmuir 20 (22) (2004) 9703-9713.

67. A.P. Serro, M.P. Gispert, M.C.L. Martins, P. Brogueira, R. Colaco, B. Saramago, *Adsorption of albumin on prosthetic materials: Implication for tribological behaviour,* Journal of Biomedical Materials Research (A) 78(3) (2006) 581-589.

68. C.P. Sharma., G.C.F. Clark, D.F. Williams, *The adsorption of proteins on metal surfaces*, Engineering in Medicine 10(1) (1981) 11-16.

69. P. Bernabeu, L. Tamisier, A. de Cesare, A. Caprani, *Study of the adsorption of albumin on a platinum rotating disk electrode using impedance measurements.* Electrochimica Acta 33(8) (1988) 1129-1136.

70. K.H. Choi, J.M. Friedt, W. Laureyn, F. Frederix, A. Campitelli, G. Borghs, *Investigation of protein adsorption with simultaneous measurements of atomic force microscope and quartz crystal microbalance*, Journal of Vacuum Science & Technology B (Microelectronics and Nanometer Structures) 21(4) (2003). 1433-1436.

71. P. Ying, A.S. Viana, L.M. Abrantes, G. Jin, *Adsorption of human serum albumin onto gold: A combined electrochemical and ellipsometric study*, Journal of Colloid and Interface Science 279 (1) (2004) 95-99.

72. M. Malmsten, *Formation of adsorbed protein layers*, Journal of Colloid and Interface Science 207 (1998) 186-199.

73. K. Merritt, S.A. Brown, *Effect of proteins and pH on fretting corrosion and metal ion release*, Journal of Biomedical Materials Research 22(2) (1988) 111-120.

74. P. Sven, *Determination of transferrin isoproteins in human cerebrospinal fluid using isoelectric focusing and zone immunoelectrophoresis assay*, Electrophoresis 8(11) (1987) 515-517.

75. M. Salim, B. O'Sullivan, S.L. McArthur, P.C. Wright, *Characterization of fibrinogen adsorption onto glass microcapillary surfaces by ELISA*, Lab on Chip, 7 (2007). 64 - 70.

76. P.Geborek, F.A. Wollheim, *Synovial fluid*, in *Mechanics of Human Joints, Physiology, Pathophysiology and Treatment*, V. Wright and E.L. Radin, Editors. 1993, Marcel Dekker, New York. p. 117-136.

77. K.L. Jones, C.R. O'Melia, *Protein and humic acid adsorption onto hydrophilic membrane surfaces: Effects of pH and ionic strength*, Journal of Membrane Science 165 (1) (2000) 31-46.

78. N. R. Cabilio, S. Omanovic, S.G. Roscoe, *Electrochemical studies of the effect of temperature and pH on the adsorption of alpha-lactalbumin at Pt*, Langmuir 16(22) (2000) 8480-8488.

79. D.T. Hughes Wassell, G. Embery, *Adsorption of bovine serum albumin on to titanium powder*, Biomaterials 17 (9) (1996) 859-864.

80. M. Malmsten, *Biopolymers at Interfaces*, 1998 Marcel Dekker, New York.

81. Y. Okazaki, T. Tateishi,Y. Ito, *Corrosion resistance of implant alloys in pseudo physiological solution and role of alloying elements in passive films*, Materials Transactions, JIM, 38(1) (1997) 78-84.

82. F. Lacour, R. Torresi, C. Gabrielli, A. Caprani, *Comparison of the and the double-layer capacitance methods for measuring the kinetics of the adsorption of bovine serum albumin onto a gold electrode*, Journal of the Electrochemical Society 139 (6) (1992) 1619-1622.

83. S. Omanovic, S.G. Roscoe, *Electrochemical studies of the adsorption behavior of bovine serum albumin on stainless steel*, Langmuir 15(23) (1999) 8315-8321.

84. S.E. Moulton, J.N. Barisci, A. Bath, R. Stella, S.G. Wallace, *Studies of double layer capacitance and electron transfer at a gold electrode exposed to protein solutions*, Electrochimica Acta 49 (24) (2004) 4223-4230.

85. L. Gassa, M.F.L. De Mele, *Influence of the composition of the biological media on the electrochemical response of the metallic components of biomaterials*. In Proceedings of EUROCORR: European Corrosion Congress, 2005 Lisbon, Portugal.

86. Q. Tang, C.H. Xu, S.Q. Shi, L.M. Zhou, *Formation and characterization of protein patterns on the surfaces with different properties*, Synthetic Metals 147 (1-3) (2004) 247-52.

87. H.P. Tuemmler, R. Thull, *Model of the metal/tissue connection of implants made of titanium or tantalum*. in Biological and Biomechanical Performance of Biomaterials,1986 Elsevier, Amsterdam.

88. J.L. Gilbert, Z. Bai, J. Bearinger, S. Megremis, *The dynamics of oxide films on metallic biomaterials*. in Proceedings of the Materials and Processes of Medical Devices Conference, 2003 Anaheim, United State.

89. F. Lacour, J.P. Frayret, A. Caprani, A., *Effect of the electrode roughness on the kinetics of albumin adsorption at a rotating disk electrode investigated by double-layer capacitance measurements*, Journal of the Electrochemical Society, 139 (1) (1992) 153-159.

90. F. Contu, B. Elsener, H. Bohni, *Serum effect on the electrochemical behaviour of titanium, Ti6Al4V and Ti6Al7Nb alloys in sulphuric acid and sodium hydroxide,* Corrosion Science 46(9) (2004) 2241-2254.

91. H.P. Jost, *Lubrication, Education and Research - A report on the Present Position and Industry's Needs,* Her Majesty's Stationery Office, 1966 London.

92. I.M. Hutchings, *Tribology: friction and wear of engineering materials* 1992 Edward Arnold, London.

93. J.A. Williams, *Engineering Tribology* 1998 Oxford University Press, Oxford.

94. Dowson, D., *A comparative study of the performance of metallic and ceramic femoral head components in total replacement hip joints.* Wear, 1995. **190**(2): p. 171-183.

95. A. Unsworth, *The effects of lubrication in hip prostheses,* Physics in Medicine and Biology 23(2) (1978) 253-268.

96. J. Black, *Orthopaedic Biomaterials in Research and Practice* 1988 Churchill Livingstone Inc., New York.

97. S.L. Smith, D. Dowson, A.A.J. Goldsmith, *The lubrication of metal-on-metal total hip joints: A slidedown the Stribeck curve.* in Proceedings of the Institution of Mechanical Engineers (J) 215 (5) (2001) 483-493.

98. B.J. Hamrock, D. Dowson, *Elastohydrodynamic lubrication of elliptical contacts for materials of low elastic modulus. I: fill flooded conjunction*, Transaction ASME, Journal of Lubrication Technology 100(2) (1978) 236-245.

99. R.I. Tanner, *An alternative mechanism for the lubrication of synovial joints.* Physics in Medicine and Biology 11 (1966) 119-127.

100. H.P. Jones, P.S. Walker, *Casting techniques applied to the study of human joints.* Journal Inst Science Technology 14 (1968) 57-58

101. F.C. Linn, *Lubrication of animal joint II- the mechanism*, Journal of Biomechanics (1) (1968) 193-205.

102. F.C. Linn, E.L. Radin, *Lubrication of animal joints III - the effect of certain chemical alteration of the cartilage and lubricant.* Arthritis & Rheumatism (11) (1968) 674-682.

103. D. Dowson, Z.M. Jin, Z. M., *Microelastohydrodynamic lubrication of low-elastic-modulus solids on rigid substrates.* Journal of Physics (D) 25 (1A) (1992) 116-123.

104. D. Dowson, Z.M. Jin, *Micro-elastohydrodynamic lubrication of synovial joints*, Engineering in Medicine 15 (1986) 63-65.

105. B.J. Roberts, A. Unsworth, N. Mian, *Modes of lubrication in human hip joints.* Annals of the Rheumatic Diseases 41 (1982) 221-224.

106. S.C. Scholes, A. Unsworth, *Comparison of friction and lubrication of different hip prostheses.* In Proceedings of the Institution of Mechanical Engineers (H) 214(1) (2000) 49-57.

107. Jin, Z.M., Dowson, D., Fisher, J. *Lubrication mechanisms in metal-on-metal hip joint replacements*. 1996. Toronto, Can: Soc for Biomaterials, St. Louis Park, MN, USA.

108. Vassiliou, K., Elfick, A. P. D., Scholes, S. C., Unsworth, A., *The effect of 'running-in' on the tribology and surface morphology of metal-on-metal Birmingham hip resurfacing device in simulator studies.* Proceedings of the Institution of Mechanical Engineers, Part H: Journal of Engineering in Medicine, 2006. **220**(2): p. 269-277.

109. J.J. Jacobs, K.A. Skipor, P.A. Campbell, N.I. Hallab, R.M.Urban, H.C. Amstutz, *Can Metal Levels Be Used to Monitor Metal-on-Metal Hip Arthroplasties?* The Journal of Arthroplasty 19(8) (2004) 59-65.

110. D. Dowson, *Tribological principles in metal-on-metal hip joint design.* In Proceedings of the Institution of Mechanical Engineers (H) 220 (2006) 161-170.

111. A. Wang, J.D. Bobyn, S.Yue, J.B. Medley, F.W. Chan, *Residual abrasive material from surface grinding of metal-metal hip implants: A source of third-body wear?*in ASTM Special Technical Publication 1365 1999 American Society for Testing and Materials, USA. p. 125-134.

112. D.W. Howie, R.W. McCalden, N.S. Nawana, K. Costi, M.J. Pearcy, C. Subramanian, *The Long-Term Wear of Retrieved McKee-Farrar Metal-on-Metal Total Hip Prostheses*, The Journal of Arthroplasty 20 (3) (2005) 350-357.

113. A.L.I. Lippincott, J.M. Dowling, J.B. Medley, R.W. Christensen, *Temporomandibular joint arthroplasty using metal-on-metal and acrylic-on-metal configurations : Wear in laboratory tests and in retrievals,* Surgical Technology International (VIII) (2000) 321-330.

114. G. Reinisch, K.P. Judmann, C. Lhotka, F. Lintner, K.A. Zweymuller, *Retrieval study of uncemented metal-metal hip prostheses revised for early loosening,* Biomaterials 24(6) (2003) 1081-1091.

115. C. Rieker, M. Shen, P. Kottig, *In-vivo tribological performance of 177 metal-on-metal hip articulations*. In World Tribology Forum in Arthroplasty 2001 Hans Huber, Bern .

116. T.P. Schmalzried, J.J. Callaghan, *Current concept review - wear in total hip and knee replacements,* Journal of Bone & Joint Surgery (America) 81 (1999) 115-136.

117. J.A. Davidson, *Characteristics of metal and ceramic total hip bearing surfaces and their effect on long-term ultra molecular weight polyethylene wear*, Clinical orthopaedics & Related Research 294 (1993) 361-378.

118. R. Büscher, G. Tager, W. Dudzinski, B. Gleising, M.A. Wimmer, A. Fischer, *Subsurface microstructure of metal-on-metal hip joints and its relationship to wear particle generation*, Journal of Biomedical Materials Research (B) 72(1) (2005) 206-214.

119. M. Silva, C. Heisel, T.P. Schmalzried, *Metal-on-metal total hip replacement.* Clinical orthopaedics & Related Research 430 (2005) 53-61.

120. Z.M. Jin, J.B. Medley, D. Dowson, *Fluid film lubrication in artificial hip joints.* in Proceedings of the 29th Leeds-Lyon symposium of Tribology 2003.

121. J.L. Tipper, E. Ingham, J.L. Hailey, A.A. Besong, J. Fisher, B.S. Wroblewsky, M.H. Stone, *Quantitative analysis of polyethylene wear debris, wear rate and head damage in retrieved Charnley hip protheses.* Journal of Materials Science: Materials in Medicine 11 (2000) 117-124.

122. J,L,Tipper, P.J.Firkins, E. Ingham, J. Fisher, M.H. Stone, R. Farrar, *Quantitative analysis of the wear and wear debris from low and high carbon content cobalt*

chrome alloys used in metal on metal total hip replacements. Journal of Materials Science: Materials in Medicine 10(6) (1999) 353-362.

123. T.R. Green, J. Fisher, J.B. Matthews, M.H. Stone, E. Ingham, *Effect of size and dose on bone resorption activity of macrophages in vitro by clinically relevant ultra high molecular weight polyethylene particles.* Journal of Biomedical Materials Research: Applied Biomaterials 53 (2000) 490-497.

124. M.A. Germain, *Biological reactions to cobalt chrome wear particles*. PhD dissertation in School of Biochemistry and Molecular Biology. 2002, University of Leeds: Leeds.

125. M.A. Germain, A. Hatton, S. Williams, J.B. Matthews, M.H. Stone, J. Fisher, E. Ingham, *Comparison of the cytotoxicity of clinically relevant cobalt-chromium and alumina ceramic wear particles in vitro,* Biomaterials 24 (2003) 469-479.

126. C.G. Lewis, F.W. Sunderman Jr., *Metal carcinogenesis in total joint arthroplasty: Animal models*, Clinical Orthopaedics 329 (S) (1996) S264-S268.

127. A.L. Galvin, M.M. Endo, J.L. Tipper, E. Ingham, J. Fisher, *Functional biological activity and osteolytic potential of non-crosslinked and cross-linked UHMWPE hip joint prostheses*. In Transactions of the 7th World Biomaterials Congress 2004 Sydney.

128. J.Q. Yao, M.P. Laurent, T.S. Johnson, C.R. Blanchard, R.D. Crowninshield, *The influences of lubricant and material on polymer/CoCr sliding friction*, Wear 255(1-6) (2003) 780-784.

129. T. Ahlroos, *Effect of lubricant on the wear of prosthetic joint materials*, PhD Thesis, in School of Mechanical Engineering. 2001, Helsinki University of Technology: Finland

130. B. Zhou, S. Shi, X. Wang, *Microstructures and wear resistance of medical CoCrMoC alloys*, Rare Metal Materials and Engineering 35(1) (2006) 105-109.

131. P. Huang, A. Salinas-Rodriguez, H.F. Lopez, *Tribological behaviour of cast and wrought Co-Cr-Mo implant alloys*, Materials Science and Technology 15(11) (1999) 1324-30.

132. J.G. Bowsher, J. Nevelos, P.A. Williams, J.C. Shelton, *'Severe' wear challenge to 'as-cast' and 'double heat-treated' large-diameter metal-on-metal hip bearings.* In Proceedings of the Institution of Mechanical Engineers (H) 220(2) (2006) 135-143.

133. Y. Yan, *Corrosion and tribo-corrosion behaviour of metallic orthopaedic implant materials*, PhD Thesis, in School of Mechanical Engineering. 2006, University of Leeds: Leeds.

134. P.E. Sinnett-Jones, J.A. Wharton, R.J.K. Wood, *Micro-abrasion-corrosion of a CoCrMo alloy in simulated artificial hip joint environments*, Wear 259(7-12) (2005) 898-909.

135. D. Sun, J.A. Wharton, R.J.K. Wood, L. Ma, M.W. Rainforth, *Microabrasion-corrosion of cast CoCrMo alloy in simulated body fluids*, Tribology International 42(1) (2009) 99-110.

136. T. D. Warner, I. Vojnovic, D. Bishop-Bailey, J.A. Mitchell, *Influence of plasma protein on the potencies of inhibitors of cyclooxygenase-1 and -2*, The FASEB Journal 20 (2006) 542-544.

137. D. Landolt, *Corrosion and surface chemistry of metals* 2007 EPFLPress, Switzerland.

138. *Impedance Spectroscopy: Theory, Experiment, and Applications*, E. Barsoukov and J.R. Macdonald Editors. 2005 Wiley-IEEE.

139. J.J. Jacobs, J.L. Gilbert, R.M. Urban, *Current concepts review: Corrosion of metal orthopaedic implants*, Journal of Bone Joint Surgery (America) 80 (1998) 268-282.

140. M.G. Fontana, *Corrosion engineering* (2nd ed.) 1978 McGraw-Hill, New York

141. F. Contu, B. Elsener, H. Bohni, *Electrochemical behavior of CoCrMo alloy in the active state in acidic and alkaline buffered solutions*, Journal of Electrochemistry Society, 150(9) (2003) B419-B424.

142. J.B. Park, R.S. Lakes, *Metallic Implant Materials*, in *Biomaterials - an Introduction* 1992, Plenum Press, New York. p. 75-115.

143. R.M. Urban, J.J. Jacobs, J.L. Gilbert, J.O. Galante, *Migration of corrosion products from modular hip prostheses - Particle microanalysis and histrophathological findings*. Journal of Bone & Joint Surgery 76 (A) (1994) 1345-1359.

144. S.J. MacDonald, R.W. McCalden, D.G. Chess, R.B. Bourne, C.H. Rorabeck, D. Cleland, F. Leung, *Metal-on-metal versus polyethylene in hip arthroplasty: a randomized clinical trial*, Clinical Orthopaedics 406 (2003) 282-296.

145. D. Jones, H. Lucas, M. O'Driscoll, C. Price, B. Wibberley, *Cobalt toxicity after McKee hip arthroplasty*, Journal of Bone Joint Surgery 57(3) (1975) 389-396.

146. K. Merritt, S.A. Brown, *Release of hexavalent chromium from corrosion of stainless steel and cobalt-chromium alloys*, Journal of biomechanical Materials Research 29 (1995) 627-633.

147. A. Sargeant, T. Goswami, *Hip implants- Paper VI- Ion Concentrations*, Materials & Design 28(1) (2005) 155-171.

148. M.T. Clarke, P.T.H. Lee, A. Arora, R.N. Villar, *Levels of metal ions after small- and largediameter metal-on-metal hip arthroplasty*, Journal of Bone & Joint Surgery 85-B (6) (2003) 913-917.

149. C. Montero-Ocampo, A.S. Rodriguez, *Effect of carbon content on the resistance to localized corrosion of as-cast cobalt-based alloys in an aqueous chloride solution*, Journal of Biomedical Material Research 29 (4) (1995) 441-453.

150. A. Igual Munoz, S. Mischler, *Interactive effects of albumin and phosphate ions on the corrosion of a CoCrMo implant alloy.* Journal of Electrochemistry Society 154 (10) (2007) C562-C570.

151. S. Kurz, A.W. Hodgson, S. Virtanen, V. Fervel, S. Mischler, *Corrosion characterisation of passive films on CoCrMo with electrochemical techniques in saline and simulated biological solutions,* European Cells & Materials 3(1) 2002 26-27.

152. G.J. Fagan, H. Wayment, D.L. Morris, P.A. Crosby, *The Albumin Cobalt Binding Test: Analytical Performance of a New Automated Chemistry Assay for the Detection of Ischemia Modified Albumin (IMA™)*, Journal of Clinical Ligand Assay 25(2) 2002 178-187.

153. J.P. Lassac, B. Sakar, *Characterization of the copper (II) and nickel (II) transport site of human serum albumin. studies of copper (II) and nickel (II) binding to peptide 1-24 of human serum albumin by 13 C and 1 H NMR spectroscopy*, Biochemistry 23(12) (1984) 2831-2838.

154. W. Bal, J. Christodoulou, P. Sadler, A. Tucker, *Multi-metal binding site of serum albumin*, Journal of Inorganic Biochemistry, 70 (1998) 33-39.

155. http://commons.wikimedia.org/wiki/File:Vitamin_B12.png. Access date: 01.01.2009.

156. J.J. Jacobs, H.J. Hallab, A.K. Skipor, R.M. Urban, *Metal degradation products: a cause for concern in metal-metal bearings?* Clinical Orthopaedics Related Research 417 (2003) 139-147.

157. D.F. Williams, G.C.F. Clark, *The corrosion of pure cobalt in physiological media*, Journal of Materials Science 17(6) (1982) 1675-1682.

158. R.L.Williams, S.A. Brown, K. Merritt, K., *Electrochemical studies on the influence of proteins on the corrosion of implant alloys*, Biomaterials 9 (1988) 181-186.

159. A.C. Lewis, M.R. Kilburn, I. Papageorgiou, G.C. Allen, C.P. Case, *Effect of synovial fluid, phosphate-buffered saline solution, and water on the dissolution and corrosion properties of CoCrMo alloys as used in orthopaedic implants*, Journal of Biomedical Materials Research (A) 73(4) (2005) 456-467.

160. F. Contu, B. Elsener, H. Bohni, *Corrosion behaviour of CoCrMo implant alloy during fretting in bovine serum,* Corrosion Science 47 (2005) 1863-1875.

161. J.R. Goldberg, J.L. Gilbert, *Electrochemical response of CoCrMo to high-speed fracture of its metal oxide using an electrochemical scratch test method*, Journal of Biomedical Materials Research 37(3) (1997) 421-431.

162. Jones, D., *Principals and Prevention of Corrosion*. 2 ed. 1996: Prentice-Hall. 84-86.

163. R. Cottis, S. Turgoose, *Electrochemical Impedance and Noise*, in Corrosion Testing Made Easy , B.C. Syrett editor, 1999 NACE International, USA.

164. J.L. Dawson, *Electrochemical Noise Measurement*, in electrochemical noise measurement for corrosion applications, J.R. Kearns and J.R. Scully, editors. 1996 ASTM International. p. 3-35.

165. S. Mischler, *Triboelectrochemical techniques and interpretation methods in tribocorrosion: A comparative evaluation*, Tribology International 41(7) (2008) 573-583.

166. D. Landolt, S. Mischler, M. Stemp, *Electrochemical methods in tribocorrosion: a critical appraisal*, Electrochimica Acta 46 (2001) 3913-3929.

167. D. Sun, J. Wharton, R.J.K. Wood, *Effect of protein adsorption on the wear-corrosion behaviour of cast CoCrMo alloy in simulated healthy and infected joint environments*, in the 16th International Colloquium of Tribology 2008 Stuttgart/Ostfildern, Germany.

168. K.S. Tan, J.A. Wharton, R.J. Wood, *Solid particle erosion-corrosion behaviour of a novel HVOF nickel aluminium bronze coating for marine applications - Correlation between mass loss and electrochemical measurements*, Wear 258(1-4 Special issue) (2005) 629-640.

169. R.J.K. Wood, J.A. Wharton, A.J. Speyer, K.S. Tan, *Investigation of erosion-corrosion processes using electrochemical noise measurements*, Tribology International 35(10) (2002) 631-641.

170. R.J.K. Wood, A.J. Speyer, *Erosion-corrosion of candidate HVOF aluminium-based marine coatings*, Wear 256(5) (2004) 545-556.

171. Y. Yan, A. Neville, D. Dowson, *Understanding the role of corrosion in the degradation of metal-on-metal implants*. In Proceedings of Institution of Mechanical Engineers (H) 220(2) (2006) 173-181.

172. S.W. Watson, F.J. Friedersdorf, B.W. Madsen, S.D. Cramer, *Methods of measuring wear-corrosion synergism*, Wear 181-183(2) (1995) 476-484.

173. *ASTM G119-93 Standard guide for determining synergism between wear and corrosion*, in ASTM handbook. 1993. p. 502-507.

174. X.Y. Wang, D.Y. Li, *Application of an electrochemical scratch technique to evaluate contributions of mechanical and electrochemical attacks to corrosive wear of materials*, Wear 259(7-12) 2005 1490-1496.

175. P.Q. Wu, J.P. Celis, *Electrochemical noise measurements on stainless steel during corrosion-wear in sliding contacts*, Wear 265(5) (2004) 480-490.

176. P. Ponthiaux, F. Wenger, D. Drees, J.P. Celis, *Electrochemical techniques for studying tribocorrosion processes*, Wear 256(5) 2004 459-468.

177. J.L. Gilbert, J.J. Jacobs, *The Mechanical and Electrochemical Processes Associated with Taper Fretting Crevice Corrosion.*, in Modularity of Orthopedic Implants, ASTM STP 1301, J.E. Parr, M.B. Mayor, and D.E. Marlow, Editors. 1997 ASTM Philadelphia, US. p. 45-49.

178. J.L. Gilbert, C.A. Buckley, E.P. Lautenschlager, *Titamium oxide film fracture and repassivation: The effect of potential, pH, and aeration*, in Medical Applications of Titanium and Its Alloys: The Materials and Biological Issues, ASTM STP 1272, S.A. Brown and J.E. Lemons, Editors. 1996 ASTM Philadelphia, US. p. 199-218.

179. J. Gilbert, *Novel Electrochemical Techniques for Analysis of Metallic Biomaterials Surfaces.* Medical Plastics and Biomaterials, May 1998. p.16.

180. I. Garcia, D. Drees, J.P. Celis, *Corrosion-wear of passivating materials in sliding contacts based on a concept of active wear track area*, Wear 249(5-6) (2001) 452-460.

181. M. Stemp, S. Mischler, D. Landolt, *The effect of mechanical and electrochemical parameters on the tribocorrosion rate of stainless steel in sulphuric acid*, Wear 255(1-6) (2003) 466-475.

182. S. Hiromoto, S. Mischler, *The influence of proteins on the fretting-corrosion behaviour of a Ti6Al4V*, Wear 261(9) (2006) 1002-1011.

183. A. Iwabuchi, J.W. Lee, M. Uchidate, *Synergistic effect of fretting wear and sliding wear of Cr-alloy and Ti alloy in Hanks' solution*, Wear 263(1-6) (2007) 492-500.

184. R. Oltra, B. Chapey, L. Renaud, *Abrasion-corrosion studies of passive stainless steels in acidic media: combination of acoustic emission and electrochemical techniques*, Wear 186-187(2) (1995) 533-541.

185. D. Sun, D., J.A. Wharton, R.J.K. Wood, *Tribo-Corrosion of cast CoCrMo alloy - abrasive size and concentration effects*. In the 35th Leeds-Lyon Tribology Symposium 2008 Leeds. Tribology International (2009), doi:10.1016/j.triboint.2009.03.018.

186. D. Sun, J. Wharton, R.J.K. Wood, *The Effects of Proteins and pH on Tribo-Corrosion Performance of Cast CoCrMo – a Combined Electrochemical and Tribological Study*. In the 5th China International symposium on Tribology. . Beijing 2008. Tribology – Materials, Surfaces & Interfaces (2009), doi: 10.1179/175158309X408315.

187. D. Sun, J.A. Wharton, R.J.K. Wood, *Microabrasion mechanisms of cast CoCrMo in simulated body fluids*. In the 1st International Conference on Abrasion Processes 2008 Cambridge. Wear (2009), doi: 10.1016/j.wear.2009.03.005.

188. D. Sun, J.A. Wharton, R.J.K. Wood, *Microabrasion-corrosion of cast CoCrMo-Effects of micron and sub-micron sized abrasives*. In *the 17th International Conference on Wear of Materials* 2009 Las Vegas, US. Wear (2009) (doi:10.1016/j.wear.2009.01.011)

189. A. Neville, M. Reyes, H. Xu, *Examining corrosion effects and corrosion/erosion interactions on metallic materials in aqueous slurries*, Tribology International 35(10) (2002) 643-650.

190. B.T. Rubin, *Kinetics of oxide film repair on titanium.* Electroanalytical Interfacial Electrochemistry 58 (1975) 323-337.

191. M. Seo, M. Chiba, K. Suzuki, *Nano-mechano-electrochemistry of the iron (100) surface in solution,* Journal of Electroanalytical Chemistry 473(1) (1999) 49-53.

192. M. Seo, M. Chiba, *Nano-mechano-electrochemistry of passive metal surfaces*, Electrochimica Acta 47(1) (2001) 319-325.

193. K. Fushimi, K.I. Takase, K. Azumi, M. Seo, *Current transients of passive iron observed during micro-indentation in pH 8.4 borate buffer solution*, Electrochimica Acta 51(7) (2006) 1255-1263.

194. D. Landolt, *Electrochemical and materials aspects of tribocorrosion systems*, Journal of. Physics (D) 39 (2006) 3121-3127.

195. Y. Yan, A. Neville, D. Dowson, *Biotribocorrosion of CoCrMo orthopaedic implant materials--Assessing the formation and effect of the biofilm.* Tribology International 40 (2007) 1492-1499.

196. Y. Yan, A. Neville, D. Dowson, *Biotribocorrosion - an appraisal of the time dependence of wear and corrosion interactions: II. Surface analysis.* Journal of Physics D (Applied Physics) 39(2006) 3206-3212.

197. Y. Yan, A. Neville, D. Dowson, S. Williams, J. Fisher, *Tribo-corrosion analysis of wear and metal ion release interactions from metal-on-metal and ceramic-on-metal contacts for the application in artificial hip prostheses.* Proceedings of IMechE (J) Engineering Tribology, 222(2008) 483-492.

198. Y. Yan, A. Neville, D. Dowson, S. Williams, J. Fisher, *The influence of swing phase load on the electrochemical response, friction and ion release of metal-on-metal hip prostheses in a friction simulator.* Proceedings of IMechE (J) Engineering Tribology 223(2009) 1-8.

199. Lucas Anissian, H., Stark, A., Good, V., Dahlstrand, H., Clarke, I.C., *The wear pattern in metal-on-metal hip prostheses.* Journal of Biomedical Materials Research, 2001. **58**(6): p. 673-678.

200. M.G. Gee, A.J. Gant, M. Hutchings, Y. Kusano, K. Schiffman, K. Van Acker, S. Poulat, Y. Gachon, J. von Stebut, P. Hatto, G. Plint, *Results from an interlaboratory exercise to validate the micro-scale abrasion test*, Wear 259 (2005) 27-35.

201. K.L. Rutherford, I.M. Hutchings, *A micro-abrasive wear test, with particular application to coated systems*, Surface and Coatings Technology 79(1-3) (1996) 231-239.

202. A. Mersmann, *Crystallization Technology Handbook* 2001 CRC Press.

203. R.I. Trezona, D.N. Allsopp, I.M. Hutchings, *Transitions between two-body and three-body abrasive wear: Influence of test conditions in the microscale abrasive wear test*, Wear 225-229(I) (1999) 205-214.

204. M.M. Stack, *Bridging the gap between tribology and corrosion: From wear maps to Pourbaix diagrams*, International Materials Reviews 50(1) (2005) 1-17.

205. *NanoTest TM user manual. MicroMaterials Ltd. 2001.*

206. D. Newey, M.A. Wilkins, H.M. Pollock, *An ultra-low-load penetration hardness tester.* Journal of Physics E (Scientific Instruments)15(1) (1982) 119-122.

207. Bello, J.O., Wood, R. J. K., Wharton, J.A. *Micro abrasion-corrosion of AISI 316L stainless steel*. in *Proceedings of the IRG-OEDC on Wear of Engineering Materials, June 2005, Uppsala, Sweden.* 2005.

208. J.C. Zhao, *Methods for Phase Diagram Determination* 2007 Elsevier.

209. F. Contu, B. Elsener, H. Bohni, *Characterization of implant materials in fetal bovine serum and sodium sulfate by electrochemical impedance spectroscopy. I. Mechanically polished samples*, Journal of Biomedical Materials Research, 62(3) (2002) 412-421.

210. A.W.E. Hodgson, S. Kurz, S. Virtanen, V. Fervel, C.O.A. Olsson, S. Mischler, *Passive and transpassive behaviour of CoCrMo in simulated biological solutions*, Electrochimica Acta 49 (13) (2004) 2167-2178.

211. A. Ouerd, C. Alemany-Dumont, B. Normand, S. Szunerits, *Reactivity of CoCrMo alloy in physiological medium: Electrochemical characterization of the metal/protein interface*, Electrochimica Acta 53(13) (2008) 4461-4469.

212. A. Igual-Muñoz, S. Mischler, *Influence of proteins and phosphates on the tribocorrosion behaviour of High Carbon and Low Carbon CoCrMo biomedical alloys*. In the *211th ECS Meeting* 2007 Chicago, USA.

213. F. Contu, B. Elsener, H. Bohni, *Stability and repassivation of metallic implants in serum bovine*, European Cells and Materials 1(1) (2001) 14-15.

214. H. Zitter, H., Plenk Jr., *The electrochemical behavior of metallic implant materials as an indicator of their biocompatibility*, Journal of Biomedical Materials Research 21(7) (1987) 881-896.

215. M. Metikos-Hukovic,Z. Pilic, R. Babic, D. Omanovic, *Influence of alloying elements on the corrosion stability of CoCrMo implant alloy in Hank's solution*, Acta Biomaterialia 2(6) (2006) 693-700.

216. F.B. Growcock, R.J. Jasinski, *Time-Resolved Impedance Spectroscopy of Mild Steel in Concentrated Hydrochloric Acid*, Journal of The Electrochemical Society 136(8) (1989) 2310-2314.

217. D.R. Jackson, S. Omanovic, S.G. Roscoe, *Electrochemical studies of the adsorption behaviour of serum proteins on titanium*, Langmuir 16 (2000) 5449-5457.

218. J. Hubrecht, *Electrochemical impedance spectroscopy as a surface analytical technique for biomaterials*, in Metals as biomaterials, J.A. Helsen and J. Breme, Editors. 1988 John Wiley & Sons New York. p. 405-466.

219. *Dekker Encyclopedia of Nanoscience and Nanotechnology*, Vol 4, J.A. Schwarz, C. I. Contescu, and K.Putyera, Editors. 2004 CRC Press.

220. S. Xiao, M. Wieland, S. Brunner, *Surface reactions of 4-aminothiophenol with heterobifunctional crosslinkers bearing both succinimidyl ester and maleimide for biomolecular immobilization*, Journal of Colloid and Interface Science,290(1) (2005) 172-183.

221. D. Jermakowicz-Bartkowiak, B.N. Kolarz, W. Tylus, *Sorption of aurocyanide and tetrachloroaurate onto resin with guanidine ligand--an XPS approach*, Polymer 44(19) (2003) 5797-5802.

222. M. Salavati-Niasari, *Nanoscale microreactor-encapsulation 14-membered nickel(II) hexamethyl tetraaza: synthesis, characterization and catalytic activity.* Journal of Molecular Catalysis A: Chemical 229(1-2) (2005) 159-164.

223. H. Wang, H.P. Ho, K.C. Lo, K.W. Cheah, *Growth of p-type ZnO thin films by (N, Ga) co-doping using DMHy dopant*, Journal of Physics D (Applied. Physics) 40 (2007) 4682-4685.

224. D. Marton, K.J. Boyd, A.H. Al-Bayati, S.S. Todorov, J.W. Rabalais, *Carbon Nitride Deposited Using Energetic Species: A Two-Phase System*, Physical Review Letters 73(1) (1994) 118-121.

225. C. Ton-That, A.G. Shard, R.H. Bradley, *Thickness of spin-cast polymer thin films determined by angle-resolved XPS and AFM tip-scratch methods*, Langmuir 16 (2000) 2281-2284.

226. J. Sainio, *Electron spectroscopy studies of vacuum deposited chromium and cobalt layers*, PhD thesis, in Department of Engineering Physics and Mathematics. 2005, Helsinki University of Technology: Finland.

227. A. Jablonski, C.J. Powell, *Comparisons of practical attenuation lengths obtained from different algorithms for application in XPS*, Surface Science, 520(1-2) (2002) 78-96.

228. R.A. Buchanan, E.D. Rigney Jr., J.M. Williams, *Ion implantation of surgical Ti-6Al-4V for improved resistance to wear-accelerated corrosion*, Journal of Biomedical Materials Research 21(3) (1987) 355-366.

229. C. Leinenbach, C. Fleck, D. Eifler, *Characterization of mechanically induced surface damage on the implant alloy TiAl6Nb7 in quasi-physiological media.* Materialwissenschaften und Werkstofftech 33(8) (2002) 442-447.

230. G.H. Isaacs, *The localized breakdown and repair of passive surfaces during pitting*, Corrosion Science 29(2/3) (1989) 313-323.

231. G.H. Isaac, *Comments*. Corrosion Science 34(3) (1993) 525-528.

232. A.C. Lewis, P.J. Heard, *The effects of calcium phosphate deposition upon corrosion of CoCr alloys and the potential for implant failure*. Journal of Biomedical Material Research - Part A 75 (2) (2005) 365-373.

233. K.P. Ishida, P.R. Griffiths, *Investigation of Polysaccharide Adsorption on Protein Conditioning Films by Attenuated Total Reflection Infrared Spectrometry II. Thin Copper Films*, Journal of Colloid & Interface Science 213(2) (1999) 513-524.

234. F. Georges-Louis, *Interaction of deamidated soluble wheat protein (SWP) with other food proteins and metals*, PhD thesis, 1996, the University of Surrey: UK.

235. V.B. Galazka, D.A. Ledward, I.G. Sumner, E. Dickinson, *Influence of High Pressure on Bovine Serum Albumin and Its Complex with Dextran Sulfate*, Journal of Agricultural Food Chemistry 45(9) (1997) 3465-3471.

236. X.F. Yang, D.S. Wang, Z.X. Sun, H.X. Tang. *Adsorption of phosphate at the aluminum (hydr)oxides–water interface: Role of the surface acid–base properties*, Colloids & Surfaces A: Physicochemical and Engineering Aspects 297(1-3) (2007) 84-90.

237. T. Band, J. Metcalf, H. Jones, *Metal on metal bearing wear of femoral hip orthopaedic implants produced in cobalt chromium molybdnum alloy*, Journal of Bone & Joint Surgery 86B (2001) 402-403.

238. B. Kasemo, J. Gold, *Implant surfaces and interface process*, Advanced Dental Research 13 (1999) 8-20.

239. T. Murakami, Y. Sawae, K. Nakashima, S. Yarimitsu, T. Sato, *Micro- and nanoscopic biotribological behaviours in natural synovial joints and artificial joints*, In Proceedings of the Institution of Mechanical Engineers(H) 221(3) (2007) 237-245.

240. M.A. Wimmer, C. Sprecher, R. Hauert, G.Tager, A. Fischer, *Tribochemical reaction on metal-on-metal hip joint bearings: a comparison between in-vitro and in-vivo results*, Wear 255 (2003) 1007-1014.

241. Y. Takami, S. Yamane, K. Makinouchi,G. Otsuka, J. Glueck, R. Benkowski, Y. Nos, *Protein adsorption onto ceramic surfaces*, Journal of Biomedical Materials Research 40(1) (1998) 24-30.

242. W.D. Callister, *Materials science and engineering: an introduction*, 5th Ed. 1999 John Wiley & Sons Inc.

243. R. Büscher, A. Fischer, *Metallurgical Aspects of Sliding Wear of fcc Materials for Medical Applications.* Materialwissenschaft und Werkstofftechnik 34(10-11) (2003) 966-975.

244. S.A.V. Swanson, M.A.R. Freeman, *The Scientific Basis of Joint Replacement* 1977 Wiley, New York.

245. V.I. Levitas, *A microscale model for strain-induced phase transformations and chemical reactions under high pressure*, Europhysics Letters 66(5) (2004) 687-693.

246. Z. Lu, H. McKellop, *Frictional heating of bearing materials tested in a hip joint wear simulator.* Proceedings of the Institution of Mechanical Engineers(H) 211(1) (1997) 101-108.

247. V.B. Galazka, I.G. Sumner, D.A. Ledward, *Changes in protein-protein and protein-polysaccharide interactions induced by high pressure*, Food Chemistry 57 (1996) 393-398.

248. Y.S. Liao, P.D. Benya, H.A. McKellop, *Effect of protein lubrication on the wear properties of materials for prosthetic joints*, Journal of Biomedical Materials Research 48(4) (1999) 465-473.

249. C. Suzuki, K. Suzuki, K. Kitamura, J. Osvgi, *The protein denaturation under high pressure- Effects of pH and Some Substances on the Pressure Denaturation of Ovalbumin Solution*, The review of physical chemistry of Japan 32(1&2) (1962) 37-42.

250. B. Lu, A. Marti, H. McKellop, *Wear of a second-generation metal-on-metal hip replacement effect of third-body abrasive particles*, In the *Sixth World Biomaterials Congress* 2000 USA.

251. S.S. Brown, I.C. Clarke, *A review of lubrication conditions for wear simulation in artificial hip replacements,* Tribology transactions 49(1) (2004) 72-78.

252. J.C. Hamer, R.S. Sayles, E. Ioannides, *Deformation mechanisms and stresses created by 3rd body debris contacts and their effects on rolling bearing fatigue,* in Proceedings of the 14th Leeds-Lyon Symposium on Tribology, 1987.

253. M. Mirghany, Z.M. Jin, Z. M., *Prediction of scratch resistance of cobalt chromium alloy bearing surface, articulating against ultra-high molecular weight polyethylene, due to third-body wear particles.* Proceedings of the Institution of Mechanical Engineers (H) 218(1) (2004) 41-50.

254. R.S. Sayles, E. Ioannides, *Debris damage in rolling bearings and its effects on fatigue life*, Transaction ASME, Journal of Tribology 110 (1988) 26-31.

255. J. Fisher, X.Q. Hu, J.L. Tipper, T.D. Stewart, S. Williams, M.H. Stone, C. Davies, P. Hatto, J. Bolton, M. Riley, C. Hardaker, G.H. Isaac, G. Berry, E. Ingham, *An in vitro study of the reduction in wear of metal-on-metal hip prostheses using surface-engineered femoral heads.* In Proceedings of the Institution of Mechanical Engineers (H) 216(4) (2002) 219-230.

256. K. Adachi, I.M. Hutchings, *Sensitivity of wear rates in the micro-scale abrasion test to test conditions and material hardness*, Wear 258 (2005) 318-321.

257. D. Landolt, D. Mischler, M. Stemp, S. Barril, *Third body effects and material fluxes in tribocorrosion systems involving a sliding contact*. Wear 256 (2003). 517-524.

258. L.G. Wright, V.K. Sethi, *Some thoughts on the contributions of bed particle properties to the FBC tube wastage problem,* in Proceedings of the Symposium on Corrosion and Particle Erosion at Elevated Temperatures 1989 Las Vegas.

259. J.O. Bello, R.J.K. Wood, J.A. Wharton, *Synergistic effects of micro-abrasion-corrosion of UNS S30403, S31603 and S32760 stainless steels*, Wear 263 (2007) 149-159.

260. T. Yamamoto, K. Fushimi, M. Seo, S. Tsuri, T. Adachi, H. Habazaki, *Current transient during repeated micro-indentation test of passive iron surface in pH 8.4 borate buffer solution*, Electrochemistry Communications 9 (2007) 1672-1676.

261. A. Chiba, K. Kumagai, N. Norura, S. Miyakawa, *Pin-on-disk wear behavior in a like-on-like configuration in a biological environment of high carbon cast and low carbon forged Co-29Cr-6Mo alloys*, Acta Materialia 55(4) (2007)1309-1318.

262. *Dislocations and properties of real materials*. *Proceedings of the conference to celebrate the fiftieth anniversary of the concept of dislocation in crystals*. 1984. London: The Institute of Metals.

263. H.R. Shetty, T.H. Kosel, N.F. Fiore, *A study of abrasive wear mechanisms in cobalt-base alloys*, Wear 84(3) (1983) 327-343.

264. H.R. Shetty, T.H. Kosel, N.F. Fiore, *A study of abrasive wear mechanisms using diamond and alumina scratch tests*, Wear 80 (1982) 347-376.

265. G.B. Olson, M. Cohen, *Kinetics of strain-induced martensitic nucleation,* Metallurgical Transactions A 6A (1975) 791-795.

266. A. Salinas-Rodriguez, J.L. Rodriguez-Galicia, *Deformation behavior of low-carbon CoCrMo alloys for low-friction implant applications,* Journal of Biomedical Material Research 31 (1996) 409-419.

67. X. Wu, N. Tao, Y. Hong, J. Lu, K. Lu, $\gamma \rightarrow \xi$ *martensite transformation and twinning deformation in fcc cobalt during surface mechanical attrition treatment*, Scripta Materialia 52 (2005) 547-551.

268. J.C. Walker, I.M. Ross, W.M. Rainforth, M. Lieblich, *TEM characterisation of near surface deformation resulting from lubricated sliding wear of aluminium alloy and composites*, Wear 263(1-6) (2007) 707-718.

269. K. Adachi, I.M. Hutchings, *Wear Mode Mapping for the Micro-scale Abrasion Test*, Wear 255 (2003) 23-29.

270. P.H. Shipway, C.J.B. Hodge, *Microabrasion of glass - the critical role of ridge formation*, Wear 237 (2000) 90-97.

271. R.S. Dwyer-Joyce, J. Heymer, *The entrainment of solid particles into rolling elastohydrodynamic contacts*. In Proceedings of the 22nd Leeds-Lyon Symposium on Tribology, 1995, Lyon, France.

272. P.H. Shipway, J.J. Hogg, *Dependence of microscale abrasion mechanisms of WC-Co hardmetals on abrasive type*, Wear 259 (2005) 44-51.

273. P.H. Shipway, *A mechanical model for particle motion in the micro-scale abrasion wear test*, Wear 257 (2004) 984-991.

274. P.H. Shipway, S. Wirojanupatump, *The role of lubrication and corrosion in abrasion of materials in aqueous environments*, Tribology International 35(10) (2002) 661-667.

275. H. Mishina, M. Kojima, *Changes in human serum albumin on arthroplasty frictional surfaces*, Wear 265(5-6) (2008) 655-663.

276. M.A. Wimmer, R. Nassutt, C. Sprecher, J. Loos, A. Fischer, *Investigation on stick phemomena in metal-on-metal hip joints after resting period.* In Proceedings of Institution of Mechanical Engineers (H) 220 (2006) 219-227.

277. L. Que, D.T. Topoleski, *Third-body wear of cobalt-chromium-molybdenum implant alloys initiated by bone and poly(methyl methacrylate) particles*, Journal of Biomedical Materials Research 50(3) (2000) 322-330

278. *Shreir's Corrosion*. In Print. Tony Richardson, Bob Cottis, and S.L. Rob Lindsay, David Scantlebury, Howard Stott, Mike Graham, Editors. Elsevier.

279. W. Lia, D.Y. Li, *Variations of work function and corrosion behaviors of deformed copper surfaces*, Applied Surface Science 240(1-4) (2005) 388-395.

280. J. Enerhaug, U. Steinsmo, O. Grong, L.R. Hellevik, *Dissolution and Repassivation Kinetics of a 12.3Cr-2.6Mo-6.5Ni Super Martensitic Stainless Steel*, Journal of Electrochemistry Society 149(6) (2002) B256-B264.

281. F. Contu, B. Elsener, F. Assi, H. Bohini, *Repassivation Behavior of Metallic Implants in Inorganic and Physiological Electrolytes*, in Materials for Medical Engineering, H. Stallforth and P. Revell, Editors. 2005. WILEY-VCH. p. 236-242.

.

Appendix

Herzian contact calculation for Table 8.1.

Contact area radius:

$$a = (\frac{3WR}{4E*})^{1/3} = 1.94\ \mu\text{m}$$

Where $\frac{1}{E*} = \frac{1-v_{sample}^2}{E_{sample}} + \frac{1-v_{ball}^2}{E_{ball}}$, $E* \sim 203$ GPa

$$\frac{1}{R} = \frac{1}{R_{ball}} + \frac{1}{R_{sample}} = \frac{1}{R_{ball}} + \frac{1}{\infty},\ R = R_{ball} = 12.7\ \text{mm}$$

W=200 mN

Maximum shear stress $\tau_{\max}$ takes place at 0.48 *a* below the surface, $\tau_{\max} = 0.31 p_0$

$$p_0 = \frac{3W}{2\pi a^2} \approx 25\ \text{GPa}$$

Hence $\tau_{\max} = 0.31 p_0$ =7.8 GPa

Depth at which maximum shear occurs is 0.48 a, or 0.93 µm

Mean contact pressure $p_{mean} = \frac{2}{3} p_0 = 16$ GPa

Load at first yield $W_y = 21.17 Y^3 / E*^2 = 185$ mN

Where $Y = \frac{p_0}{1.6}$